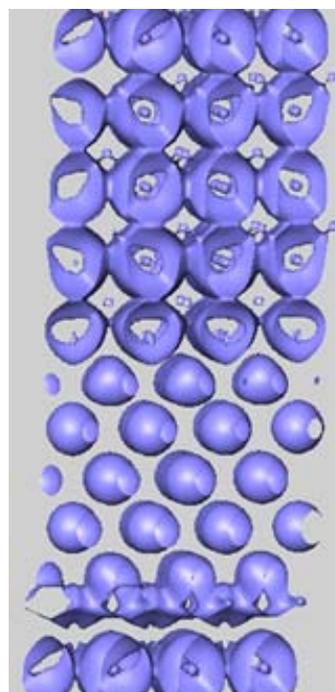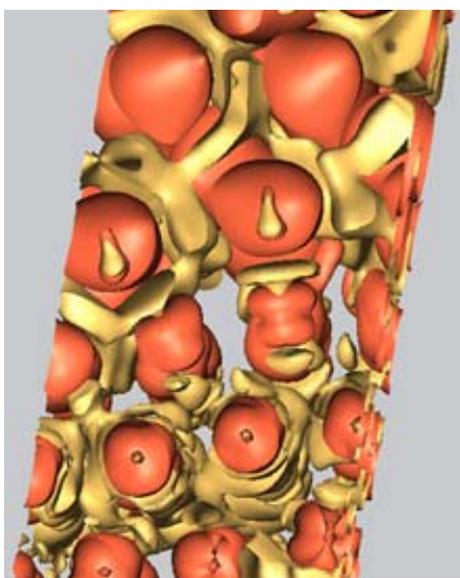# FIRST-PRINCIPLES STUDY OF THE ATOMIC PROPERTIES AND ADHESION AT METAL-CERAMIC INTERFACES

BY

JUAN I. BELTRÁN FÍNEZ

phD THESIS

Mª Carmen Muñoz de Pablo, Advisor

November 13, 2006

A mi padres y a Cris.

Agradecimientos/Acknoledgments

Table of Contents

List of tables

List of figures

Resumen

Nuevos materiales con propiedades diseñadas a medida pueden obtenerse combinando componentes de muy diversas características. Entre ellos, los sistemas cuyos constituyentes son materiales cerámicos y metales muestran propiedades que cubren los requerimientos de un amplio espectro de aplicaciones multifuncionales. La capacidad y confianza que otorgan, sin embargo, viene determinada en ocasiones por la calidad de la intercara y especialmente por la adhesión que presenta la misma.

Un gran esfuerzo científico se ha centrado en caracterizar y comprender los mecanismos atómicos que ocurren en la intercara. Experimentalmente los avances en técnicas microscópicas y espectroscópicas, como la microscopía electrónica de transmisión de alta resolución (HRTEM) y espectroscopía de pérdida de energía de electrones (EELS), han permitido acceder al conocimiento de la estructura atómica y las propiedades electrónicas en las intercaras y su comparación con cálculos teóricos de escala atómica.

El fin de este estudio es investigar la adhesión mediante cálculos teóricos *ab-initio* de las intercaras que se forman entre diferentes metales y óxidos cerámicos iónicos. Se prestará atención especial al estudio sistemático de las intercaras de superficies de ZrO_2 para analizar el papel del metal en la adhesión. Sin embargo, también se analizará la interacción de ciertos metales con los materiales cerámicos: MgO, α-Al_2O_3 y HfO_2. Nuestro propósito es extraer tendencias generales y predecir las propiedades de adhesión de las intercaras metal-óxido.

Primeramente estudiamos la estructura de volumen y las propiedades electrónicas de las fases a baja presión de ZrO_2 mediante un método de *primeros principios* dentro de la teoría del funcional de la densidad. Investigamos la evolución de la estructura cúbica a fases de más baja simetría, transformaciones inducidas al aplicar una tensión externa. Dicha tensión externa se puede descomponer en una componente hidrostática, que cambia con el volumen, y una tensión de cizalla.

También discutiremos la estabilización de ZrO_2 por Y_2O_3, acción muy frecuente para obtener a temperatura ambiente las fases de la ZrO_2 de alta simetrías, cúbica y tetragonal. En este mecanismo el catión Y^{3+} del óxido aliovalente, al tener distinto estado de oxidación que el catión a sustituir, Zr^{4+}, induce vacantes de O para mantener la neutralidad de carga en el compuesto. Este tipo de vacantes, llamadas "cargadas", se estudiarán junto con la simple eliminación de átomos de O, las vacantes llamadas "neutrales" y obtenidas sinterizando en ambientes reductores, para comparar las propiedades estructurales y electrónicas resultantes con las ya obtenidas de la fase c-ZrO_2, y así obtener el papel que juegan ambos tipos de vacantes de O.

Hemos realizado un estudio general de las superficies polares y no polares de las fases volúmicas de ZrO_2. Ya que en la bibliografía existe una deficiencia de conocimiento en las propiedades estructurales a nivel atómico, nuestro objetivo es el de investigar la estabilidad, estructura y las propiedades electrónicas de dichas fases. Para esta labor empleamos diferentes tipos de *slabs* (simétricos, asimétricos… etc) para estudiar su influencia en los resultados finales.

Hemos investigado las superficies de ZrO_2 cúbica con orientaciones de bajo índice: (001), (110) y (111), al igual que la terminación (001) de las fases tetragonal y monoclínica. Para las superficies polares hemos considerado las terminaciones en Zr o O, al igual que también hemos estudiado terminaciones con la mitad de los átomos de O. Discutimos la estructura y las propiedades electrónicas junto con las energéticas tomando en consideración la contribución dipolar de los slabs asimétricos. En estos slabs, a partir de la dependencia con el espesor de las energías superficiales estimamos el valor de la constante dieléctrica de las superficies cúbicas bajo estudio.

Además, investigamos las relaciones estructurales de c-ZrO$_2$ causadas por los grados extra de libertad que se introducen por las condiciones periódicas en el slab en contacto con el vacío, y lo relacionamos con distorsiones locales hacia la estructura tetragonal. Finalmente, discutimos brevemente la estabilidad de las superficies de ZrO$_2$ mediante la combinación de cálculos de *primeros principios* con consideraciones termodinámicas.

Igualmente hemos investigado efectos magnéticos en las superficies y el volumen de ZrO$_2$. Recientemente se han obtenido medidas de ferromagnetismo de alta Tc en óxidos aislantes que no contienen ningún elemento magnético. Consideramos desde un principio el papel de los defectos de red (vacantes de Zr y de O) en las propiedades magnéticas de volumen de c-ZrO$_2$. Los resultados obtenidos para la ZrO$_2$ de volumen nos permiten establecer que la fuente principal de la magnetización local es la reducción de más del 50% de la coordinación del O con Zr. Este hecho sugiere que las superficies polares con un exceso de O son el escenario ideal para la creación del magnetismo en la ZrO$_2$, tal y como demuestran nuestros cálculos. Además, las superficies polares terminadas en O se pueden considerar como defectos de catión de dimensión quasi-2D, favoreciendo el orden magnético de largo alcance a través de una interacción de canje directo. Mostramos que esta propiedad puede ser generalizada a otros óxidos iónicos.

La parte de investigación sobre las intercaras comienza con el estudio del sistema ideal c-ZrO$_2$ /Ni, combinando diversas orientaciones relativas entre el metal y ZrO$_2$. Además de la consideración de ZrO$_2$ ideal, realizamos cálculos que incluyen la presencia actual de defectos creados por los mecanismos de estabilización de c-ZrO$_2$, para comparar más precisamente los valores de adhesión con aquellos obtenidos experimentalmente. En el caso ideal y sin defectos nos restringiremos a c-ZrO$_2$ estudiando diversas geometrías, correspondientes al ajuste de diferentes terminaciones relativas del cristal de Ni y de ZrO$_2$ como: c-ZrO$_2$(001)/Ni(001) ‖ c-ZrO$_2$[100]/Ni[110] observada experimentalmente mediante micrografías de HRTEM en compuestos nanocermet, y también un caso de intercara no polar constituido por el Ni(001) y c-ZrO$_2$(110).

Para calcular intercaras más realistas tenemos que incluir la presencia actual de óxidos dopantes en la cerámica. Hemos realizado cálculos de c-ZrO$_2$(001)/Ni(001) añadiendo tanto vacantes de O neutrales como un 20% molar en concentración de Y$_2$O$_3$ con vacantes termodinámicas. Para constituir la configuración atómica inicial nos basamos en experimentos de superficie donde añadiendo un 9.5% de Y$_2$O$_3$ a la ZrO$_2$(001) se encuentra que existe una importante densidad de vacantes de O en el plano superficial. Este dopaje confiere estabilidad a temperatura ambiente a la estructura c-ZrO$_2$ mediante la creación de vacantes de O para compensar la carga del catión aliovalente Y^{3+}. Las vacantes neutrales no están relacionadas con la compensación de carga sino con la pérdida de átomos de O de la red de ZrO$_2$. Además de las vacantes puras neutrales, hemos estudiado geometrías intermedias incluyendo ambas vacantes, neutrales y cargadas, siendo las últimas debidas a dopaje mediante Y$_2$O$_3$. Las propiedades de adhesión se muestran principalmente dependientes del tipo de vacantes de O y de la capacidad de la ZrO$_2$ para reconstruir a las fases de mayor estabilidad.

La última parte de este trabajo se enfoca a la investigación sistemática de las propiedades de adhesión de varias intercaras cerámica/metal, para establecer tendencias en la fortaleza del enlace de la intercara. Específicamente, intentamos correlacionar el trabajo de separación (Wsep) con las propiedades inherentes de los materiales que constituyen la intercara. En los cálculos modelamos las intercaras ideales sin defectos, como por ejemplo las vacantes o átomos intersticiales. Realizamos un estudio sistemático de la dependencia de las propiedades de adhesión con la elección del metal y las orientaciones relativas de metal y cerámica. Calculamos las intercaras formadas

por varios metales bcc y fcc unidos a los materiales cerámicos α-Al_2O_3, MgO, c-HfO_2 and c-ZrO_2.

Realizamos dos tipos de cálculos que dependen del desajuste entre el metal y la cerámica. Cuando el desajuste es menor que el 10%, nuestro modelo se aproxima al de intercaras formadas entre dos materiales volúmicos, mientras que cuando es mayor que el 10% modelamos el deposito de metales sobre un substrato cerámico. Clasificando las intercaras según la cerámica establecemos varias relaciones de las propiedades de adhesión con la estructura, la estabilidad y la carga electrónica del metal. También discutimos estos resultados según los mecanismos de fractura para estimar en qué intercaras es más favorable encontrar un reforzamiento de las propiedades mecánicas mediante deformación plástica.

<<Hasta el más largo camino comienza con un primer paso>>

<<Even long distances begin with a first step>>

(Proverbio chino/Chinese proverb)

Chapter 1

Introduction

1.1 Ceramic/metal interfaces

New technological needs have arisen in the last years which require the search of new systems with tailored properties obtained combining by different classes of materials. Systems which constituents are ceramics and metals are generally found as composites, Cermets, ceramic coatings on metals, or metal clusters supported by ceramic substrates. Each of the constituents has very interesting and dissimilar properties: ceramics show low thermal and electrical conductivities together with high chemical inertness, while metals present properties such as high thermal and electrical conductivity as well as plastic deformation under external pressure. All these mechanical, electrical and chemical properties can be used in an additive way to fulfill multifunctional applications [1] for example in high technology ceramics, ionic conductors, fuel cells, thermal barriers coatings (TBC), cutting tools, heterogeneous catalysis [2], and high k-dielectric materials for future transistors [3].

Independently of the final form in which the constituents are joined together, the performance and reliability of these applications are largely determined by the strength and adhesion properties at the interface, specially by the interface fracture resistance [1]. Nevertheless, although desirable, accurate predictions of fundamental adhesion properties as the fracture resistance of real ceramic/metal interfaces are not possible [4, 5] due to the inherent complexity of the problem. Even real interfaces are macroscopic objects, their properties are determined by the atomic structure of the junction, where uncertainties about the location of dopants, point defects [6] dislocations and local chemistry when reactions occur, difficult the theoretical assumptions required to build up tractable models [6-8]. In fact it is well known that the detailed structure of the interface at the atomistic level is intimately related to the interface electronic properties which in turn control the adhesion properties [9]. At present, theoretical calculations of the interface adhesion properties of specific systems are performed either applying various methods [9] based on different approximations to a particular interface configuration, or modeling different atomic structures, which makes difficult a direct comparison between the different theoretical results. Furthermore, there is a lack of systematic studies of interfaces from which, due to their complexity, general trends and interface bonding mechanisms can hardly be elucidated. Nevertheless in the last years there has been an important development of *ab-initio* calculations which have succeeded in the explanation of experimental results and the prediction of adhesion properties of simple interfaces.

On the other hand, experimental studies of interfaces are difficult and traditionally they have been obtained from macroscopic measurements of the wettability of liquid metals on ceramic surfaces [10] or of the mechanical properties of Cermets and composites for which the detailed atomic and electronic structure at the junction is unknown. On the other hand, fracture energy measurements contain information not only of the interface strength but also of the real processes of material failure which include plasticity and friction [11]. They are related to lattice dislocations and thus manifest in a length scale of more than dozens of Å [9].

Only recently, the advancements in microscopy and spectroscopy techniques together with the investigation of ceramic/metal interfaces by surface science

technology have allowed to access to the knowledge of the atomic structure and electronic characterization, and to their comparison with atomic scale theoretical calculations [8]. The future advances in this field are subject on one hand to the ability to perform theoretical models of realistic interfaces including dopants, defects, reconstruction, and on the other to control at the atomic level the conditions and processes at the interfaces.

In the following, some of the basic concepts related to the study of fracture properties will be introduced.

1.2 Interface fracture

There are different ways to perform a fracture experiment depending on the direction of the applied load with respect to the crack propagation plane [12, 13]. We will only consider the case in which the load is applied perpendicularly, that is called the opening mode, or mode I. The measured quantity is the interface fracture energy (Γ), which is defined as the energy consumed by the system when the crack propagates; the larger this value, the higher the resistance. This fundamental adhesion magnitude includes various contributions and can be expressed as:

$$\Gamma = \Gamma_0 + \Gamma_\Pi + \Gamma_\phi ,$$

where Γ_0 is the decohesion energy or adhesion energy (Wad), Γ_Π is the plastic contribution and Γ_Φ involves the friction along contact crack faces, which will be not considered.

There are two different mechanical fracture mechanisms: interface separation, or brittle debonding, and ductile interface fracture that involves plastic energy dissipation. In the former, the major contribution to the interface fracture energy comes from the decohesion energy, which takes values around 5-10 J/m^2 and can be compared with first-principles calculations of the separation energy (Wsep). This Wsep is defined as the energy required to break interface bonds and reversibly separate an interface into two free surfaces However, when plastic deformation occurs, the plastic zone nearby the crack enlarges and the fracture energy increases largely in an extremely non-linear effect reaching values above 100 J/m^2.

Plastic deformation is a notable reinforcement process of the interface since fracture energies are one order of magnitude larger than those of brittle debonding. This mechanical improvement takes place when the stress in the material shifts the metal to the plastic regime, by emitting dislocations, before any other part of the system fails. Indeed, in most ceramic/metal systems the interface is the region that fails, not allowing this process to occur. The stress intensity needed for a metal to start the first dislocation emission, and thus the plastic deformation, is called local stress intensity (K_i^e) and it has been calculated for fcc metals [14]. This parameter, when compared with the maximum stress intensity associated to the interface adhesion (K_{IC}), indicates whether the interface makes the system fail. K_{IC} can be obtained from the following expression [15]:

$$K_{IC} = \sqrt{\frac{Wsep*E_{YOUNG}}{(1-\nu^2)}} ,$$

where ν and E_{YOUNG} are the Poisson and Young modulus of the metal, respectively.

Due to the fact that a correct model of a plastic dissipation process needs to include metal dislocations, which extends along regions of at least 10-100 Å, unaffordable for a calculation, only a qualitative estimation can be provided from theory. This estimation is obtained by comparing K_i^e to K_{IC} to identify whether the interface stress intensity is larger than that needed for the metal to deform plastically.

1.3 Present state of the study of specific ceramic/metal interfaces

The state of art has been previously reviewed, both considering the theoretical and experimental results on different ceramic/interface aspects as structure, bonding, chemical reactions [16, 17], adhesion properties [18], theoretical methods available [8, 11, 19].

We will concentrate on interfaces where the ceramic material is a simple binary oxide. Many of these studies have benefited from the recent advances on several microscopy and spectroscopy techniques. One particularly useful for the analysis of ceramic/metal interfaces is the transmission electron microscopy (TEM) and high resolution TEM (HRTEM). TEM provides valuable information concerning the interface morphology, identification of reaction phases and analysis of interfacial dislocations. This technique has benefited from advances in electron imaging and data analysis to increase the capacity to quantify structure, chemistry and electronic structure of interfaces. A spectroscopic technique which has been also very important for the characterization of ceramic/metal interfaces is the electron energy loss spectroscopy (EELS). EELS provides information about the bonding type, which is determined by the mechanical and electronic properties of the interface. Usually, the core-loss region of the EEL spectrum is analyzed to obtain insight into the interface composition and electronic structure. In addition, the ionization edge onsets and EELS near-edge fine structures (ELNES) are sensitive to the local coordination and electronic structure. These techniques have been frequently employed to characterize the interface structure and bonding in many systems.

The interface structure and chemical information obtained by diverse experimental techniques is extremely useful to perform models, otherwise it is difficult to predict *a priori* preferred interfacial configurations that will lead to low-energy interface structures. A wide range of quantum mechanical computational methods have been applied to metal/ceramic systems, which can be roughly classified in empirical or semiempirical and first-principles (*ab-initio*). While the former relay on some experimental parameters, in the *ab-initio* calculations interactions are treated at the quantum level by a self-consistent solution of the Schrödinger equation. Oxide/metal interfaces may involve a variety of bonding types from ionic interactions to covalent and metallic bonds, due to the difference of the electronic structures of metal and ceramic materials. This disparity makes difficult to apply semiempirical or empirical models which require a detailed knowledge of the atomic interactions, particularly those occurring at the interface. However, the nature of the interface bonding is a result of the self consistent *ab-initio* calculations, and thus they are specially appropriate to investigate this kind of systems formed by dissimilar materials.

Recently advances in *ab-initio* calculations have allowed no only to calculate interfaces with large mismatch [20] but also to investigate defects and dopants effects [6] as well as interface depth effects [21]. Further, there have been studies combining first principles calculations with thermodynamic approaches to obtain interfacial energies of heterogeneous systems. The interface energy can be calculated for different

orientations and their comparison allows one to discuss the thermodynamic stability of the interfaces.

We will now summarize the results obtained for several specific oxide/metal systems together with some general information about the interface formation.

The {100}MgO/Ag interface has been widely studied by means of *ab-initio* calculation due to its simplicity [9]. Both materials have cubic structure with a lattice parameter 3% larger for MgO, and the interface is not reactive. High resolution electron microscope images show the presence of periodic misfit dislocations with a spacing of around 6.5 nm along <100> orientation, which was consistent with the existence of a square network of <100> edge dislocations with Burgers vector ½*a_{Ag}<100>.

Nevertheless, one of the systems that has been most investigated over the past decade is α-Al$_2$O$_3$(0001)/Nb(111), whose constituents have very similar thermal expansion coefficients so that the interface do not show residual stresses. Some of the preparation techniques employed have been molecular beam epitaxy (MBE) growth of Nb on sapphire substrates [22], and diffusion bonding [23]. The interface has been studied in detail using HRTEM and ELNES. By means of HRTEM it is known that the interface in the MBE samples is sharp and the Nb atoms at the interface layer continue the Al sublattice of the sapphire.

Bruley *et al.* [24] used interface-specific ELNES to determine the α-Al$_2$O$_3$ terminating plane of a specimen produced by MBE. While the ELNES of the Al L-edge is not changed at the interface, interface-specific components are observed in both the Nb M- and O K-edges, which leads to the conclusion that the sapphire terminates in an oxygen plane, having O-Nb bonds across the interface. However, different results are obtained in the diffusion bonding samples, where sapphire terminates in a Al layer in good agreement with multiple scattering calculations [25]. These studies indicate that the interface chemistry of some systems is highly dependent upon processing conditions.

The ZrO$_2$/Ni system has been probably the most extensively studied among the ZrO$_2$/metal combination, due to its wide technological applications. As the α-Al$_2$O$_3$/Nb system, the thermal expansion coefficients of the ZrO$_2$ and Ni are very similar, therefore the system shows no residual stresses. Dickey *et al.* [26] have shown that ZrO$_2${100}/Ni{100} interfaces are formed by the reduction of a ZrO$_2$/NiO directionally solidified eutectic. The same group also demonstrated that highly textured Ni films growth by MBE on a (100) cubic-ZrO$_2$ substrate, being the predominant orientation relationship Ni(111)/ZrO$_2$(100) although Ni(100)/ZrO$_2$(100) was also observed. In the latter observed orientations [27] the interface directions Ni[011]/ZrO$_2$[001] exhibit the smallest unit cell in the Near Coincidence Site Lattice (NCSL) theory [28].

Recently, Pecharroman *et al.* [29] have found, in ZrO$_2$ Cermets of nanometer size, by means of high resolution TEM (HRTEM) that the previous highly coincident orientation: Ni(001)/ZrO$_2$(001), Ni[110]/ZrO$_2$[100] is produced by precipitation, reduction and sinterization of nickel salts on ZrO$_2$ powder [30]. On the same system, Laguna-Bercero and co-workers grew channeled Ni-YSZ Cermets by reduction of laser-assisted directionally solidified lamellar eutectic [31]. Among the interfaces they found, the one previously shown by Pecharroman was commented to be probably one of the most stable which is also evidenced by its formation during the reduction of NiO, apart of being the interface with the best matching.

In general, the theoretical results about ceramic/metal interfaces have concentrated on MgO and Al$_2$O$_3$ with a wide variety of metals, but specially Ag, Al, Ni, Cu. For other ceramic systems the number of works is scarce, particularly for the ZrO$_2$/metals there are only results for Ni, Pt and Pd.

Probably the first *ab-initio* calculation was made by Gubanov and Dunaevskii [32]. The metal was represented by a jellium surface whose electron density is corrugated by the external potential due to the ionic crystal, treated as a half-space of ionic charge densities, described by constant spherical clouds rigidly superimposed.

Li *et al*. [33] by means of the full potential linear augmented plane-wave (FLAPW) method, found that for one monolayer of Ag on MgO the preferred coordination of the metal atoms at the interface was ontop the O atoms, at a spacing of 2.6 Å. Schönberger *et al*. [34] obtained similar results for 3 layers of MgO and 3 layers of Ag and also showed O bridge sites to be the second most favorable and ontop to Mg as the third one. Later, on the MgO(111) polar system, Goniakowski and Noguera [35] calculate the interfaces with different transition metals determining that the interfacial effects result from the combination of two mechanisms: one is the band filling modification necessary for suppressing the macroscopic dipole moment in the polar substrate, which is the one that governs the adhesion difference with non-polar interfaces, and the other is the orbital hybridization which remains essentially similar to that of a nonpolar. Moreover they predict that O-terminated interfaces have Wsep in the range 2-6 eV per metal atom while for Mg terminated it range from 0-3 eV.

The first calculations of the α-Al$_2$O$_3$(0001)/Nb(111) system by Kruse *et al*. [36] demonstrates that strong bonds result when the Nb continues the Al sublattice structure. Relaxation of the substrate atoms was essential in order to compare energies at different interface atomic sites. Batyrev *et al*. [37] and Zhang and Smith [38] incorporated the chemical potential influence using the Gibbs free energy thermodynamic potential. Zhang *et al*. determined that the interface between Al(111) and α-Al$_2$O$_3$(0001) is oxygen terminated, except at the lowest oxygen potentials range, while for Ag(111) on α-Al$_2$O$_3$(0001) the interface is Al terminated almost through all oxygen potential range. Batyrev *et al*. work was performed on α-Al$_2$O$_3$(0001)/Nb(111) and established that the expected interface is Al enriched, despite the O terminated one is much stronger. They also calculate the work of separation.

Further, Wang *et al*. [39] compared for the α-Al$_2$O$_3$(0001)/Al(111) system *ab-initio* calculations with fracture experiments and concluded it is necessary to include 1/3 ML of C impurity to correctly describe the experimental finding of Al bulk failure. In addition, Zhang *et al*. [40] compared *ab-initio* calculations of Ni and Cu interfaces on α-Al$_2$O$_3$ with sessile drop and fracture measurements. α-Al$_2$O$_3$/Ni interfaces have a large work or separation which could explain the high interface toughness due to plastic dissipation observed in O-rich interfaces produced by diffusion bonding. However, when formed by oxidation of NiAl alloys, the interface is predicted to be Al terminated with lower Wsep, which is also in accordance with the experimental observation of lack of plasticity.

For ZrO$_2$/Ni systems, the first study was performed by Christensen and Carter [41] on the ZrO$_2$(111)/Ni(111) orientations. The results indicated that image charge interactions are dominant for thick ceramic films, while for monolayers the covalent interactions are the dominant ones. This works illustrates the power of *ab-initio* calculations to extract out the bonding contribution dependence with the thickness of the slab. Up to now and to our knowledge, on ZrO$_2$/metal interfaces the existing *ab-initio* calculations, not only concerning the determination of the adhesion properties, are performed on tetragonal-ZrO$_2$/Pt by Eichler [42] on c-ZrO$_2$/Pd, Pt by Alfredsson [43,

44], and C. Jung [45, 46] and works on c-ZrO$_2$/Ni performed by Christensen and Carter [41] and X. Han et at [47]. However, concerning interface adhesion calculations among those works, we remark that each group considers a different geometry, readily, Alfredsson's calculates metal monolayers, Eichler by Pt clusters and Christensen consider ZrO$_2$ overlayer on Ni. While for the Pt and Pd adlayer on ZrO$_2$ of the former group concludes that the interface interactions are characterized by electrostatic forces and slight hybridization, Carter *et al.* conclude on ZrO$_2$(111)/Ni(111) than from small number of layers covalency character dominates.

1.4 Goals of the present study

The purpose of this study is to investigate the adhesion of different metals on ionic ceramic oxides by *ab-initio* theoretical calculations. Special attention is paid to the systematic investigation of interfaces between several metals and ZrO$_2$ surfaces in order to analyze the role of the metal component on the adhesion. Nevertheless, the interaction of particular metals on MgO, α-Al$_2$O$_3$ and HfO$_2$ surfaces is also studied. Our aim is to predict the structural and electronic properties of various interfaces and try to extract general trends. Although most of the calculations have been performed for ideal interfaces, the role of oxygen vacancies and yttrium dopant on the adhesion of the ZrO$_2$/Ni systems has also been investigated.

The work is organized as follows:

In chapter 2 we present the general concepts of *ab-initio* calculations focusing on DFT. We discuss the different approximations considered: exchange-correlation models, pseudopotentials ...etc, and gives the parameters to be employed. It also describes the theoretical tools used to characterize the interface bonding. The chapter concludes with a discussion of the stability and the thermodynamical approach used to obtain interface and surface energies.

In chapter 3 we describe deeply the electronic and structural properties of all low pressure ZrO$_2$ phases, and briefly those of the rest of the ceramics investigated, that is, HfO$_2$, α-Al$_2$O$_3$ and MgO. ZrO$_2$ is also studied under external stress effect in order to get insight into its phase transformations. Then, we discuss a more realistic c-ZrO$_2$ in which aliovalently oxides are included, adding O vacancies and dopant oxide cations, to study its differences with the ideal c-ZrO$_2$. We also describe the pseudopotential parameters of all the elemental atoms employed on the interface calculations, both using the GGA and LDA exchange-correlation approximations.

In chapter 4 we study the surfaces of low pressure ZrO$_2$ phases, focusing on the stoichiometry, symmetry and outer layer polarity. We discuss structural and electronic properties together with energetic taking into account the correction to the electric dipole contribution of the asymmetric slabs. We also analyze the structural relaxation of the c-ZrO$_2$ surfaces to relate with possible local distortions towards the tetragonal phase.

Surface and bulk magnetic effects are investigated in chapter 5. In addition to the SIESTA calculations we have studied t-HfO$_2$ surfaces with the VASP code. We consider O and Zr vacancies in ZrO$_2$ bulk systems and surfaces of ionic oxides, namely: ZrO$_2$, α-Al$_2$O$_3$ and MgO. The origin of the magnetism is investigated and analyzed in the surfaces in terms of the ionic charges, cation-O coordination… etc.

Interface results are presented in chapters 6 and 7. Chapter 6 regards on the study of the c-ZrO$_2$/Ni interfaces both for ideal and more realistic models, the latter with the inclusion of defects at the interface. The adhesion properties are shown to depend mainly on the O vacancies type and the ability of the ZrO$_2$ to reconstruct to more stable phases.

Chapter 7 compiles the entire number of interfaces calculated, formed by several bcc and fcc metals joined to α-Al_2O_3, MgO, c-HfO_2 and c-ZrO_2 ceramic materials. We perform two different types of calculations depending on the misfit between the metal and the ceramic. Interfaces between two bulk materials described for supercells for mismatch less than 10%, and free surface metal overlayer for more than 10%. Classifying the interfaces by the ceramic we establish several relations of the adhesion properties to the structure, stability and electronic metal charge. We also discuss these results in terms of the fracture mechanisms in order to estimate which interfaces are the most likely to exhibit mechanical properties enhancement by plastic deformation.

Finally conclusions are given in chapter 8.

Chapter 2

Methodology

2.1 Introduction

The macroscopic physical phenomena that occur when two dissimilar materials are brought into contact like adhesion, friction, surface tension of a liquid drop on a solid surface etc..., are ultimately determined by atomic mechanisms. This involves processes at the atomic length scale which are ruled by quantum mechanics laws. The Schrödinger equation is the simplest expression that compiles all the relevant interactions, and even in this simplest case, the solution may be extraordinarily complex when a large number of atoms need to be considered.

Although Schrödinger equation was formulated early in the 20th century, at present there is still a large effort to obtain new solutions. One of the most extended and successful solutions of the Schrödinger equation was developed in 1964 when Hohenberg and Kohn postulated the two theorems [48] which constitute the basis of the Density Functional Theory (DFT) [49]. Despite DFT has been a very popular method for calculations in solid state physics since the 1970s, it was not increasingly employed until the 1990s when it started to be applied in quantum chemistry, mainly due to the refinements introduced to better model the exchange-correlation interactions.

The calculations presented here are based on DFT. In the following the state of art of DFT calculations is discussed and explained in terms of the approximations that are considered.

2.2 Quantum mechanical Many body problem

The Schrödinger equation expresses within a Quantum Mechanics framework the solution of the Hamiltonian (H) of a system formed by electrons and ionic nuclei mutually interacting. This equation has the following expression [50]:

$$H\Psi = E\Psi , \qquad (2.1)$$

where the wave function (WF) $\Psi = \Psi(x_1,...,x_N; R_1,...,R_M)$ depend on the coordinates of the N electrons x_i (i<N) and M ions R_j (j<M), and E is the system energy. Ψ and E are the solutions of the Schrödinger equation, while H contains both electronic and ionic terms. The general expression of H is;

$$H = Te + T_I + Ce + C_I + V$$
$$= -\frac{1}{2}\sum_{i=1}^{N}\nabla_i^2 - \frac{1}{2}\sum_{A=1}^{M}\frac{\nabla_A^2}{M_A} + \sum_{A=1}^{M}\sum_{B>A}^{M}\frac{(Z_A Z_B)}{R_{AB}} + \sum_{i=1}^{N}\sum_{j>i}^{N}\frac{1}{r_{ij}} - \sum_{i=1}^{N}\sum_{A=1}^{M}\frac{Z_A}{r_{iA}} \qquad , \qquad (2.2)$$

where the first two terms are the kinetic energies of the electrons and the ions, respectively, the third and fourth terms are the Coulomb repulsions between electrons and between ions respectively and the fifth term is the Coulomb attraction between electrons and ions.

The situation, as described above, express a many body problem that was simplified by Born and Oppenheimer [51] considering the nucleus stationary, so that the nuclear contributions can be solved by classical expressions, while the electrons are mobile and treated quantum-mechanically. This is justified by the big difference of mass and mobility between them. Thus, the quantum mechanical problem of nuclei and electrons is reduced from 3N+3M to 3N coordinate variables describing the stationary electronic state.

Therefore the Schrödinger equation can be written as a set of electronic terms in the following way:

$$H\Psi = [T+V+U]\Psi = -\frac{1}{2}\sum_{i=1}^{N}\nabla_i^2 + \sum_{i=1}^{N}V(r_i) + \sum_{i=1}^{N}\sum_{j>i}^{N}U(r_i,r_j) = E\Psi \qquad , (2.3)$$

where T and U are the kinetic and e-e interaction universal operators, while V is system dependent or non-universal term.

2.3 Density Functional Theory

DFT provided a way to systematically map the many-body problem, with U, onto a single-body problem without U, which was based on the introduction of the density variable:

$$n = |\Psi * \Psi*| = N\int d^3r_2 \int d^3r_3 \int d^3r_N \Psi(r_1,...,r_N) * \Psi*(r_1,...,r_N) \qquad (2.4)$$

Hohenberg and Kohn proved in 1964 [48] with their first DFT theorem, that the former expression can be reversed and write Ψ as a functional of the electronic density Ψ (n). Following this procedure any other observable is also a functional of n. In particular, Hohenberg and Kohn's second theorem states that the total energy of an electronic system is an universal functional of the density E{n(r)}, and that the global energy minimum E_0 corresponds to the ground state charge density $n_0(r)$ [52].

This new theory was just previous to what Kohn and Sham (1965) [53] proposed, in order to change from a many-body electron interacting problem, with an external potential, onto a non-interacting electron problem with an effective potential. The Kohn-Sham equation is a density functional expression of a non-interacting system with the same solutions than the Schrödinger equation only when the energy is minimized. The Kohn-Sham expression is written as [52]:

$$[T_S + V_S]\Psi = E\Psi \qquad (2.5)$$

$$V_S = V + \int e^2 \frac{n_S(r')}{|r-r'|}d^3r' - V_{XC}[n_S(r)] \qquad (2.6)$$

$$= V + U + U_{NCL} - (T_S - T) = T + U + V_{XC} \quad , \qquad (2.7)$$

where V_S is the effective potential constituted by the nucleus-electron potential V, the classical Coulomb term of the e-e interaction (Hartree term) U, and V_{XC} is the sum of the non-classical Coulomb term (U_{NCL}) plus the residual factor of the kinetic energy (-

T$_s$+T), which expresses the kinetic interaction between electrons. The exchange-correlation term V$_{XC}$, is the sum of all unknown terms and must be treated generally by some approximation [52]. This treatment is exact only in the simplest systems, like the free electron gas case.

2.3.1 Exchange and correlation

By defining the XC energy density per electron $\varepsilon_{XC}\left[n(r)\right]$, E$_{XC}$ can be analytically expressed as:

$$E_{XC} = \int \varepsilon_{XC}[n_-, n_+]d^3r \qquad (2.8)$$

If, with this linear density dependence of the E$_{XC}$, we use the $\varepsilon_{XC}\left[n(r)\right]$ value from the free electron gas, we are considering the local (spin) density approximation L(S)DA [52] for the XC term. In this approximation, the electron density is constant so the XC effects come predominantly from the immediate vicinity and are not dependent on inhomogeneities of the electron density away from the reference point "r". The calculations we have performed with L(S)DA are based on parameterizations [54] of exact many-body calculations performed by Ceperley and Alder (CA) [55].

If we consider L(S)DA, and its linear density dependence, as the first term of a Taylor series expansion of the energy density, we can go one step further in the XC approximation including also some gradient corrections of the density. This is the generalized gradient approximation (GGA), introduced by Becke [56] and Perdew [57] and Perdew and Wang [58] which adopts a gradient expansion from the LDA to account the inhomogeneities of the electron density, leading to the following expression:

$$E_{GGA}(n) = \int \varepsilon_{XC}\left(n_-, n_+, \nabla n_-, \nabla n_+\right)d^3r \qquad . (2.9)$$

Although after this first trial, the GGA functional generally offered improved accuracy over the LDA, they tended to underestimate binding energies and failed in those cases where the electrons are delocalized in the uniform gas, such as metal oxides. To account for these failures Perdew, Burke and Ernzenhof constructed from first principles a numerical GGA functional called PBE [59], which constitutes the scheme we are using in our GGA calculations [59-62]. This functional involves a second-order density gradient expansion for the XC hole surrounding the electron in a system of slowly varying density. In condensed matter calculations, the GGA is known to provide an improved description of cohesive energies and magnetic properties [63] over LDA.

Some other functionals for the XC term are the hybrid ones, as the B3LYP [64-66] in which the exchange term is obtained as a combination of the DFT exchange functional and the exact exchange functional from Hartree-Fock theory. For general information about hybrid functionals see references [62, 67].

In our calculations both approximations, LDA and GGA, have been used to describe bulk properties, while the rest of results have been obtained using the GGA, which provide a better general description of the systems we have consider.

2.3.2 Method of solving: self-consistency

Since the U and V_{XC} terms of eq. 2.5 and 2.7 depends on the electronic density, they are solution dependent, which implies that in order to solve the Kohn-Sham equations; we have to proceed in a self consistent (SCF) way [53]. First, an initial guess for the density is used to obtain H, and the resulting solution of this H provides the next guess for the density in an iterative way until the solution for the density is close, measured by some tolerance parameter, to the last guess density used [68, 69].

The whole process, including SCF, to obtain the ground state of a quantum mechanical system is schematically depicted in the flux diagram:
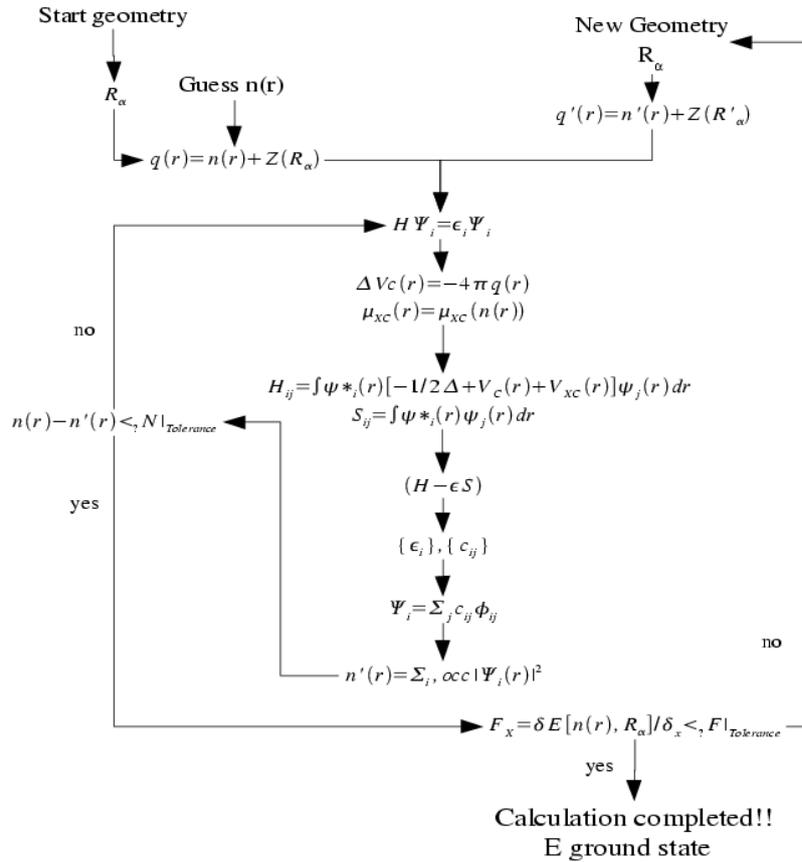
Figure 2.1: Computational process in DFT calculations from the electronic density guess and initial ionic geometry to the electronic density self consistently calculated and the equilibrium geometry.

The procedure employed to calculate the equilibrium atomic distances has been performed with the Hellmann-Feynmann theorem [70, 71]. The theorem states that in the ground state the partial derivatives of the total energy with respect to the ionic positions result into the force experienced by the ions.

The search for the minimum energy state is achieved in an iterative way as depicted in figure 2.1. First we consider the initial ionic geometry, and start the self consistent procedure to calculate the electronic density, and then we calculate the forces and use them to determine the next trial for the ionic geometry by means of the conjugate-gradient algorithm [72]. After an iterative process on the ionic forces, we reach the final

situation when the forces on every atom are less than certain tolerance parameter, chosen as explained in the section 2.4.

2.3.3 Basis sets

There are several types of basis sets in DFT calculations, but mainly two are mostly employed: Plane waves (PW) and atomic orbitals [52] (pp 97). The construction of the WF, and then the density, for different choices of the basis set implies different computational procedures that we describe in the following.

A plane waves expansion is the most straightforward extension of Bloch theorem with Periodic Boundary Conditions (PBC) [73]. Considering these assumptions we can model an infinite crystal by the repetition of a periodic cell along the three space directions. This allows us to determine the crystal properties by evaluating them at a finite number of points inside the periodic cell [74, 75]. The PW expression of the WF for a *n* band in a periodic cell reads like:

$$\Psi_{kn}(r) = e^{(ikr)} U_{kn}(r) = \sum_G C_G(kn) e^{(i(k+G)r)}, \qquad (2.10)$$

where k is the point in reciprocal space within the Brillouin Zone (BZ) and $U_{kn}(r)$ is the WF periodic part on the BZ, which can be expressed as a plane waves expansion using the reciprocal lattice vectors (G) as the wave vectors.

The main advantages of PW are: they are simple to implement, the PW basis is an orthonormal and complete set, and the accuracy of the basis set can be systematically improved by simply increasing the number of basis functions, thereby making it easy to perform convergence checks. But the main drawback arises from the non-local nature of the PW. PW's basis put weight in regions devoid of charge where no basis is needed (e.g. the vacuum region in a surface calculation).

The use of an atomic orbitals construction for the WFs is more efficient in a context that involves localized bonding. Since the shape of the system orbitals often is similar to that of atomic orbitals, usually only a small number of basis functions are needed to expand the WFs. Exploiting this natural expansion we can have a closer approach to the molecular orbital theory obtaining more intuitive values of charges, densities of states (DOS) and crystal orbital overlap populations (COOPs) projected on atoms and orbitals, which are discussed in section 2.5.

There are two main classes of atomic orbitals: Gaussian-type-orbitals (GTO) [76], and Slater-type-orbitals (STO) [77, 78]. GTO are commonly used in calculations involving multicenter integrals because they are less computational expensive [79]. STO orbitals are the most natural choice as they are the closest to the exact WF of a solid state problem. In order to have the same accuracy for GTOs than for STOs, three times more functions need to be employed. As STOs are one of the basis set type we will use in our calculations, we will briefly discuss their general properties.

The general expression of STOs reads:

$$X_{[n,m,l,\xi]}(r,\theta) = N Y_{(l,m)} r^{(n-1)} e^{(-\xi r)}, \qquad (2.11)$$

where the parameters n,l and m are quantum numbers, $Y_{l,m}$ are the spherical harmonics and ξ characterizes the size of the basis function [79].

12

STOs exhibit the correct cusp behavior at r->0 and an exponential decay when $r \to \infty$.

This expression for STOs basis set separates the angular and radial parts. The radial part can be classified in terms of the ξ exponent: the minimal basis set will employ a single ξ value called single ξ; if two basis functions are employed for the radial part then the basis is called double ξ or DZ. Three basis functions will be triple ξ and so on. Another approach used here is the "split-valence" concept, which is based on the idea that the valence orbitals are those that hold most of the information in chemical processes. Therefore with split-valence basis we can use multiple ξ for valence orbitals, while for core orbitals a single ξ is employed. The possibilities to choose the basis set are also increased with the so called Polarization orbitals. These orbitals include higher angular orbitals than those existing in the atoms studied, e.g. p-orbitals for H atom, d for first row elements... etc. This assures that orbitals can distort from their original atomic symmetry to adapt to the new environment [52] (pag 100). When a polarization function is combined with a double ξ basis set, a double zeta polarized (DZP) function is obtained. We will use DZP and DZ functions in our calculations, see chapter 3 for details.

2.3.4 Pseudopotentials

The pseudopotential (PP) formalism is an attempt to replace the complicated interactions of the nucleus and the core electrons with the valence electrons by an effective potential [80] or PP, so that the Schrödinger equation contains a modified potential term instead of true Coulomb potential terms.

Thus the core electrons and nucleus potentials are replaced by an equivalent PP, which generates a set of modified valence WF, or "pseudowavefunctions" (pWF). Figure 2.2 represents the different spatial dependences derived from the PP with respect to the original potential.

The PP approach is justified by the fact that most chemical properties are governed by the valence electrons. Thus the tightly bound core electrons are usually shielded from interactions with other species, and they do not change with different atomic environments.

The use of PP reduces the number of terms required in the calculations and hence, the computational cost [81] (page 156). The major drawback is that it introduces another approximation to the solution of the Schrödinger equation which can reduce the accuracy of the results [82].

The construction of the more accurate "norm-conserving" PP is based on four conditions due to Troullier and Martins [83]. The first is that the pWF originated from the PP contains no nodes in order to reach maximum smoothness. The second is that the pWF must be the same that the all-electron-WF beyond certain radius cut off, r_{CL}, when both radial parts are normalized. The third is that the charge enclosed within r_{CL} for these two WFs must be equal. And the last is that the eingenvalues of both potentials (*all-electron* and that related with the pWF) must be the same.

A PP is called "local" when there is no distinction among its angular momentum components. But in order to obtain more accurate approximations we can use non-local ones with different scattering behavior for each angular momentum [83].
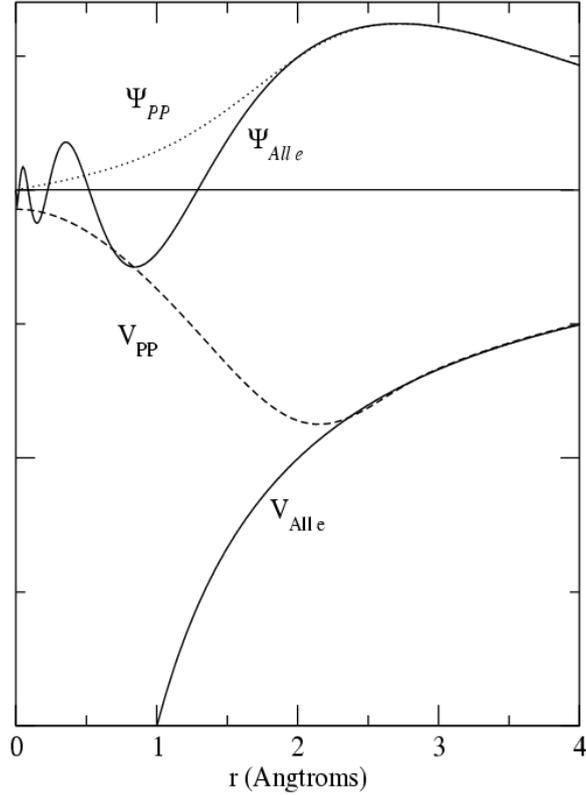
Figure 2.2: Comparison between the wave functions and potentials of the all electron calculations and those of the pseudopotentials we have employed for a transition metal.

These concepts have been employed for the pseudopotential generation in codes that employ linear combination of atomic orbitals as the basis set. However when plane waves are used some modifications are required because the calculation of pseudopotentials for first row, transition and rare-earth elements are computationally demanding.

Based on the ultrasoft PP concept developed by Vanderbilt [84] and combining it with the ideas of the linearized augmented-plane-wave (LAPW) method proposed by Blöchl [85] a so called projected augmented wave (PAW) method was created [86]. These PAW potentials are more accurate that the ultra-soft PP as they deserve smaller radial cutoffs and also provide the solution to the exact valence wave function with all nodes in the core region.

More information about PP can be found in the literature [82, 83, 87-89] and references therein.

2.4 Computational codes: SIESTA and VASP

All results presented here have been obtained using two codes based on the above formalisms, SIESTA (Spanish Initiative for Electronic Simulations with Thousands of Atoms) [90] and VASP (Vienna *Ab-initi*o Simulation Package) [91]. We have used SIESTA for calculations concerning bulk, surface and interfaces systems, VASP has been employed for surface calculations.

Both codes are based on the standard Kohn-Sham SFC DFT theory with the use of PP. In SIESTA the PP are norm-conserving in their fully nonlocal Kleinman-Bylander form [88] while in VASP the projector augmented wave method (PAW PP) is used [86].

The results of both are obtained from static calculations of the ground state (0 K) of the system. The charge density and energy of the ground state are calculated by the conjugate gradient minimization algorithm [72, 92] coupled with a Pulay-like mixing scheme [68, 93, 94]. Ground state geometries are obtained by minimizing the Hellman-Feynman forces [70, 71] up to a certain maximum force. Assigned to the 0 K distribution of the Dirac function there are numerical instabilities, therefore we have performed all calculations by setting an electronic temperature or level broadening of 100 meV.

The K point sampling of the Brillouin zone is performed with a regular Monkhorst-Pack grid [74]. Almost all the calculations we have performed with both codes are done within the GGA approximation in the PBE scheme [59] only some bulk calculations have been performed using the LDA and CA scheme [55].

A general feature of both codes is that they use slab geometries with periodic boundary conditions, the so called slab approach. Within this treatment the Bloch theorem is applied, and the calculations are done for a cell considered as a 3D periodic unit cell. This way to calculate, based on the existence of translational symmetry, does not exclude the possibility to model surfaces or crystal defects. For surfaces, a vacuum region is included in the supercell between neighbors surfaces. However, care needs to be taken in order to assure that we are not introducing any artificial interaction between the surfaces edges or defects. In addition, in the case of interfaces, a commensurable 2D cell between two different materials needs to be set; in our case of ceramic/metal interfaces, we choose to modify the metal lattices to make it match to that of the ceramic. This assumption is well justified by the more plastic behavior of metals compared to ceramic materials.

The most important difference between SIESTA and VASP is that SIESTA employs a flexible and numerical linear combination of atomic orbitals (LCAO), while VASP uses a plane-wave basis set for the expansion of the single particle WFs.

The general set of parameters we have used to evaluate the accuracy of our calculations are the standard ones specific to the SIESTA code, for further information about the computational procedure see [69, 90, 95]. Unless otherwise stated all calculations have been performed with an electronic temperature value equal to 100 meV and as energy shift of 100 meV. The energy shift is the maximum energy difference at a finite radius between the atomic-like wave function, when no r-cutting is involved and the approximate wave function employed in the atomic basis set. We have considered that all atomic basis sets have two valence orbitals, the outer energy shell of DZP type and the other one of DZ type. The mesh cutoff parameters [96] employed to perform real space integrations was set to 300 Ryd. with this value a convergence in total energy within $1.0*10^{-3}$ eV was obtained for all elements. In the case of bulk calculations, a grid in reciprocal space of Monkhorst-Pack form was used [74] with an homogeneous cutoff of at least 15.0 Å. All the atomic positions were relaxed until the atomic forces were less than $1.5*10^{-2}$ eV/Å and each stress tensor element lower than $2.5*10^{-3}$ eV/Å^3.

The settings that correspond to calculations involving surfaces were: stress tensors smaller than $2.5*10^{-3}$ eV/Å^3, atomic forces lower than $3.0*10^{-2}$ eV/Å and K-grid cutoff ranging from 11 to 16 Å with no cell repetition along the surface direction (1 K point in the Monkhorst-Pack grid).

For interface calculations the requirements were: atomic forces lower than 0.1 eV/Å and K-grid cutoff ranging from 8 to 13 Å with 1 K point along the interface direction.

The different choices depend on the geometry and size and correspond to a compromise between computational cost and accuracy.

2.5 Bonding analysis

A significant part of the work is based on the discussion of the bonding properties [97, 98] of the systems under study. To determine the bonding character from electronic structure calculations is not straightforward, particularly for heterogeneous systems as metal-ceramic interfaces, where materials with very different electronic properties are joined. Therefore the analysis of the bonding relies on various and complementary magnitudes as degree of covalency, hybridization, or transferred charge among others. In this section we summarize briefly the different quantities used to determine the electronic density distribution and bonding properties.

2.5.1 Density of States and band structure

The density of states (DOS) provides the number of electronic states as a function of the energy. It is intimately related to the band structure defined as the band energy dispersion along high-symmetry directions in reciprocal space, E(k). In general, the DOS is proportional to the inverse of the slope of E(k) [97]. Usually the results are analyzed in terms of the partial DOS, which is the projection of the DOS either on selected atoms, angular momenta, spins... etc.

The expression of the DOS is the following:

$$D\left(E, r_\alpha\right) = \sum_{nk} \int dr \Theta\left(R_\alpha - |r - r_\alpha|\right) \Psi *_{nk}\left(r\right) \Psi_{nk}\left(r\right) f\left(E - E_{nk}\right), (2.12)$$

where r_α is the position of the atom α, R_α is the chosen atomic radius, $\Theta(x)$ is the Heaviside function, and $f(E-E_{nk})$ is the occupancy of the state with energy E_{nk}. When LCAO are used as basis set, R_α is determined by the extension of the AO. However, for a PW basis set, the DOS depend on the choice of R_α and in this case the DOS can be considered only qualitatively.

2.5.2 Mulliken Populations

The Mulliken population is the energy integration of the DOS and we will refer to it from now on as the total charge. Similarly to the DOS, the total charge can be projected onto atoms, orbitals and so on, in a natural way using LCAO as basis set. When there exist an overlap population between two centers, which can be orbitals, atoms..., the Mulliken population is equally distributed among the centers that participate on it [97].

The Crystal Orbital Overlap Population (COOP) is an overlap population weighted density of states and it can adopt positive values (corresponding to a bonding interaction) and negative values (antibonding) [97].

The energy integration of the COOP is defined as the bonding overlap population (BOP) [97] which gives information about the charge shared in a bond (bond order) mediated by the Mulliken population.

Although Mulliken populations and COOPs are dependent on the AO basis set, they correctly give trends on the amount of charge transfer or AO hibridization if the calculations are performed within a consistent scheme.

2.5.3 Electronic charge density

The electronic charge density (CD) provides a very useful and illustrative tool to show the electronic charge localization. Due to the deep variations in its value depending on the different types of bonding, it is generally used after subtracting the superposition of atomic charge densities. The charge density difference (CCD) is defined in this way as:

$$\Delta n(r) = n(r) - \sum_i n_i^{atom}(r) \qquad (2.13)$$

Then positive values mean a gain of charge while negative values mean a depletion of electronic charge with respect to the isolated atoms.

Δn has been used to evaluate the bonding properties of elements and compounds [99]. In ref [99] the authors compare the CD differences with some electronegativity parameter assigned to the system.

The information from the CD would be obtained from 2D contour plots, which corresponds to isolines for cross sections containing the bonding directions.

2.6 Bulk modulus calculation from Murnaghan equation

The bulk modulus measures the response in pressure due to a change in relative volume, essentially measuring the resistance to uniform compression. It is given by:

$$B_0 = -V \frac{\partial P}{\partial V} \qquad (2.14\ a)$$

In order to calculate the bulk modulus we have used the Murnaghan equation of state. This equation was formulated by F.D. Murnaghan in 1944 [100] to express the relation in solids between the total energy and the thermodynamic quantities. It is more accurate than the previous harmonic solid and constant bulk modulus approach [101]. The Murnaghan equation has the following expression:

$$E(V) = E_0 + \frac{B_0 V}{B_0'} \left(\frac{(V_0/V)^{(B_0')}}{(B_0'-1)} + 1 \right) - \frac{(B_0 V_0)}{(B_0'-1)} , \qquad (2.14\ b)$$

where the subscript "0" indicates quantities in the equilibrium state, E(V) and $E_0(V_0)$ are the total energy at volume V or V_0 while B_0 and B_0' are the bulk modulus and its pressure derivative at constant temperature, respectively.

The Murnaghan equation is used to determine the bulk modulus from the total E obtained from first principles calculation, on a volume range of $\pm 7\%$ around the equilibrium value V_0 .

2.7 Energetic of surfaces and interfaces

The section describes the thermodynamic approach used in the calculation of the stability of surfaces and interfaces.

2.7.1 Surface and interface free energies

We are interested in the interaction of the quantum system with the surroundings or reservoirs, particularly in the surface and interface energies, which allows to know the surface and interface stability, respectively. To calculate by *ab-initio* methods the thermodynamic potential is not straightforward for materials with more than one element, as the ceramic oxides studied in this work.

Concerning a surface of a generic oxide MxOy, in contact with an O atmosphere of pressure P and temperature T, which acts as a reservoir of oxygen particles (N_O) without changing T or P, the surface Gibbs free energy (G) is given by:

$$G\ (T,P,\mu)= E + PV - TS - \mu_O N_O - \mu_M N_M, \qquad (2.15)$$

where E is the total energy, V the volume, S the entropy, μ_O and μ_M is the chemical potential of the O and metal in the oxide, and N_O and N_M is the number of the corresponding atoms, respectively.

For usual conditions of P and T, the PV and TS term can be omitted since their contributions are negligible [40, 102] and eq. 2.15 becomes:

$$G = E - \mu N = E - N_M\,\mu_M - N_O\,\mu_O , \qquad (2.16)$$

In thermodynamic equilibrium, the chemical potential of the oxide constituents is related to the Gibbs free energy of the bulk oxide g^{bulk}_{MxOy}, obtaining:

$$x*\mu_M + y*\mu_O = g^{bulk}_{MxOy} \qquad (2.17)$$
$$= x*g^{bulk}_M + (y/2)*g^{gas}_{O2} + \Delta G^f \qquad , (2.18)$$

where g^{bulk}_M and g^{gas}_{O2} are the Gibbs free energy of the metal bulk and of the O_2 molecule, respectively, and ΔG^f is the formation Gibbs free energy of the oxide. Thus, the G potential is given by:

$$G = E - \frac{N_M*g^{bulk}_{MxOy}}{x} - \mu_O(N_O - \frac{N_M*y}{x}) \qquad (2.19)$$

Therefore, the surface energy per unit area, of a system modeled by a slab with equal surfaces can be obtained from:

$$\sigma = G/(2A) , \qquad (2.20)$$

where A is the cross-sectional area.

When the system is stoichiometric the coefficient of the last term of eq. 2.19 vanishes and σ can be calculated from the total energy of the system and the Gibbs free energy of the bulk oxide. However, for non-stoichiometric systems, G will be a function of μ_O. Furthermore:

$$\mu_M \leq g^{bulk}_M \qquad \mu_O \leq \frac{1}{2} g^{gas}_{O_2} \quad , \qquad (2.21)$$

otherwise the oxide would be unstable and decompose into the elemental constituents.

Thus, σ is given by expression (2.20) and (2.19) for the range:

$$\frac{\Delta G_f}{y} \le \mu_O - \frac{1}{2}(\mu^{gas}{}_{O_2}) \le 0 \qquad\qquad (2.22)$$

The $\mu_O - 1/2$ ($\mu^{gas}{}_{O2}$) range of variation only depends on the stoichiometry of the oxide and on the ΔG^f term, which can be obtained from thermodynamic tables. This implies that $g^{gas}{}_{O2}$ is the Gibbs free energy at normal conditions, i.e., at 1 atm of pressure and T =293 K. Since *ab-initio* total energy calculations are carried out at T=0 K, the calculated values should be considered as approximate when comparing with experimental results. Nevertheless, as explained above previous calculations of surface oxides energies indicate that the T dependence contributes slightly [40, 102].

The extension to the calculation of interface stability is straightforward. In this case the system is formed by the oxide and the metal slab. Therefore:

$$\gamma = \frac{G_{INT}}{2A} = \frac{(E_{INT} - \dfrac{N_M * g^{bulk}{}_{MxOy}}{x} - \mu_O(N_O - \dfrac{N_M * y}{x}) - N_{MET} * g^{bulk}{}_{MET})}{2A}, \qquad (2.23)$$

where E_{INT} is the total energy of the interface, N_{MET} is the number of metal atoms and $g^{bulk}{}_{MET}$ is the Gibbs free energy per atom.

2.7.2 Theoretical calculation of adhesion

In order to compare the adhesion measurements of fracture energy (Γ) with *ab-initio* atomic simulations we have calculated the work of separation (Wsep). Wsep is defined as the energy required to break interface bonds and thus is the reversible work needed to separate the interface into two free surfaces if the plastic and diffussional degrees of freedom are suppressed.

$$\text{Wsep} = \sigma_{MET} + \sigma_{MxOy} - \gamma = (E_{INT} - (E_{MET} + E_{MxOy})) / (2A) , \qquad (2.24)$$

where E_{MET} and E_{MxOy} is the total energy of isolated metal and oxide systems, and σ_{MET} and σ_{MxOy} are the corresponding surface energy, respectively. If diffusion process occurs when the interface is broken to attain chemical equilibrium, Wsep would be smaller than the actual energy. Moreover, the fracture energy includes also plastic and elastic deformations [103, 104] which are dependent on Wsep although the exact expression is unknown. Therefore since dissipative processes are not considered, Wsep represents a lower bound for the actual energy involved in any experiment of fracture.

Chapter 3

Bulk properties

3.1 Introduction

In this chapter we present bulk calculations for the elemental solids and compounds, which will serve as the basis for the study of the surface and interface systems we are interested in. In addition, a comparison with the experimental data for physical magnitudes as the lattice parameter, bulk modulus and cohesive energy provides an estimate of the validity of the approximations inherent to our models. We divide our results into two groups, ceramics and metals. The ceramic group is constituted by binary oxides in their most stable thermodynamic form: ZrO_2, α-Al_2O_3, MgO and HfO_2, with special attention to ZrO_2. Afterwards metals will be briefly described. These results will serve to choose the best suited approximation for the XC potential. Finally, we include the pseudopotential and bulk structural parameters of all the elements involved in the calculations.

Ceramic oxides exhibit mostly ionic bonding character, but with some degree of covalency, which is related to the structure they form and the ratio between the radii of the anion and the cation [105]. Due to this, they show a wide range of properties like high hardness, high compressive strength, low thermal and electrical conductivity and chemical inertness [106]. The origin of the ionic bonding lies in the presence of O, one of the most electronegative elements, so that metals can transfer easily electrons to it. Among all the ceramic materials, Al_2O_3 and ZrO_2 are some of the most employed by far, and their applications extend to a wide range going from traditional pottery to engineering ceramics dealing with electronic devices, heat resistant liners, mechanical and pump seals [107]. Nowadays ZrO_2 and HfO_2 are investigated with the purpose to exploit their high values of dielectric constant and bulk modulus [108]. The former makes them good candidates for semiconductor devices as a substitute of SiO_2, while the large bulk modulus gives the possibility to use them as hard materials in different devices [109].

Zirconia or zirconium dioxide, ZrO_2, has three low pressure phases [19, 110-113] see figure 3.1, that can be ordered according to both their stability from low till melting temperatures, and to their increasing structural symmetry as: monoclinic, tetragonal and cubic. Monoclinic ZrO_2 exists in nature in the baddeleyite structure, being stable from 0 K to around 1480 K. Above 1480 K, the monoclinic structure undergoes a first-order martensitic transition to the tetragonal phase which is the most stable phase in the temperature range from 1480 to 2650 K. And finally, the most symmetric structure, cubic ZrO_2, becomes stable from 2650 K till melting temperature, 2983K. Even though at room temperature the stable phase is the monoclinic one, it is also possible to stabilize the rest of the phases by the common procedure of doping with aliovalent oxides [114] as will be explained on more detail in section 3.2.4.

HfO_2 is very similar to ZrO_2 and these similarities extend to their common structural symmetry, with a similar low pressure phases diagram [109]. One noticeably difference is that the lattice parameter of HfO_2 is smaller than that of ZrO_2, due to the lanthanide contraction [115].

Although alumina can also exist in different phases, here we will only consider the most stable phase, corundum or $\alpha-Al_2O_3$ [116, 117]. Apart of its use in technological applications, it is also employed in jewellery in the forms of ruby and sapphire that correspond to the red and blue gem quality corundum crystals.

MgO, magnesium oxide, often called magnesia, is a white solid mineral that occurs naturally as periclase and is used as a source of magnesium. Some of the most common applications of MgO are as refractories, crucibles, cements, heating elements, thermocouple tubes, brake linings, plasma Display Screens, or substrate for thin film growth [118].

We will start describing the bulk properties of ZrO_2, studying the low pressure phases separately and the transformation from the cubic structure to the high temperature phases when applying an external stress. After that, the electronic properties of the ideal phases, together with the inclusion of defects will be analyzed.

3.2 Ceramic oxides: ZrO_2

3.2.1 ZrO_2 bulk structure

The cubic phase has a space group O_{5h} or Fm3m [119] with a crystal structure known as the fluorite structure. It is characterized by a lattice parameter "a" and has a primitive cell defined by an fcc lattice and a basis of three atoms: one Zr and two O. Both O atoms occupy the tetrahedral interstitial sites of the Zr fcc substructure, being four-fold coordinated to the Zr atoms (Zr-O distance of 2.20 Å), while Zr is eight-fold coordinated to the O atoms, see left panels of figure 3.1.

The crystal structure of tetragonal zirconia has a D_{4h} or $P4_2/nmc$ space group [119] and can be viewed as a distortion of the cubic structure, as will be discussed in section 3.2.3. The distortion is characterized not only by the change of the cell symmetry, but also by a displacement of the O sublattice along the direction of the X_2^- phonon vibration [120, 121]. The sublattice displacement is described by an alternative shift up and down of the O neighbouring rows, see middle panels of figure 3.1. The tetragonal structure is characterized by two lattice parameters, "a" and "c", and a parameter $\delta = dz*c$ which evaluates the distortion of the O sublattice. Despite of the δ distortion, the Zr coordination is the same than in the cubic structure, although the eight O neighbors of Zr now are not equidistant, four being arranged in a flattened tetrahedron at short Zr-O distance, around 2.07 Å, and the rest in an elongated tetrahedron rotated 90º at a distance of 2.46 Å.

The crystal structure of the monoclinic phase has a space group C^5_{2h} or $P2_1/c$ [119]. This structure can again be regarded as a further and different distortion from the cubic structure, see unit cell at the right panels of figure 3.1. The monoclinic phase is the one with the lowest symmetry, and to be totally specified we need four lattice parameters: a,b,c and β and the nine internal coordinates of the three atoms basis of the primitive cell. The Zr coordination is reduced to seven O atoms. Here there is an additional distinction between the O atoms in the basis that does not exist in the high symmetry phases: O_I is three-fold coordinated to Zr and O_{II} four-fold, see figure 3.1. The location of the O_{II} atoms is nearly tetrahedral, with one angle (134.5º) in the structure differing significantly from the tetrahedral value (109.5º). Therefore, the structure of the O is not planar: a buckling occurs in the O_{II} plane and the distribution of the O_I atoms is quite

irregular. There is a large dispersion of interatomic Zr-O distances, with average values of 2.07 Å and 2.21 Å for Zr-O_I and Zr-O_{II}, respectively.
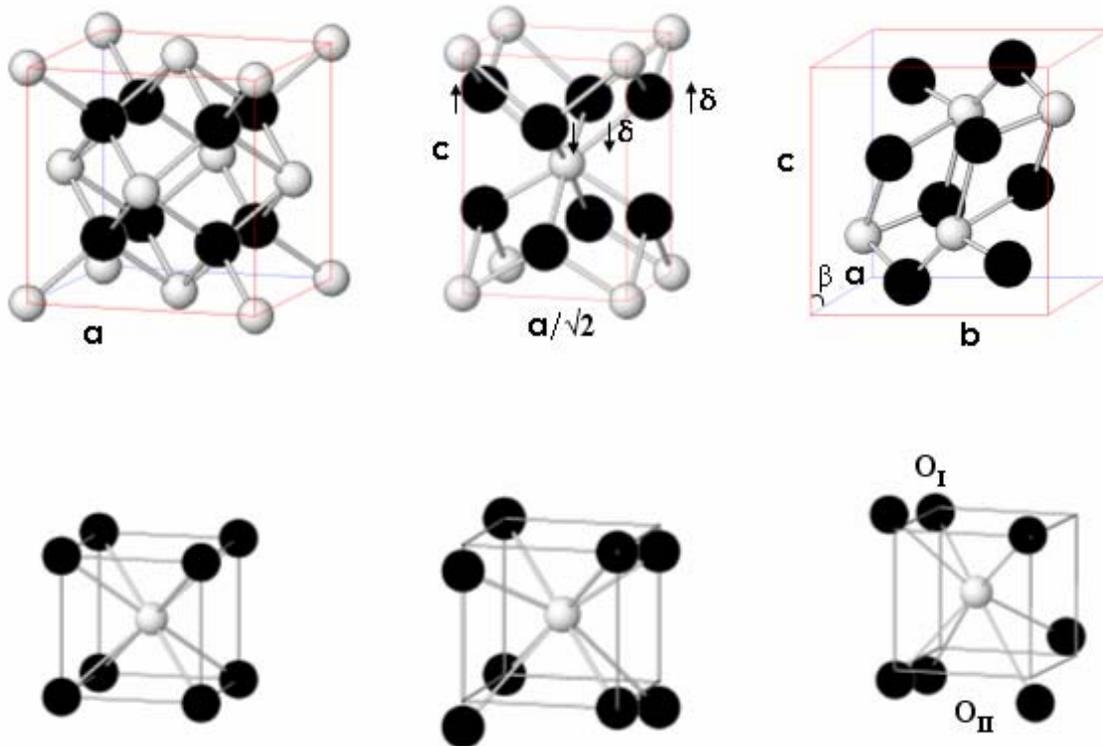
Figure 3.1: Atomic structure (top) and Zr to O coordination units (bottom) for the three low-pressure polymorphs of ZrO_2: cubic (left), tetragonal (middle) and monoclinic (right). Big dark circles denote O atoms, small light circles, Zr. The depicted cubes are a guide to the eye, and their size corresponds in all cases to the unit cell (top row) or coordination unit (bottom row). The lattice parameters of each structure and the two non-equivalent O sites at m-ZrO_2 are indicated.

Crystallographic data and lattice constants for the three low pressure ZrO_2 crystal structures are summarized in table 3.1 according to different calculations including the GGA and LDA approximations, and are compared with experimental measurements. It should be taken into account that the experimental value for the lattice parameters of c- and t-ZrO_2 are extrapolated from the actual values measured at high temperatures or in the presence of stabilizing dopant, and thus are subject to large error bars.

First of all, we can see that the theoretical calculations performed with GGA overestimate the structural values obtained experimentally, while LDA underestimates them, which is a common feature of both XC approximations [122]. All the lattice parameters we obtain with our calculations are from 2 % higher to 2.5 % lower than the experimental values obtained by neutron diffraction [123, 124].

In addition we obtain that for LDA the cubic phase does not retain the cubic symmetry when relaxed, while the monoclinic structure relaxes to a cell with a<c<b, instead of the correct order. This, together with the non correct phase energy hierarchy, we obtain $E_t<E_c<E_m$ instead of $E_m<E_t<E_c$, makes us consider GGA as a better approximation to describe ZrO_2.

Method	c-ZrO$_2$ a(Å)	t-ZrO$_2$ a(Å)	c(Å)	δ(c units)	m-ZrO$_2$ a(Å)	b(Å)	c(Å)	β	Em-Ec	Et-Ec	Refs.
Exp(ND)	5,090 [i]	5,050 [i]	5,182 [i]	0,057 [i]	5,151 [j]	5,212 [j]	5,317 [j]	99,230 [j]	-0,120	-0,057	[123] [i]
											[124] [j],[125]
HF	5,154	5,152	5,178	0,024	5,234	5,272	5,398	98,250	0,005	-0,008	[126]
LDA	5,080	5,077	5,227	0,050	5,159	5,221	5,324	99,230			[129]
LDA	5,037	5,041	5,126	0,044	5,102	5,181	5,264	99,650	-0,113	-0,049	[127]
SC-TB	5,020	5,021	5,119	0,047	5,076	5,081	5,172	98,000	-0,101	-0,041	[130]
GGA	5,164	5,168	5,364	0,060	5,192	5,254	5,358	99,230			[129]
GGA	5,090	5,131	5,250	0,049	5,192	5,265	5,358	99,810	-0,170	-0,070	[128]
Present GGA	5,160	5,134	5,280	0,050	5,170	5,280	5,410	99,780	-0,110	-0,090	
Present LDA	5,085	5,088	5,154	0,038	5,095	5,261	5,199	98,483	0,142	-0,130	

Table 3.1: Structural parameters (in Å) of cubic, tetragonal and monoclinic ZrO$_2$ according to experiment and previous calculations. The experimental data correspond to neutron diffraction (ND) [123, 124] and [125]. The theoretical values have been obtained from *ab-initio* HF [126] or DFT calculations, the latter based both in LDA [127] or GGA [128, 129], and from self-consistent semiempirical tight-binding models (SC-TB) [130]. Our results, obtained within DFT-GGA, are compiled at the end.

When GGA is used, we obtain a β angle for the monoclinic phase close to experiment and to similar theoretical calculations, and the correct energy hierarchy between phases is reproduced: $E_m < E_t < E_c$. The energy differences between phases are very close to the experimental ones, specially between the monoclinic and cubic phases. The theoretical values of the bulk modulus are difficult to compare accurately, as occurs for the lattice parameters, because the experimental measurements for the cubic and tetragonal phases include the doping oxides required to stabilize them at low temperatures. The experimental values range from 194-220 GPa for cubic [131], 190 GPa tetragonal [132], and 95-189 GPa for monoclinic [124] and our values are 235, 230 and 214 GPa with GGA for the cubic, tetragonal and monoclinic phases respectively. Our values for the bulk modulus compare well and agree with the trend of decreasing value with decreasing phase symmetry, and are similar to previous theoretical calculations [109].

In summary, we consider the description obtained by GGA for the ZrO$_2$ system better suited [133] than that obtained with LDA, according to the experimental and previous theoretical results for the values and trends of the structural parameters and bulk modulus of the different ZrO$_2$ phases. Thus, GGA will be employed from now on to calculate the ZrO$_2$ properties.

3.2.2 Ideal ZrO$_2$: Electronic structure

Within a rough ionic picture we can describe ZrO$_2$ electronic structure as a valence band formed by filled O 2p orbitals and a conduction band formed by the Zr 4d metal orbitals. We will now discuss and compare the electronic structure of the three low pressure ZrO$_2$ bulk phases by means of the dispersion relation, the total DOS and its atomic projections, the charge density differences (CDD), the COOPs and BOP. We will show that the ionic picture is too simple, and that there exist significant hybridization in the valence band (VB).

Our calculations, being based on a DFT, do not describe properly the band gap, underestimating its value respect to the experimental one by 45%, 59% and 52% in cubic, tetragonal and monoclinic phases, respectively.

Dispersion relation:

The band structures are presented in figure 3.2 for the three phases of ZrO_2. Comparing them, we can see that they are very similar in some aspects. First the lowest energy levels are the O 2s orbitals, located around 18 eV below the Fermi level (E_F). The next group of electronic levels constitutes what we previously described as VB O 2p electrons, although they contain some hybridization with the Zr levels (5s and 4d). Second, we can also see that in all phases the maximum of the VB is located at a different reciprocal point than the minimum of the conductions bands (CB), therefore the band gap is indirect, with values for our calculations (experimental) of 2.8(6.10), 3.4(5.78) and 3.0 eV (5.83) in the cubic, tetragonal and monoclinic phases respectively. The energy width of the VB differs among phases being 6 for the cubic phase and 5 eV for the tetragonal and monoclinic cases. The CB is mainly constituted by the Zr 4d orbital electron levels but, as occurred with the VB, it shows some hybridization, this time with the O 2p levels.
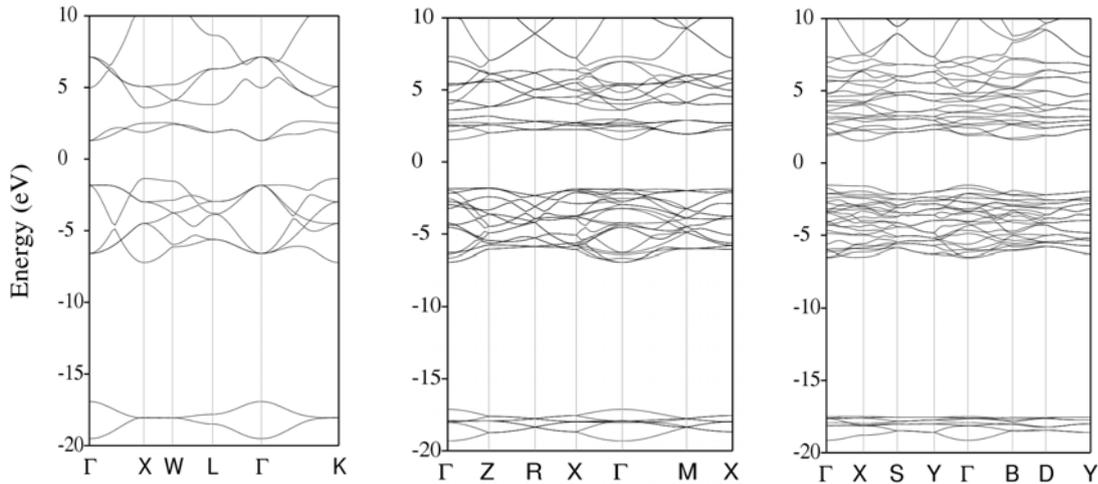
Figure 3.2: Band structure of cubic (left), tetragonal (middle) and monoclinic (right) ZrO_2 along high symmetry directions. The zero energy is set at the Fermi level.

In spite of the similarities, there are also important differences from phase to phase. Concerning the electronic levels in the CB, the minimum in each phase occurs at a different reciprocal point, and similarly occurs for the maximum in the VB. It is also noticeably how the symmetry influences the CB. For example, in the cubic and tetragonal phases we can distinguish the e_g symmetry states from those of t_{2g} symmetry due to the existence of a band gap between them. However, in the monoclinic phase this band gap no longer exists, which can be regarded as a consequence of the partly octahedral and partly tetrahedral crystal field in the monoclinic structure.

The calculated electronic properties are in good agreement with available experimental data [111] and with previous theoretical calculations [127, 134].

DOS:

Complementary information of the electronic states closely related to the band structure is the density of states (DOS) together with its projections (PDOS) on each atom, which is shown in figure 3.3. The DOS is similar in all phases, in good agreement

24

with x-ray photoemission spectra [111, 135] and previously reported theoretical studies [127, 129, 134]. Also, the experimental valence XPS spectra do not vary between the different phases [111] and show a main peak and a shoulder downshifted by ~2 eV. The valence band is predominantly occupied by O states (2p) while the conduction band is mainly occupied by Zr states (4d). The VB structure is characterized by two peaks and that of higher energy is flattened in the tetragonal and monoclinic phases, as expected from the dispersion curves. The formation of a gap between e_g-t_{2g} conduction states is clearly seen in the cubic and tetragonal phases while, as commented previously, the monoclinic one exhibits a continuous and wide structure. The absence of e_g-t_{2g} gap has been confirmed by the experimental Bremsstrahlung isochromat spectrum [135].
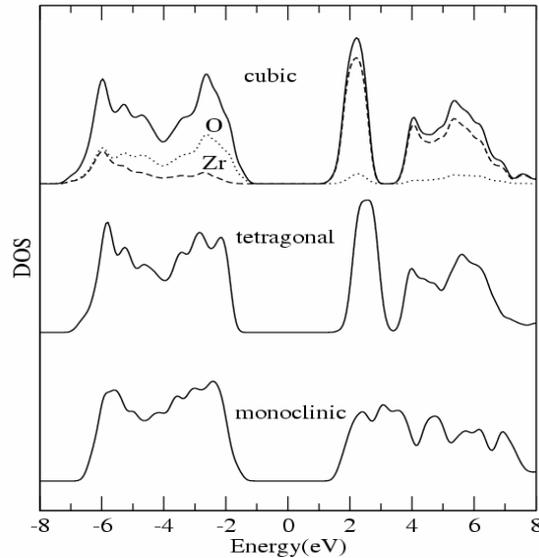
Figure 3.3: Total density of states of the three low pressure polymorphs of ZrO_2. The partial contributions of O and Zr atoms are shown for c-ZrO_2, being very similar for all structures. The zero energy is set at Fermi level.

Charges:

The specific values of the atomic Mulliken populations depend on the particular basis set we choose, but within a chosen basis, qualitative trends among phases can be defined. In particular, the degree of ionicity can be estimated from the charge transfer difference. As can be seen in table 3.2 the ionicity decreases as the symmetry decreases, the monoclinic phase being the less ionic phase, in good agreement with the experimental evidence [136]. We can also see that in c-ZrO_2 and t-ZrO_2 the O charge takes only one value, while two values are present in the monoclinic phase, related with the two types of O, figure 3.4.

COOPs:

Continuing with the study of the charge distribution we can extract additional information from the crystal orbital overlap population (COOP) between Zr and O atoms, figure 3.4. Zr-O COOPs provide a complement to the information about the electron transfer character obtained from Mulliken populations, as they give information about the Zr charge projected into the O atoms, or the amount of charge shared by Zr and O atoms. In the t-ZrO_2 phase two different types of Zr-O interaction can be distinguished that correspond to the flat tetrahedron with short Zr-O distance (upper curve) and the one with elongated distance (lower curve), while for the cubic symmetry

there is only one type of Zr-O distance. It is also clearly shown by the COOPs the previously commented difference between O_I and O_{II} oxygen types in m-ZrO_2 phase. We notice that for almost all the energy range of every phase there is a positive COOP value, and so bonding character, but just before the E_F the COOP goes to negative values, antibonding interaction, specially for Zr-O_{II} interaction in m-ZrO_2.

Structure	Q(Zr)	Q(O)	BOP	<BOP>
c-ZrO$_2$	2,424	6,788	0,142	0,142
t-ZrO$_2$	2,484	6,758	0.096,0.197	0,143
m-ZrO$_2$	2,494	6.678 O$_I$	0.207 O$_I$	0,169
		6.828 O$_{II}$	0.155 O$_{II}$	

Table 3.2: Mulliken populations (Q) of the Zr and the O atoms, together with the individual and mean values of the Zr-O bonding overlap population (BOP and <BOP>, respectively) for the cubic, tetragonal and monoclinic phases of ZrO_2. The values of BOP for O_I and O_{II} correspond to the mean of all individual Zr-O bonds for each atom.
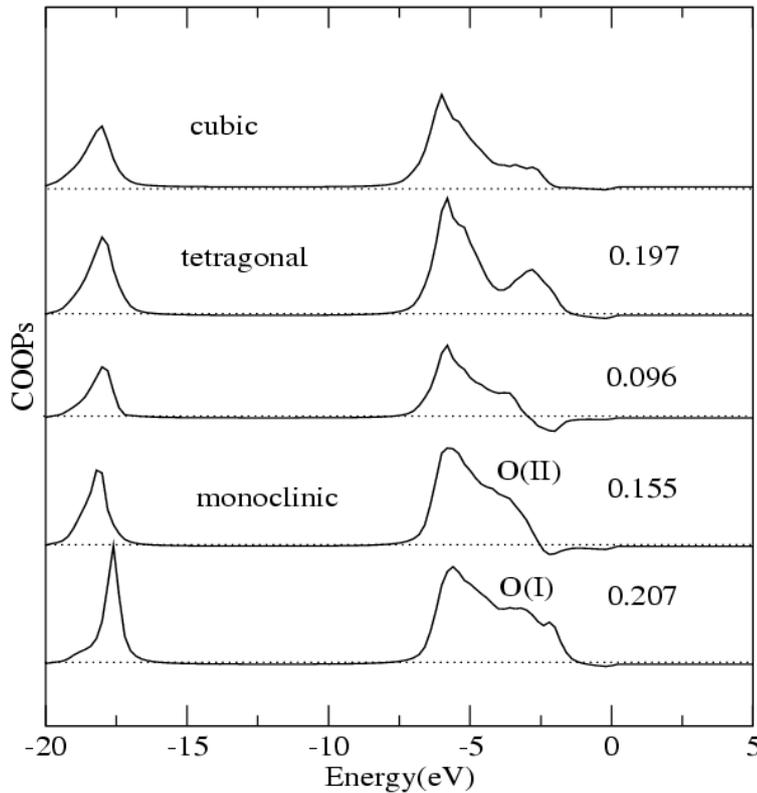
Figure 3.4: Crystal orbital overlap populations for the Zr-O bonds of the three low pressure polymorphs of ZrO_2. The zero energy is set at the Fermi level. The values at the right hand side indicates for the tetragonal phase the two Zr-O BOP values for the different types of atoms, while for the monoclinic represents two out of the seven types it can be found.

BOPs:

The COOPs can be quantitatively compared for different interactions by integrating its contribution over the energy range up to the E_F, and this way we obtain the bonding overlap population (BOP), also included in table 3.2. We show the average value of the BOP and all individual values for every Zr-O bond except for the m-ZrO_2 phase, which

has seven different values and only two are included, one of each O type. The higher the BOP value the higher the covalent character of the Zr-O interaction, and as we can see the average value follows the opposite trend to the ionicity: the less symmetric the phase, the more covalent the interaction.

CDDs:

Important information can be obtained from the plot of the electronic distribution in real space, specially along the bond directions. This is provided by the charge density differences (CDD), depicted in figure 3.5. The CDD correspond to the total charge density (CD) minus a superposition of the neutral atom CDs. Figure 3.5 is a plot of the contour lines, equally spaced by $8*10^{-4}$ electron charge, along the {110} plane of c-ZrO_2 that contains both the Zr and O atoms. The thicker line corresponds to zero CDD value that separates the electron depletion region with more concentrated lines just at Zr lobes, and the spherical electron accumulation located around the O atoms. There are lots of lines from the zero CDD value to the extremes which mean a large transfer of electron charge from one atom to the other, showing the dominant ionic character of the c-ZrO_2 phase.
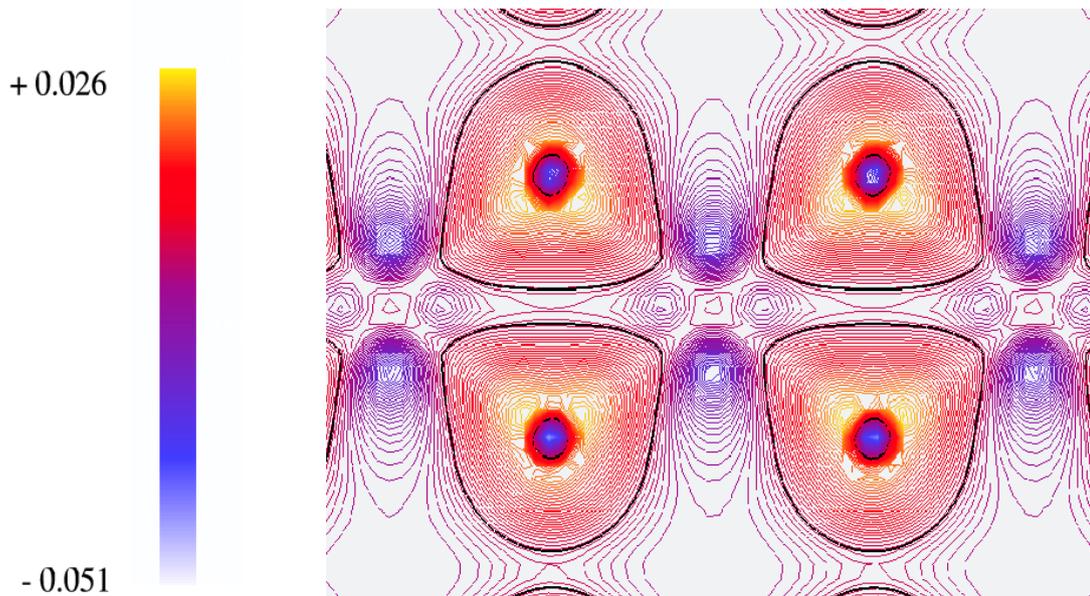
Figure 3.5: Spatial distribution of the charge density with respect to the atomic charge for c-ZrO_2, along a plane containing the Zr-O bonds and the directions $[1\bar{1}0]$ and $[001]$. The contour lines are taken in steps of $8*10^{-4}$ electron charge, and the zero level has been marked with a thicker contour line.

3.2.3 c-ZrO_2 vs external pressure

As previously commented the two lowest symmetry phases of ZrO_2 can be viewed as distortions of the cubic structure. In this section we focus on the procedure induced by an external stress to transform the cubic structure into the other phases.

Two different ways of applying the stress can be considered: the first is a hydrostatic stress with the same magnitude along the three orthogonal axis of the cubic structure, while the second is a "shear" stress applied as a rotation of the angle formed between the initial orthogonal axis and the resulting vector after the shear stress is

applied. In fact these are extreme types of external stresses, and we can consider any realistic stress to be decomposed into two contributions, one relative to volume changes and given by the hydrostatic stress, and a volume-conserving rotation specified by the shear.

These stresses are applied to both the positions of the atoms and the cubic cell in which they are contained, and afterwards it may be considered or not to let the system relax. Our calculations are focused on knowing what type of distortion needs to be applied and which symmetry elements need to be broken for the cubic phase to approach the tetragonal or monoclinic phases, which are identified essentially by means of the atomic charges.

Cubic to tetragonal:

The ZrO_2 phase transformations have been previously studied by some DFT calculations modeling the cubic to tetragonal transition [129]; together with a molecular dynamics study [120] where the δ parameter was determined to be well defined at T=0 K but not at any other finite temperature. Our interest in this section is to study such a transition from the point of view of the stress applied. This will be useful to understand the effect on the initial atomic configuration of distortions induced by realistic structural modifications like surfaces or vacancies.

We find that the cubic to tetragonal distortion, when letting the system relax till the atomic forces are less than 0.1 eV/$Å^3$, is achieved from an initial situation with a very slight shift (0.001 Å) at the O sublattice along the direction δ. As already mentioned δ characterizes only the t-ZrO_2 phase and is defined by a displacement between two O atoms in their internal sublattice, see figure 3.1. In table 3.3 it can be seen how the lattice parameters and the atomic charges rapidly evolve from characteristic values of the cubic structure to those of the tetragonal ones already obtained after the first distortion step. This quickly convergence to tetragonal phase is known to be due to an atomic metastable situation of the cubic δ=0 parameter [129] which finish after relaxing to the bulk value of the δ distortion and the corresponding transition.

Initial δ distortion	a(Å)	c(Å)	δ (c units)	Zr charge	O charge
c-ZrO₂ and 0.000	5,160	5,160	0,000	2,420	6,790
0.001	5,158	5,294	0,051	2,490	6,756
0.002	5,154	5,267	0,046	2,472	6,764
0.003	5,154	5,258	0,046	2,473	6,764
t-ZrO₂	**5,131**	**5,250**	**0,050**	*2,484*	*6,758*

Table 3.3: Structural information of the relaxed bulk cubic ZrO_2 calculations for different initial δ values, given in Å. The final values of the a, c, and δ lattice parameters together with the charge of the Zr and O atoms are shown for each initial situation.

Cubic to monoclinic:

There are two different types of O atoms in m-ZrO_2, while only one in c-ZrO_2. This atomic change from the cubic to monoclinic structure can be achieved by two procedures in terms of the stress applied. The first and more intuitive one is to apply a tensile hydrostatic stress in order to increase the volume of the cubic unit cell up to the monoclinic size, then to further apply a shear stress to create a non-orthogonal lattice vector at an angle beta characteristic of m-ZrO_2. After this initial configuration, and by letting the system relax, the transformation is achieved. But there is another way

directly related with the shear stress: after applying it, we analyze the charges that are originated when we only let the atomic positions relax till the atomic forces are lower than 0.05 eV/Å^3. Looking at table 3.4, several ranges can be distinguished when increasing the shear angle, given in radians (rad). First, we distinguish a range (0.01 – 0.10) where there exists two types of Zr charges in the cell and only one type of O, instead of one type of Zr and two of O, with ionic values closer to those characteristic of the high symmetry phases, see table 3.3. From angle 0.11 to 0.15 two kinds of O appear, while the ionic charge transfer starts to reduce. In the next range, from angle 0.16 to 0.20, it can be seen how the charges and ionic character approach to the values of m-ZrO$_2$. In particular for an angle of 0.20 rad, or 11.46 degrees, it is shown in the table that the charges almost correspond to the values characteristic of bulk m-ZrO$_2$.

Initial angle	Final angle	Zr charge	O$_I$ charge	O$_{II}$ charge
0,01	0,10	<2.465>-<2.471>	6.768-6.764	6.768-6.764
0,11	0,15	<2.472>-<2.485>	6.768-6.782	6.759-6.725
0,16	0,20	2.489-2.500	6.796-6.815	6.714-6.680
Bulk values	*m-ZrO2*	*2,494*	*6,828*	*6,678*
0,20		2,500	6,815	6,680
0,21	...	2.503-2.610	6.815-6.745	6.681-6.643

Table 3.4: Atomic charge values of the cubic structure after relaxation when applying an external shear stress given in radians. The evolution to the monoclinic structure can be seen as the angle increases, the monoclinic like values being obtained for an initial rotating angle of 0.20 rad, as compared to the bulk monoclinic phase values in bold.

For higher values of the angle, the Zr atomic charge increases while the O charge decreases, therefore lowering the ionic character below what is found in the monoclinic phase.

These calculations show that even tiny distortions in the atomic positions can lead to important transformations in the ZrO$_2$ structure. This needs to be taken into account when forming surfaces or interfaces, as the stress-strain relation may involve phase transformations.

3.2.4 c-ZrO$_2$ with defects

As commented in the introduction, the high symmetry ZrO$_2$ phases are commonly stabilized at room temperature by doping with aliovalent oxides, leading to partially stabilized zirconia (PSZ) or tetragonal zirconia polycrystal (TZP) depending on which is the phase stabilized, cubic or tetragonal respectively. The cation of these aliovalent oxides has different oxidation state than Zr in ZrO$_2$, which is (4+), and then when it substitutes the Zr^{4+} ions in the lattice forming a solid solution, O vacancies are created in order to maintain charge neutrality. Our calculations will focus on the very well know Y$_2$O$_3$ doping oxide which creates one O vacancy per each two substitutional Y atoms. These O vacancies are responsible for the high importance of this compound as an ionic conductor and O sensor. But doping is not the only way to create O vacancies: the standard sintering methods performed in a reducing atmosphere result in another kind of O vacancies by removing directly O atoms inside the structure, these are called neutral or thermodynamic vacancies. Such thermodynamic vacancies have been demonstrated to take part in the stabilizing process of t-ZrO$_2$ [137]. The existence of O vacancies and dopant cations locally alters the electronic density, and therefore it is worth to analyze

their influence for a further understanding of the structural and electronic role of these defects on the ideal c-ZrO$_2$.

Those systems with Y$_2$O$_3$ as doping oxide, called 3Y-TZP when t-ZrO$_2$ is stabilized by adding ~3% molar concentration of Y$_2$O$_3$ and YSZ when c-ZrO$_2$ contains more than 8% molar concentration of Y$_2$O$_3$, have been extensively studied both experimentally [138-150] and theoretically [151-153] but a final conclusion about the defect localization and the electronic effects is still uncertain. Up to relatively recent time, one of the most investigated aspects was the preferred position of the O vacancies with respect to the cation lattice. Different and contradictory conclusions were reached: some reports concluded that the most favorable nearest neighbors to the O vacancies were Y dopant cations [138-144] while others reported that O vacancies were more likely bonded to the Zr host cations [145-150]. This controversy was overcome by the authors of reference [114] who found out that the NN of the O vacancies are those cations with less ionic radii in the lattice. Further studies performed by GGA [153] showed that ordering tendencies can be well understood in terms of a balance between competing electrostatic and elastic defect interactions, the latter depending on the dopant identity. Therefore, in the Y$_2$O$_3$ doped ZrO$_2$ system, O vacancies will be NN to the Zr, while NNN to the Y cations [114, 151, 153]. This was used by Eichler [152] to perform *ab-initio* calculations of t-ZrO$_2$ for different positions of the O vacancies, Zr and Y atoms to finally conclude that YY-vacancy trimmers are formed and arranged to maximize distances between O vacancies. By further increasing the Y$_2$O$_3$ content, these trimmers were also maximizing the distance between Y and the vacancy of neighbors trimmers.
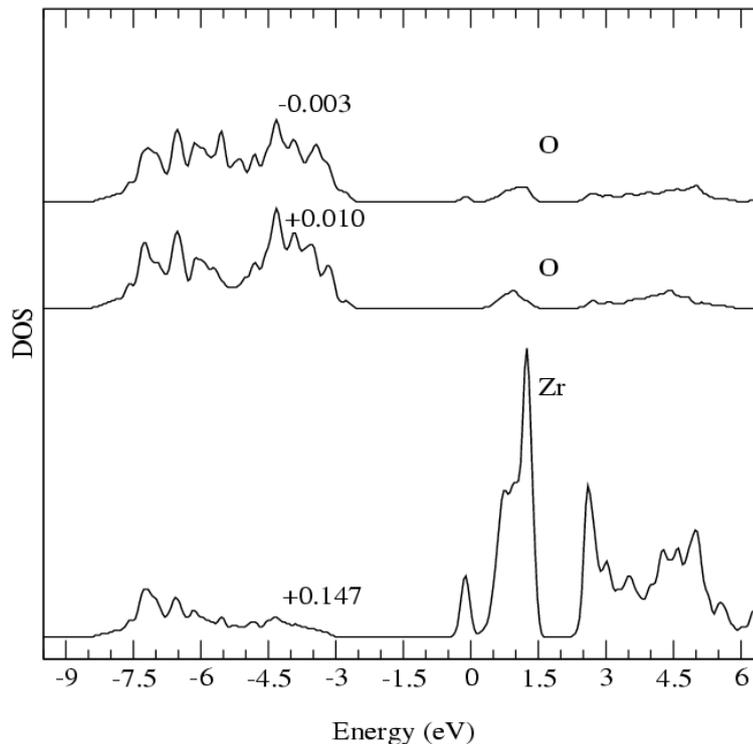
Figure 3.6: Density of states of Zr and O atoms close to an O vacancy site for c-ZrO$_2$ with neutral vacancies. The charge gain with respect to the undefected bulk, defined as $\Delta Q=Q-Q_{ideal}$, is indicated for each atom. Energies are referred to the Fermi level.

We have performed two different calculations to model O vacancies on c-ZrO$_2$, the first containing only thermodynamic vacancies (Y0) and the second related to the addition of Y$_2$O$_3$ as dopant aliovalent oxide (YSZ). Both calculations were performed until relaxation forces were lower than 0.1 eV/Å^3 on the atoms of a supercell formed repeating 2x2x2 times the cubic unit cell, so initially containing 96 atoms.

Y0			YSZ	
Zr$_V$	Zr		Zr$_V$	Zr
0,200	0,144		0,164	0,138

Table 3.5: Mean BOP of Zr-O pairs involving Zr atoms NN (Zr$_V$) or NNN (Zr) to O vacancies in the cases of c-ZrO$_2$ with neutral O vacancies (Y$_0$) and YSZ.

Thermodynamic vacancies: Y0

In the Y0 calculation we subtracted one O atom from the above mentioned supercell, and studied the PDOS, Mulliken population values, distances, BOPs and CDDs. In figure 3.6 we can see the DOS projected on the Zr and O atoms around the vacancy site. The Zr structure is almost unaltered respect to that of the ideal c-ZrO$_2$, even the e$_g$-t$_{2g}$ gap of the CB is maintained, although a new peak appears in the band gap which has an important weight on the Zr 4d orbital. The charge of this Zr atom indicates a noticeably charge increase of 0.15 electrons, while the O atoms are not much affected by the presence of the vacancy. The PDOS shows that two types of O can be found, the closest ones to the O vacancy (top graph) have an unaltered charge while the others show a slight increase of 0.01 electrons (middle curve). Zr-O distances show an average dispersion from the non defected c-ZrO$_2$ equilibrium bond length of ~0.1 Å. Two different Zr-O BOPs are shown in table 3.5, indicating a significant enhancement of covalency. CDD is depicted in figure 3.7 to compare the electronic spatial redistribution with that of the ideal c-ZrO$_2$, figure 3.5. Both color and spacing between lines of the contour plot have been preserved from that of the ideal c-ZrO$_2$ for a straightforward comparison. In fact, as for Y0 larger extreme CDD values occur, we saturate the color scale to that of figure 3.5. This way we can see that the contour lines distortion nearby the vacancy is local, because the effect is only observed in the nearest neighbors and also in the interatomic space regions close to the vacancy.

Y$_2$O$_3$ oxide doping: YSZ

The above model of thermodynamic vacancies is valid only for those formed by sintering ZrO$_2$ in a reducing atmosphere [137]. However, a more important contribution in realistic systems is that of the charged vacancies in yttria stabilized zirconia (YSZ). The same supercell consisting on 96 atoms is used, which represent a 14% molar addition of Y$_2$O$_3$ also studied in [151]. This implies substituting eight Zr atoms by eight Y, while four O are removed to maintain charge neutrality. We set the position of the O vacancies equidistant along the <111> direction while the Y atoms are arranged trying to satisfy Eichler's condition of maximizing Y-Y trimmer distance. The projection of the DOS is depicted in figure 3.8, where the curves from top to bottom represent respectively three types of anions, a Zr not close to the vacancy, a Zr NN to the O vacancy, and a Y atom.
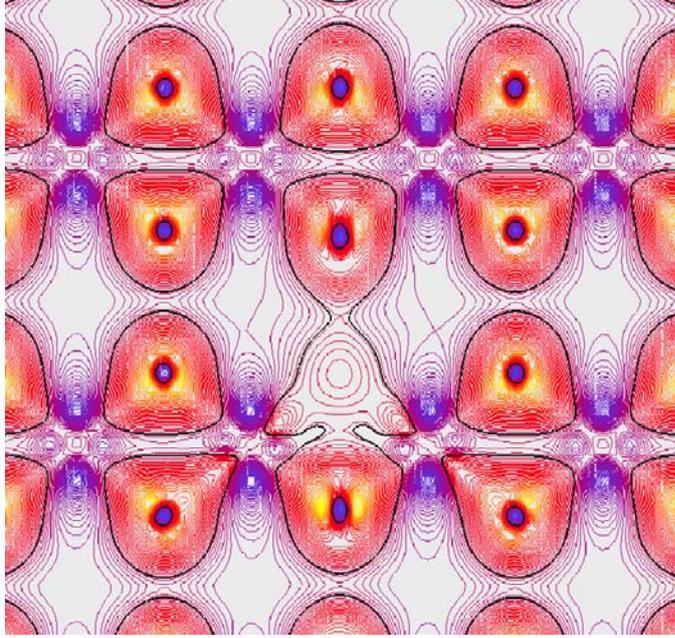
Figure 3.7: Same as figure 3.5 for c-ZrO$_2$ in the presence of neutral O vacancies.
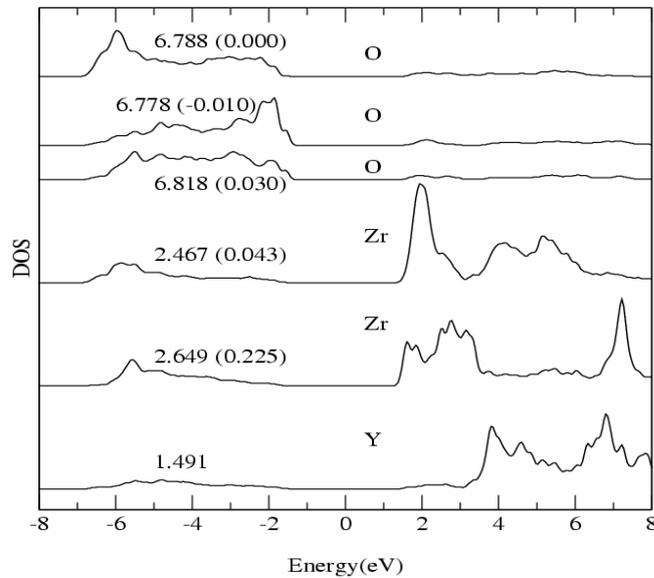
Figure 3.8: Density of states of representative cations and O atoms for 14% mol-YSZ. The corresponding Mulliken populations are indicated, giving in parenthesis the charge gain respect the undefected bulk for Zr and O atoms.

Compared to the cases without defects and with neutral vacancies, there is a redistribution of the electronic states. The vacancy level is not occupied, and the insulating character of the undefected band structure is recovered. Atomic relaxations play an important role: whereas in the unrelaxed model there are midgap states, they are eliminated by relaxation of the O atoms NN to the vacancy, which shifts the defect states inside the conduction band. For Zr, the e$_g$-t$_{2g}$ gap at the CB is lost. In addition, those atoms closer to vacancy sites present an important reshape of the DOS, revealing some hybridization with the neighbouring Y. All Zr cations gain charge, from 0.03 to 0.22 electrons with respect to ideal c-ZrO$_2$, the largest gain corresponding to the atoms

closest to vacancies. The O DOS is also significantly reshaped. Three kinds of anions can be distinguished, with the largest values of the DOS peaked either at the bottom, the middle or the top of the VB, as shown in the figure 3.8. Globally, half of the O ions lose charge with respect to the undefected case, approximately 0.02 electrons, and the rest gain around 0.02 electrons. However, there is a large dispersion of values, related to the simultaneous presence of O vacancies and Y cations, leading to a maximum charge gain of 0.07 for particular atoms.

Atomic relaxation indicates that O moves towards the vacancy with values that range from 0.49 to 0.14 Å with an average value of 0.32Å, while the maximum Zr displacement is 0.22 Å, less than for O but not negligible. This compares well with Parrinello's structural calculation [151] which states that O moves 0.3 Å on average and other atoms can move as much as 0.2 Å.

The mean BOPs of the Zr-O for each of the Zr atoms present in the YSZ supercell can be seen in table 3.5. The BOP value of Zr_V, close to the O vacancy, is increased from that of the ideal c-ZrO_2 one, see table 3.2, and therefore shows a more covalent character, while the other Zr slightly reduces it. The overall BOP result is that YSZ has a closer value to the ideal c-ZrO_2 than Y0.
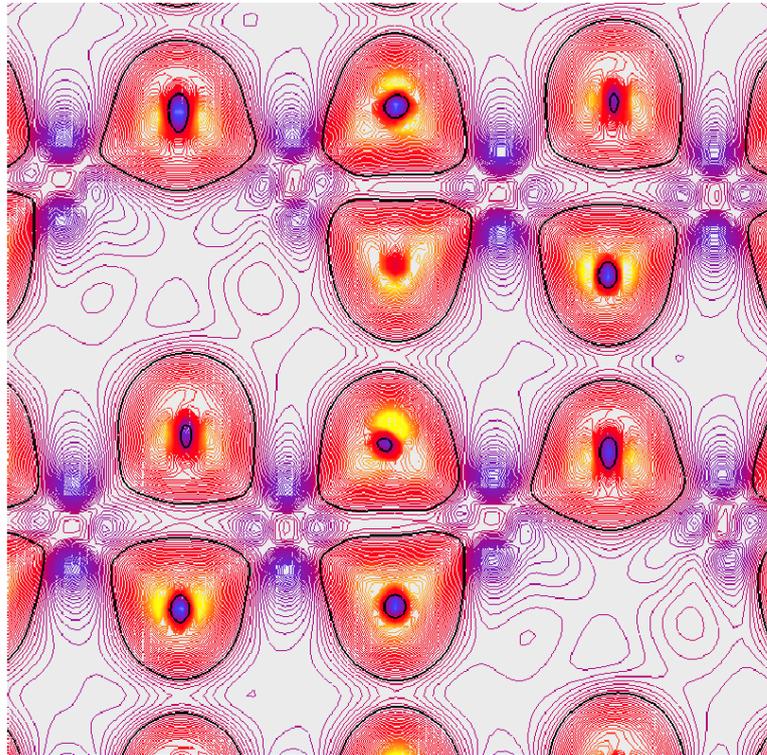
Figure 3.9: Same as figures 3.5 for cubic YSZ.

In figure 3.9 we show the CDD plot, where we have saturated the color scale according to figures 3.5 and 3.7 also retaining the same line spacing. From the Zr-O bonding regions it is noticeable the trend to recover the spatial charge distribution of ideal c-ZrO_2 (figure 3.5), and in contrast to it, the large differences between O atoms specially in the inner regions of highest charge accumulation. Of course, the presence of Y atoms, not shown in the figure, implies areas with a different aspect. We can conclude that the drastic changes introduced in the global properties (conductivity, ionicity) by neutral O vacancies with respect to undefected c-ZrO_2 are greatly reduced

in the case of YSZ; however, the particular distribution is profoundly altered, due to the combined presence of two types of defects.

3.3 Ceramic oxides

After discussing the structural and electronic properties of all ZrO_2 bulk phases and the influence of defects, we will describe briefly in particular Al_2O_3, MgO and HfO_2 lattice parameters and bulk modulus calculated with the SIESTA code.

3.3.1 α-Al_2O_3

The crystal structure of α−Al_2O_3 is the hexagonal-rhombohedral system, space group D6(3d) or R-3C, that in crystallography is often referred to as "corundum structure". This structure was completely determined by Pauling and Hendricks (1925) [154] following earlier work by Bragg and Bragg (1916) [155].

The structure can be viewed as a hexagonal close packing of O ions forming layers parallel to the (0001) plane. Each Al^{3+} ion is coordinated to six O^{2-} ions, and the Al^{3+} ions occupy only two-thirds of the octahedral interstitials sites to maintain charge neutrality. The lattice, thus, consists roughly of alternating layers of O and aluminum ions planes along (0001), see figure 3.10. Identifying the different position in each O (Al) layer by capital (small) letters, we have the complete stacking sequence of the layers as A-a-B-b-A-c-B-a-A-b-B-c-. So the 30 atoms hexagonal unit cell is obtained after 3 times the layers {A-B} O repetition, or 2 times the {a-b-c} Al repetition, while the primitive cell corresponds to the rhombohedral structure which contains 10 atoms [4]. Lattice parameters are referenced in the following work [156].

We have studied the bulk Al_2O_3 using the SIESTA code and hexagonal cell in the corundum structure. The Mohnhorst pack k-grid used was 6x6x2, which corresponds to a cutoff close to 13 Å. The atoms were relaxed till the forces were lower than 0.04 eV/Å. We show in figure 3.10 the density of states (DOS) projected on each atom type: Al, O. We obtain a band gap value close to 5.2 eV while the experimental one is 8.0 eV [157]; this is due to DFT eingenvalues do not correspond to the excitation energies and then band gaps are generally not correctly described. There is a noticeable electron transfer from the Al to the O, the valence band being mainly populated by the latter, which makes reasonable to describe within a full ionic picture.

In table 3.6 we can see the values of the lattice parameters together with those of bulk modulus for theoretical DFT methods performed with different basis sets, and the experimental ones.

3.3.2 MgO

The structure of MgO is the cubic rock salt lattice with space group Fm3m, which is sometimes referred to as "NaCl structure". It can be viewed as a fcc lattice with two atoms basis, or alternatively as two interpenetrating face-centered cubic structures, with each element 6 fold coordinated to the other element type, see figure 3.11.

The calculations of the structure and electronic properties of bulk MgO have been performed using a k-grid 7x7x7, which corresponds to a cutoff of 15.2 Å, with atomic forces lower than 0.02 eV/Å. The DOS projected to the atomic species of MgO is depicted in figure 3.11.

34
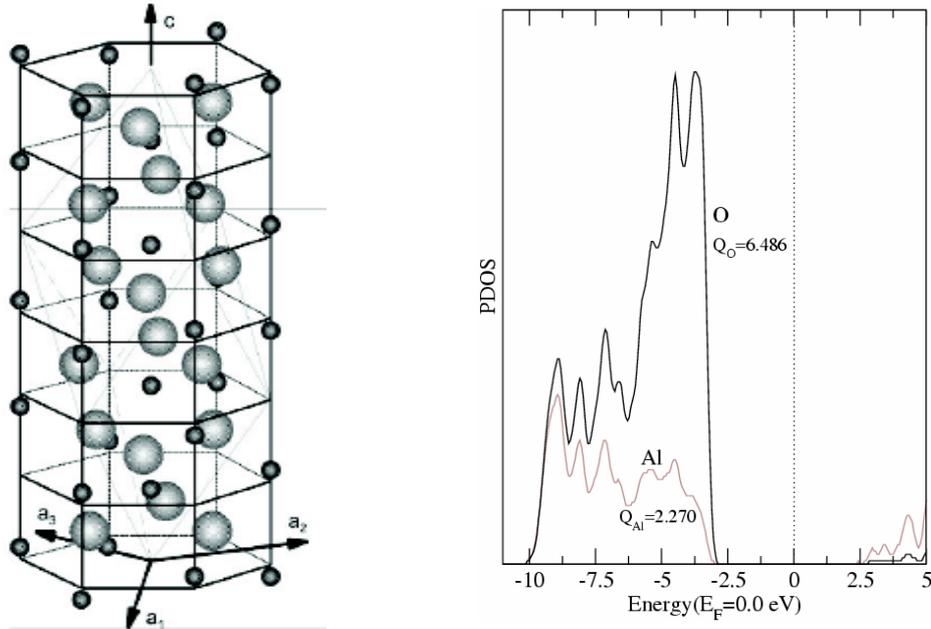
Figure 3.10: On the left side it is shown the hexagonal unit cell of the Al_2O_3 compound, the small circles represent the Al atoms while the larger ones are O. On the right side a GGA calculation of the DOS projected on the Al and O atoms is shown, the Fermi level being placed at the middle of the band gap. It is also included the Mulliken population of the Al and O atoms.
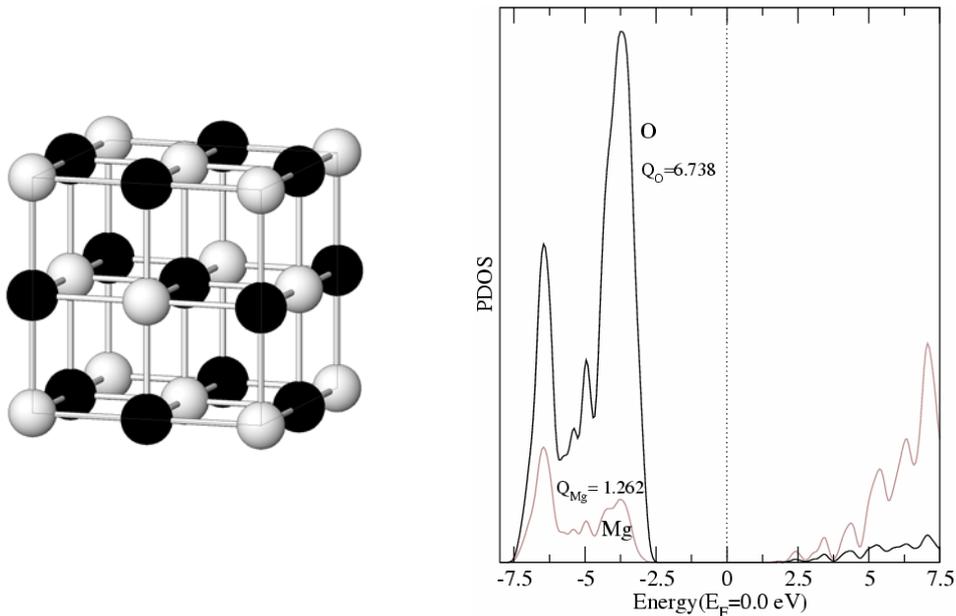
Figure 3.11: On the left side it is shown the cubic unit cell of the MgO compound, the light circles represent Mg while the dark ones represent O. On the right side a GGA calculation of the DOS projected to the Mg and to the O atoms is shown, with the Fermi level placed at the middle of the band gap. It is also included the Mulliken population of the Mg and O atoms.

It is noticeable the larger contribution of the O atoms with respect to the Mg in the valence band (VB), as occurs in the Al_2O_3 compound, eventhough MgO shows a larger

ionicity as indicated by the Mulliken populations of figure 3.11. The band gap value we obtain is close to 4.0 eV while the experimental one is 7.8 eV [158].

We also compare theoretical and experimental values for the structural parameters and bulk modulus in table 3.6.

3.3.3 HfO$_2$

Hafnium oxide, as previously commented, is very similar to zirconium oxide [109, 159]. Here we will only study the cubic phase which has the same space group than c-ZrO$_2$, constituted by a primitive cell with an fcc lattice and three atoms basis, one Hf and two O.

Bulk calculations of c-HfO$_2$ have been performed using a 9x9x9 k-points grid and atomic forces less than 0.02 eV/Å.
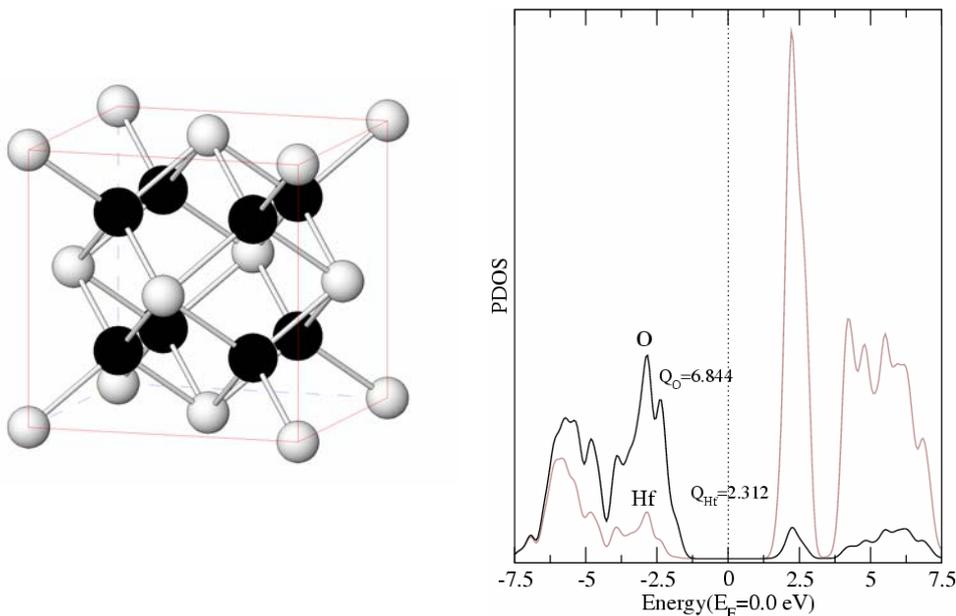
Figure 3.12: On the left side we show the cubic unit cell of the c-HfO$_2$ compound, the small circles represent the Hf atoms, while the large ones are the O. On the right side, the DOS projected on the Hf and the O atoms is shown, the Fermi level being at the middle of the band gap. It is also included the Mulliken population of the Hf and O atoms.

In figure 3.12, it can be see that the band gap that we obtain for HfO$_2$ is slightly larger than 3.5 eV while the experimental measurements [160] give 5.8 eV.

Table 3.6 also includes for HfO$_2$, both the structural lattice parameters and bulk modulus values experimental measurements and previous theoretical calculations. All structural parameters in this table are obtained after full relaxation of the cell and atomic positions and the bulk modulus value is calculated by fitting our data to the Murnaghan equation [100].

Compounds		a	c	B_0 [Gpa]	Refs.
α-Al2O3	Present/GGA	4,85	13,16	213	
	Present/LDA	4,78	12,96	239	
	PW/PW91	4,79	13,08	246	[4]
	PW/LDA	4,72	12,86	239	[4]
	OLCAO	4,83	12,61	242	[161]
	Exp	4,76	13,00	253	[156],[4], [165]
MgO	Present/GGA	4,27		118	
	Present/LDA	4,14		158	
	GGA	4,24		161	[162]
	LDA	4,16		182	[162]
	GGA/ECP	4,27		151	[163]
	GGA/PAW	4,25		151	[163]
	Exp	4,21		152	[162]
c-HfO2	Present/GGA	5,11		254	
	Present/LDA	5,02		290	
	GGA	5,15		257	[108]
	GGA/PW91	5,00			[164]
	LDA	5,14		280	[109]
	LDA	5,09		289	[108]
	Exp	5,08		280	[164]

Table 3.6 Lattice parameters and bulk modulus value of the three ceramics studied: Al_2O_3, MgO and HfO_2, in addition to ZrO_2, where it has been compiled information about previous theoretical calculations [4, 108, 161-164]; the scheme is also indicated, as well as the experimental data [164, 165].

We can see in table 3.6 the tendency to overestimate (underestimate) the lattice parameters by GGA (LDA), as it was noticed for ZrO_2. The bulk modulus holds the opposite trend by underestimating (overestimating) the experimental value when the GGA (LDA) XC approximation is considered. Our results compare well with experimental values although the bulk modulus obtained for MgO by GGA is too low. In general our LDA calculations provide better values for the bulk modulus, while both are similarly good to determine the lattice parameters, with values usually within a 2 % difference respect to the experimental ones. Therefore we can conclude that our results are close to experiments within the limits of accuracy of previous theoretical studies based on the same formalism and XC approximations.

3.4 Metals and non metals pseudopotential generation

In this section we will briefly analyze the structural, elastic and electronic properties of metals and elements studied in this work. We will classify according to the families of the periodic table.

Alkali metals and Alkaline Earth metals: Na and Mg
Transition metals with bcc structure: Mo, Nb, Ta and W
                 with hcp structure: Hf, Y and Zr

	with fcc structure :	Ag,Cu,Rh,Ni,Pd, and Pt
Other metals	:	Al
Nonmetals	:	O

Alkali metals and alkaline earth metals:

Some physical properties of these elements are their high thermal and electrical conductivity. They also present high ionization energies (IE), specially the 1st IE for alkali, and the 2nd for alkaline earth metal, due to their low number of valence electrons in the last shell: s1 and s2 respectively [133]. The compounds formed with any other elements, specially those of the fluor or O family, are highly ionic because there is a great difference in electronegativity between the constituents [166].

Transition metals:

Also called d-block elements, they include an extensive range of metals with different properties that share a common feature: their outermost level contains at most two electrons, while the next level has incomplete filled d sub-orbitals that are progressively filled from the IIIb to the IIb family. Some of these elements show different oxidation states which makes them useful as catalysts. They have fairly constant atomic radii and low ionization energies [167]. Within this group there are three ferromagnetic elements: Fe, Co, Ni; but also paramagnetic elements (when the electrons are not paired in the d-orbitals) and diamagnetic ones (when the electrons are paired).

In figure 3.13 we show the atomic and electronic structure for the d-metals Nb and ferromagnetic Ni.
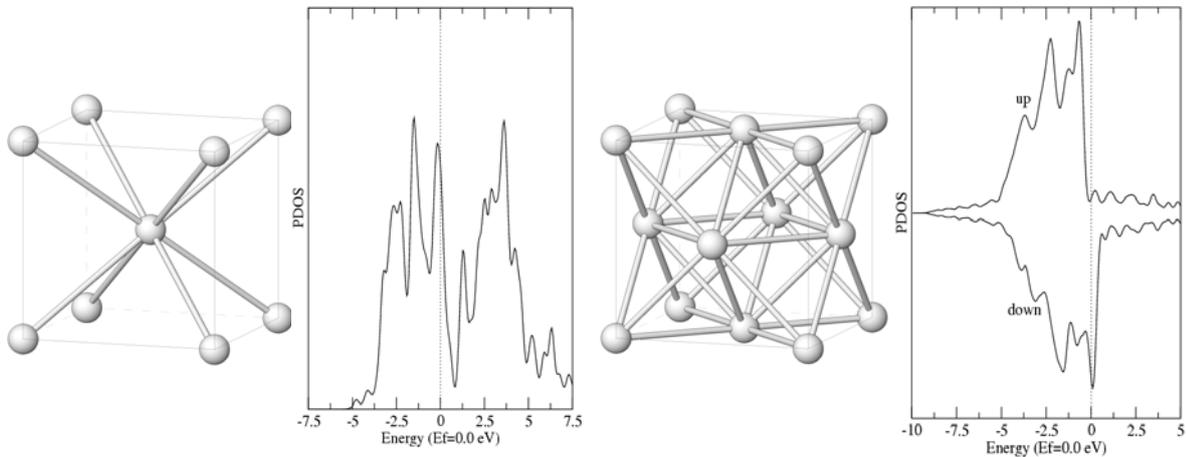
Figure 3.13: On the left side we show the cubic unit cell of the Nb metal together with its DOS, and on the right side the structure and DOS of the ferromagnetic Ni, where the DOS has been split into spin up (upper graph) and spin down (bottom graph).

In figures 3.13 the spin contributions of Ni are shown separately, the final magnetic moment being 0.60 μ_B that compares well with the experimental value of 0.62 μ_B [168].

Al:

This metal is in the IIIa family and Al's valence electrons stay on the p-orbital while the 3s is filled.

Nonmetals:

Non-metals are the most electronegative elements of the periodic table, and when forming compounds with other elements they use to show important ionicity, specially with alkali and alkaline earth elements [169].

Pseudopotentials:

From now on we focus on the comparison of the results obtained for the different elements from different pseudopotential generation, using both XC approximations: LDA and GGA. Table 3.7 indicates the electronic configuration and the radii employed for each angular orbital of all elements.

Elements	Electronic conf.	rs	rp	rd
O	[He]2s2 2p4	1,45	1,45	1,45
Na	[Ne]3s1 3p0	3,10	3,10	3,10
Mg	[Ne]3s2 3p0	2,30	3,00	4,00
Al	[Ne]3s2 3p0.5 3d0.5	2,30	2,30	2,30
Ni	[Ar]4s1 3d9	2,05	2,05	2,05
Cu	[Ar]4s2 3d9	2,05	2,05	2,05
Y	[Kr]5s2 4d1	3,67	3,50	2,28
Zr	[Kr]5s1 4d3	3,00	3,00	2,50
Nb	[Kr]5s0 4d5	3,20	3,50	1,10
Mo	[Kr]5s1 4d5	3,20	3,50	1,60
Rh	[Kr]5s1 4d8	2,50	2,60	2,20
Pd	[Kr]5s0 4d10	2,70	2,60	1,30
Ag	[Kr]5s1 4d10	2,70	2,60	1,30
Hf	[Xe]6s1 5d3	3,00	3,00	2,50
Ta	[Xe]6s1 5d4	3,00	3,00	2,50
W	[Xe]6s1 5d5	3,00	3,00	2,50
Pt	[Xe]6s0 5d10	2,65	2,65	2,10

Table 3.7: Orbital radii and electronic configuration that has been used for generating the pseudopotential of each element in this work.

Some computational requirements related with the generation of a PP and the chosen radii have to do with its softness and transferability. The concept of "soft" PP generation was commented in chapter 2, while transferability is the validity of the PP to be used in different environments (solids, surfaces, etc.), which increases as the radii cut off (r_{CL}) is smaller. Transferable PP thus require a high computational cost, as computational parameters like the mesh and energy cut off need to be increased. Our PP were generated trying to find a compromise between softness, transferability and low computational cost.

Structural, elastic and energetic results

Table 3.8 shows the lattice structural parameters, bulk modulus and cohesive energies of our calculations both with GGA and LDA together with experimental data. Almost all elements present a cubic symmetry in their crystal bulk structure, therefore only one lattice parameter ("a") is specified, but for those elements with hcp structure we have also included the ("c") parameter in the row underneath.

Elements	Structure	a/c				B0				Ecoh		
		GGA	LDA	Expt.	Refs.	GGA	LDA	Expt.	Refs.	GGA	LDA	Expt.
Na	BCC	4,20	4,04	4,23	[162]	6,2	8,2	7,5	[162]	1,01	1,29	1,11
Mg	HCP	3,23	3,14	3,21	[170]	34	40	35	[170]	1,56	1,77	1,51
		5,24	5,11	5,21								
Al	FCC	4,04	3,99	4,03	[162]	79	85	79	[162]	3,96	4,43	3,39
Ni	FCC	3,55	3,40	3,52	[171]	183	286	186	[171]	5,50	7,51	4,44
Cu	FCC	3,66	3,50	3,60	[162]	143	197	142	[162]	4,35	6,45	3,49
Y	HCP	3,70	3,60	3,65	[172]	47	48	41	[176]	4,32	4,94	4,37
		5,85	5,70	5,73								
Zr	HCP	3,25	3,17	3,23	[173]	86	95	97	[173]	6,54	7,36	6,25
		5,21	5,09	5,15								
Nb	BCC	3,32	3,26	3,25	[176]	136	160	170	[176]	6,28	7,53	7,57
Mo	BCC	3,19	3,16	3,15	[174]	239	257	230	[176]	6,19	7,35	6,82
Rh	FCC	3,87	3,80	3,80	[162]	247	311	269	[162]	6,63	8,28	5,75
Pd	FCC	4,01	3,91	3,88	[162]	148	211	195	[162]	4,32	5,62	3,89
Ag	FCC	4,17	4,02	4,07	[162]	89	139	109	[162]	3,25	4,41	2,95
Hf	HCP	3,20	3,12	3,19	[175]	100	116	110	[175]	7,30	7,72	6,44
		5,05	4,93	5,04								
Ta	BCC	3,32	3,26	3,30	[172]	197	216	200	[176]	8,48	9,78	8,10
W	BCC	3,20	3,15	3,16	[172]	285	319	310	[176]	8,28	10,41	8,90
Pt	FCC	4,03	3,91	3,92	[176]	221	287	230	[176]	6,11	7,54	5,84

Table 3.8: Structural parameters (a and c), bulk modulus (B_0) and cohesion energy (Ecoh) of the bulk phases of the fcc, bcc and hcp elements obtained from the pseudopotential listed in table 3.7 and compared to the experimental values [170-176]. The experimental values of Ecoh have been obtained from [177].

In order to generalize and compare easily the results from both XC approximations, we calculate the averaged value per element (AVPE) between the theoretical and experimental values, for the lattice parameters, the bulk modulus and the cohesion energy, obtained as:

$$AVPE = \frac{\sqrt{\left(\Sigma (\frac{theor - \exp}{\exp})^2 \right)}}{N},$$

where N is the number of elements included.

This way we obtain values, referred to the experimental measurements, of the average for GGA and LDA. The lattice parameter is overestimated by GGA, but the AVPE goes from 0.994 for Na to 1.032 for Pd with an average overestimation of 1.6%. The LDA AVPE goes from 0.956 for Na to 1.008 for Pd with an average underestimation of 1.9 %. Regarding the bulk modulus, the AVPE of GGA ranges from 0.76 for Pd to 1.14 for Y with an average underestimation of 12%. For LDA it goes from 0.938 for Si to 1.591 for Ni with an overestimation of 22%. Finally, for the cohesive energies, the GGA AVPE goes from 0.835 to 1.246 with an average of 13 % over the experimental value, while for LDA it goes from 0.994 to 1.849 with an averaged overestimation of 37%.

In general terms, these numbers indicates a better agreement to experiment for GGA than for LDA, even excluding the cohesive energies which always favor GGA. In

addition, we observe that for GGA a large deviation in lattice parameter (>3%) is accompanied by a large deviations (>20%) in bulk modulus, while in LDA there is no such a relation for these extreme bad cases. Therefore from now on we will choose GGA as the XC approximation to be employed.

Chapter 4

ZrO$_2$ surfaces: structural and electronic properties

4.1 Introduction

In spite of recent studies of ZrO$_2$ surfaces, a detailed understanding of the surface properties at the atomic level is still lacking. Experimental investigations face the difficulty of preparing well-defined surfaces, since ZrO$_2$ frequently presents a granular and often polymorphic fine structure and there are also dopants effects. Most experimental investigations have been performed for polycrystalline zirconia and have shown that the preferential surface orientations are highly dependent on the preparation method and the environmental conditions. For example, in polycrystals the low-index crystal surfaces are usually favored, being the (110) face probably the most common [178].

The surface structure of single crystalline ZrO$_2$(001) stabilized with 9.5 % molar of Y$_2$O$_3$ was determined by high-resolution medium-energy ion scattering [179]. The surface is strongly reconstructed with a rumpled Zr(Y)O plane at the top. Moreover, analysis by impact collision ion scattering spectroscopy suggests that about 10% of the top layer O sites are vacant. On the other hand, thin films of YSZ deposited by sputtering on non-aligned polycrystalline stainless steel and glass substrates show a clear correlation between the plasma composition, the resulting microstructure and the preferential orientation, which changes from [002] to a mixture of [220] and [111] with increasing reactive gas flow [180]. Also, experimental data including Auger, photoelectron and vibrational spectroscopies, as well as electron microscopies and x-ray diffraction have been reported. However, they only provide indirect information on the surface structure [181-184].

The theoretical calculations of the ZrO$_2$ surface refer mainly to structural [178, 185, 186], and electronic properties [187, 188], as well as to the stability [178, 185] and the dopant segregation and distribution [178]. Nevertheless, general studies of the stability of the polar and non-polar surfaces for the different bulk phases are still missing. Concerning *ab-initio* calculations, a detailed study of ZrO$_2$ surfaces was performed by Christensen and Carter [185] which provided surface energies and relaxations for the low index surfaces of different bulk phases. Further, the stability and structure of various terminations of pure and yttria doped surfaces of tetragonal ZrO$_2$ have been investigated by Eichler and Kresse [178]. They studied the surface properties as a function of the film thickness for different non-stoichiometric and symmetric configurations.

The aim of the present chapter is to investigate the stability, structure and electronic properties of ideal ZrO$_2$ surfaces of the low pressure phases. Moreover, surface relaxations of c-ZrO$_2$ are analyzed in relation to the c-t phase transformation. Different types of slabs (symmetric, asymmetric... etc) are used in order to study their influence on the surface properties.

4.2 Surface geometries and slab model

We have investigated the low-index (001), (110) and (111) surfaces of cubic ZrO_2 and the (001) surfaces of tetragonal and monoclinic ZrO_2. As it is well known, surfaces of ionic compounds can be classified in non-polar and polar. Except the (110) of c-ZrO_2, all the surfaces are polar and therefore they can present different terminations. In non-polar surfaces, the atomic planes contain atoms of both species maintaining charge neutrality. On the other hand, in the polar surfaces each atomic plane is formed solely by either cations or anions, resulting in an alternated distribution of charge; in different perpendicular dipole moments [189]. In figure 4.1 the top and lateral views of the low-index surfaces of the c-ZrO_2 phase are shown. The 2D unit cells are represented by the discontinuous lines, and contain respectively one atom for the (001) and (111) terminations and three for the (110) surface.
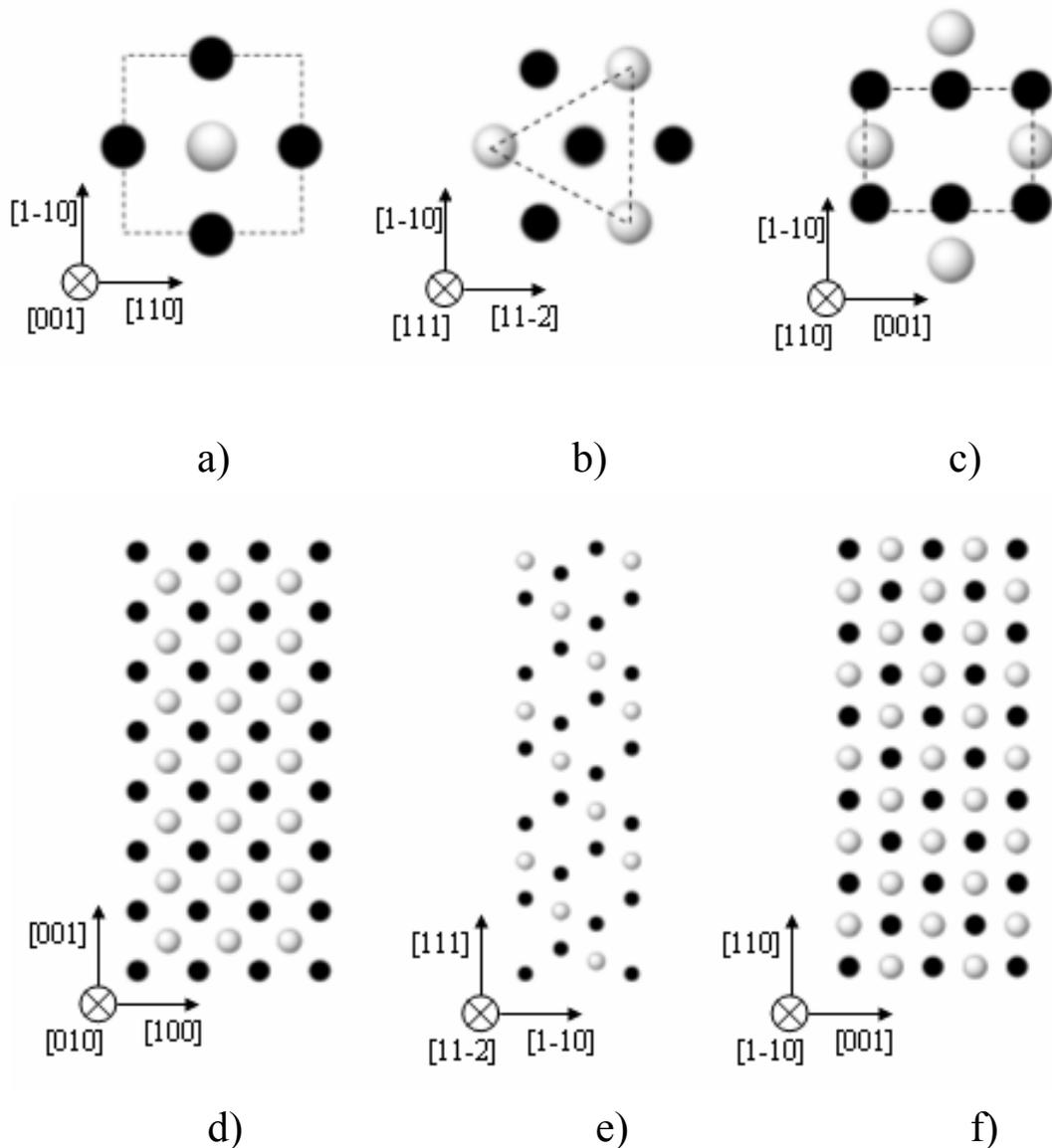
Figure 4.1: Top and side views of different c-ZrO_2 surfaces: a-d) (001), b-e) (111) and c-f) (110). Black circles correspond to O atoms and white ones to Zr. The side views at the bottom panels do not include relaxations.

Due to their crystallographic structure, the polar surfaces (001) and (111) can present different terminations. In the (001) surface the Zr and O planes alternate, therefore there are two possible terminations, either on Zr and O plane. The second termination has two times more atoms in the surface plane. On the other hand along the (111) orientation there is a Zr plane and two consecutive oxygen planes with Zr-O and O-O interplane distances of $a * \frac{\sqrt{3}}{12}$ and $2a * \frac{\sqrt{3}}{12}$, respectively. Thus three terminations are possible: on a Zr plane, see figure 4.6.a or two O-terminated surfaces, one ending in a single O layer (-O) and the other in a double O layer (-O-O), see figure 4.6.b. Hereafter, we refer to the possible terminations as:

Zr-, OO-   for the c-(100)
ZrO_2-   for the c-(110)
O-O-, O- and Zr-   for the c-(111)

For the t-ZrO_2(001) surface we have considered all possible terminations: t-$(001)_{OO}$, t-$(001)_{Zr}$, and t-$(001)_O$, labelled following the above notation, while for the monoclinic phase only the m-$(001)_{OO}$ surface has been studied. The tetragonal (001) 2D surface unit cell is analogous to that of the cubic (001), see figure 4.1.a, although in this case the O are distributed in a double layer separated by $\delta=0.050$ c. The monoclinic surface is similar to the c-(001) case, but with double cell size and O-O interplane distance around 1.75 Å.

Systems without translational invariance along a direction, as the surfaces described above, can be modeled using a periodic supercell approach leaving a vacuum region in the direction perpendicular to the surface of the 3D unit cell. Thus, there are always two surfaces per unit cell. The width of the vacuum region is chosen large enough to inhibit interactions between neighboring surfaces, and ranges from 9 to 15 Å in the slabs discussed here. The number of layers of the slab can be varied since some properties are studied as a function of the slab thickness, the minimum number being imposed by the requirement that bulk-like behavior is attained at the central slab layers. The calculations presented here ranges from 5 to 9 ZrO_2 oxide units in the entire slab, depending on the particular surface structure.

We use both symmetric and asymmetric slabs. In the former the surface termination is the same on both sides while asymmetric slabs end with layers of different kind on each surface.

Further, we considered stoichiometric slabs, where the unit cell consists of an integer number of ZrO_2 formula units, and non-stoichiometric ones for which the number of atoms in the unit cell is not an integer number of ZrO_2 units.

In table 4.1 is shown the influence of the slab thickness on the surface energy as well as on the atomic charges and O-Zr distances of both surface and bulk-like layers of the c$(001)_{OO}$ surface, modeled by a symmetric slab. Charges and interlayer distances of the surface layers are well converged even for the thinner slab. Using a slab of 17 atoms, which correspond to 9 atomic planes, all the quantities are sufficiently well converged, as evidenced by the differences with a 35 atoms slab, which are smaller than 0.3 %, 0.6 % and 0.5 % for the surface energy, bulk-like O charge and Zr-O distance, respectively.

			c-(001)$_{OO}$				
n° of Atoms	11	14	17	20	23	29	35
$Q_S(O)$	6,30	6,30	6,30	6,30	6,30	6,30	6,30
$d_S(Zr\text{-}O)$ (Å)	2,10	2,10	2,10	2,10	2,11	2,10	2,10
σ (eV)	15,76	15,79	15,81	15,84	15,83	15,85	15,85
$Q(O)$	6,77	6,78	6,78	6,79	6,79	6,79	6,79
$d(Zr\text{-}O)$ (Å)	2,22	2,25	2,22	2,24	2,23	2,23	2,23

Table 4.1: O charges, Q(O) ($Q_S(O)$), and Zr-O distances, d(Zr-O) ($d_S(Zr\text{-}O)$) for the bulk-like (outer surface) planes together with surface energies, σ, for the c-(001)$_{OO}$ slab, as a function of the slab thickness.

4.3 c-ZrO$_2$ surfaces: atomic and electronic structure

4.3.1 (001) surface

First, we will analyze the ideal c-(001)$_{Zr}$ and c-(001)$_{OO}$ surfaces obtained by just breaking bonds between planes. To model these surfaces we used both symmetric and asymmetric slabs. The thickness of the symmetric slabs is 11 layers, distributed in 6 Zr and 5 O layers for the Zr termination and on 5 Zr and 6 O layers for the O-ended slab, while the asymmetric slab is formed by 12 atomic planes. Only the asymmetric slab is stoichiometric while the symmetric Zr-ended case corresponds to a defect of O atoms and the O-ended case to an O excess.

Table 4.2 provides the layer resolved atomic charges and interatomic distances for the optimized geometries. $\Delta d_\perp$ is the percentage of variation of the interlayer distance between two consecutive planes with respect to the ideal bulk value, while d_B is the corresponding Zr-O bond distance. Notice that in the table we only provide information for one half of the symmetric slabs, both halves of each slab being equivalent, while each panel of layer resolved quantities for the asymmetric slab refers to one of the slab halves. The relaxed structure of the entire asymmetric supercell is depicted in figure 4.4.c.

	Symmetric							Asymmetric					
	Zr				OO				Zr	...		OO	
	Zr...Zr				OO...OO						..		
OO				-17	2,10	**6,30**					-21	2,09	**6,32**
Zr	-17	2,12	**3,24**	18	2,37	**2,73**	-24	2,08	**3,16**	24	2,42	**2,77**
OO	7	2,29	**6,75**	-5	2,19	**6,73**	19	2,38	**6,72**	-16	2,12	**6,72**
Zr	-4	2,21	**2,48**	5	2,26	**2,45**	-16	2,13	**2,54**	19	2,38	**2,54**
OO	2	2,26	**6,79**	0	2,22	**6,77**	19	2,39	**6,73**	-16	2,13	**6,74**
Zr	-1	2,23	**2,44**	0	2,22	**2,43**	-16	2,13	**2,54**	-19	2,38	**2,53**
OO	0	2,23	**6,78**	0	2,22	**6,77**	19	2,39	**6,73**	-16	2,13	**6,73**
	$\Delta d_\perp$	d_B	Q	$\Delta d_\perp$	d_B	Q	$\Delta d_\perp$	d_B	Q	$\Delta d_\perp$	d_B	Q

Table 4.2: Layer-resolved charges and interatomic distances corresponding to a c-ZrO$_2$(001) surface modeled either by symmetric Zr-ended and OO-ended slabs or by an asymmetric supercell. For each slab panel, we provide from left to right the percentage of variation with respect to the bulk of the interlayer distance $\Delta d_\perp$ and the Zr-O bond distance (d_B) given in Å, both referred to the layer immediately below, and the Mulliken population (in bold). The layers are ordered from the surfaces (top row) to the bulk (bottom row).

Concerning the symmetric slabs both the Zr and O-ended surfaces exhibit the same relaxation pattern. The subsurface plane relaxes outwards reducing the first interlayer distance and increasing the second one. For the metallic Zr terminated surface, these results in Zr-O bond lengths of 2.12 and 2.29 Å for the first and second bonds, respectively. This alternation of short and long Zr-O bonds decays when going into the bulk, and at the third Zr layer the bonds are similar to bulk bonds. The same pattern is observed for the OO terminated surface, except the difference with respect to the bulk is slightly larger. In the case of the asymmetric slab the shorter and longer Zr-O bonds alternate independently on each side and thus is maintained slightly damped even on the central layers. The surface induced structural changes are accompanied by a redistribution of the electronic charge. Zr and OO surfaces present respectively an increase and a decrease of charge with respect to the ionic bulk values. This is just due to the loss of coordination of the surface atoms. However, the gain/loss of charge is almost restricted to the outermost layers. As can be seen in figure 4.2, which represents the charge density difference plots for the $(001)_{OO}$ surface, the electronic distribution is highly asymmetric in the O atom and there is a spill over of the charge at the surface. However, in spite of the decrease of electronic charge of O atoms, there is a charge accumulation along the Zr-O bond direction, since O attracts electrons from the bulk towards the surface, which in turn leads to an attraction of the positively charge Zr atoms towards the surface, resulting in a smaller Zr-O bond length. Similar effects have been predicted for t-(001) surfaces [178].
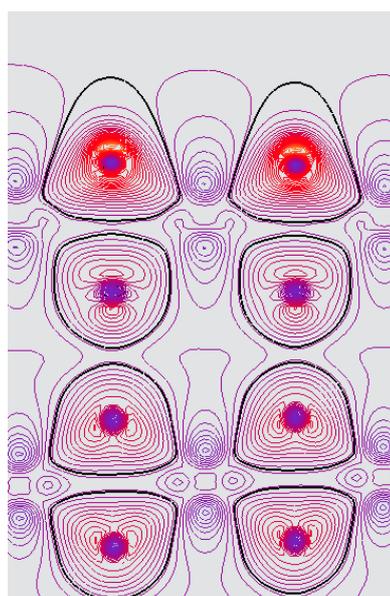
Figure 4.2: Surface charge density difference (CDD) plots for the c-$(001)_{OO}$ surface along a plane defined by the vectors [001] (vertical axis) and [110] (horizontal axis). A high density of lines with almost spherical shape characterized the O atoms, while the line shape around Zr is lobular.

The layer resolved DOS, for the Zr and OO terminations are represented in figure 4.3 for the surface and bulk-like layers. In both terminations surface effects are restricted to the planes closer to the surface, and a bulk like DOS is obtained beyond the third or fourth atomic plane. There is a general narrowing of the surface VB as a consequence of the reduction of NN with respect to bulk zirconia. Both surfaces are metallic. For the Zr-termination, gap states formed by the Zr d electrons develop at the surface layer. The Fermi level lies above these gap states at the CB minimum. Contrary,

on the OO surfaces the Fermi level crosses the O 2p VB. On the right panel of the figure, the DOS for the asymmetric supercell is also shown. In the asymmetric slab the Fermi levels at both surfaces (Zr and OO) become aligned, and then there is a band bending between both ends of the slab, as can be seen in figure 4.3.c. In spite of this, the general features of the DOS are analogous to those of the symmetric slabs.

a)   b)   c)
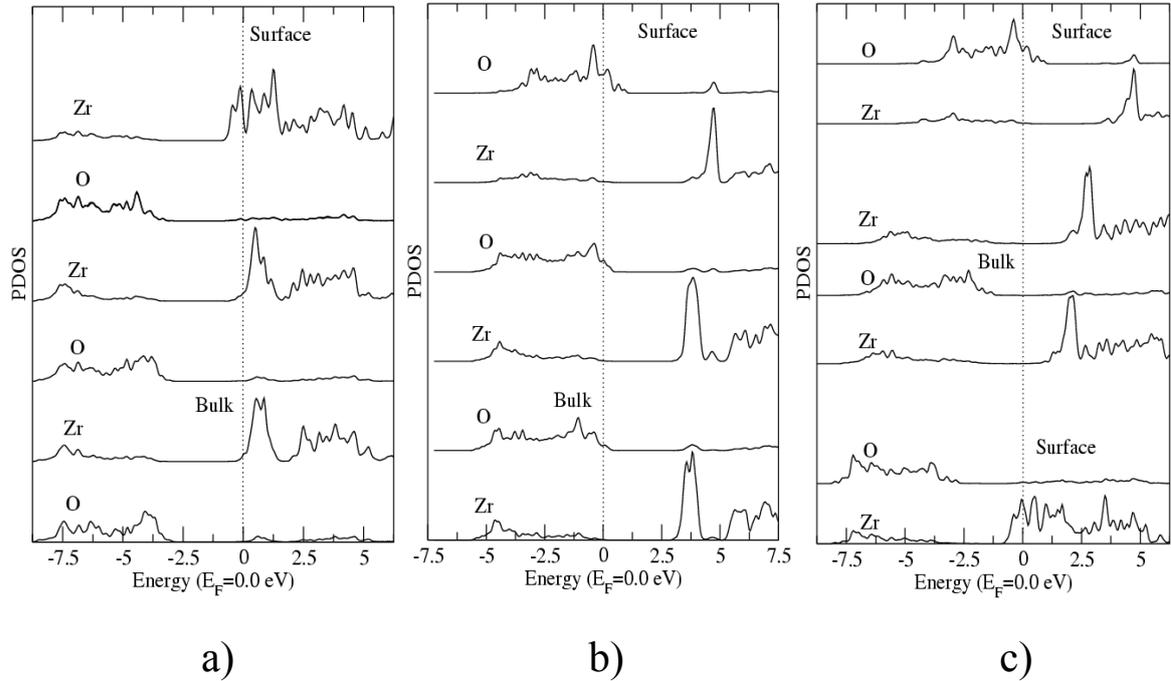
Figure 4.3: DOS for the supercells corresponding to a) c-$(001)_{Zr}$, b) c-$(001)_{OO}$ and c) the asymmetric slab, projected on the atoms nearby the surface and those at the inner bulk-like planes (bottom curves for a) and b) and middle curves for c)). For cases a) and c) the DOS for the Zr layer closest to the surface are scaled by 3/5 and 4/7, respectively.

We have also performed a calculation for an O-ended surface removing half of the O at the outermost plane, so O surface layer contains only one O atom per unit cell. We modeled the surface by two different slabs. In one of them, c-$(001)_{O}|_1$ the two O surfaces on each side of the slab are equivalent and the slab possesses inversion symmetry with respect to the centre of the slab. In the c-$(001)_{O}|_2$ slab although both surfaces are equivalent, there is not an inversion centre. Both slabs are stoichiometric. The relaxed geometries of c-$(001)_{O}|_1$ and c-$(001)_{O}|_2$ are displayed in figure 4.4 a) and b) respectively, and the atomic charges and structural parameters are given in table 4.3. There is a new parameter in the table with respect to table 4.2, δ, due to the fact that in the relaxed geometries the O planes split in a double layer; δ gives in Å the distance between the distorted O layers.

These surfaces exhibit similar relaxation patterns than those corresponding to the OO termination, with a reduction of the O-Zr surface spacing. However, the internal buckling of the O layer results in the coexistence of short and long Zr-O bonds for the second O double layer, analogously to the bond distribution in the tetragonal ZrO_2 phase. The effect is larger for the slab without inversion symmetry, c-$(001)_{O}|_2$. As before, the O surface atoms reduce their charge with respect to the bulk values, although the decrease is much smaller than that obtained for the OO surface.

<div align="center">a)   b)   c)</div>
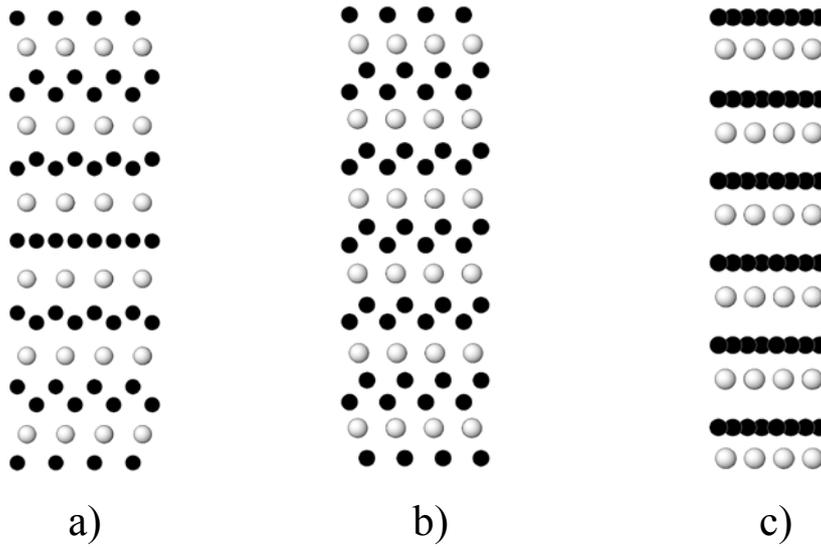
Figure 4.4: Same as the side views of figure 4.1 for the a) c-$(001)_O|_1$, b) c-$(001)_O|_2$ and c) asymmetric slabs of the c-(001).

	c-$(001)O|_1$				c-$(001)O|_2$		
		O...O				O...O		
O	-22,8	2,07		**6,56**	-18,8	2,03		**6,55**
Zr	30,8	2,07		**2,64**	28,8	2,09		**2,63**
O			0,31	**6,75**			0,38	**6,78**
O	-18,0	2,09		**6,76**	-26,8	2,11		**6,78**
Zr	16,8	2,14		**2,50**	29,6	2,05		**2,54**
O			0,17	**6,78**			0,29	**6,72**
O	-10,0	2,15		**6,78**	-15,2	2,06		**6,73**
Zr	2,4	2,22		**2,44**	26,4	2,13		**2,50**
O			0,01	**6,79**			0,32	**6,78**
O	0,4	2,23		**6,78**	-23,5	2,13		**6,78**
	$\Delta d_\perp$	d_B	δ_{O-O}	**Q**	$\Delta d_\perp$	d_B	δ_{O-O}	**Q**

Table 4.3: Same as table 4.2 for the c-$(001)_O|_1$ and c-$(001)_O|_2$ surfaces. An additional structural parameter, δ_{O-O}, is included, which provides the interlayer distance between two consecutive O planes (in Å).

Figure 4.5 represents the LDOS for the O-terminated. The surface O 2p VB shows important changes with respect to the bulk. Besides the narrowing due to the loss of coordination, there is an important redistribution of the O states. The effect is almost restricted to the first layer and the second O layer, further is almost bulk-like. There are no surface induced gap states and, contrary to the Zr and OO terminated surfaces, the Fermi level is located in the gap and the surface remains insulating.
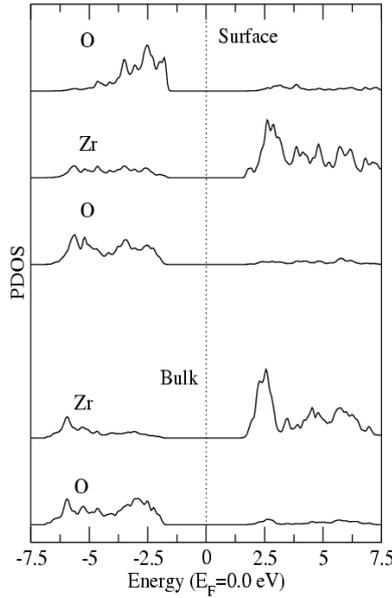
Figure 4.5: Same as figure 4.3 for the case c-(001)$_\text{O}|_2$. Case c-(001)$_\text{O}|_1$ show similar general features.

4.3.2 (111) and (110) surfaces

As occurred for the (001) orientation, for the (111) surface there are again different possible terminations, either on the Zr, on a double O layer or on a single O layer. Only the single O-terminated surface is stoichiometric. Note that the Zr-O and O-O interplanar distances are $a * \dfrac{\sqrt{3}}{12}$ and $2a * \dfrac{\sqrt{3}}{12}$ respectively. Therefore, it is expected that since O-Zr-O is the unit block, the surface with single O termination would be the most stable. We have modeled these surfaces using symmetric slabs, and the resulting relaxed structures for the Zr and O-O (111) termination are represented in the leftmost panels of figure 4.6. Table 4.4 compiles the corresponding interatomic distances and local charges following the same scheme of table 4.3. The results are qualitatively similar to the use of the (001) surface.

In the Zr- terminated surface the subsurface O atoms relax outwards, reducing the distance to the surface Zr layer while increasing the interlayer distance to the Zr layer underneath. The effect propagates into the bulk and is larger than for the (001) case, see table 4.2, although the variations of the bond distances are here smaller. Further, there is a gain of charge at the top metal layer which decays into the bulk. The corresponding DOS is similar to that obtained for the (001) orientation in figure 4.3.a. Again, gap states develop close to the CB minimum, where the Fermi level is located.

The changes of the double layer O termination are more significant with respect to the O-ended (001) surface. There is again an alternation of short and long Zr-O bond and interlayer distances, but now with enhanced variations with respect to the bulk. In addition, a slight variation of the O-O interlayer distance occurs near the surface, being damped at the bulk-like layers of the slab. The surface most O atoms almost loose all the transferred cationic charge, approaching the neutral atom state. The charge variation induced by the surface is almost restricted to the three outermost surface layers. This is reflected in the DOS, shown in figure 4.7. For the O surface atoms, there are VB states at the Fermi level, resulting in a metallic surface.

<div align="center">a)   b)   c)</div>
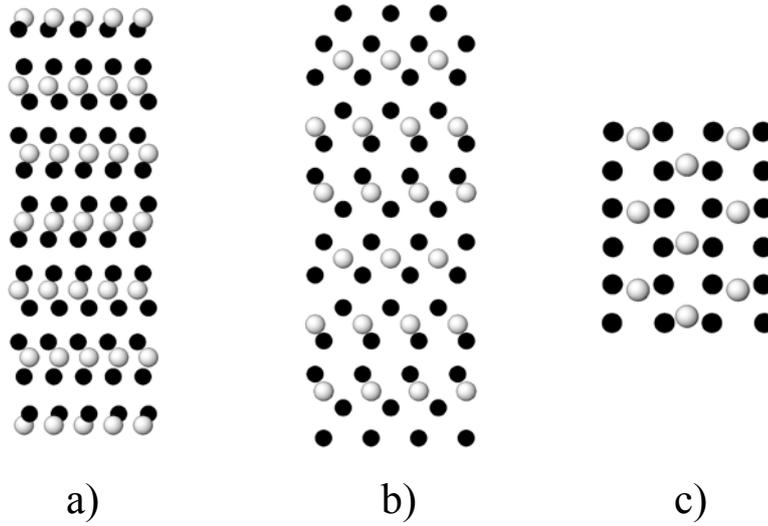
Figure 4.6: Side views of the slabs corresponding to the relaxed surface structures a) c-(111)$_{Zr}$, b) c-(111)$_{O\text{-}O}$, c) c-(110) slabs. Black circles correspond to O atoms and white ones to Zr.

	Zr				O				OO			
	Zr...Zr				O...O				OO...OO			
O											0,29	**6,10**
O					13,1	2,23		**6,68**	-35,0	2,17		**6,51**
Zr	-37,0	2,15		**3,17**	4,8	2,21		**2,49**	24,8	2,31		**2,69**
O			0,32	**6,71**			0,28	**6,79**			0,30	**6,76**
O	15,9	2,26		**6,79**	5,5	2,21		**6,79**	-12,4	2,21		**6,75**
Zr	-9,6	2,20		**2,54**	4,8	2,21		**2,44**	8,3	2,26		**2,45**
O			0,29	**6,77**			0,29	**6,79**			0,29	**6,77**
O	7,6	2,24		**6,78**	4,1	2,21		**6,80**	-4,1	2,23		**6,78**
Zr	-2,0	2,22		**2,45**	4,1	2,21		**2,43**	1,8	2,24		**2,43**
O			0,29	**6,79**			0,29	**6,79**			0,29	**6,78**
O	2,0	2,23		**6,79**	4,1	2,21		**6,79**	0,7	2,24		**6,78**
	$\Delta d_\perp$	d_B	δ_{O-O}	Q	$\Delta d_\perp$	d_B	δ_{O-O}	Q	$\Delta d_\perp$	d_B	δ_{O-O}	Q

Table 4.4: Same as table 4.3 for the different (111) surfaces modeled by symmetric slabs.

The surface terminated in a O-single layer exhibits the smallest relaxations. In fact, only the top surface interplane distance experiences a slight increase, while the rest of the slab remains almost bulk-like. Further, Zr-O bond lengths are almost unaltered with respect to the bulk values. Also, the net charge of the surface O atoms is quite close to the ionic bulk charge. The DOS does not show any surface induced states, remaining insulator, and the only effect is the usual narrowing of the topmost layer DOS.
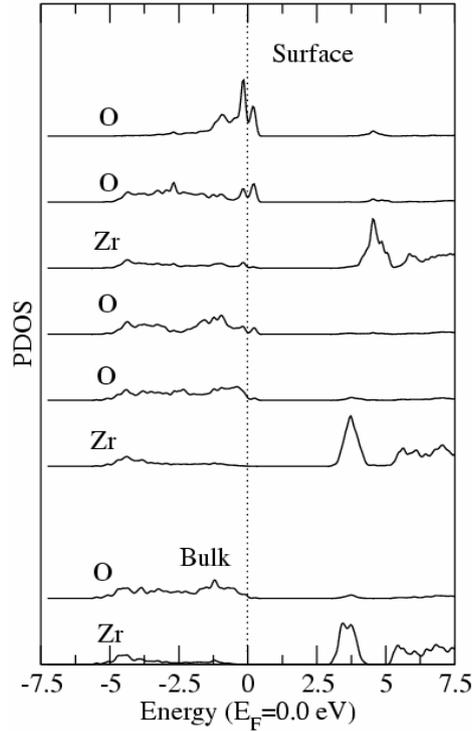
Figure 4.7: Layer resolved DOS for the c-(111)$_{O-O}$ surface. The layers are ordered from the surface (top) to the bulk (bottom).

Finally we have also modeled the non-polar (110) c-ZrO_2 surface. The relaxed slab structure is shown in the rightmost panel of figure 4.6. All the planes contain a complete ZrO_2 formula unit, thus there is not alternation of positively and negatively charged planes. The interatomic distances and charges of the relaxed structure are given in table 4.5. The effect of relaxation is small. The major result is the buckling of all the layers due to the displacement of the Zr atoms, which move alternatively to the upper and to the lower adjacent layer. Also there are small changes in the O interplane distances. In figure 4.8 we show the atom resolved DOS. The variation of the DOS almost only affects the surface atoms. There is a reduction of the gap at the surface due to the development of surface induced states close to the maximum of the VB. Nevertheless, the surface maintains the insulator character of the bulk.

	$\Delta d_\perp$(%)	$\Delta d_\perp$(Å)	d_B(Å)	Q
OO		0,07	2,18	**6,65**
Zr	-0,09		2,13	**2,67**
OO		-0,06	2,20	**6,76**
Zr	0,13		2,43	**2,50**
OO		0,04	2,20	**6,76**
Zr	-0,05		2,15	**2,48**
OO		-0,037	2,20	**6,76**

Table 4.5: Same as table 4.3 for the c-(110) ZrO_2 surface. Due to the bucking of the ZrO_2 planes, two interlayer distances are provided: the usual $\Delta d_\perp$ (in %) referred to the bulk value, and the distance (in Å) between the Zr and O atomic planes of a given layer ($\Delta d_\perp$ in Å).
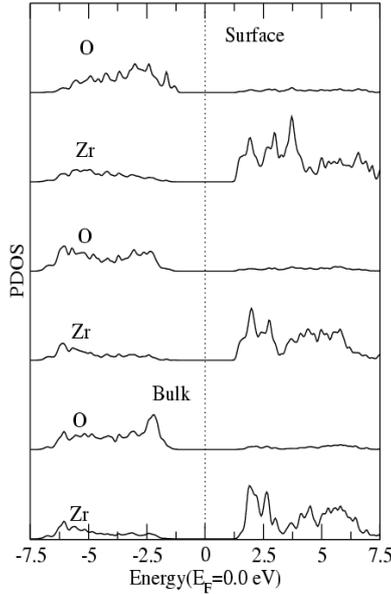
Figure 4.8: Layer resolved DOS of the surface and inner bulk like atoms of the c-(110)ZrO$_2$ surface.

4.4 t-ZrO$_2$ and m-ZrO$_2$ (001) surfaces

Most low index surfaces of t- and m- phases have been previously studied with *ab-initio* calculations. Christensen and Carter [185] performed a detailed investigation of the principal surfaces of the three low-pressure phases, while Eichler and Kresse [178] focused on tetragonal zirconia. Their results indicate that most relaxation effects at the surface are similar to those shown by the cubic phase surface. We have only investigated the (001) surface of the t- phase. Although we have considered both symmetric and asymmetric slabs, the effect of the asymmetric supercell are those already shown for the cubic surface, thus we will restrict to the symmetric case.

The results for the different terminations of the (001) orientation of t-ZrO$_2$ are included in table 4.6. The general pattern is analogous to that previously discussed for the cubic phase and coincides except for the Zr terminated with the results obtained by Eichler and Christensen for the same surface. In general, the relaxation gives rise to changes of the interlayer distances between Zr and O planes and the distortion parameter δ of the O plane. In fact δz experiences three different behaviors depending on the slab termination. In Zr terminated, δz is equal to zero along the entire slab while for OO terminated δz is almost zero at the outer surface plane increasing towards the center of the slab. In O terminated, the buckling between Os is maximized due to the presence at the outer surface of just one O atom, reducing δz along the slab.

This is accompanied by the variation of the Zr-O interlayer distances which is larger than in c-ZrO$_2$. In the three terminations the subsurface layer relaxes outwards reducing the first interlayer distance and increasing the second one. However, as we deepen into the slab the behavior is different. In Zr terminated d(Zr-O) steady approaches the cubic bulk distance, while in both OO and O- terminated the two distances of bulk tetragonal phase are recovered.

Relaxations effects occur together with gain/loss of ionic charge for Zr and O atoms respectively, mainly in the surface layers. The results for the LDOS, not shown, are also similar to those found for the (001) surfaces of the c-phase, metallic character for the Zr- and OO termination with induced surface states at the CB minimum and VB

maximum, respectively. The Fermi level is also located at the CB and VB respectively. For the O-surface charge reduces and increases only slightly for O and Zr outer layers while there are not surface induced states and thus no surface metallization occurs and the surface remains insulating.

	Zr				O				OO			
	Zr...Zr				O...O				OO...OO			
O											0,01	**6,28**
O					-21,0	2,03		**6,55**	-21,0	2,09		**6,32**
Zr	-29,2	2,08		**3,24**	-31,1	**2,10; 2,40**		**2,63**	3,0	**2,27; 2.41**		**2,72**
O			0,00	**6,73**			0,76	**6,78**			0,26	**6,73**
O	8,1	2,34		**6,73**	-28,0	2,11		**6,78**	-16,5	2,13		**6,73**
Zr	-9,4	2,21		**2,51**	-17,7	**2,05; 2,49**		**2,54**	-12,7	**2,15; 2,38**		**2,47**
O			0,00	**6,77**			0,56	**6,73**			0,39	**6,76**
O	-0,7	2,27		**6,77**	-17,5	2,06		**6,73**	-16,0	2,12		**6,76**
Zr	-3,9	2,25		**2,46**	-25,1	**2,13; 2,37**		**2,50**	-16,9	**2,13; 2,38**		**2,47**
O			0,00	**6,78**			0,62	**6,78**			0,45	**6,76**
O	-4,4	2,25		**6,78**	-25,0	2,13		**6,78**	-16,7	2,13		**6,77**
	$\Delta d_\perp$	d_B	δ_{O-O}	Q	$\Delta d_\perp$	d_B	δ_{O-O}	Q	$\Delta d_\perp$	d_B	δ_{O-O}	Q

Table 4.6: Same as table 4.3 for the t-(001) ZrO_2 surface modeled with symmetric slabs. Notice in bold letter the two types of Zr-O distances.

Summarizing, low index surfaces of the three low pressure phases of ZrO_2 have been modeled using both symmetric and asymmetric slabs. For the polar surfaces, the different possible terminations have been considered, Zr or O. The most important relaxation effects are exhibited by the (001) surfaces of the t-ZrO_2 phase, followed by the (111) surfaces of c-ZrO_2 and finally by the (001) surfaces of c-ZrO_2. Every termination of these polar orientations follows a relaxation pattern which tends to decrease the first Zr-O surface distance and increase the second one. In terms of the electronic properties studied by the PDOS, surface effects are shown for outer planes where the loss of coordination implies a narrowing of the VB. (110) orientation and O terminated of c-(001), c-(111) and t-(001) surfaces show a no metallic electronic structure. However, both OO and Zr polar terminated exhibit metallic structures with a Fermi level crossing the VB and the CB, respectively.

4.5 Cubic to tetragonal distortion

Along this chapter it has been shown that some of the features of the ZrO_2 surfaces depend on the surface termination, but that there are also some properties common to all surfaces. In particular, for the cubic ZrO_2 surfaces the shortening of the first Zr-O surface interlayer distance and the subsequent enlargement of the next Zr-O distance is common to all polar surfaces. In addition, for some O-ended c-(001) surfaces (namely $O|_1$ and $O|_2$) a non-vanishing corrugation occurs at the O planes. All these features resemble the structure of the more stable tetragonal phase, where the alternated shift of the O atomic positions in the unit cell is measured by the parameter δ, see figure 4.9, which occurs along the X_2^- phonon direction [120, 121] commonly taken along the z-axis. Eventhough δ is usually defined from the ratio between the actual shift of the O positions (δz) and the tetragonal "c" lattice parameter, along this section we will give

δ in Å, which experimentally corresponds to δ_{EXP}=0.295 Å [123, 124] comparing well with our calculation of bulk t-ZrO$_2$ (δ_{t-ZrO2}=0.264 Å), see table 3.1.

In this section we will study whether the extra degrees of freedom introduced by the boundary to vacuum are enough to induce a restructuring of the cubic phase to the tetragonal structure. To this end, we define two parameters: δ and Σ. δ corresponds to half of the interplane distance between adjacent surface O atoms, and thus provides the corrugation at the O surface plane. Σ is the difference between O-Zr interplane distances corresponding to the outermost O plane and that immediately underneath, see figure 4.9. The existence of non-null values for δ indicates a separation from the c-ZrO$_2$ structure to approach the tetragonal one, while a non-null Σ value provides an indication that the d(Zr-O) is not only of one kind as in the cubic phase, but two different distances appear as occur in the t-ZrO$_2$ structure.
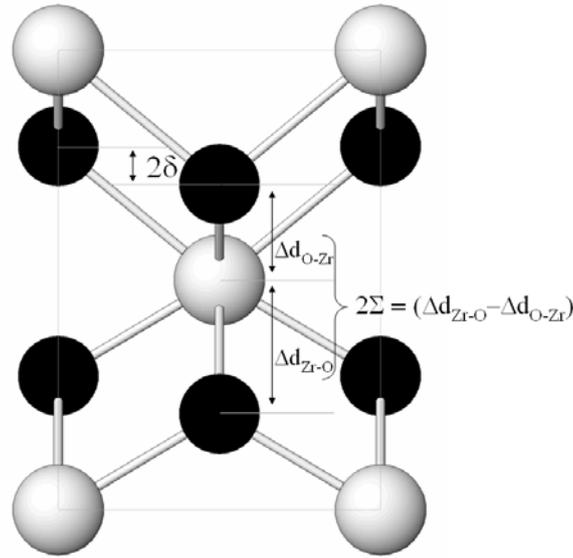
Figure 4.9: Schematic definition of the parameters δ and Σ.

In table 4.7 we show the values of the δ and Σ together with the relaxed 2D in-plane lattice parameter (a) compared to that corresponding to the ideal cubic bulk value for the different c-ZrO$_2$ surfaces. The lattice parameter variations lie within 2% of the ideal cubic bulk value, except for the c-(110) which corresponds to 5 %. Moreover, in all cases the relaxation maintain the initial symmetry of the surface cell, except for the c-(001)$_O|_2$ which becomes with rectangular shape.

Concerning the non-polar c-(110) termination, the most important surface effect is the distortion of the O atoms, respect to its coplanar Zr layers that extends along the entire slab and actually leads to O-ended polar surfaces. Despite this fact, neither the values of δ nor Σ resemble the t-ZrO$_2$ structure.

For the c(111) surfaces, in spite of the non-null δ value and the existence of two Zr-O distances of neither the δ shift nor the interlayer distances can be compared to those of the t-ZrO$_2$ lattice, probably due to the symmetry of the (111) orientation.

Only for the c-(001) surfaces there are several indications of a tendency to reconstruct towards a tetragonal structure. First, the largest values of δ and Σ are found for some of the c-(001) terminations. In particular, c-(001)$_O|_1$ and c-(001)$_O|_2$ exhibit the largest δ, close to δ_{EXP}, and corresponding to an O buckling distribution similar to that of t-ZrO$_2$ (an alternated shift of O columns along the X_2^- phonon direction), as shown in

54

figures 4.4.a and 4.4.b. Also the existence and values of long and short Zr-O distances, coming up from the Σ values, resemble those of tetragonal phase.

	a (in-plane)	$\delta(\text{Å})$	$\Sigma(\text{Å})$
c-(110)ZrO$_2$	3.49/3.65	0,02	0,03
	5,23/5,16		
c-(111)Zr	3,63/3,65	0,11	0,10
c-(111)O-O	3,62/3,65	0,05	0,02
c-A(111)	3,63/3,65	0,00	0,02
c-(111)O	3,59/3,65	0,06	0,03
c-(001)Zr	5,19/5,16	0,00	0,07
c-(001)OO	5,17/5,16	0,00	0,20
c-A(001)	5,20/5,16	0,00	0,22
c-(001)O$|_1$	5,16/5,16	0,38	0,31
c-(001)O$|_2$	5,12/5,12	0,31	0,34

Table 4.7: Values of the 2D lattice parameter (a, in Å), $\delta(\text{Å})$ and $\Sigma(\text{Å})$ for all c-ZrO$_2$ surfaces under study, together with the ideal a$_{2D}$ corresponding to the bulk lattice. Notice that two values of 2D lattice parameters are required for the rectangular (110) cell and that the experimental value of δ is δ_{EXP}=0.295 Å.

All these results indicate that, eventhough the cubic structure tends to profit the additional degrees of freedom provided by the surface to reconstruct towards a tetragonal structure, the symmetry constraints imposed by the particular termination may inhibit this reconstruction.

Although, a c->t transformation at the ZrO$_2$ surfaces has not been observed experimentally, the phase diagram of phase ZrO$_2$ may not be adequate for nanocrystalline samples, as t-ZrO$_2$ nanocrystals are stabilized at room temperature without addition of dopants [190-192]. One of the earlier explanations of this effect [190] proposed that the stabilization mechanism was based on the existence of O vacancies, which favored the nucleation of t-ZrO$_2$ instead of m-ZrO$_2$. Our slab models O$|_1$ and O$|_2$ in fact represent a nanodimensional structure, and a tendency to stabilize the tetragonal phase without O vacancies is found.

4.6 Surface energy and asymmetric slabs of finite thickness

The asymmetric slabs described in this chapter present different terminations at both surfaces, on one side a Zr layer and on the second an O layer. Thus the slab preserves the bulk stoichiometry and in the direction perpendicular to the surface positive and negative charges alternate.

In an ideal asymmetric slab with polar surfaces formed by breaking bulk ZrO$_2$, all the repetition units through the material bear a non-zero dipole moment and therefore the electrostatic potential increases monotonically throughout the system. In the limit of infinite layers, the electrostatic contribution to the surface energy would diverge creating an electrostatic instability. This can be cancelled by a redistribution of the charge density in the outer layers resulting in charge compensation. Figure 4.10 represents schematically the process taking place from the situations corresponding to symmetric slabs to the compensated surface charge of the asymmetric slab.
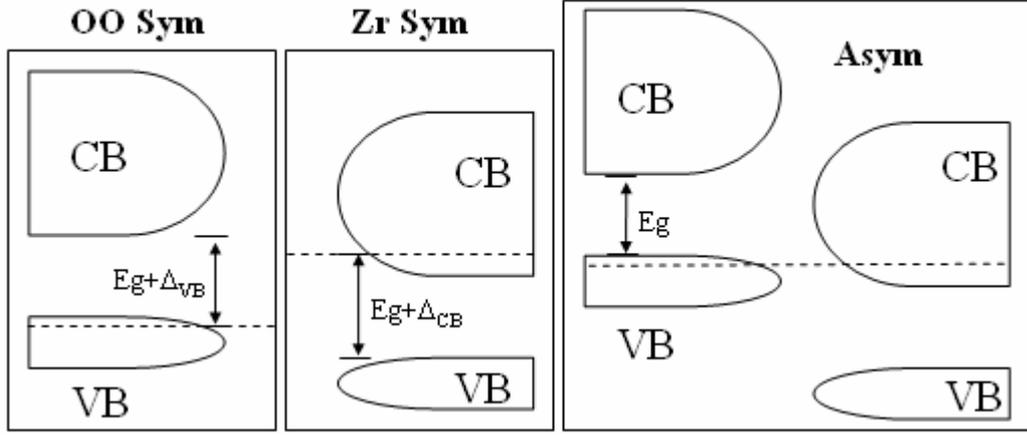
Figure 4.10: Schematic illustration of the Fermi level, by dashed line, and the band bending effect through a slab with asymmetric surfaces, depictured on the right side, compared to the situation with symmetric surfaces: Zr and OO terminated left side of the figure. Eg is the band gap, Δ_{VB} (Δ_{CB}) is the E width from the E_F to the bottom (top) of the CB(VB) when Zr(OO) symmetric terminated.

In the asymmetric slab the Fermi level in the Zr surface will be close to and above the CB minimum, while in the O surface E_F goes below the VB maximum, see figure 4.3.c, resulting in a net potential across the slab slightly larger than the energy gap (Eg): Uo=Eg+Δ_{VB}+Δ_{CB}. This leads to a field dependent on the film thickness which induces a redistribution of the charge density. As a consequence of the alignment of E_F there is a band bending across the slab. Thus, considering that the charge is transferred to the surface (in fact the redistribution of charge takes place along an extended surface layer) the potential driving the charge transfer is [178]:

$$U(q)= Uo - \frac{(qd)}{\varepsilon \varepsilon_0},$$

where εo and ε are the vacuum and zirconia dielectric constants, q the transferred charge and d the slab thickness. The lowering of the surface energy is obtained by integrating the potential over the transferred charge that is determined by the condition U(q)=0, which leads to $\delta q = \frac{\varepsilon \varepsilon_0 U_0}{d}$. Thus the surface energy is given by:

$$\sigma = \int_0^{\delta q} (U_0 - \frac{qd}{\varepsilon \varepsilon_0})dq = \frac{\varepsilon \varepsilon_0 U_0^2}{2d}.$$

σ increases quadratically with U_0 and decrease with the thickness.

We have plotted in figure 4.11 the calculated surface energy of the (100) and (111) asymmetric slabs of c-ZrO$_2$ as a function of the slab thickness from 4 to 14 oxide layers. Note that the σ corresponds to the average σ(Zr)+ σ(O), since the asymmetric slab presents two different surface terminations. As can be seen in figure 4.11, the surface energies show a linear dependence with 1/d. In the limit of infinite layers $\sigma(\infty)$, the linear regression extrapolates to 11.73 and 13.24 J/m^2 for the (100) and (111) slabs respectively. This value is within 0.27 J/m^2 to the average values obtained for the symmetric slabs OO and Zr terminated 11.52 and 12.97 for both the (100) and (111) c-ZrO$_2$ surfaces.
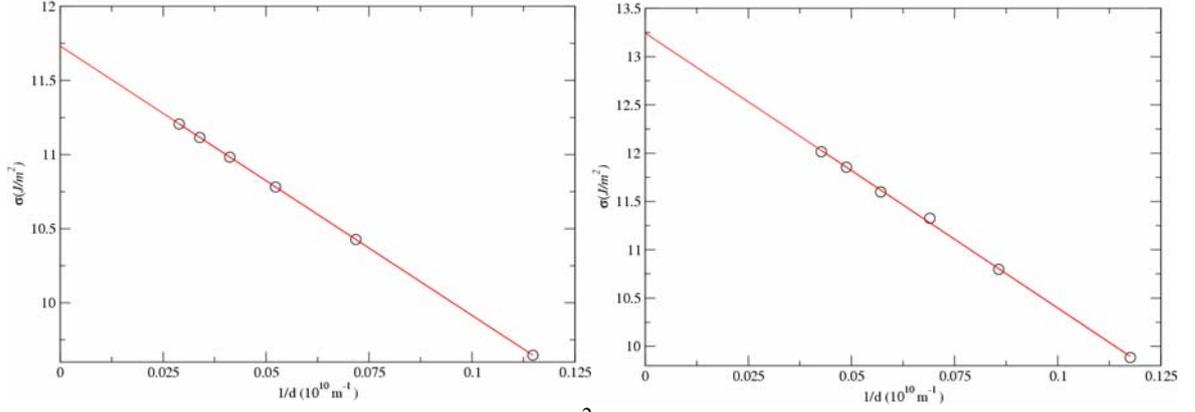
Figure 4.11: Surface energy (σ, in J/m^2) of the two cubic asymmetric slabs a) c-A(100) and b) c-A(111) plotted as a function of the inverse of the slab thickness (1/d in m^{-1}).

The calculated dielectric constant are compiled in table 4.8 and obtained from the surface energies versus the inverse of the slab thickness curves using $U_0 = 3.78$ eV, which correspond to the difference of the Fermi level of the symmetric Zr and OO termination. They compare better with experimental results than those obtained in previous theoretical calculations for the cubic ZrO$_2$.

	Slope(J/m)	εOUR	εEXP	εTEOR
c-(111)	2,84E-009	45,0	47,1;50,8	61,5
c-(100)	1,08E-009	28,6	27,2;29,3	35,5

Table 4.8: Slope values of the linear curves of figure 4.11 and resulting dielectric constants of ZrO$_2$ compared with experimental results from [193] and [194] respectively, and previous theoretical results [195].

On the other hand t-ZrO$_2$ has a different dielectric constant than c-ZrO$_2$, experimental measurements vary between ε_{t-ZrO2}=34.5 [193] and 39.8 [194]. The fact that the value of ε is close to that of c-ZrO$_2$ is consistent with the relaxation pattern observed in both the (111) and (001) c-ZrO$_2$ slabs, in which in spite of the variation of the interlayer distances close to the surfaces, the O atoms remain in plane and do not display the alternated shift characteristic of the tetragonal phase.

As was discussed above, the redistribution of charge in the surface region is a mechanism to stabilize the otherwise unstable polar surfaces and would lead to a cancellation of the charge transfer related to the net dipole moment. Consequently, as shown in figure 4.3.c for the (001) surface, the DOS of symmetric and asymmetric slabs of finite thickness are analogous, with filled surface induced states leading to surface metallization. Even the distribution of charges in the surface region were quite similar although still remain small differences.

Table 4.9 gives the charge in the surface region for symmetric and asymmetric slabs of intermediate thickness. In fact, the asymmetric slabs present a small non-zero dipole moment (p). Therefore, we have also performed calculations for those slabs in the presence of an electric field that completely cancels the dipole moment. The corresponding surface charges are also included. As it is seen, the presence of the external field slightly modifies, particularly for the Zr termination the electronic density in the surface region, which is closer to that of symmetric slabs. Thus, due to the small differences asymmetric slabs can be used to properly describe polar surfaces.

	$Q_{TRANSF} = p/d$	d	Zr term	Next O	Bulk-L	Next Zr	Next O	O term
c-A(111)	0,07	17,52	3,10	6,64	...	2,68	6,59	6,11
c-A(111) Eext		17,47	**3,18**	6,63	...	2,67	6,59	**6,06**
c(111)Zr		17,88	**3,17**	6,72	...	-	-	-
c(111)O-O		19,11	-	-	...	2,60	6,57	**6,02**
c(111)O		16,91	-	-	...	2,49	6,68	-
c-A(100)	0,07	13,93	3,16	6,72	...	2,77	2,77	6,32
c-A(100) Eext		13,83	**3,23**	6,72	...	2,76	2,76	**6,30**
c-(100)Zr		12,50	**3,23**	6,75	...	-	-	-
c-(100)OO		12,90	-	-	...	2,72	2,72	**6,29**
t-A(100)	0,06	13,87	3,18	6,72	...	2,77	6,31	**6,31**
t-A(100) Eext		13,86	**3,23**	6,72	...	2,76	6,29	**6,30**
t-(100)Zr		12,23	**3,24**	6,73	...	-	-	-
t-(100)OO		15,58	-	-	...	2,72	6,32	6,28
t-(100)O		15,34	-	-	...	2,63	6,55	-

Table 4.9: Atomic charges are shown for the asymmetric, with and without external electric field (Eext), and symmetric slabs at the surface layer (Zr, O) and subsurface layers. The transferred charge (Q_{TRANSF}) shown in the leftmost column have been obtained from the dipole moment at finite thickness (p) divided by the slab thickness (d), which is shown in the next column and is given in Å.

4.7 Surface Stability

Finally, we will briefly discuss the stability of the ZrO_2 surfaces. As explained in chapter 2, they have been studied combining first-principles calculations with thermodynamics approaches to obtain surface energies for both stoichiometric and non-stoichiometric surfaces. Their comparison allows one to discuss the thermodynamic stability of the surfaces. Since symmetric slabs are not stoichometric it is not possible a simple comparison of Zr and O terminated surfaces. Only the non-polar surfaces or those terminated with half of the O atoms, this is stoichiometric relations, have a well defined σ. For the polar surfaces σ is obtained as a function of the chemical potential of either Zr or O(μ_O). For surfaces with different polarity the σ values are compiled in table 4.10, which compares within 5.4%, 2.6% and 18.2% for t-(001)$_{Zr}$, t-(001)$_O$ and t-(001)$_{OO}$ with Eichler's results [178]. We have followed the procedure described in section 2.7, and we have calculated the surface energy by eq. 2.20 as a function of the chemical potential μ_O, limited by the value in the O_2 molecule and the formation Gibbs free energy per formula unit of ZrO_2, ΔG^f_{ZrO2}, ranging between the following extremes:

$$1/2 \, (\Delta G^f_{ZrO2}) < \mu_O - 1/2 \, (\mu^{gas}_{O2}) < 0$$

, from now on discussed by means of $\Delta\mu_O = \mu_O - \frac{1}{2}(\mu^{gas}_{O2})$, as explained in 2.7.1. The chemical potential μ_{ZrO2} has been computed as the difference in total energy of relaxed bulk-like slabs with N and N+1 units, evaluated at a constant cross-sectional area A in such a manner that the bulk slabs are subject to the same strain conditions than the surface slabs. We use these values instead of bulk ZrO_2 in order to eliminate the contribution coming from the strain energy. Moreover, as previously reported in some of the slabs used to calculate the surface energy relaxation is not restricted to the top surface layer, as shown in table 4.9, but it extends two or three layers into the slab. Since we used unrelaxed slabs in the calculation of the bulk contribution, there can be some small contribution coming from the difference perpendicular strain condition.

Nevertheless, the differences with the values obtained using unrelaxed slabs are small, about 1% or 2%, so the conclusions concerning the stability of the surfaces are almost unaltered.

	$\mu_O(min)$	$\mu_O(max)$
c-(111)$_O$	0,97	0,97
c-(111)$_{Zr}$	2,38	10,38
c-(111)$_{O-O}$	11,60	3,75
c-(110)	1,30	1,30
c-(001)$_{Zr}$	2,33	9,08
c-(001)$_{OO}$	9,60	2,70
c-(001)O|$_1$	0,75	0,75
c-(001)O|$_2$	1,48	1,48
t-(001)$_{Zr}$	2,58	9,16
t-(001)$_{OO}$	9,94	3,07
t-(001)$_O$	1,09	1,09

Table 4.10: Surface energies values at the two extremes of the μ_O for polar and non-polar c- and t-ZrO$_2$ surfaces.

The surface energy as a function of $\Delta\mu_O$ is represented in figure 4.12 and 4.13 for the low-index surfaces of the cubic and tetragonal phases, respectively.
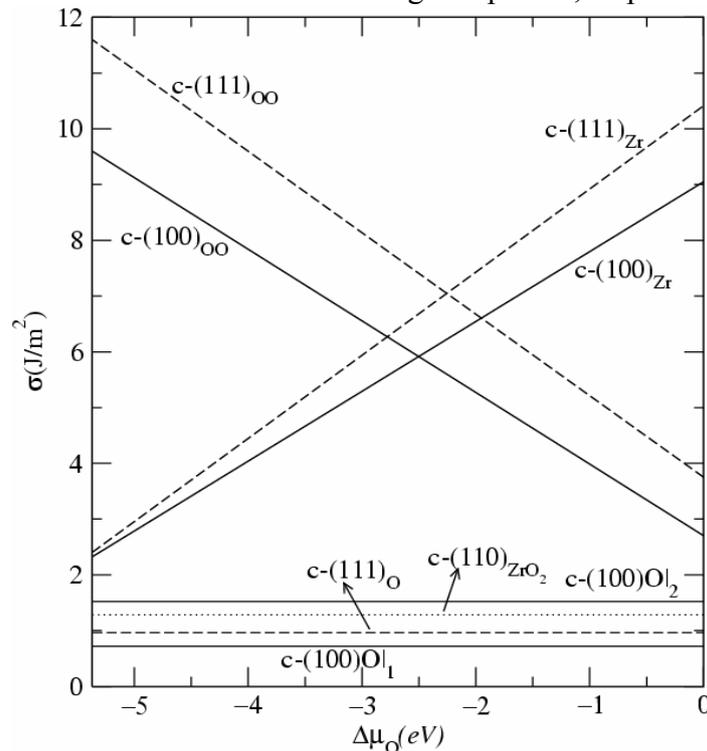
Figure 4.12: Surface energy (σ) plotted in function of $\mu_O-(\frac{1}{2}(\mu^{gas}_{O2}))$ for all cubic calculations, c-(001) slabs in continuous line, c-(110) in small dotted line and c-(111) in dashed line, discussed in table 4.2, 4.3, 4.4 and 4.5. The thermodynamic more stable lines, at the bottom of the figure, correspond to those symmetric and stoichiometric relations.
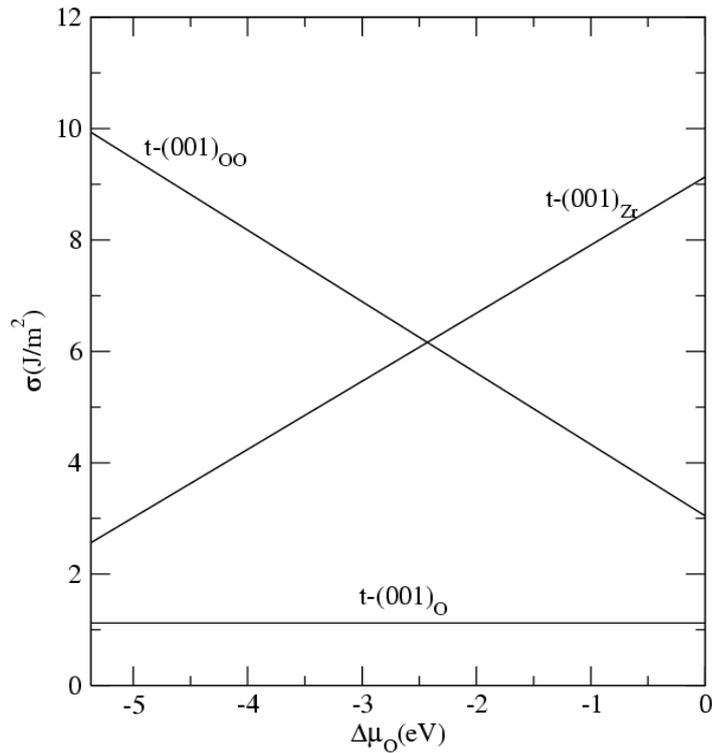
Figure 4.13: Surface energy (σ) plotted as a function of $\mu_O-(\tfrac{1}{2}(\mu^{gas}_{O2}))$ for symmetric t-(001) slabs of table 4.6.

As expected, for both cubic and tetragonal surfaces either the non-polar (110) or those O-ended terminations with half of the oxygen atoms are the thermodynamically most stable, thus these will be the surfaces found in nanocrystals. The Zr and O polar surface both for the (100) and (111) orientations are more stable in opposite ranges of allowed values of $\Delta\mu_O$. While Zr surfaces are stable for $\Delta\mu_O > 2.5$ eV, for lower $\Delta\mu_O$ values the O surfaces are the more stable. Since $\Delta\mu_O$ can be correlated with the concentration of O, our results indicate that Zr/O will be the stable surfaces in equilibrium with low/high partial O pressures.

Chapter 5

Magnetic moment at the bulk and surfaces of ceramic oxides: the role of vacancies

5.1 Introduction

Traditional magnets, which can be described within a local moment picture or an itinerant electron model [196] include 3d transition metal and 4f elements. Their long range magnetic order is supported by the strong direct exchange between adjacent moments, leading to high Tc well above RT. During second half of last century, a new class of indirect exchange interaction was discovered, which extended the family of magnetic materials to non-magnetic elements capable of acting as exchange carriers. A huge set of new magnetic materials and artificial structures appeared, including oxides of 3d transition metals like Fe, Mn or Co. The drawback of the indirect exchange is its weakness as compared to the direct interaction, which causes lower Tc frequently below RT.

In the last years a step forward in the search for new magnetic materials has taken place. High Tc ferromagnetism has been measured for a wide variety of systems, usually of low dimensions, not containing any traditional magnetic element, or only traces of them. Among these systems we find C-based structures prepared by pyrolisis or under irradiation of organic precursors [197, 198], doped or undoped hexaborides [199], or diluted magnetic semiconductors (DMS) [200]. The DMS are non-magnetic insulating oxides or semiconductors doped with diluted amounts of magnetic transition metals which in some cases exhibit high Tc ferromagnetism. More recently, the existence of long-range magnetism has been claimed for oxides doped with non-magnetic transition metals, or even undoped, like the case of HfO_2 [201, 202]. Large magnetic moments over 150-400 μ_B/nm^2 were reported for thin films of HfO_2, as well as a high transition Tc around 500 K [203]. These unusual magnetic properties were attributed to surface or interface effects, and initially assigned to the existence of O vacancies.

At present, the origin of the high Tc ferromagnetism observed in diluted or undoped insulating oxides is under debate. The experimental conditions leading to the onset of ferromagnetism are not clear, and the existence of parasitic ferromagnetic phases has been suggested. On the other hand, there is a lack of models able to explain the long range coupling and high Tc of these systems, which would require a much higher density of magnetic moments or a new class of carriers mediated interaction.

We have investigated the existence of magnetism in ZrO_2 [204], which is very similar to HfO_2. Our results indicate that there is a new type of magnetism rooted in the O p-orbitals and based in the introduction of holes in the VB of the oxide. This is a general property which can be extended to other simple oxides like HfO_2, Al_2O_3 or MgO. In addition, it can explain the origin of the unexpected magnetism measured in HfO_2, which would require the presence of cation vacancies instead of O vacancies [202, 205]. Although we have dealt with ideal models, this p-magnetism may participate in the mechanism supporting the long range ferromagnetism of low dimension insulation oxides.

5.2 Magnetism in bulk c-ZrO$_2$: lattice defects

We first consider the role of different lattice defects in the magnetic properties of bulk c-ZrO$_2$. We use a supercell of 96 atoms (obtained from a 2x2x2 unit cell, see figure 5.1.a) and perform a spin-polarized calculation with the SIESTA package. These calculations start setting as initial guess for the electronic density that assigning the maximum magnetic moment to each atom in the structure. This moment is adjusted during the SCF procedure as the rest of parameters described in chapter 2.

We start considering different numbers of O vacancies within the supercell, placing them along the low index orientations at nearest neighbors (NN) or next nearest neighbors (NNN) relative atom distances when more than one vacancy is present. Precisely the following calculations have been performed: first, with one O vacancy, second, with two O vacancies: either at NN and NNN atom distances along the (111) direction, NNN along (110), or NNN along (001); and finally, four vacancies at NN distance along each of the low index orientation, this is, $\frac{a}{2}\sqrt{3}$ along (111), $\frac{a}{2}$ along (001) and $\frac{a}{\sqrt{2}}$ along (110). The results show that no magnetic moment, within the error of the calculations, is obtained for any atom in the structure.

Next we considered spin polarized calculations with one, two and four Zr vacancies, which will be referred as 1, 2 and 4V$_{Zr}$. The former is a point defect in the lattice, while the other two imply a distribution of vacancies chosen always along the [110] direction, as shown in figure 5.1.b. For the 2V$_{Zr}$ each vacancy has a cation and a Zr vacancy as NN along [110] figure 5.1.b top, while the 4V$_{Zr}$ can be regarded as a linear sequence of defects, see figure 5.1.a and 5.1.b bottom, and therefore can be viewed as a one-dimensional (1D) lattice defect instead of the 0D one corresponding to V$_{Zr}$.

We show in table 5.1 the energy comparison between spin polarized (SP) and non-polarized (NP) calculations, together with the total magnetic moment of the cell and the values per V$_{Zr}$. In all cases the SP situation is more favorable than the NP one, and for more than one V$_{Zr}$ the moments align ferromagnetically (FM). The largest energy differences correspond to the situation with higher magnetic moments: 4V$_{Zr}$, 2V$_{Zr}$, and finally with negligible magnetization V$_{Zr}$. An increase of magnetic moment per V$_{Zr}$ is observed till reach a value close to the number of doped holes [205] by keeping the system in high spin state, as also noticed by Weng [206].

The presence of V$_{Zr}$ modifies the electronic structure of the adjacent atoms. Figure 5.2 shows the DOS projected on representative atoms being NN to one or two V$_{Zr}$ for structures having different numbers of V$_{Zr}$, as well as the DOS of bulk like atoms for comparison. In addition, we provide in table 5.2 the magnetic moments (Mom) and charge values (Q) of the corresponding atoms of the figure.

	$\Delta E_{SP\text{-}NP}$	Mom/V$_{Zr}$
V$_{Zr}$	-0,13	0,13
2V$_{Zr}$	-0,39	1,65
4V$_{Zr}$	-1,66	3,45

Table 5.1: Energy difference between SP and NP calculations ($\Delta E_{SP\text{-}NP}$, in eV), together with the magnetic moment per V$_{Zr}$(Mom/V$_{Zr}$ in μ_B).
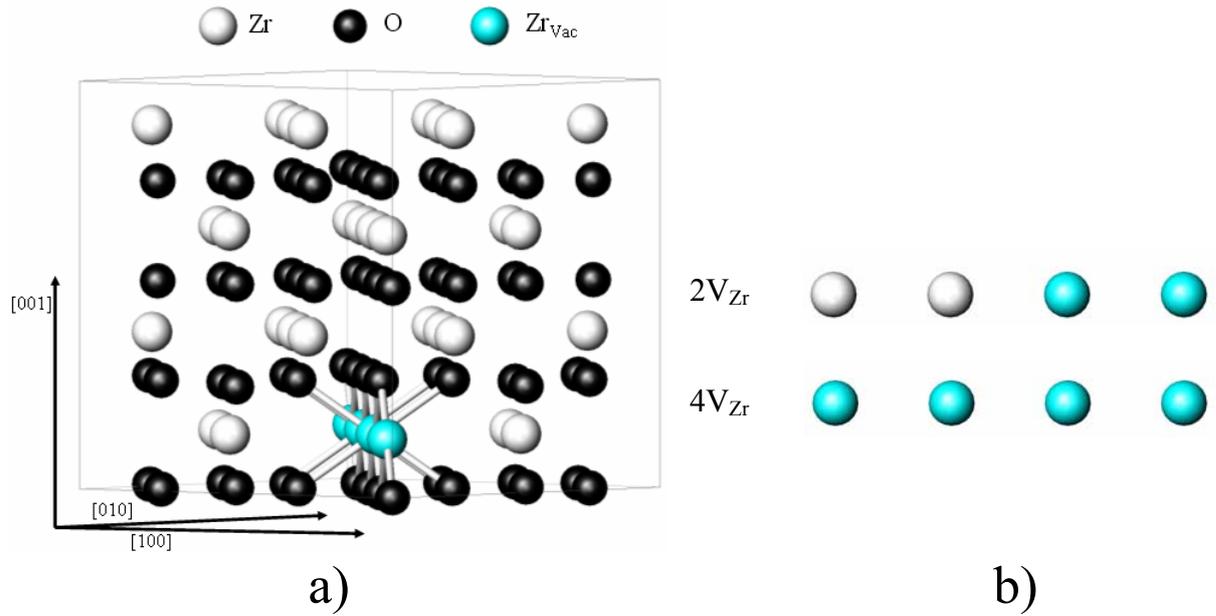
Figure 5.1: a) Schematic representation of the cubic supercell with 96 atoms indicating the position of the Zr vacancies (V_{Zr}) along the <110> direction for the 4 V_{Zr} case.

b) Sequence of the V_{Zr}, medium-bright color, and Zr atoms, brighter color, along the <110> direction for the $2V_{Zr}$, top figure, and $4V_{Zr}$, bottom figure, along <110>, O is represented in black.

Atom Environ	V_{Zr} Mom(μ_B)	Q	$2V_{Zr}$ Mom(μ_B)	Q	$4V_{Zr}$ Mom(μ_B)	Q
O_{BULK}	0,00	6,78	0,00	6,78	0,04	6,79
O V_{Zr}	0,02	6,61	0,02	6,61	0,31	6,58
O $2V_{Zr}$	-	-	0,92	6,30	0,93	6,31
Zr $_{BULK}$	0,00	2,45	0,00	2,44	-0,01	2,48
Zr V_{Zr}	0,00	2,47	-0,01	2,43	-	-
Zr $2V_{Zr}$	-	-	-0,07	2,52	-0,04	2,43

Table 5.2: Charge (Q) and magnetic moment (Mom) for all atoms of the magnetized calculations indicated on the top: $1V_{Zr}$, $2V_{Zr}$ and $4V_{Zr}$. The row indicates different representative atoms in terms of the number of V_{Zr} that are NN.

From the left side of figure 5.2 we notice that for the V_{Zr} few changes in the electronic structure are induced for both the Zr and O atoms closest to V_{Zr}, the major change being the metallic character induced in the O VB of the supercell. The unbalanced charge introduced by V_{Zr} induces a slight magnetization affecting only to the O atoms NN to V_{Zr}. Eventhough the moments are very low, we checked that their value is not an artifact of the calculation and do not vary for more restrictive convergence conditions. Table 5.2 shows that the difference between Os NN and those far to V_{Zr} corresponds to a charge decrease (momentum increase) of 0.17 electrons (0.02 μ_B), while for Zr only a charge increase of 0.02 electrons takes place.
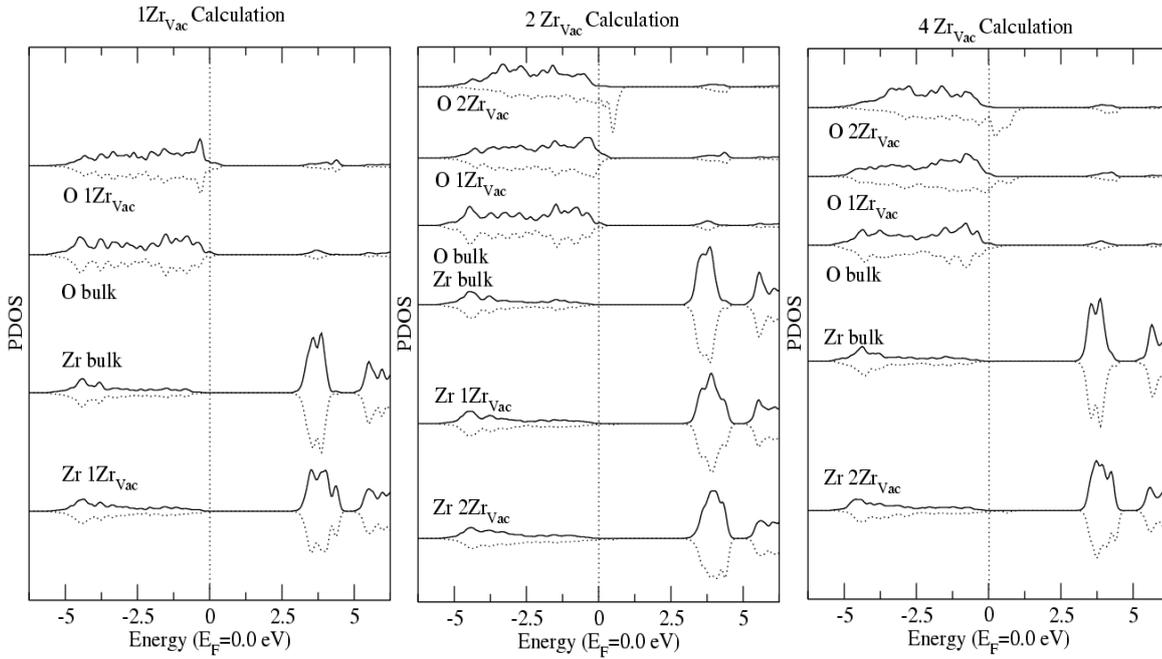
Figure 5.2: PDOS of O and Zr atoms being NN to one or two V_{Zr} for the three different calculations considered. The notation O $2V_{Zr}$ indicates that the O atom is NN to 2 Zr vacancies... etc. Positive DOS values correspond to the majority spin while negative values to the minority spin.

For the case of $2V_{Zr}$ noticeably changes occurs mainly due to the enhancement of the magnetic effects. Figure 5.2 shows that all O exhibit a metallic structure and in addition, the O $2V_{Zr}$ atom present a notable increase in the magnetic moment and a half-metallic character, the majority spin band being completely filled while the minority spin band crosses E_F. Both the O and Zr atoms with none or one NN and Zr are similar to the case $1V_{Zr}$, eventhough the number and distribution of Zr vacancies is different in both calculations. On the other hand, the Zr bonded to $2V_{Zr}$ develops some half-metallicity reflected in the slightly increase of the magnetic moment. It is also worth mentioning the opposite spin polarization of the Zr and O atoms in the structure. The spin development of magnetism seems to be very dependent on the NN local environment, and thus a local property.

The case $4V_{Zr}$ is very similar to $2V_{Zr}$, eventhough only two types of Zr atoms are present, with none or two NN Zr vacancies. Again the O NN to two Zr vacancies (O $2V_{Zr}$) show the largest magnetic moments of almost the same value than the corresponding O in the case $2V_{Zr}$, and with also similar values of the Q, see table 5.2. The main difference between both cases corresponds to the O atoms bonded to just one vacancy (O V_{Zr}), which only for the $4V_{Zr}$ develops and appreciable magnetic moment. This indicates that even when the largest magnetic moments can not overcome that of $2V_{Zr}$, an additional source of magnetism with a reduced contribution is present for $4V_{Zr}$ not so dependent on the NN local environment. Table 5.2 reflects that the magnetic moments reside mainly in the O atoms, and among them, in those with the largest number of neighboring vacancies. There is also a correlation between the reduction of electronic charge and the moment magnitude; the smaller the charge (that is, the largest the loss of transferred cationic charge), the higher the moment.

Another general feature evidenced in figure 5.2, is that the O atoms with the largest magnetic moment, those NN to $2V_{Zr}$ in the calculation with $2V_{Zr}$ and those with one or two NN V_{Zr} in the $4V_{Zr}$ one, exhibit half metallicity. This property seems to appear when the magnetic moment is over 0.3 μ_B.

64

In summary, magnetic properties develop in bulk c-ZrO_2 upon removal of at least two adjacent Zr vacancies. The main magnetic polarization resides on the O atoms NN's to two vacancies. The presence of vacancies implies a non stoichiometric situation where the O atoms exceed the nominal 1:2 ratio. This is reflected in the local reduction of charge of the O atoms bonded to the vacancies, leading to a direct relation between the loss of charge and the intensity of the magnetic moments. This sort of magnetism has been also found theoretically by C. Das Pemmaraju and S. Sanvito [205] for the m-HfO_2 system but their results differ from ours for the case of cation point defect. Das Pemmaraju claims that the presence of one Hf vacancy is enough to lead to a high-spin state with an associated magnetic moment of ~3.5 μ_B, which is carried mainly by the O atoms coupled across the bridging Hf sites.

5.3 Magnetism at ZrO_2 surfaces

The unexpected magnetism observed in oxides, in particular for the case of HfO_2, seems to be related to thin films [203] where the role of surfaces is enhanced. Following also our previous calculation of Zr vacancies in bulk ZrO_2, the magnetic properties are inherently related to the loss of O-cation bonds and the subsequent O excess. This suggests polar surfaces with an O excess as the best scenario for the development of magnetism in ZrO_2. In addition, O polar surfaces can be seen as quasi 2D cation defects, which would enhance the long-range order of the O magnetic moment favoring geometries where a direct exchange interaction occurs.

We start performing SP calculations of different ZrO_2 surfaces terminated in two O planes. This terminations, already studied in the previous chapter, correspond to c-$(111)_{O-O}$, t-$(001)_{OO}$ and c-$(001)_{OO}$ ZrO_2 slabs, whose magnetic properties will be now addressed.

A summary of our results appears in table 5.3, referred to the outermost O atoms. It provides, for each kind of surface atom in the unit cell, the magnetic moment (m_{TOT}), its projection on the surface plane ($m_{TOT(\parallel}{}^p)$), the charge (Q), the difference with the bulk charge(Q_{BULK}-Q), the ratio between the number of Zr-O bond at the surface with respect to those at the bulk (SB), and finally the energy difference between SP and NP relaxed calculations (ΔE) and its relaxation contribution (ΔE_{RELAX}).

	c-(111)O-O		t-(001)OO		c-(001)OO
O sort	O1	O2	O1	O2	O
m_{TOT}	1,56	0,47	1,20	0,58	0,83
$m_{TOT}(\parallel p)[\mu_B]$	1,50	0,20	0,54	0,54	0,61
Q	6,02	6,57	6,20	6,37	6,29
Q_{BULK}-Q	0,77	0,22	0,56	0,39	0,50
SB	1/4	3/4	2/4	2/4	2/4
ΔE	-2,509		-1,171		-0,497
ΔE_{RELAX}	-1,009		-0,657		-0,112

Table 5.3: Properties of the surface O atoms of the different ZrO_2 polar surfaces under study: magnetic moment (m_{TOT}), and its projection on the surface plane ($m_{TOT(\parallel}{}^p)$), charge (Q) and the difference with the bulk charge (Q_{BULK}-Q), number of Zr-O bonds of the surface O atoms divided by those at bulk (SB); total energy difference between the SP and NP relaxed calculation (ΔE) and the SP energy difference between relaxed and unrelaxed configuration (ΔE_{RELAX}), both given in (J/m^2).

For all surfaces there is a reduction of energy with respect to a NP calculation. This energy difference includes two contributions: the magnetic one related to spin degree of freedom, and that related to relaxation, which is briefly summarized by the energetic contribution (ΔE_{RELAX}). The values of the difference in energy per area (energy) goes from -0.50 (-412) to -2.51 J/m^2 (-1797 meV). It is noticeable the correlation between the magnitude of the moments and the loss of charge with respect to the bulk. This way, the larger the difference between the O charge of the surface atom and that of the bulk compound, the bigger the O magnetic moment. The magnetic moment increase can also be related with the loss in cation coordination, represented by the ratio between the number of Zr-O bonds at the surface and the number of bulk bonds. Therefore, the more reduced is the cationic coordination from that of the bulk compound, the larger is the magnetic moment. Apart from this, it can be seen the anisotropic distribution of the magnetic moments for all surfaces with a large component along the surface plane for most cases.

5.3.1 Magnetic ZrO$_2$ surfaces: Energetic contribution of spin

Table 5.4 show the layer by layer evolution of the magnetic moments for the SP calculations, together with that of the Mulliken population both for SP (Q_{SP}), and NP(Q_{NP}) calculations along the ZrO$_2$ slab from the top surface planes to the bulk-like planes. The large magnetic moment localize at the top layers of the surfaces decreasing with increasing depth, so that it almost disappear three layers below the surface. The charges differ slightly between NP and SP calculations, being the largest differences close to 2% at the top layers of the t-(001)$_{OO}$ and c-(111)$_{O-O}$ slabs. The charge evolution from the surface to the bulk is also similar in both type of calculations.

	c-(111)O-O			t-(001)OO			c-(001)OO		
	SP		NP	SP		NP	SP		NP
	Mom(μ_B)	Q	Q	Mom(μ_B)	Q	Q	Mom(μ_B)	Q	Q
O	1,56	6,02	6,10	1,20	6,20	6,28	0,83	6,29	6,30
O	0,47	6,57	6,51	0,58	6,37	6,32	0,83	6,29	6,30
Zr	-0,13	2,60	2,69	-0,16	2,69	2,72	-0,20	2,71	2,73
O	0,07	6,79	6,76	0,32	6,74	6,73	0,13	6,76	6,73
O	0,01	6,80	6,75	0,01	6,77	6,73	0,13	6,76	6,73
Zr	0,00	2,44	2,45	-0,01	2,50	2,47	-0,02	2,44	2,45
O	0,00	6,79	6,77	0,05	6,74	6,76	0,04	6,78	6,77
O	0,00	6,79	6,78	0,00	6,74	6,76	0,04	6,78	6,77
Zr	0,00	2,42	2,43	0,00	2,49	2,47	-0,01	2,43	2,43
O	0,00	6,79	6,78	0,01	6,77	6,76	0,04	6,78	6,77
O	0,00	6,79	6,78	0,01	6,77	6,77	0,04	6,78	6,77
E$_{SPIN}$(J/m^2)	-1,490			-0,529			-0,401		

Table 5.4: Magnetic moment (μ_B) and charge values for the SP and NP calculations from the outer atoms of the surface, at the top, to the central layers at the bottom of the table. The spin energy difference (E$_{SPIN}$), between SP and NP calculation both in the relaxed NP atomic configuration, is also included.

Table 5.4 also includes a comparison between the E gain induced by the development of magnetic moments in the relaxed geometries, thus it corresponds to the onset of magnetism in the relaxed surfaces.

5.3.2.1 Electronic structure

In figure 5.3 the PDOS is shown for atoms nearby the surface compared to those at planes, both for SP and NP calculations. At the top of each panel, it can be seen the outer layer of the surface slab together with the two layers underneath, while the O and Zr bulk like contributions appear at the bottom of each panel.

a)   b)

c)
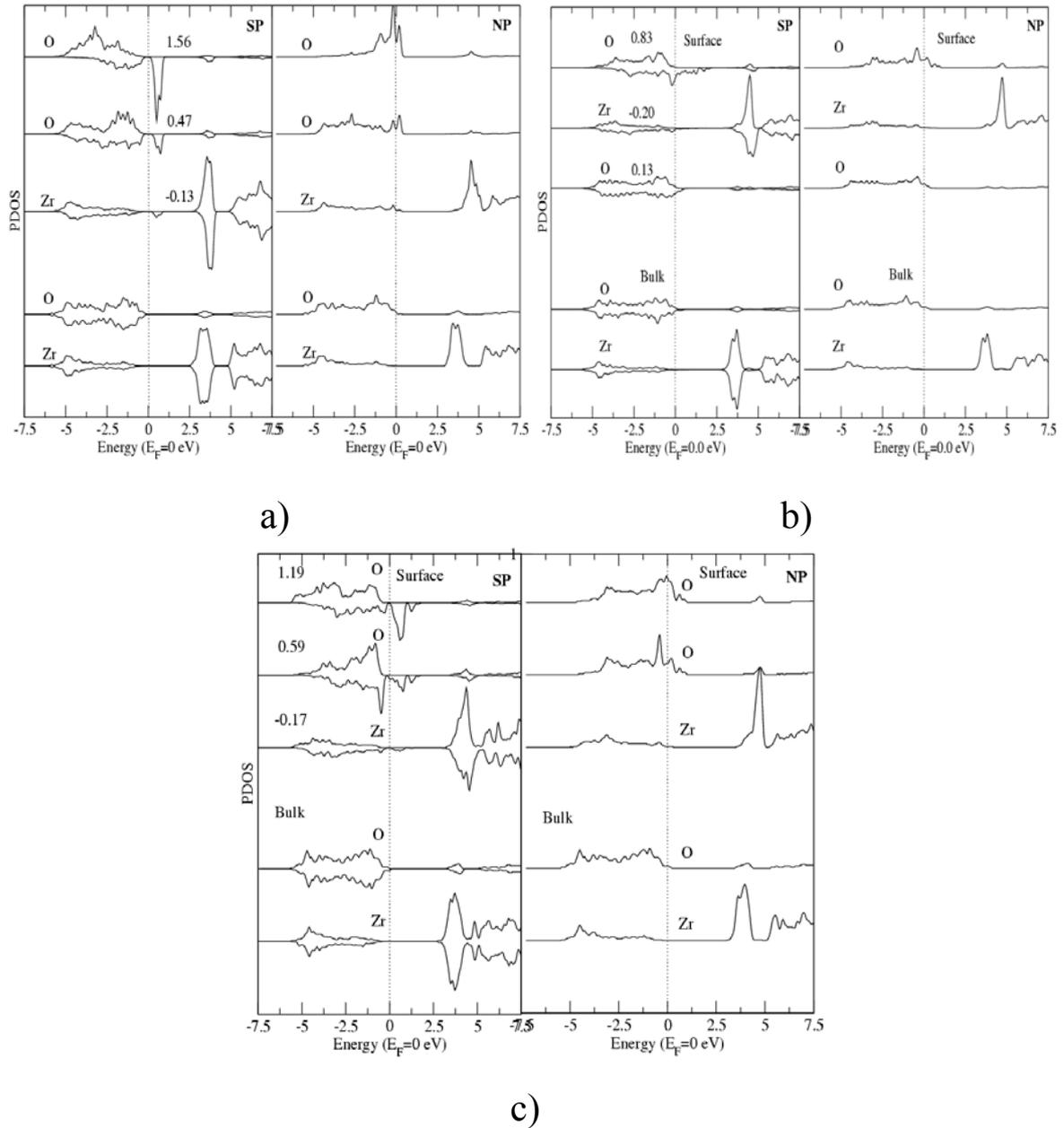
Figure 5.3: PDOS for the atoms of the a) c-(111)$_{O-O}$, b) c-(001)$_{OO}$ and c) t-(001)$_{OO}$ slabs showing both the spin polarized results, SP on the left side of each panel, and NP (right side). The positive DOS values correspond to the majority spin contribution, negative to minority spin. For each surface and calculation, the three curves on the top are the three outermost surface atoms, while the bottom curves correspond to the bulk. The magnetic moments at the surface planes are also provided.

Notice the half-metallic character of the surface atoms of the c-(001)$_{OO}$, which extends some layers below. For the c-(111) and t-(001) surfaces the Fermi level is at a

local gap of the minority spin band. While the completely filled majority spin band shows no major differences with the bulk DOS, the minor spin contribution is significantly reshaped. As usual, the band structure is slightly narrowed at the top most surface planes, as a consequence of the loss of neighbors.
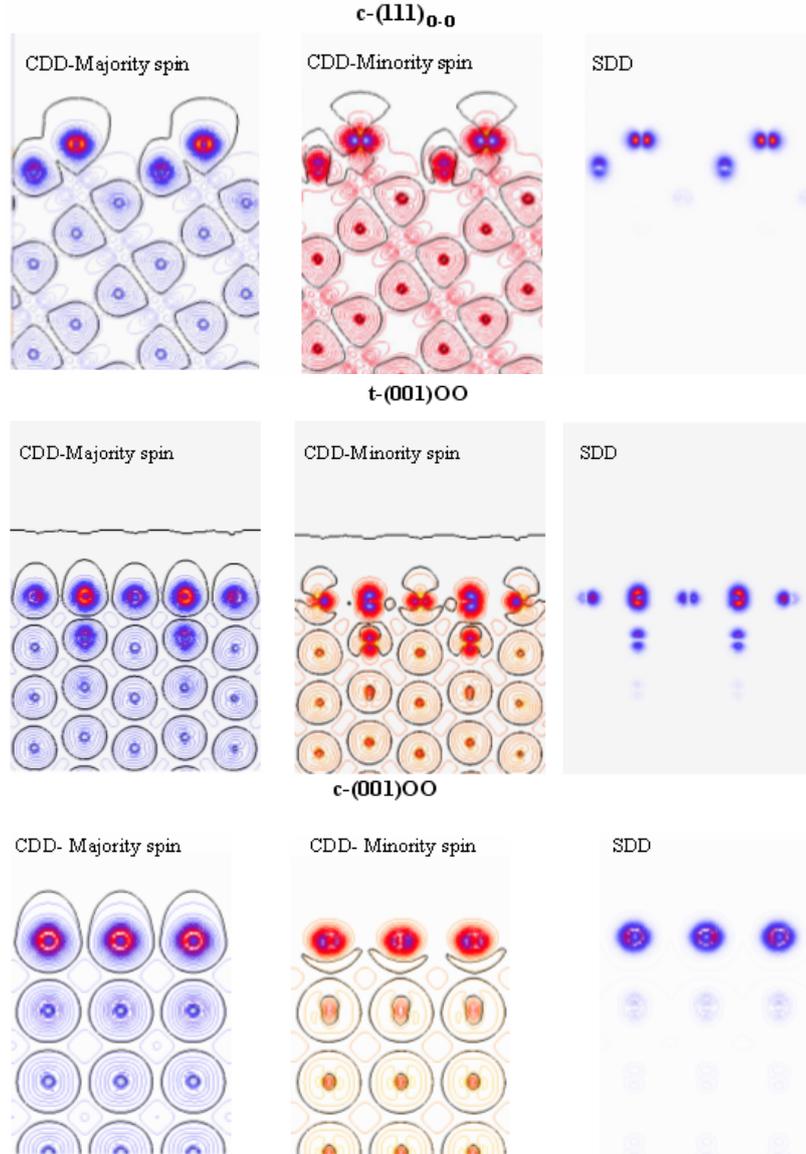
Figure 5.4: CDD graphs from up to down of the c-(111)$_{O-O}$, t-(001)$_{OO}$ and c-(001)$_{OO}$ slabs respectively. The CDD value between consecutive lines is $2.52*10^{-3}$ in all cases. Left, middle and right panels indicates majority, minority and magnetic moment respectively, which is very anisotropic depending mainly on the minority CDD features.

Charge density differences (CDDs) have been depicted in figure 5.4 to study the spatial distribution of the spin-polarized surface electronic charge. These CDDs are shown as contour plots in a plane defined by two vectors: the first is along the nearest neighbors (NN) direction in the O outer surface plane, and the second is along that connecting the surface O atom to the O of the plane underneath. The separation value between two consecutive contour lines is $2.52*10^{-3}$ electron charge for each of the three surface calculations. The thick black lines indicate the zero CDD value, that is, the one corresponding to the superposition of atomic densities, see section 2.5.3 for more information. For all CDD plots shown here the areas with a higher density of contour

lines correspond to the O positions, while Zr atoms occupy the interstitial regions with a lower density of lines.

The majority and minority spin contributions have been separated. The left side of each panel shows majority spin distribution, where the contour lines are almost constant in shape, throughout the slab, with some variations only at the outermost planes of the surface. As already observed in the PDOS, the majority spin distribution resembles the bulk, as it can be seen in the spherical regions of the left panels. The minority spin distributions, shown in the middle panels, show different features from the bulk which are not only related to the color intensity but also to the shape of the contour lines. The magnetic moment density difference (SDD) is obtained by subtracting the majority and minority distributions along the surface, which can be seen at the right side of figure 5.4. The magnetic moment distribution is very anisotropic, with a preferred alignment with respect to the surface normal either out-of-plane or in-plane.

5.4 Surface magnetism in other ceramic oxides

The previous results obtained for defected bulk ZrO_2 and polar ZrO_2 surfaces let us establish that the main source of local magnetization is the lowering over 50 % of the O coordination to Zr. In this section we will show that this property can be generalized to other ionic oxides. First, we will consider with some detail the case of HfO_2, similar to ZrO_2 and for which experimental evidence [201, 203] of magnetic properties has been found. Then, other oxides like the Al_2O_3 and MgO, with different degree of ionicity and stoichiometry than ZrO_2 will be studied.

5.4.1 t-HfO$_2$(001)

The calculations of the HfO_2 surfaces have been performed with the *ab-initio* VASP code [91] within the gradient generalized approximation (GGA) and using the projected augmented wave (PAW) in the PBE scheme for the generation of pseudopotentials [86] in order to get rid of the non-valence electron interactions.

Initially we have performed several bulk calculations of the three low pressure phases of HfO_2 to assure the feasibility of the settings used. We correctly reproduce the total energy hierarchy having: $E_m < E_t < E_c$ with energy cut off values around 350 eV. For more details of the calculation see Appendix A1.

The t-HfO_2 surfaces along (001) direction is constituted by alternating polar planes of Hf and O atoms, as t-ZrO_2 except the slight distortion of the O planes characterized by the parameter δ which experimentally is not observed. Our slab geometry allows the atomic relaxation on one half of the slab, while the other half is kept fixed with the t-HfO_2 bulk positions. We have considered both O and Hf terminations in the symmetric slab configurations t-HfO_2(001)$_{OO}$ and t-HfO_2(001)$_{Hf}$, left and middle panels of figure 5.5 respectively, in order to avoid artificial electric dipolar contributions to the energy.

These t-HfO_2 (001) surface calculations have been performed with a 283 eV energy cut off value, 4x4x1 K point mesh and a vacuum region of at least 15 Å. Convergence on a 8x8x1 K point mesh have been studied slab resulting differences of less than 0.3 % in surface energy.

We have varied the number of atomic layers, related to the number of stoichiometric formula units, from 3 to 11.
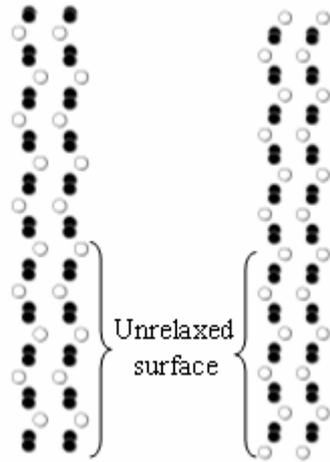
Figure 5.5: Structural geometry of the two (001) t-HfO$_2$ slabs where left and right panels are respectively the OO ended and Hf ended symmetric slabs, t-HfO$_2$(001)$_{OO}$ and t-HfO$_2$(001)$_{Hf}$, only relaxed in the upper part while in the lower bulk positions are fixed. O are represented as the dark circles while Hf are the brighter ones.

When performing calculations allowing the spin degree of freedom on the symmetric slabs, we obtain magnetic effects only for the OO termination, while for Hf termination no reduction of energy due to the spin polarization results, as otherwise expected. Table 5.5 compiles the magnetic moments obtained for the OO symmetric slab at the outer surface layers of both sides, relaxed at the upper half, and unrelaxed at the bottom one as a function of the number of layers in the slab. The magnetic moments are localized on the outer layers, being higher for the O atoms and with opposite polarization at the nearest Hf planes. The relaxed side exhibits a lower magnetic moment than the unrelax one, but as we deepen into the slab the magnetic moment effects are extended along three planes for the relaxed side while for the unrelaxed one they reach only two planes. At the relaxed side of the 11 layer slab, the maximum magnetic moment corresponds to the outer O, with a value of 1.078 μ_B, while for the O just 0.25 Å below it is just 0.537 μ_B, the entire polarization almost corresponds to p-orbitals. Magnetic moment values are fully converged with 9 layers, and with a negative energy contribution, which indicates that SP is more stable than NP. The energy gain with respect to a NP calculation shown at the bottom of the table is -0.790 eV for 11 layers slab, ~50 % larger than the contribution of atomic relaxation. These values correspond to surface energies of around 0.96 J/m^2, which compares well with the value 1.17 J/m^2 obtained for t-(001)ZrO$_2$, see table 5.3.

t-(001)$_{OO}$	n^o layers			
	5	7	9	11
OO	1,07	1,13	1,07	1,08
	0,52	0,51	0,53	0,53
Hf	-0,04	-0,06	-0,06	-0,06
OO	0,21	0,18	0,24	0,23
	0,03	0,03	0,02	0,02
Hf	0,00	0,00	0,00	0,00
OO	0,04	0,03	0,04	0,04
	0,02	0,00	0,00	0,00
...				
Hf	0,00	0,00	0,00	0,00
	0,04	0,04	0,03	0,03
OO	0,06	0,06	0,05	0,05
Hf	-0,06	-0,04	-0,04	-0,04
	0,53	0,54	0,54	0,54
OO	1,26	1,27	1,27	1,26
ΔE_{SPIN}(eV)	-0,777	-0,778	-0,793	-0,790

Table 5.5: Atomic magnetic moment for the outer layers of the t-HfO$_2$(001)$_{OO}$ slab at relaxed side, top, and unrelaxed, bottom, with bulk like region indicated by dots.

5.4.2 Al$_2$O$_3$ and MgO

The finding of magnetism in HfO$_2$ after our calculations for ZrO$_2$ is not surprising due to the similar atomic and electronic structures of both oxides. Here we will address the study of different ceramics which exhibit significant differences with ZrO$_2$, not only in their structure, but also in the oxygen stoichiometry, ionicity and electronic structure. We will consider different O-rich polar surfaces to see if the development of spin polarization takes place: Al$_2$O$_3$ (0001), Al$_2$O$_3$ (10$\bar{1}$2) and MgO (111).

The Al$_2$O$_3$ (0001) surface consist of alternating Al and O planes where the O plane have 3/2 times more density than the Al planes. We model the O terminated surface. As explained in section 3.3.1, the stacking along the [0001] direction is A-a-B-b-A-c-B-a-A-b-B-c-A, where the capital (small) letters indicate O (Al) plane. We have also calculated the O termination of the Al$_2$O$_3$ (10$\bar{1}$2) surface, which consist of alternated Al and O planes. In the surface MgO(111) Mg and O planes alternates with a stacking a-C-b-A-c-B... where capital (small) letter indicates Mg (O) atomic positions.

Table 5.6 compiles our main results, following the same scheme than table 5.3. Again the SP is favored over a non-magnetic state, as occurred for ZrO$_2$ and HfO$_2$. The reduction of energy ranges between the values obtained for c-(111)$_{O-O}$ (2.51 J/m^2) and c-(001)$_{OO}$ (0.50 J/m^2). The obtained relations between the magnetic moment and charge for O in ZrO$_2$ are also satisfied for Al$_2$O$_3$ and MgO systems, the magnetic moment increases the more the surface charge reduces from the bulk value and also increases as the cation coordination (SB) reduces. However, the Al$_2$O$_3$ and MgO surfaces show a magnetic charge distribution of anisotropy opposite to that of ZrO$_2$. For these surfaces, only Al$_2$O$_3$(0001) has a major contribution along the in-plane direction, while for the other the magnetic charge is mainly aligned along the out of plane direction.

	$(0001)_{OO}$	$(10\text{-}12)_{OO}$		$(111)_{OO}$
O sort	O	O1	O2	O
m_{TOT}	0,97	0,92	0,71	0,83
$m_{TOT}(\|\rho)[\mu_B]$	0,74	0,15	0,51	0,06
Q	6,10	6,13	6,16	6,37
Q_{BULK}-Q	0,39	0,36	0,33	0,35
SB	3/6	2/6	2/6	3/6
$\Delta E(J/m^2)$	-2,166	-1,155		-1,611
ΔE_{SPIN}	-2,044	-1,051		-1,475
ΔE_{RELAX}	-0,122	-0,104		-0,136

Table 5.6: Same as table 5.3 for the different O polar surfaces of Al_2O_3 and MgO under study. In addition, we provide the decomposition of ΔE in the spin (ΔE_{SPIN}) and relaxation contributions (ΔE_{RELAX}), which are all given in (J/m^2).
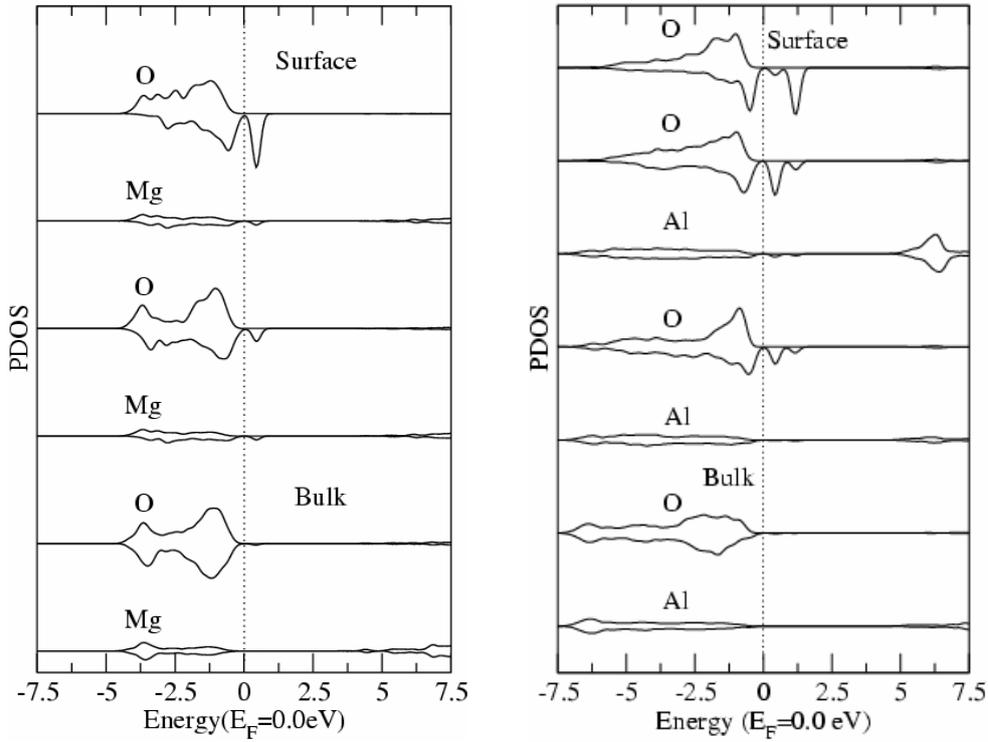
Figure 5.6: PDOS for the atoms of the $MgO(111)_{O\text{-}O}$ and $Al_2O_3(10\overline{1}2)_{OO}$ showing the spin polarized results. The positive DOS values correspond to the majority spin contribution, negative to minority spin. For each surface and calculation, the first curves on the top are the outermost surface atoms, while the two bottom curves correspond to the bulk.

The analysis of the PDOS of the two Al_2O_3 and MgO(111) surfaces provide similar characteristics to those of ZrO_2, as can be seen in figure 5.6. The largest magnetization resides in the O atoms at the outer surface layer, while the surface effects extend around three layers in depth. None of these surfaces the Fermi level within a local minimum in the minority spin band. The majority spin DOS is closer to the bulk than the minority spin DOS. This is also reflected in the CDDs plots shown in figure 5.7.

The contour plot of the CDDs for $Al_2O_3(0001)_{OO}$ and $MgO(111)_{OO}$ slabs are shown in figure 5.7 along a plane defined by two vectors: the first is along the nearest neighbors (NN) direction in the O outer surface plane, and the second is along that connecting the O atom to the O of the plane underneath. Again, like in figure 5.4, it can be easily recognized the O surroundings by a more dense concentration of lines, while the cation distribution exhibit a less dense squared shape between O planes, evident in both slabs.
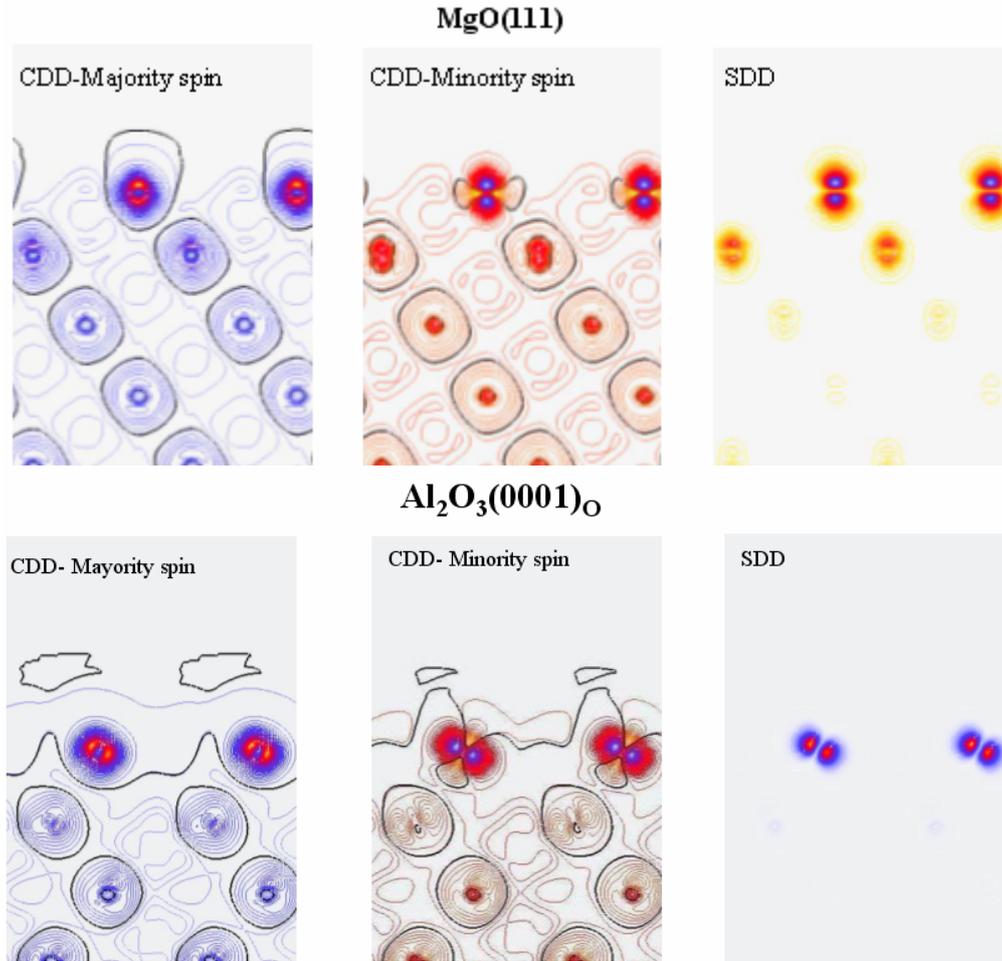
Figure 5.7: Contour lines of CDD graphs of the $Al_2O_3(0001)$, at the bottom, and $MgO(111)_{OO}$ slabs, at the top. The distance between consecutive lines is $1.97*10^{-3}$ and $2.05*10^{-3}$ for $MgO(111)_{OO}$ and $Al_2O_3(0001)$, respectively. Left, middle and right panels indicates the majority, minority and magnetic moment distributions, following figure 5.4.

The majority spin band, left panel of figure 5.7, is completely filled and the corresponding CDD adopts spherical O shapes throughout the entire slab, only with minor intensity changes at the outer plane compared to the bulk. In contrast, anisotropic lobe-type shapes appear in the minority spin distribution, middle panel, resulting mainly into an in-plane spin magnetic distribution for $Al_2O_3(0001)$ and a dominant perpendicular to the surface distribution for $MgO(111)$, as evidenced in the SDD in the rightmost panels. The majority spin band being filled, this anisotropic spin distribution is mainly due to the minority spin charge, as also observed for ZrO_2.

Chapter 6

ZrO$_2$/Ni Interfaces: structural, electronic and adhesion properties

6.1 Introduction

ZrO$_2$/Ni cermets play a crucial role in a wide range of technological applications as thermal barrier coatings [207], microelectronics [159], ionic conductors [110, 193], structural components [208, 209], solid oxide fuel cells (SOFC) [210] or as multifunctional devices [211, 212].

The reason why this system is used in such a variety of fields is because it combines very interesting properties from its individual constituents. ZrO$_2$ exhibits the highest mechanical strength and toughness at room temperature among ceramics, a very high electric and thermal resistivity, a high flexion and traction strength together with an excellent wear, chemical and corrosion resistance [213, 214]. On the other side, Nickel is hard, ductile, malleable, ferromagnetic, and a good conductor of heat and electricity [215]. In addition, an important advantage of the cermet formed combining both materials is that they are reactless when joined and they present similar values of the thermal expansion coefficient and elastic modulus [29]. This similarity implies that the cermet is free from residual stresses when acting at certain temperature and mechanical stress, which is a key property to allow the applicability of the cermet in certain devices. Apart from these parameters, the efficiency of the cermet is known to depend strongly, as commented in chapter 1, on the interface adhesion.

There are several mechanisms to increase the resistance to crack propagation (toughening) of ZrO$_2$/metal systems, but we are going to consider only two of the more important ones: the transformation toughening [216, 217] related to the ZrO$_2$ matrix, and the crack bridging [1, 13] related to the plastic deformation of the metal. The first mechanism is based on the induced transformation to the monoclinic phase when a crack tip propagates along the material. This crack tip transmits locally to the ZrO$_2$ the energy that promotes the transformation to the phase of highest volume, creating local stresses that lower the propagating energy of the crack. The second mechanism is due to the metal and its ability to deform plastically, which can bridge the crack faces behind the crack front, therefore strengthening the material. See figure 6.1 for a crack propagation and the bridging mechanism strengthening of the BaTiO$_3$/Ni system.

This last mechanical process, due to plastic dissipative mechanisms, is one of the main reasons for the employment of metals in combination with ceramics. However, in order to have such a bridging process, the interface has to show good adherence, so that the interface does not become the weakest part of the system under crack propagation [12].
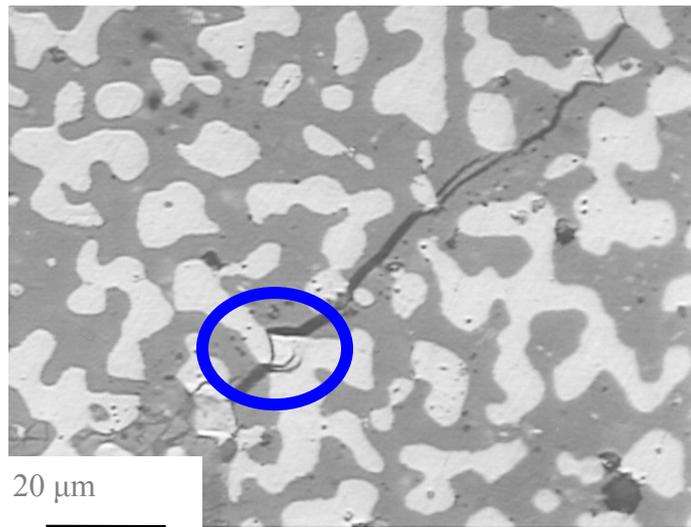
Figure 6.1: Scanning electron microscopy micrograph showing the metal bridging mechanism in a BaTiO$_3$/Ni system. Ni grains are the brighter ones.

Until recently, there have been few experimental studies trying to characterize the adhesion of ZrO$_2$/Ni interfaces, specially at the nanoscale. One of these works was performed by the group of Prof. Moya, who characterized by HRTEM the interface of nanocermets formed combining nanoparticles of ZrO$_2$ and Ni. Figure 6.2 shows their result for two particular interfaces, ZrO$_2$(001)/Ni(001) and ZrO$_2$(110)/Ni(001). Eventhough for these cases the atomic matching at the interface is good, in order to know if bridging mechanisms may take place we have to obtain also good mechanical properties. Unfortunately, there are not adhesion measurements for these nanocomposite materials.

a)   b)
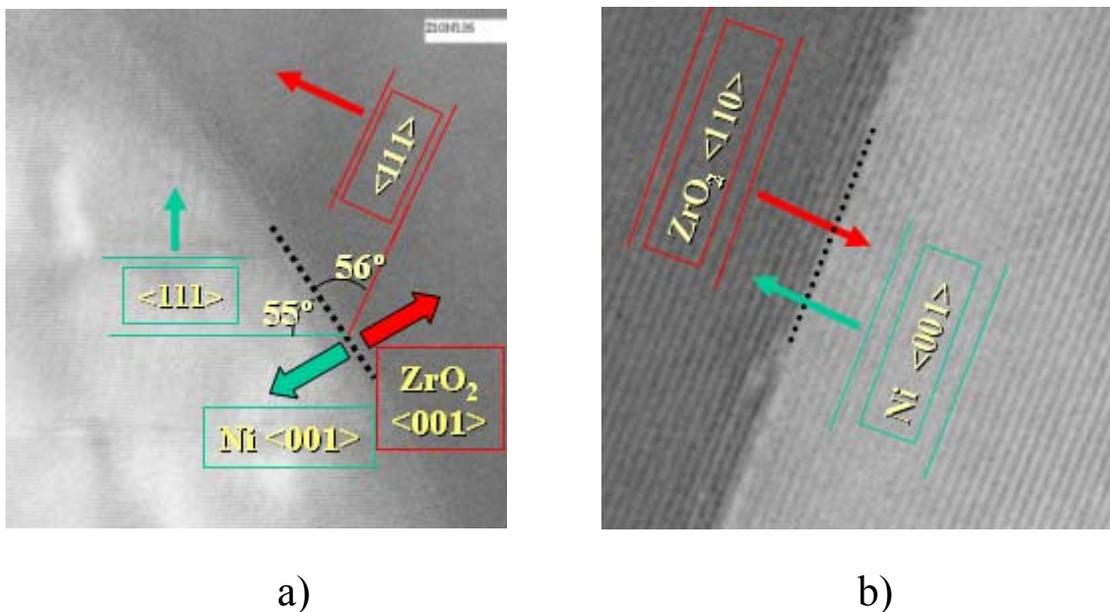
Figure 6.2: HRTEM picture of two interfaces characterized by a) ZrO$_2$(001)/Ni(001) and b) ZrO$_2$(110)/Ni(001) orientations.

The experimental information of the interface adhesion has been obtained for microscomposites, as shown in figure 6.3. This kind of samples retain certain defects,

like porosity, associated to the ZrO₂/Ni interface [29]. This leads to the result evidenced in the figure: the crack propagates along the interfaces. This information of the interface together with experimentally obtained low value of Wsep=1.1 J/m² [218] indicates a brittle adhesion mechanism without mechanical enhancement by plastic deformation.
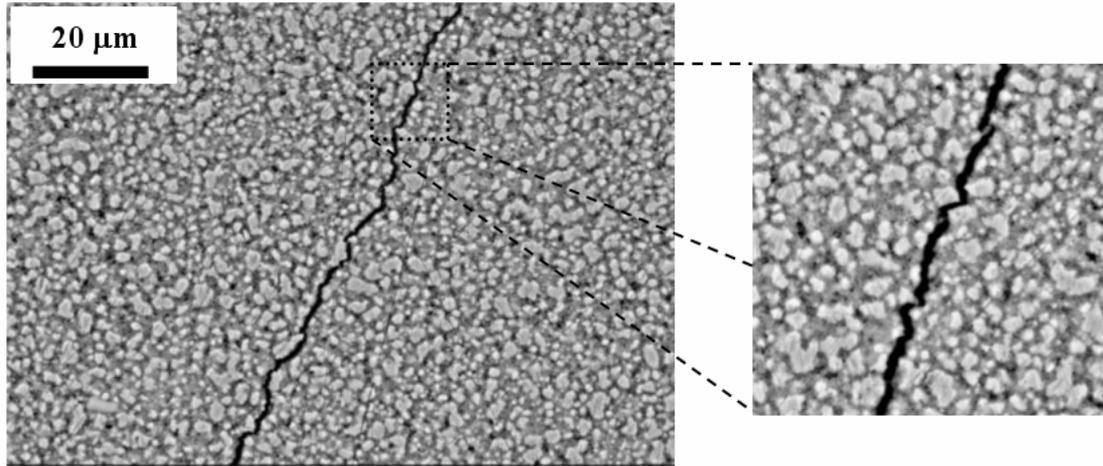
Figure 6.3: Scaning electron microscopy (SEM) image showing a crack propagating through the interface of the ZrO₂ ceramic matrix and the Ni metal particles (brighter grains), showing a brittle interaction between both materials at the microcomposite level.

In addition Dickey *et al.* have grown and studied the crystallographic orientations of ZrO₂/Ni interfaces by several methods. Using MBE in ultra high vacuum (UHV) polycristalline nickel films of thickness about 150 nm were grown on c-ZrO₂(001) and showed two epitaxial orientation relations (OR): ZrO₂(111)∥Ni(111); ZrO₂[010]∥Ni[$\bar{1}$10] and ZrO₂(100)∥Ni(100); ZrO₂[010]∥Ni[010] [27]. Besides, by means of reduction of NiO an interface between Ni and ZrO₂ was formed not in complete equilibrium with orientations ZrO₂(100)/Ni(100) and Zr terminated [26].

On the other hand, Laguna-Bercero and coworkers grew channeled Ni-YSZ and Co-YSZ cermets by reduction of laser-assisted directionally solidified lamelar eutectic [31]. For the Ni cermet, it was shown by TEM that initially the precursor was oriented along ZrO₂(001)/NiO($\bar{1}$11), while the ZrO₂/Ni cermet presented four different interfaces:

OR1 ZrO₂(002)∥Ni($\bar{1}$11); ZrO₂[100]∥Ni[110]
OR2 ZrO₂(002)∥Ni($\bar{1}$11); ZrO₂[110]∥Ni[110]
OR3 ZrO₂(002)∥Ni(002); ZrO₂[110]∥Ni[100]
OR4 ZrO₂(002)∥Ni(002); ZrO₂[110]∥Ni[110]

These interfaces formed in these cermets are probably the four most stable interfaces between c-ZrO₂(001) and Ni due to the repeated appearance with different techniques as those cases commented above.

This chapter is focused on the study of the ideal c-ZrO₂/Ni interfaces that result from combining relative orientations between the metal and ZrO₂. Besides considering ideal ZrO₂, we perform further calculations including actual presence of the defects created by the stabilization mechanism of c-ZrO₂, in order to compare more accurately the theoretical adhesion values with experimental results.

6.2 Theoretical model

The interfaces are described by a slab model similar to that employed to describe surfaces. However, for interface calculations we do not include a vacuum region and so the unit cell, formed by two different materials and their interface, when repeated by PBC leads to two interfaces, see figure 6.4. Unless otherwise stated we will force both interfaces to be equivalent in order to ease the analysis of the interface stability. Another initial condition in our calculations is that the Ni unit cell is strained to make it match to the ZrO_2 lattice. This approximation is supported by the larger plasticity of the metal as compared to the ceramic. In fact, the same initial condition will be used when studying the interfaces of chapter 7.
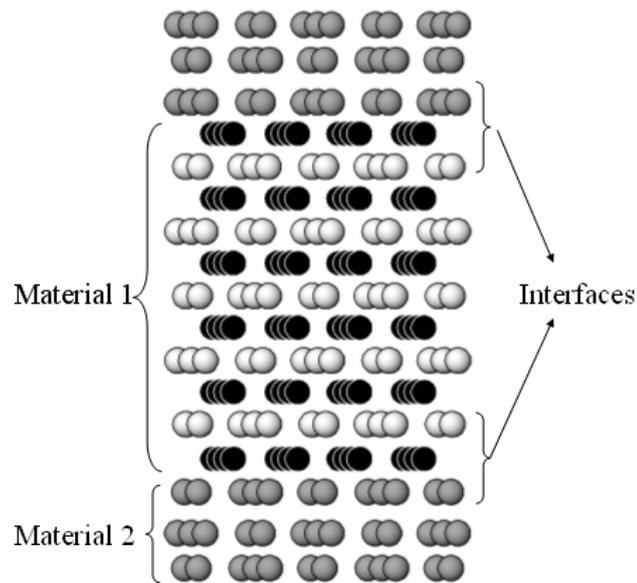
Figure 6.4: Scheme of the slab model for the interface between two materials. We consider two interfaces, which by default are identical.

As already indicated, when studying the ZrO_2 surfaces, bulk properties are expected at the central layers of both the ZrO_2 and Ni sides of the slab that will be identified mainly regarding atomic charges and atomic PDOS. This requirements determines the minimum number of atomic planes, both for the metal and the ceramic, that need to be considered in the slab, as shown in table 6.1 for the case of the $ZrO_2(001)/Ni(001)$ system.

	4 ZrO_2/4 Ni	5 ZrO_2/4 Ni	5 ZrO_2/5 Ni	7 ZrO_2/4 Ni	7 ZrO_2/4 Ni	Bulk
Q(O)	6,77	6,78	**6,78**	6,78	6,78	6,79
Q(Zr)	2,45	2,45	**2,44**	2,44	2,44	2,42
Q(Ni)	10,01	10,01	**10,00**	10,00	10,00	10,00

Table 6.1: Atomic charge values at the central planes for the constituents materials $ZrO_2(001)/Ni(001)$ interface slabs of different thickness. As a compromise, five Ni layers and five ZrO_2 have been considered sufficient to attain bulk properties at the center of the slab.

Table 6.1 provides the atomic charge values for the atoms in the layers further from the interfaces, which are those closer to a bulk-like behavior. We choose five layers-thick slabs as a compromise between accuracy and computing time.

For a complete determination of the interface, besides choosing the crystal directions perpendicular to the interface plane, the atomic coordination at the interface has to be set, that is, the relative atomic positions of both materials at the interface plane, which in turn determines the number of interface bonds.

The final geometry of the interface is obtained after allowing full relaxation of the atomic positions and the cell size and shape, until the forces on each of the atoms are less than 0.1 eV/Å. The rest of the parameters relevant to these calculations are those specified in chapter 2.

6.3 Ideal ZrO$_2$/Ni interfaces

Although in actual applications the c-ZrO$_2$ and t-ZrO$_2$ phases need the presence of stabilizing dopants and defects, it is interesting to first consider the ideal undefected structures. Due to the similarity between the cubic and tetragonal structures, as commented in section 3.2.3, we will restrict to the c-ZrO$_2$.

We will study interface geometries corresponding to the matching of different relative crystal terminations of Ni and ZrO$_2$. First, we will consider the interface ZrO$_2$(001)/Ni(001), observed experimentally by the HRTEM micrographs in nanocermets [29] see figure 6.2.a, [26, 31]. For these orientations, as the ratio between the lattice parameters of both materials is very close to $\sqrt{2}$, a low misfit (~2%) is obtained aligning the in-plane ZrO$_2$[100] direction with Ni[110]. This orientation have been found [27] to be the one that produces the smallest unit cell in the Near Coincidence Site Lattice (NCSL) theory [28]. Therefore, the interface geometry is totally specified throughout the notation: c-ZrO$_2$(001)/Ni(001) || c-ZrO$_2$[100]/Ni[110]. This is the first interface we will consider.

As the c-ZrO$_2$ termination leads to polar surfaces, it is also interesting to consider a non-polar case, namely, the Ni interface with c-ZrO$_2$(110). In fact, the HRTEM micrographs of figure 6.2.b indicate the existence of the c-ZrO$_2$(110)/Ni(001) interface. A good 2D matching is obtained with the c-ZrO$_2$[001]/Ni[010] inplane directions aligned. This is the second interface we will consider, in subsection 6.3.2.

6.3.1   c-ZrO$_2$(001)/Ni(001); c-ZrO$_2$[100]/Ni[110]

This interface can be obtained following two different methods of sintering, which is an indication of its stability. The one from which the nanocomposites of figure 6.2 have been obtained, is produced by precipitation of a nickel nitrate on t-ZrO$_2$ stabilized by 3 % molar contain of Y$_2$O$_3$ (3YTZP) particles to further decompose into the oxide, and then be reduced at hydrogen atmosphere [30]. The other sintering method is done by reduction of NiO-YSZ lamellar eutectics from an initial orientation of (111)NiO and (002)ZrO$_2$ [31]. In the latter case, after reduction, the Ni particles undergo to a crystallographic re-orientation to form (002)Ni.

Due to the fact that the ZrO$_2$ planes are polar along the (001) orientation, we have two possible atomic terminations: O planes or Zr planes. Both terminations have been energetically studied by including them in the same calculation, one ZrO$_2$ side Zr terminated while O on the other. The total energy, $\Delta E(eV)$, balance for different interface atomic coordinations is summarized in table 6.2, while the corresponding

atomic positions are depicted in figure 6.5. $\Delta E(eV)$ is referred to the most stable case, which is shown in the first row and corresponds to the middle top diagram (for Zr/Ni) and the leftmost bottom diagram (for O/Ni) of figure 6.5.

Zr/Ni	O/Ni	$\Delta E(eV)$
Hollow	Bridge	0,000
Bridge	Bridge	0,109
Hollow	Hollow	0,112
Top	Bridge	0,283
Hollow	Top	0,406
Bridge	Top	0,552
Top	Top	0,684
Bridge	Hollow	0,857
Top	Hollow	1,026

Table 6.2: Total energy difference, $\Delta E(eV)$, of the relaxed slabs modeling the different possible relative coordinations at the Zr/Ni and O/Ni interfaces with respect to the most favorable case, corresponding to the first row.
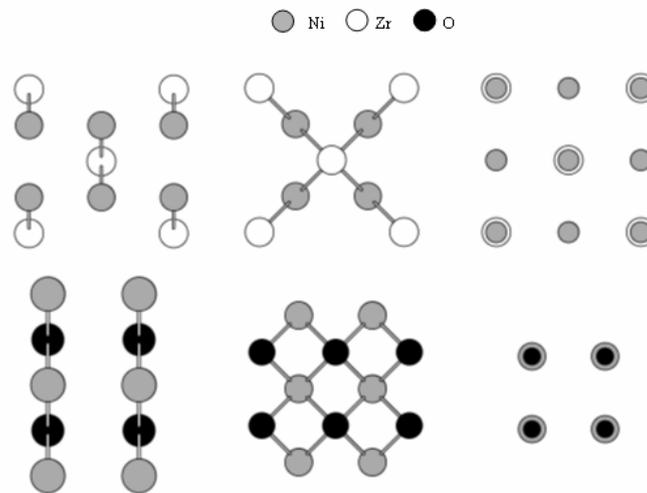
Figure 6.5: Top view of the different high-symmetry relative positions between the metal and oxide 2D lattices modeled for the $ZrO_2(001)/Ni(001)$ interface, either in the case of a Zr-ended oxide slab (top) or an O-ended one (bottom). Only the two atomic planes forming the interface, one from each material, are shown. The depicted bonds correspond to the interface bonds, not visible for the on-top positions at the rightmost panels.

From table 6.2 we finally obtain that the most stable coordinations are four fold (hollow) for Zr/Ni, and two fold (bridge) for the O/Ni interface. In the following we will model symmetric slabs, with both interfaces equal: either Zr/Ni or O/Ni. Their corresponding top and side views are depicted in figure 6.6.

For both calculations, and after letting the systems relax, the only noticeably geometric modification is the Ni 2% in-plane expansion and 3% out-of-plane compression, expected to conserve the metal volume by the Poisson effect. This slight relaxation is due to the good relative matching of the interface cells, so that initial configuration needs only minor alteration. A compilation of the interface atomic charges, interatomic distances, BOP and adhesion values is shown in table 6.3.

	Ni		Zr		O					
Interface	Q	ΔQ	Q	ΔQ	Q	ΔQ	BOP	d	Wsep	BS
Ni/Zr	10,2	0,2	2,9	0,4	6,8	0,0	0,21	2,72	5,01	1,00
Ni/O	9,7	-0,3	2,4	0,0	6,6	-0,2	0,14	1,94	5,74	1,20

Table 6.3: Bonding overlap population (BOP), interface distance (d, in Å), work of separation (Wsep in J/m^2) and bond strength (BS, in eV), which is the average Wsep per interface bond, for the Ni(001)/ZrO$_2$(001) interfaces. The columns on the left show the Mulliken population (Q) and its variation with respect to the Ni and ZrO$_2$ bulk value (ΔQ) for the atoms closer to the interface.
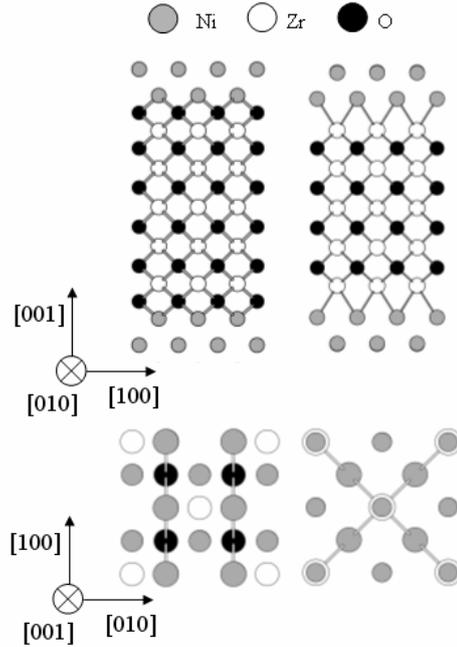
Figure 6.6: Lateral and top views of the ZrO$_2$(001)/Ni(001) supercells used to simulate the (left) Ni/O and (right) Ni/Zr interfaces. The referred crystallographic directions correspond to the ZrO$_2$ lattice. In the top views, at the bottom of the figure, the two atomic planes close to the interface have been included both from the metal and ceramic sides, while only the interface bonds are depicted.

In the following we consider separately both interfaces.

6.3.1.1 Zr/Ni interface

As shown in figure 6.6 and table 6.3, the coordination in the Zr/Ni interface corresponds to an equilibrium Ni-Zr bond length of d_{Ni-Zr}=2.72 Å, which is 0.12 Å smaller than the sum of the respective atomic radii. That is already an indication of the existence of bonding between the two atoms. Figure 6.7 provides the LDOS projected at the interface and central layers, shown by continuous and dashed lines respectively. The LDOS in both central Ni and ZrO$_2$ planes are very close to those corresponding to the bulk crystals, apart from the location of the Fermi level in the oxide, which is shifted towards the conduction band minimum (CBM), due to the finite size of the slab and the long screening length in oxides. In fact, interface effects are almost restricted to the atomic planes in contact, specially in the metal slab, where they are already screened at

the second layer. Metal induced gap states (MIGs) appear in the Zr LDOS with predominant s, d_{XZ} and d_{YZ} character.

On the Ni side there are also important changes in the occupied LDOS for both spin components. The characteristic three-peak fcc structure is lost and the d band is narrowed as a consequence of the reduction of nearest neighbors (NNs) with respect to the bulk phase (10 vs. 12 NNs). Interestingly, there is a reduction by a factor of more than 2 of the interface Ni magnetic moment, $0.25\mu_B$, as opposed to the clean Ni(001) surface case, eventhough the reduction in the number of NNs is similar. This reduction is due to the hybridization with the Zr that, as can be noticed in the COOPs of figure 6.7, extends from the top of the Ni valence band to almost all its width. Examining more carefully, we observe that the changes in the Ni LDOS shape affect most markedly AOs with z component.
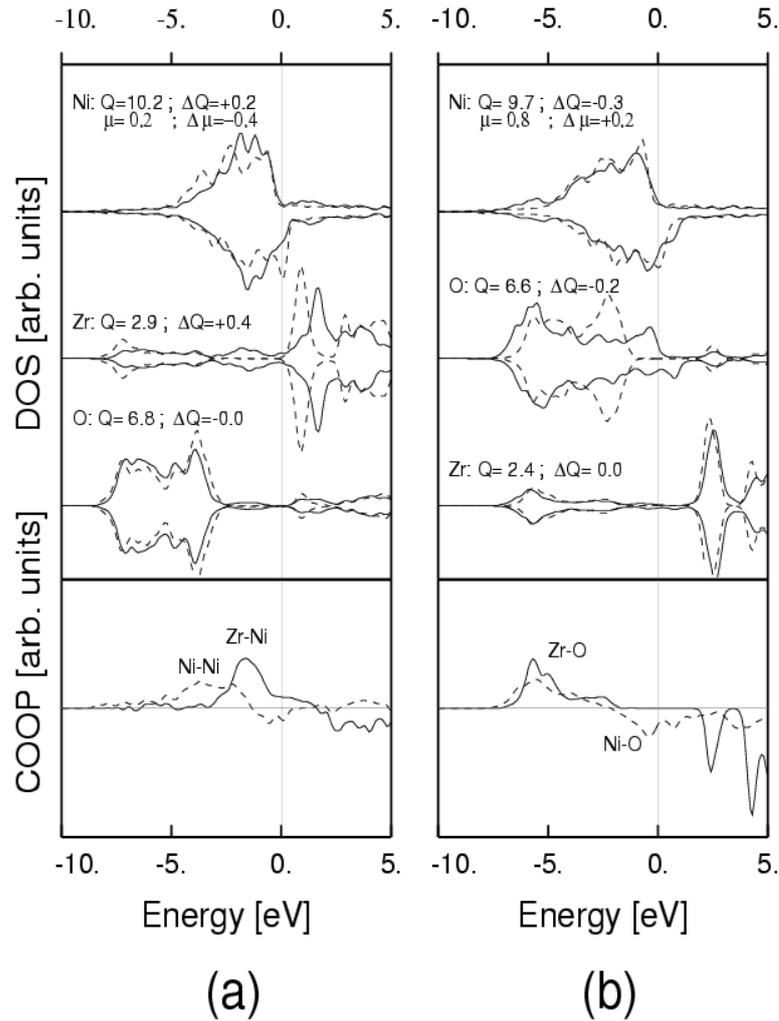
Figure 6.7: Majority (positive) and minority (negative) spin DOS of the interface atoms in the Ni/Zr (left) and Ni/O (right) interfaces. The Mulliken charges (e⁻) and magnetic moments (in μ_B) for each atom are also provided, together with their differences with respect to the bulk-like atoms at the middle of the slabs. For comparison, the DOS of these central atoms are included (dashed lines). Bottom graphs: COOPs between the Zr-Ni interface atoms (solid line) and the Ni-Ni atoms (dashed line) are shown at the bottom left corner, while on the right side are the Ni-O interface atoms (dashed line), and the Zr-O atoms at the center of the slab (solid line).

As mentioned, the Zr-Ni COOPs are also shown in the figure 6.7. They reveal a clear bonding character between Ni and Zr, which arises from s-d and d-d hybridizations. All the electrons in the occupied energy region attain positive COOP values and hence, contribute to the bond. Notice, in particular, the strong peak for the MIGs states located 1-2 eV below the Fermi level. For comparison, COOPs between two Ni adjacent layers located at the center of the slab are included. It is clear from this figure that more charge is shared in the Ni-Zr bond than in the Ni-Ni bond. Moreover, certain ionic character may be assigned to the Ni-Zr bond after inspection of the Mulliken charges quoted in table 6.3 and Figure 6.7. At the interface the Ni atoms, having a larger electronegativity than Zr, gain 0.18 electrons (that is, 0.09 electrons per Zr-Ni bond), whereas Zr gains 0.44 electrons with respect to the central layers, as a consequence of replacing O by Ni atoms.

Finally, we plot in figure 6.8 the charge density (CD) differences (total CD minus a superposition of neutral atom CDs) for a cross section along the $ZrO_2[110]$ horizontal axis of the figure, and [001] vertical axis, directions including Ni, Zr and O atoms nearby the interface. It is evident from the figure the mixed ionic-covalent nature of the bonding. The Ni atoms develop a positive charge pointing to the Zr although fairly delocalized around the interstitial region, while the Zr experiences a loss of charge but in smaller amount than with respect to the back bonds with O (notice the asymmetry of the negative CD isolines around the Zr in the figure). Moreover, both Ni spin components participate in the bond, since the spin density difference (majority spin CD difference minus minority CD difference) has a spherical shape slightly elongated in the in-plane lateral direction (not shown in the figure).
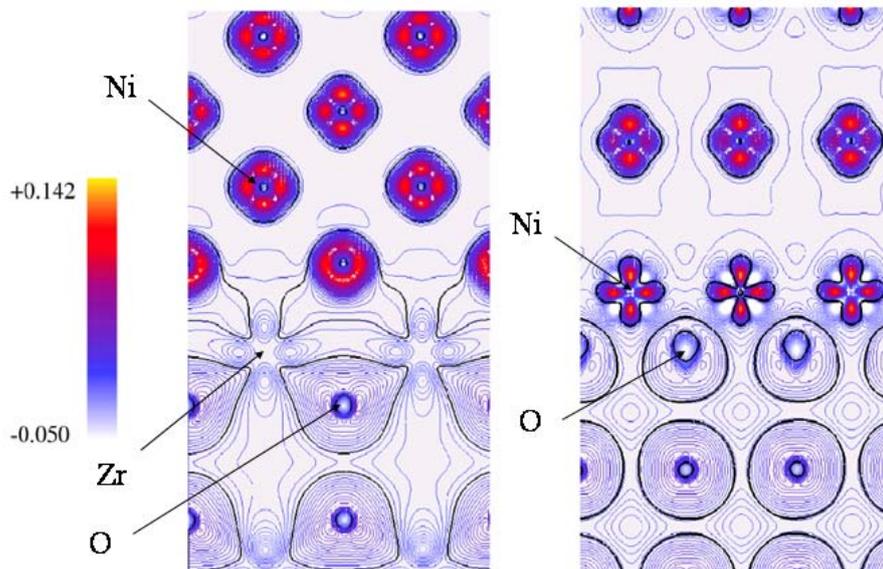
Figure 6.8: Spatial distribution of the charge density difference for (left) the Ni/Zr and (right) the Ni/O interfaces. The top half of each plot represents the Ni slab, the bottom half, ZrO_2. Contour lines correspond to steps of ~2.0 10^{-3} electrons, the black thicker line indicates the zero value.

6.3.1.2 O/Ni interface

In this interface the O occupies bridge positions and then is two fold coordinated to Ni, having an equilibrium Ni-O distance of d_{Ni-O}=1.94 Å, which is in the range of distances obtained at the ZrO$_2$(111)/Ni(111) interface in previous studies [41] although in that case the O was one or threefold coordinated. Mulliken populations evidence that there is a net charge transfer from Ni to O. At the interface, Ni atoms have a charge reduction of 0.28 electrons, mainly from the sp and d$_{YZ}$ orbitals, which are gained by the O atoms. The O has, in turn, 0.16e less than in the central layers, due to the smaller ionicity of the Ni-O bonds in comparison to the Zr-O bonds. In figure 6.7 the LDOS of the Ni and ZrO$_2$ interface planes are presented. As in the Zr/Ni case, induced interface effects show up as strong perturbations in the curves, but they are almost restricted to just one atomic plane in each material. On the Ni layer, the most important effect is the positive energy shift and broadening of the minority band, giving rise to an enhancement of the local magnetic moment by more than 30% (~0.8 µ$_B$). Decomposition of the LDOS shows different shapes for the d$_{YZ}$ components and, to a smaller extent, for the d$_{XZ}$, which stem from the broken p4m 2D interface symmetry. Intrinsic interface states appear in the oxide energy gap, but also important changes within the band continua are seen for the O. The position of the Fermi level at the MIG states corresponds to a metallic interface. All p-like O LDOS are drastically altered and a non negligible spin polarization is induced ~0.2 µ$_B$. However, Zr atoms are almost unaltered by the Ni presence. COOPs corresponding to the Ni/O interface atoms are represented in the lower graph of the figure 6.7. The Zr-O COOP for the bulk-like central layer is also included. Electrons in the energy region occupied by the oxide valence band have positive values, thus contributing to the Ni-O bond, while those at the band gap originated from the MIGS are negative. The compensation of the two regions leads to hardly any net charge sharing for this bond, indicating an almost pure ionic character.

Figure 6.8 shows the CD differences along the ZrO$_2$[010] horizontal axis, and [001] vertical axis, directions containing the Ni and O atoms (but not the Zr ones). The Ni atoms suffer strong modifications with respect to the metallic phase, presenting highly localized regions of charge depletion (dashed lobes in the figure). On the contrary, the O atoms experience minor modifications with respect to the bulk ZrO$_2$ case: there is still a large and quite spherical charge pile up around the core apart from a negative non-spherical contribution inside the spheres. This picture clearly points to an ionic type O-Ni bonding. The CD difference maps are hardly spin-dependent, except for the charge depletion at the O atom, which is dominated by the net spin density.

This electronic structure analysis gives us two well differentiated behaviors for the covalent and ionic Ni/Zr, and mainly ionic Ni/O interfaces. The adhesion properties, characterized by the values of Wsep, are Wsep$_{Zr/Ni}$= 5.01 J/m^2 and Wsep$_{O/Ni}$= 5.74 J/m^2 respectively, see table 6.3. These values, when compared with the highest theoretical values reported in the literature, for example Wsep$_{Al2O3/Nb}$=9.80 J/m^2 for the α-Al$_2$O$_3$(0001)O/Nb(111) interface [37] which is a system known to have a very good adherence, indicate that our system points to a rather strong metal-ceramic bonding. These Wsep are much more stronger than 1.1 J/m^2 value previously reported [218] for microcomposite YSZ/Ni, which can be affected by the porosity at the interface. To be able to directly compare adhesion properties for other ZrO$_2$/Ni orientations, we have to regard the average Wsep per unit bond or bonding strength (BS) values. We obtain for

the Ni/Zr and Ni/O interfaces 1.0 and 1.2 eV respectively, which are around five times larger than those obtained by Christensen *et al.* for $ZrO_2(111)/Ni(111)$ [41].

The reasons why this first interface may present such a strong bond is that it shows the smallest unit cell in the NSCL model [28]. In addition it has been obtained experimentally following two different methods of sintering [30, 31], which indicates that this interface is very favorable to appear.

6.3.2   c-ZrO_2(110)/Ni(001) ;   c-ZrO_2[001]/Ni[010]

For this interface the ceramic slab orientation is non-polar, with one ZrO_2 formula unit at the interface layer which, as will be seen, induces important differences compared with the polar termination previously studied. As only one type of atomic termination is present in the oxide, we just have to characterize the relative coordination at the interface. However due to the fact that the oxide unit cell shows a rectangular shape, instead the squared shape for Ni, the area is two times that of c-ZrO_2 and not only one kind of coordination is obtained at the interface. As we can see in the top and side view of the interface cell, figure 6.9, there are two types of NNs Zr-Ni bonds: Zr_1 is one-fold (on-top site) with Ni_1, while Zr_2 is fourfold (hollow); in addition, there are two types of NNs O-Ni bonds: one-fold (on-top) and twofold (bridge). By letting the system relax we can observe, see right side of figure 6.9, that this complex in-plane unit cell drives the system to maintain more than one type of ceramic/metal coordination. The most noticeably atomic movement is the out-of-plane buckling of the O atoms, which approximate to the Ni interface layer more than the Zr atoms do. This can be considered as a tendency to break the non-polar plane into O terminated polar planes. Such a relaxation gives a wide variety of coordinations and a large dispersion of bonding distances, that goes from 2.05 Å for Ni_4-O_1 to 2.97 Å for Ni_2-Zr_2, with average values: $<d_{Ni-O}>=$ 2.24 Å, and $<d_{Ni-Zr}>=$ 2.80 Å, that compares to 1.95 and 2.72 Å with the previously studied Ni/O and Ni/Zr polar interfaces, respectively, which is already an indication of a lower interface strength. Table 6.4 shows Mulliken charges, distances, and BOP values for the closest bonds of each Zr-Ni and O-Ni, corresponding to Zr_1-Ni_1 and O_1-Ni_4 respectively, together with Wsep and BS values for the interface. Despite the short bond distance between Ni_1 and Zr_1, the BOP is around half that in the polar Ni/Zr interface due to the reduced coordination of Ni-Zr bonds, from fourfold in Ni/Zr to one-fold here.

	Ni		Zr		O					
Interface	Q	ΔQ	Q	ΔQ	Q	ΔQ	BOP	d	Wsep	BS
Ni1-Zr1	10,1	0,1	2,7	0,2			0,09	2,57	0,93	0,30
Ni4-O1	9,8	-0,2			6,7	-0,1	0,13	2,05	0,93	0,30

Table 6.4: Same as table 6.3 but for the $ZrO_2(110)/Ni(001)$ interface. The values of Q, ΔQ, interface distance and BOP correspond to the interface atoms of figure 6.9 with the shortest Ni-Zr and Ni-O bond lengths, while Wsep and BS are global interface properties.
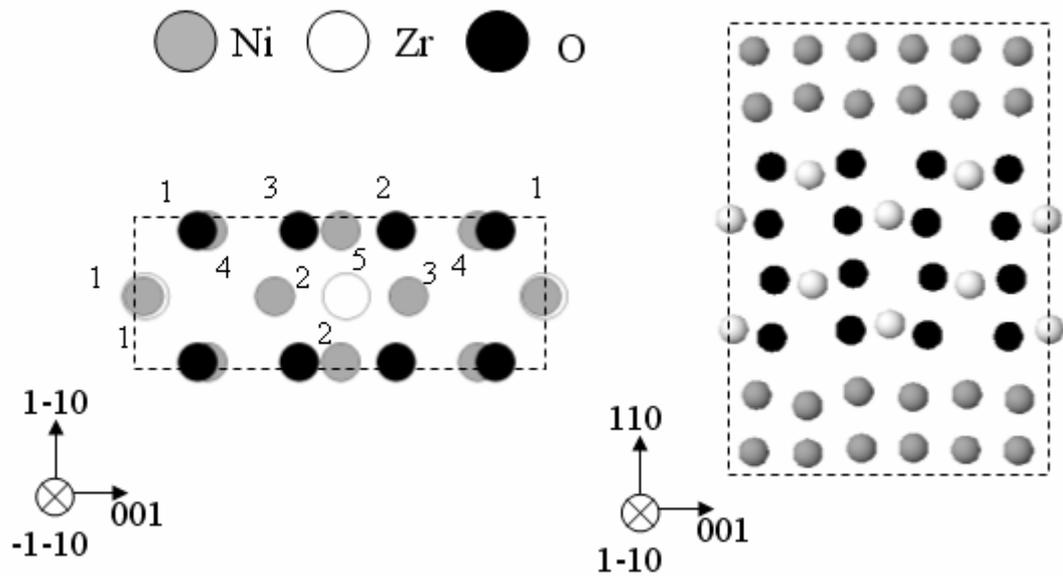
Figure 6.9: Side and top views of the supercell used to model the $ZrO_2(110)/Ni(001)$ interface. The crystallographic directions refer to the ZrO_2 lattice. The top view includes only the two closer atomic planes to the interface, and the inequivalent atomic positions are labeled with numbers, each number row corresponds to a different element: top, O; middle, Ni; bottom, Zr.

The DOS and COOPs of the interface atoms are shown in figure 6.10, while their integrated values, Q and BOP respectively, are included in table 6.4. Since they correspond to the Ni-Zr and Ni-O pairs with shortest interatomic distances, they show important changes with respect to bulk Ni, bulk ZrO_2 and the polar interfaces of section 6.3.1. Specifically, the Ni_1-Zr_1 bond length is shorter than the one obtained at the Zr/Ni interface, 2.57 vs 2.72 Å respectively. This is reflected in the DOS, which presents features that reveal the presence of tightly bound neighbors: MIGs appear in the oxide gap and the Ni DOS loses the three peak structure characteristic of the bulk. The DOS of the atoms Ni_4 and O_1 are also altered with respect to O/Ni interface, although in this case the changes reflect the weakening of the Ni-O bond. A smaller contribution of MIGs can be found in the O DOS, which is not changed significantly. However, the DOS of Ni_4 is drastically narrowed, even more than that of Ni_1. Concerning the COOPs, the hybridizations between Ni-Zr and Ni-O are important. Essentially all the electrons in the VB contribute to the Ni_1-Zr_1 bond, while in Ni_4-O_1 the antibonding MIGs partially compensate the large positive contribution of the rest of VB electrons. Nevertheless the atomic pairs shown in the figure correspond to the most tightly bound atoms at the interface unit cell, the DOS and COOPs of the rest of atoms reflecting a weaker interaction and reduced hybridization between Ni-Zr and Ni-O bonds.
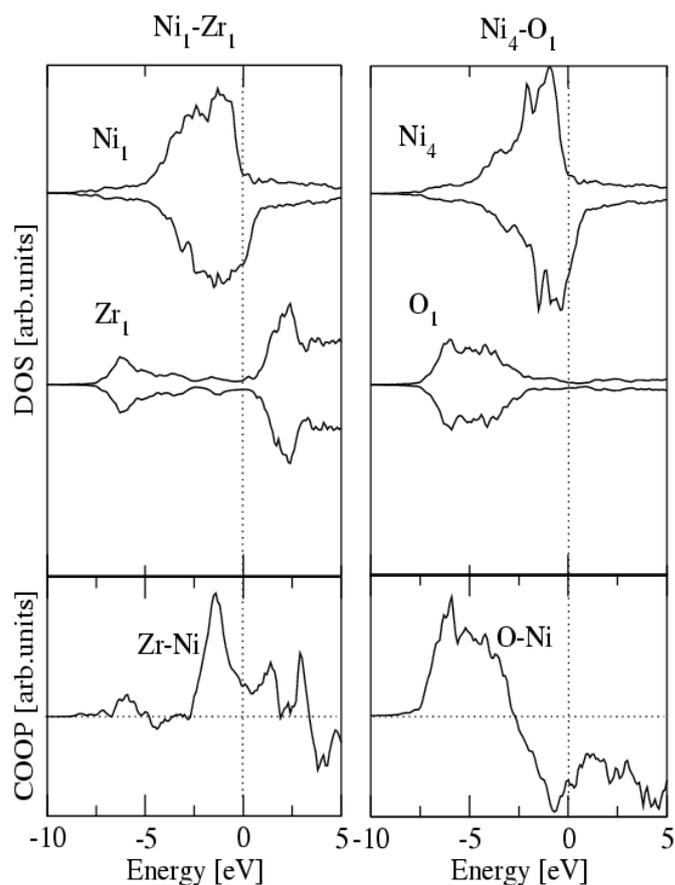
Figure 6.10: DOS and COOPs corresponding to the more strongly bonded Ni-Zr and Ni-O pairs of the $ZrO_2(110)/Ni(001)$ interface, labeled according to figure 6.9.
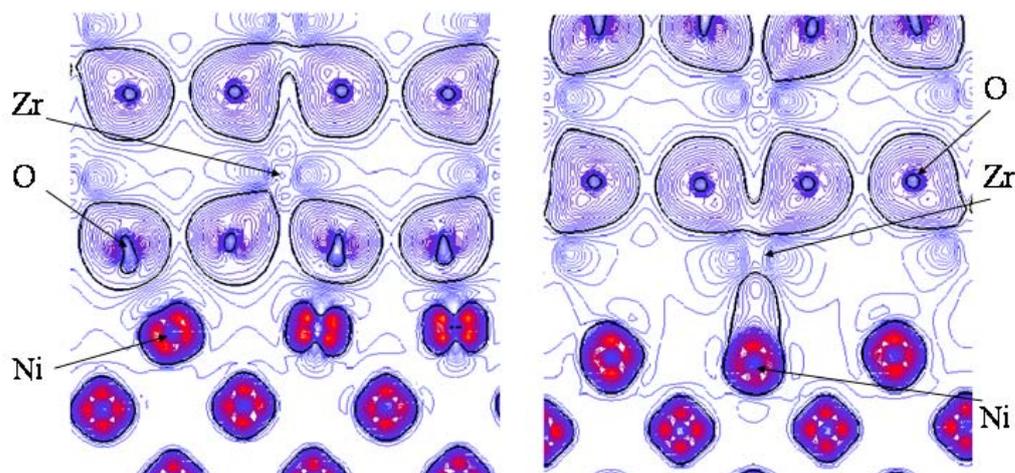
Figure 6.11: Charge density difference (CDD) plots of the $ZrO_2(110)/Ni(001)$ interface for two cross sections containing the Ni-Zr (right) and Ni-O (left) bonds. The same scale of figure 6.8 has been used.

In figure 6.11, the CDDs are represented for a cross-section along the [001] horizontal axis, and [1$\bar{1}$0] vertical axis, ZrO_2 directions containing Ni-Zr (right) and Ni-O (left) interface bonds, ZrO_2 being represented at the top side while Ni occupies the bottom half of the figure. On the right hand side interface we can distinguish the two types of Zr bonding to Ni atoms. The Ni that is one fold coordinated to Zr, on-top

position, shows a long tail of electronic density, which is related to the existence of hybridization. We also notice a Zr_1-Ni_1 charge redistribution in p_z orbital characterized by the increase and decrease of the Ni and Zr respectively. Nevertheless the Zr_2 is more similar than Zr_1 to the orbital charge distribution of Zr in the Zr/Ni interface, with an increase of charge mainly for p_z and s orbitals. At the top side of both figures, we can see the bulk-like properties of the middle ZrO_2 planes, as the spherical CDD of O and the lobular shape of Zr, which reproduce the results for thicker slabs within 5%. At the left side of the figure 6.11, we can identify the three types of Ni and four types of O atoms, which can be grouped in two types of CDD distribution features. The first group is constituted by two O_1-Ni_4 bonds nearly on-top while the second is constituted by O_2-Ni_5 and O_3-Ni_5, with bridge coordination. The latter group of atoms exhibits an orbital charge distribution closer to that of O/Ni interface, with a p_z decrease for O atoms and an increase for Ni. The weakening of the Ni-O bonds is evident in comparison to figure 6.8, as shown by the change of the orbital symmetries at the interface specially along z direction, reflecting the smaller average charge transfer from Ni to O (0.076 electrons per Ni atom). As a general remark, for all Ni interface atoms there is an important charge decrease for d_{z2} orbital and a not so important one for s orbitals, with a CDD distortion from the spherical shape shown in the bulk.

Concerning the adhesion properties given by the Wsep value we obtain 0.93 J/m^2 to be compared to the polar cases with 5.01 for Zr/Ni and 5.74 J/m^2 for O/Ni. This large adhesion difference between interfaces, a factor of six, can be understood from different points of view. A general trend is that interface bonds are longer for the non-polar interface, except for the Zr_1-Ni_1 bond, which implies an overall weakening of the ZrO_2-Ni interaction, compare tables 6.4 and 6.3. Besides it, the non-polar interface presents a large variety of coordinations: on-top, bridge and hollow. This non-polar plane termination implies a coexistence of the two terminating atoms, Zr and O, with inherent differences in electronegativity and bond radius, which tend to reduce the global ionic interaction with Ni. This reduced ionicity with respect to the polar interface, together with the increased bonding distance and the loss of hybridization shown in the LDOS/COOP graphs lead to weakened interface interaction and thus to a lower adhesion.

We can conclude that the adhesion between ideal ZrO_2 and Ni is improved for those relative orientations leading to only one type of bonding, which corresponds to small interface cell of low mismatch materials. The non-polar termination of ZrO_2 does not optimize the adhesion as indicated by the low value of Wsep. On the contrary, good bonding is found for the $ZrO_2(001)/Ni(001)$ interface, the O termination of ZrO_2 showing better adhesion that the Zr termination. For this interface, we have found that the preferential coordination sites for Ni corresponds to bridge and hollow positions for the Ni/O and Ni/Zr cases, respectively.

6.4 ZrO_2/Ni stability and work of adhesion

In addition to the cases already studied we have performed other ZrO_2/Ni interfaces calculations with different orientations, in order to analyze the interface stability and to compare our results with previous theoretical studies.
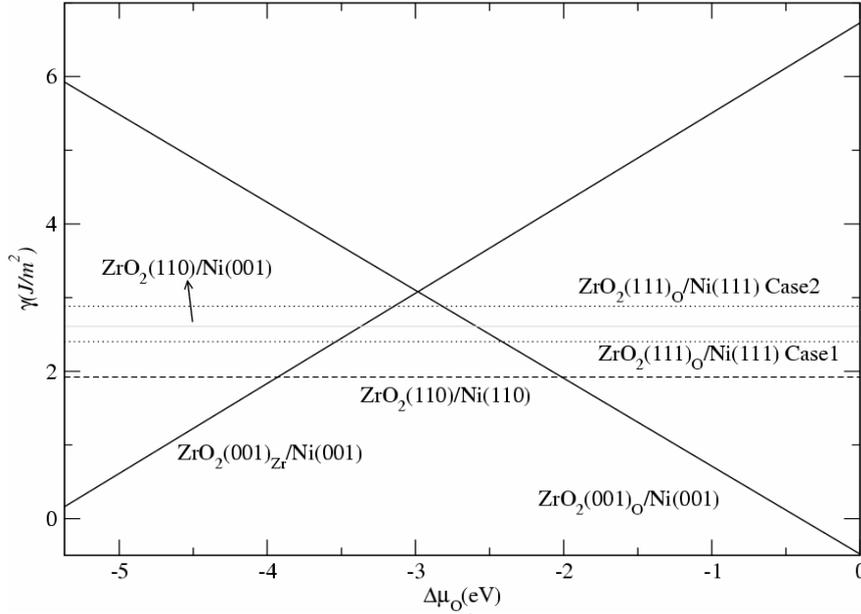
Figure 6.12: Interface energy (γ in J/m^2) of all the ZrO$_2$/Ni interfaces studied vs $\Delta\mu_O$, or $\mu_O - \frac{1}{2}(\mu^{gas}_{O2})$, where μ_O is the O chemical potential and $\frac{1}{2}(\mu^{gas}_{O2})$ is the maximum value of it, see section 2.7.1. $\Delta\mu_O$ ranges from ($\frac{1}{2}$ ΔG^f_{ZrO2}, 0) the O poor region and rich one respectively.

We have performed two calculations of ZrO$_2$(111)/Ni(111), depending on the in-plane orientations, Case1 with ZrO$_2$[$\overline{13}$ 4]/Ni[0$\overline{4}$4] and Case2 with ZrO$_2$[1$\overline{1}$ 0]/Ni[1$\overline{1}$0]. Former geometry has been previously studied theoretically [41], while the latter has been found by experimental techniques [219]. None of these cases show larger Wsep than those of ZrO$_2$(001)/Ni(001) interfaces, the value of Wsep for Case1 being 1.28 J/m^2, that compares well with that of the previous study Wsep=1.00 J/m^2, while for Case2 we obtain Wsep=1.20 J/m^2. Besides this we have also calculated the interface ZrO$_2$(110)/Ni(110), with the in-plane parallel alignment ZrO$_2$[001]/Ni[$\overline{1}$10] and Ni-O on-top and Ni-Zr hollow coordinations in order to minimize the interface distance. This interface has a small cell and a non-polar termination plane, and the value of Wsep for this interface is Wsep=1.12 J/m^2. Regarding the stability curve, figure 6.12, we identify the ZrO$_2$(110)/Ni(110) interface as the most stable in the range of intermediate μ_O values, although for high μ_O the ZrO$_2$(001)$_O$/Ni(001) interface is more stable, and for low values it is the ZrO$_2$(001)$_{Zr}$/Ni(001) interface. As already shown in the study of the surfaces in the last section of chapter 4, the μ_O dependence of γ leads to constant lines for stoichiometric ZrO$_2$ terminations, while a negative or positive slope develops for O over or under stoichiometry respectively. Considering average values, the interface can be ordered by decreasing stability as ZrO$_2$(001)$_{Zr}$/Ni(001), Case2, ZrO$_2$(001)$_O$/Ni(001), ZrO$_2$(110)/Ni(001) Case1 and the lowest interface energy corresponding to ZrO$_2$(110)/Ni(110). It can be seen that the interface stability order is related with the stoichiometry and polarity, the non-stoichiometric ceramic slabs being the less stable, while the most stable one is the stoichiometric and non polar one.

6.5 ZrO$_2$(001)$_{Zr}$/Ni interfaces with defects

To calculate more realistic interface we have to include the actual presence of doping oxides in the ceramic. To set the initial atomic configuration we base on surface

experimental measurements [179] of 9.5% Y_2O_3 molar stabilized ZrO_2(001), terminated in a O layer, where an important density of O vacancies is found at the outer plane. This doping, as explained in chapter 3, makes the c-ZrO_2 structure to be stable at room temperature by creation of O vacancies in order to compensate the charge of the aliovalent Y^{3+} cation that substitutes Zr^{4+}. The Y_2O_3 molar quantity that stabilizes c-ZrO_2 ranges from 8% to 40 % [151], over this quantity $Y_4Zr_3O_{12}$ compound crystallizes. Within these values of Y_2O_3 concentration, it enters as solid solution into the ZrO_2 structure, which means substituting Zr^{4+} cation by Y^{3+} in the corresponding amount.

6.5.1 YSZ

We have performed an initial calculation of c-ZrO_2(001)/Ni(001) with a 20% molar concentration of Y_2O_3, that corresponds to a cell of 29 atoms with two Y atoms included into solid solution, one O vacancy and eleven O atoms in the structure (YSZ). The vacancy is considered to be at the interface [179]. Besides this, other experimental and theoretical studies have concluded that the O vacancies are located NNN to Y rather than NN, as said section 3.2.4. These results are also incorporated by us not placing the Y atoms in the cation plane underneath of the O vacancy.

We have increased the interface cell from our previous calculation of the ideal interface to a p(2x2) and a c(2x2) for the Ni and ZrO_2 slabs respectively, in order not to have a very large concentration of vacancies in the same plane when applying PBC. Therefore, by considering bridge coordination for O/Ni and hollow for Zr/Ni, we finally obtain the slab geometry depicted in figures 6.13 and 6.14, corresponding respectively to the side and top views.
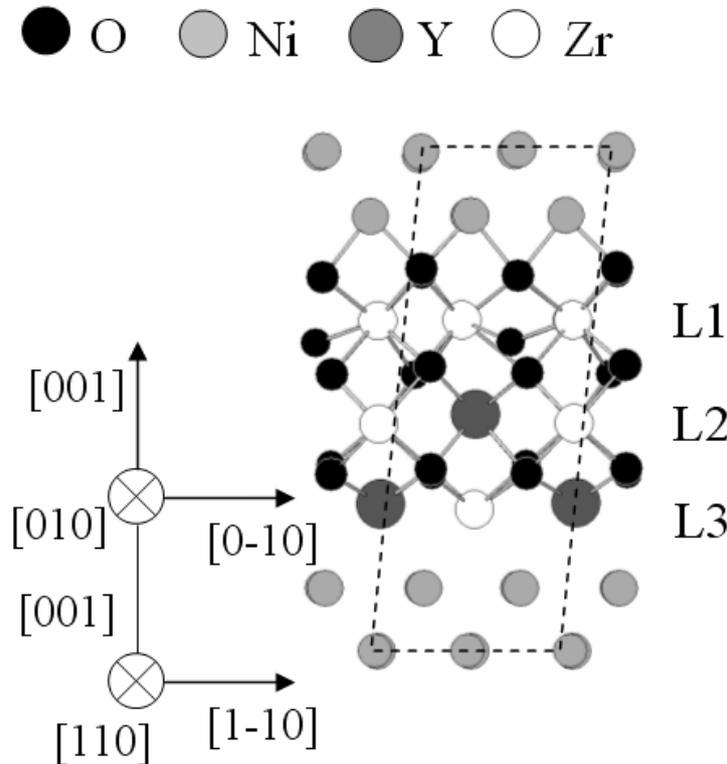
Figure 6.13: Side view of the YSZ slabs under study. The cationic planes are numbered as L1-3. The dashed lines indicate the supercell employed. The horizontal axis on the right refers to the ZrO_2 (upper) and Ni (bottom) lattices.
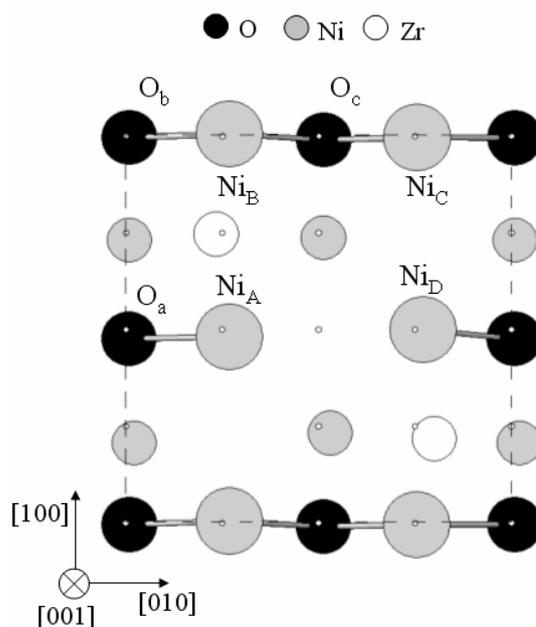
Figure 6.14: Top view of the relaxed c-ZrO$_2$(001)/Ni(001) interface plane when Y and O defects are introduced. The four atomic planes closer to the interface are depicted, one pair from each material, the size of the atoms being proportional to their distance to the interface. The small dots indicate the starting ideal atomic positions in the non-relaxed lattice.

From the top view of figure 6.14 we can see that all O atoms are 2-fold coordinated to Ni, which adopts two types of sites at the interface: first, that of Ni$_A$ and Ni$_D$, NN to the vacancy and 1-fold coordinated to O; and second, the 2-fold O-coordinated Ni$_B$ and Ni$_C$ sites.

For this interface, we obtain Wsep=4.15 J/m^2 which is reduced from the ideal value, Wsep=5.74 J/m^2, see table 6.3. This corresponds to a decrease of the adhesion of more than 25 %, which can be due to the reduction of bonds caused by the O vacancy or to a lower interaction among interface atoms. To differentiate between both causes, we calculate the bonding strength (BS) value, giving the value 1.19, which is the same value that we obtained for the Ni/O interface. This implies that the reduction of adhesion when doping with Y$_2$O$_3$, and placing the O vacancies at the interface is proportional to the number of bonds lost. A further insight on this result can be gained comparing the bond distances and BOPs for Ni-O and Zr-O at the YSZ interface and the ideal O/Ni case.

For YSZ, the Ni-O distances at the interface layers have an average value of 1.99 Å, which corresponds to a relatively high 0.14 BOP, reflecting that BOPs are inversely proportional to distance. The BOP value of the ideal interface, with a shorter Ni-O distance of 1.94 Å, is 0.14 and therefore the same than the average of YSZ. Then we obtain slightly different Ni-O average distances, but with the same hybridization value between the YSZ and the ideal case. When analyzing the Zr-O interactions at the interface, we have almost the same slight differences, distances are 2.20 for YSZ and 2.23 Å for the ideal Ni/O, while the BOPs values are 0.13 and 0.12 for the YSZ and ideal interfaces, respectively. Furthermore, when comparing the Mulliken charges to analyze the ionic contribution, also small differences are found. The average O charge at the interface plane is 6.66 and 6.63 for the YSZ and ideal case, while for Ni it is 9.77 and 9.73 respectively.

Then in summary, we can conclude that doping with Y_2O_3, does not alter significantly the electronic structure and neither the adhesion, thus not justifying the embrittlement shown in the microcomposite SEM graphs of figure 6.3.

6.5.2 Thermodynamic vacancies

Besides the charged vacancies related with Y_2O_3 there also exist thermodynamic, or neutral, vacancies when ZrO_2 is sintered at reducing atmosphere [137]. These vacancies are non related to charge compensation but only to a depletion of O atoms from the ZrO_2 lattice.

Apart from the pure O thermodynamic vacancies, we consider to study intermediate geometries including both neutral and charged ones, where all O vacancies are not due to the Y_2O_3 doping. To properly study the electronic and adhesion effects related to the incorporation of O vacancies and Y atoms we calculate several situations, see figure 6.15. In figure 6.15 the left panel corresponds to a case similar to that already studied for the ideal $ZrO_2(001)/Ni(001)$ interface, with a symmetric O termination, although with a reduction of thickness for direct comparison to the rest of calculations, which we called V_0^{sym}. In order to obtain another O/Ni interface calculation with less degrees of freedom we eliminate the symmetry of latter case by removing one of the O interface planes, setting therefore the asymmetric case V_0 shown in the middle panel of figure 6.15. The next step calculation is performed from an initial atomic configuration like previous one but removing one O interface atom, that is, generating a thermodynamic vacancy, referred as Y_0. We also calculate two intermediate situations, not shown in figure 6.15, between Y_0 and the YSZ previously analyzed, by locating one Y atom in the L2 and L3 layers respectively for each calculation, structures labeled by Y_1^{L2} and Y_1^{L3} respectively.

For non defected ZrO_2 cases, V_0^{sym} and V_0, a perfect matching is assumed between the c(2x2) and p(1x1) cells of the Ni and ZrO_2 slabs respectively, similarly to the Ni/O ideal interface, while for the rest of structures we double the cell size, employing a p(2x2) and a c(2x2) cell for the Ni and ZrO_2 slabs respectively, similarly to the YSZ case shown in figure 6.14. For the ideal structures, V_0^{sym} and V_0, only one Ni site can be distinguished, bonded to two O atoms similarly to $Ni_{B,C}$.
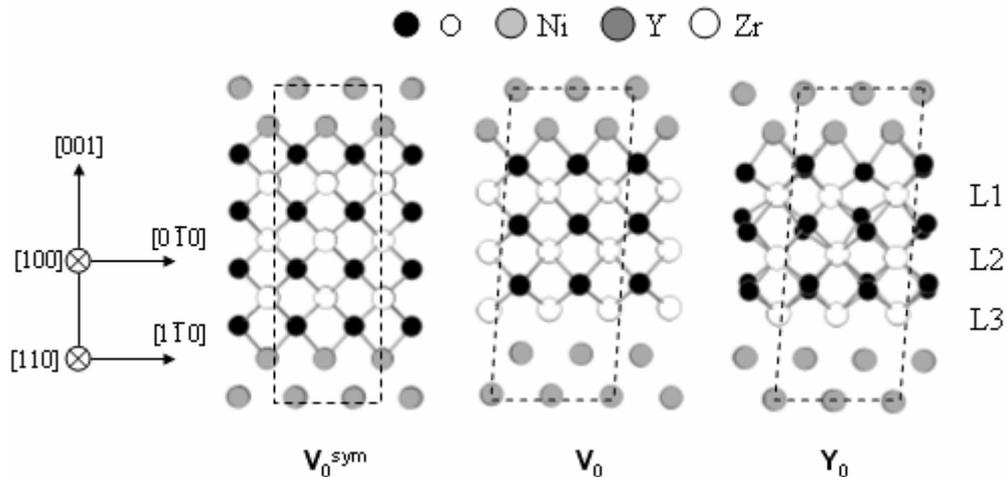
Figure 6.15: Same as 6.13 but for the V_0^{sym}, V_0 and Y_0 slabs.

In table 6.5 we give the Wsep and average BS of the structures considered. Though Wsep is a lower bound to the experimental work of adhesion [9] it provides a direct

measure of the interface BS, obtained taking into account all NN's interactions. The most significant effect shown in the table 6.5 is the dramatic decrease of the interface adhesion for Y_0. This evidences that increasing the degrees of freedom of the ceramic structure has a direct impact on the interface adhesion. As we move from V_0^{sym} to Y_0, there is a clear weakening of the metal-ceramic bonding. Notably, enhancing the presence of Y near the interface gradually restores the BS to the ideal 1.19 value that is obtained for the YSZ calculation.

	Wsep	BS
V_0^{sym}	5,63	1,19
V_0	4,93	1,04
Y_0	1,22	0,34
Y_1^{L3}	3,25	0,91
Y_1^{L2}	3,74	1,06
YSZ	4,15	1,19

Table 6.5: Works of separation (J/m^2) and bond strengths (BS) for the Ni/O interfaces of all the slabs.

As we will demonstrate here, these results are intimately related to the internal reconstruction of the ceramic lattice. When bulk bonds are broken to form the interface, the oxide compensates the unbalanced charge either by binding to the adjacent Ni atoms or by an internal restructuring. For the cases V_0^{sym}, V_0 and YSZ, the inner bulk charges are in equilibrium, and the interface O atoms need the additional Ni cations to stabilize their valence state. On the contrary, when thermodynamic O vacancies exist, the unstable c-ZrO_2 structure has room to restructure towards the stable m-ZrO_2 phase, and this is preferred over the binding to Ni. In support of this, the intermediate situations represented by Y_1^{L2} and Y_1^{L3} are respectively more similar to the cases YSZ and Y0, indicating that the proximity of the Y atom to the defected interface is relevant for the bonding. The validity of the above reasoning is evidenced by the structural and bond properties of the systems considered. The first hint comes from the equilibrium interface structures of figures 6.13, 6.15. They show that here the metal atoms do not segregate into the ceramic slab, contrary to other metal-ceramic interfaces with vacancies. This has an effect in the bonding, as [220] reports a strong enhancement of the metal adhesion induced by the interface defects. The detailed analysis of the O-Ni distances at the interface confirms this idea. They are given, together with their corresponding average values, at the bottom left panel of figure 6.16 for all structures under study. The variation of the mean bond distances between the different structures can be anticorrelated to that of the BOP (see figure 6.16): the shorter the distance, the larger the BOP. There is a significant dispersion of the individual interatomic values when O vacancies are included. This seems to confirm that, even if the global interface adhesion is reduced, some of the O-Ni bonds are weakened at the cost of reinforcing the others, in agreement with the results of [41]. The top left panel of figure 6.16 shows the O-Zr distances for the interface O atoms. Taking V_0^{sym} as reference, in all cases an enlarged O-Ni distance corresponds to a shortened O-Zr distance, implying that the O-Ni BOP results from the interplay between the forward and back bonds of O. These alternations between short and long O bonds can be also traced as we penetrate into the ZrO_2 slab for the cases V_0 and Y_0. This indicates that ZrO_2 profits from the additional structural

degrees of freedom in order to approach to the low temperature phases, where long and short O-Zr bonds coexist[1].

The most significant variations of the bond lengths correspond to Y_0, where Wsep drops dramatically. The situation is different in the presence of charged vacancies. The Y atoms, being larger than those of Zr, limit the magnitude of the atomic displacements, preventing a transition to more stable phases characterized by the wide range of O-Zr bond distances.
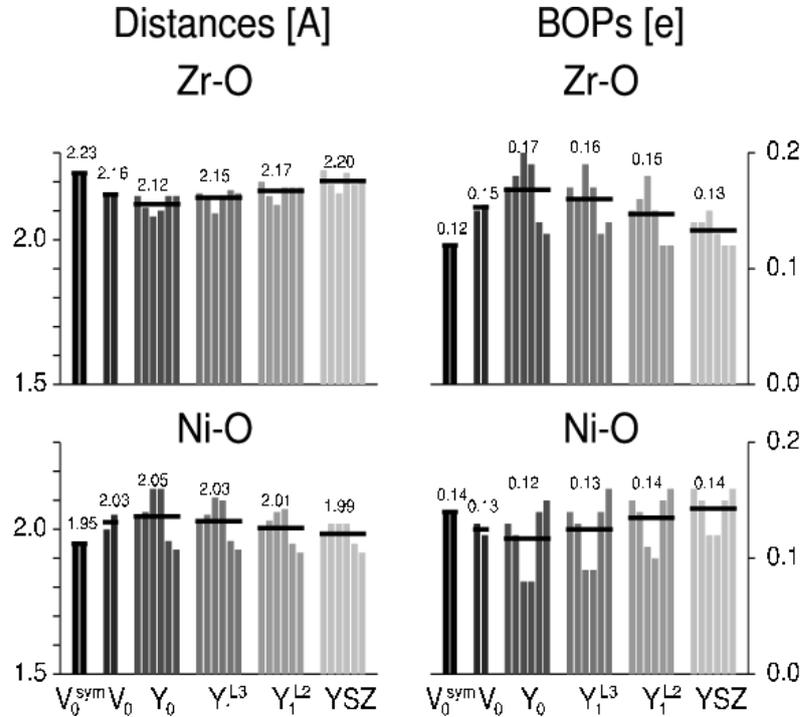
Figure 6.16: Bar diagrams showing the interatomic distances (in Å) and bonding overlap populations (BOPs) between the interface O atoms and the adjacent (bottom) Ni and (top) Zr cations, for all slabs under study. Numbers and horizontal lines indicate the average value for each bar diagram.

The right panels of Figure 6.16 show the bonding overlap populations (BOPs) of the interface O atoms with their Ni (bottom) and Zr (top) neighbors. They provide an estimate of the amount of hybridization of the bonding orbitals. In addition, the Mulliken populations of the corresponding atoms are given in table 6.6. In general, for both the BOPs and charges there is a significant dispersion of the individual values at the defected interfaces, as previously observed for the interatomic distances. But clearly, there is an uniform reduction of the mean O-Ni BOP as we move to Y_0 either from V_0^{sym} or from YSZ. This suggests a less covalent character of the O-Ni bonds in the presence of thermodynamic O vacancies. On the other hand, the Mulliken populations show a lower electron transfer from Ni to O as we approach to the situation of Y_0, indicating a reduced ionicity of the interface O-Ni bonds. The reduction of both the ionic and covalent character of the interface bonds implies their global weakening, as already evidenced by the interatomic distances. The same analysis of the BOPs and charges for the O-Zr pairs reveals higher hybridization and lower ionicity as we move to

---

[1] the 7-fold coordination unit of m-ZrO_2 contains three ranges of interatomic distances: below 2.10 Å, around 2.17 Å and over 2.25 Å. Also t-ZrO_2 is characterized by two kind of Zr-O distances, about 2.40 and 2.05 Å.

Y_0. This enhancement of the covalent character for the O-Zr bonds resembles the situation of the m-ZrO_2 structure, the stable phase at room temperature.

Therefore, there is a transition towards a monoclinic-like structure induced by the thermodynamic O vacancies.

In figure 6.17 we depict the different kinds of Zr-O bonding units encountered in the relaxed slab. The ZrO_2 side displacements are not only restricted to the planes closer to the vacancy site, but extend even 4 planes below as can be seen in figure 6.17. The largest displacements correspond to the O atom immediately below the vacancy along the normal to the interface (O_V), which shifts from its ideal position by more than 0.35 Å in all directions (0.39 Å towards the vacancy site along the normal to the interface). Among the Zr atoms, those closest to the vacancy show the largest displacements and both exhibit a 7-fold coordination. The corresponding Zr-O bond distances range from 2.07 to 2.45 Å. Also one of the atoms of the underlying Zr plane exhibits this behavior, induced by the large shift of O_V. The rest of Zr atoms maintain the 8-fold coordination, although the dispersion of Zr-O distances resembles the situation of the monoclinic phase, with values ranging from 2.05 to ~ 2.40 Å. This effect is less pronounced on the Ni side, where the largest shifts from the ideal positions correspond to the interface layer, and there is no net tendency of distortion around the vacancy site.
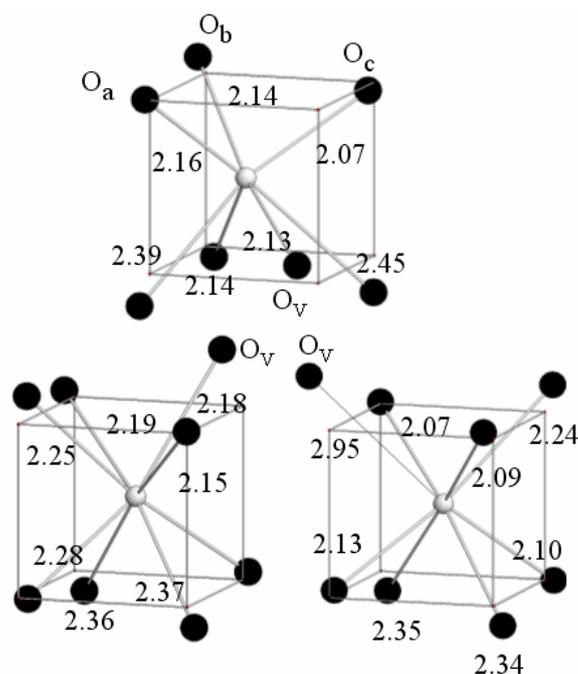
Figure 6.17: Zr-O bonding units for the Zr layer closest to the interface (upper) and for the two kinds of Zr atoms at the layer below. Numbers indicate the corresponding bond lengths in Å.

To summarize, realistic calculations of the ZrO_2/Ni interfaces modeling the actual presence of O vacancies at the interface plane, both related to YSZ and thermodynamic, have been performed and two different behaviors have been obtained. Despite the general fact that both kinds of O vacancies decrease the number of interface bonds, the thermodynamic ones induce in the ceramic material an internal restructuring of the ceramic slab to approach to the lowest temperature phase, the monoclinic. This

relaxation resembles a phase transformation which increases the Zr-O hybridization interaction at the cost of weakening the interface bonds. On the other hand, when O vacancies are related with Y_2O_3 doping, charged vacancies, the presence of the large Y cations clips the ceramic structure preventing its internal reconstruction. This implies that the Zr-O interaction cannot be strengthened and the interface BS is not actually reduced.

		V_0^{sym}	V_0	Y_0	Y_1^{L3}	Y_1^{L2}	YSZ
Q(Zr)		2,42	2,48	2,59	2,60	2,57	2,56
				2,59	2,55	2,54	2,53
(O)	Mean	6,63	6,62	6,63	6,65	6,65	6,66
Q(Ni)	A	9,73	9,74	9,85	9,85	9,84	9,83
	B			9,76	9,76	9,75	9,74
	C			9,75	9,75	9,74	9,73
	D			9,85	9,85	9,84	9,84

Table 6.6: Mulliken charges of the Ni, O and Zr atoms closer to the Ni/O interface for the slabs under study. The Ni sites for the interfaces with vacancies have been labeled following figure 6.15.

Our results indicate that the metal-ceramic adhesion in ZrO_2 is not only an interface property, but it is governed by an internal tendency of the ceramic to locally set the most stable bulk phase. In other words, intraceramic interactions prevail over metal-ceramic interactions, reducing the metal adhesion. Similar effects occur in the transformation toughening where, inside a t-ZrO_2 matrix, a crack propagates facilitating the transformation to the monoclinic phase, which by volume expansion increases the resistance of the ceramic to crack propagation.

Chapter 7

Interface adhesion of ceramic oxides/metal systems

7.1 Introduction

The final part of this work is devoted to a systematic investigation of the adhesion properties of various ceramic/metal interfaces, in order to establish trends in the strength of the interfacial bonding. Specifically, we will try to correlate the work of separation (Wsep) with some inherent properties of the materials forming the interface. Few systematic *ab-initio* studies have been performed in this sense. Most investigations have focused on one or two particular interface systems, like Cu, Pd and Pt on ZrO_2, considering the metals mainly in the form of isolated atoms or single monolayers [19]. To our knowledge, the only two systematic investigations are on the adsorption of metal overlayers on aluminum oxide [221] and the broad study of Siegel on different Al/ceramic systems including Al_2O_3, carbides and nitrides [222].

All the interfaces we have investigated are non-reactive, that is, there are not interface reactions so that intermetallic phases are not formed. Also, toughening mechanisms are not taken into account. Thus, the calculated adhesion properties correspond to the elastic regime. Moreover, the calculations model ideal interfaces without defects as, for example, vacancies or interstitials. The misfit between the metal and the ceramic has always been initially accommodated in the metal slab, although relaxations, both in-plane and perpendicular to the interface, are allowed in the two components: the metal and the ceramic. Therefore, in the initial state the metal is compressed or stretched to match the surface lattice constant of the ceramic.

We have performed two different kinds of calculations: the first corresponds to a superlattice geometry including two slabs formed respectively by the metal and the ceramic, and the second models free overlayers of metals on top of the ceramic surface. In the former there are two identical interfaces in the supercell, so that it describes interfaces between bulk systems as those present in cermets, solid metal interfaces, composites, etc. The selected materials have always a mismatch smaller than 10%, more than this quantity in this model may lead to unphysical results. It is expected that in this mismatch range of ceramic and metal lattice parameters the actual structures of the interfaces will present large coherent regions separated by misfit dislocations or small incommensurate disorder regions. In the second type of calculations, metal overlayers, there are just one metal/ceramic interface and a free metal surface. It thus models epitaxial metal films growth on ceramics and in this case mismatches up to 23% have been considered.

7.2 Interface strength

We have performed a systematic study of the dependence of the adhesion properties on the choice of the metal at extended 2D interfaces. The selection of metals for each particular ceramic interface has been based on the value of the 2D lattice misfit. We have only considered low index surfaces with small commensurable unit cells, and tried to analyze the influence of two effects: the lattice orientations, which imply changes of both structure and oxide polarity, and the metal electronic configuration. To this end,

we have studied Na and transition metals with low and high occupancy of the d band, namely Nb, Mo, Ta and W on one side and Ni, Cu, Rh, Pd, Ag and Pt on the other. It should be noted that a different bulk crystal structure corresponds to each group, bcc for Na and the low d-band occupied transition metals and fcc for the rest.
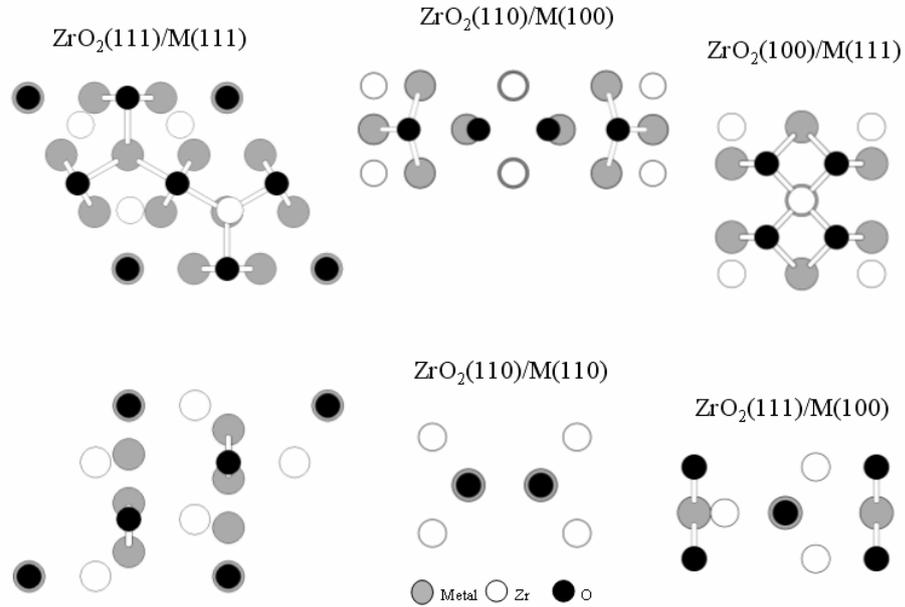
Figure 7.1: Top view of the HfO_2/metal or ZrO_2/metal interfaces modeled for different metals and relative crystallographic orientations, showing the metal-oxygen interface bonds. Only the Zr, O and metal planes closer to the interfaces are represented. The relative crystal orientations of ZrO_2 and the metal (M) are specified for each case.

The unit cells used in our ZrO_2/M and HfO_2/M calculations appear in figure 7.1, except for the $ZrO_2(100)$/M(100) interface (M denoting the metal) which was already shown in figure 6.14. All models correspond to fcc metals except the $ZrO_2(111)$/M(100) case (bottom right in the figure 7.1), which refers to bcc crystals. The unit cells corresponding to the interfaces formed by Al_2O_3 and MgO are represented in figure 7.2. For Al_2O_3 the metals investigated are all bcc, while for MgO, Na is bcc and Ag fcc. The figure shows the starting point of our calculations, where the strain induced by the misfit is assigned to the metal. For the oxide polar surfaces, where both metal-cation and O terminations are possible, we focus the analysis on the O-ended cases, but some metal terminations are also investigated.
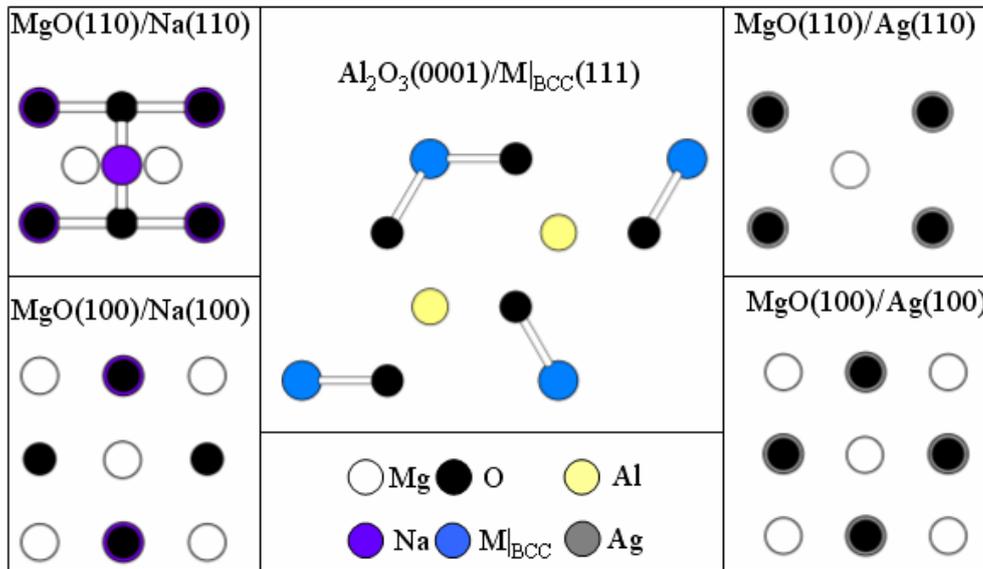
Figure 7.2: Same as figure 7.1 for the Al_2O_3/M and MgO/M systems.

A summary of our results is shown in table 7.1, where those obtained for the ZrO_2/Ni interfaces described in the previous chapter have also been included. Depending on the ceramic surface termination, the interfaces have been grouped in stoichiometric (ST), where the bulk oxide stoichiometry is preserved, and non-stoichiometric (NST). The ratio between the interface 2D unit cell area and the equivalent 2D area obtained using the corresponding bulk lattice vectors (ΔA) indicates that, after relaxation of lattice vectors and atomic positions, the initial strain assigned to the metal is usually distributed between both the metal and the oxide structures. The final ceramic strain depends on the particular ceramic and crystal orientation, but can be as large as 5% (13%) for interfaces with nominal mismatch of less (more) than 10%. In the table 7.1, instead of the actual interface ceramic-metal bond, the ratio between the interface bond length and the sum of the respective ionic radii is shown. It should be taken into account that for some interfaces there is a large dispersion of relative atomic positions, within the 2D unit cell as can be inferred from the large differences between the shortest metal-oxygen bond length (represented by Δd) and the mean bond length ($<\Delta d>$). This also leads to a null coordination for some interface metal-oxygen pairs in several cases. The disparity of the considered structures of ceramic and metals makes difficult to establish trends among structures. Even for a given ceramic, i.e. ZrO_2, there is a large variety of 2D interface unit cells, which differ in the number of metal-O bonds, in the metal to O coordination and/or in the amount of strain. In addition, some interfaces involve on the ceramic side Zr-terminations or nonpolar ZrO_2 surfaces, where the metal-Zr interaction also contributes to the adhesion.

	Δd	<Δd>	ΔQ_{CER}	ΔQ_{MET}	ΔA_{CER}	ΔA_{MET}	Wsep
NST ceramic							
$Al_2O_3(0001)_O$/Ta(111)	0,99	1,03	*-0,02*	*-0,77*	*1,00*	*1,07*	10,47
$Al_2O_3(0001)_O$/Nb(111)	1,02	1,06	*-0,08*	*-0,65*	*1,02*	1,09	9,26
$Al_2O_3(0001)_O$/Mo(111)	1,02	1,04	*-0,09*	*-0,45*	*0,97*	*1,12*	9,58
$Al_2O_3(0001)_O$/W(111)	1,04	1,06	*-0,05*	*-0,57*	*0,97*	*1,12*	9,76
$ZrO_2(100)_O$/Rh(111)	0,89	0,89	*-0,17*	*-0,22*	*1,01*	*1,03*	4,02
$ZrO_2(100)_O$/Pt(111)	0,90	0,92	*-0,21*	*-0,30*	1,05	1,00	3,37
$ZrO_2(100)_O$/Ni(100)	0,92	0,92	*-0,16*	*-0,28*	1,01	1,06	5,74
$ZrO_2(100)_{Zr}$/Ni(100)	1,05	1,05	*0,42*	*0,19*	0,99	1,05	5,01
$ZrO_2(100)_O$/Cu(100)	0,97	0,97	*-0,17*	*-0,27*	1,02	1,01	5,08
$ZrO_2(100)_{Zr}$/Cu(100)	1,10	1,10	*0,57*	*0,10*	1,02	1,01	3,66
$HfO_2(100)_{Hf}$/Ni(100)	1,03	1,03	*0,34*	*0,24*	0,99	1,02	5,54
$HfO_2(100)_O$/Ni(100)	0,92	0,93	*-0,14*	*-0,25*	1,01	1,04	6,26
ST ceramic							
$ZrO_2(111)_O$/Ni(111)|$_1$	0,93	0,97	*-0,08*	*-0,13*	*1,04*	0,94	1,28
$ZrO_2(110)$/Ni(110)	0,93	0,93	*-0,07*	*-0,12*	*0,97*	1,03	2,15
$ZrO_2(111)_O$/Ni(111)|$_2$	0,92	0,94	*-0,15*	*-0,12*	*1,05*	0,98	1,12
$ZrO_2(110)$/Ni(001)	0,95	0,97	*-0,08*	*-0,18*	*0,99*	0,98	0,94
$ZrO_2(110)$/Cu(110)	0,98	0,98	*-0,07*	*-0,10*	*1,01*	1,00	1,43
$ZrO_2(110)$/Cu(001)	1,04	1,05	*-0,09*	*-0,16*	*1,02*	0,95	0,71
$ZrO_2(111)_O$/Nb(100)	1,06	1,08	*-0,08*	*-0,14*	*0,96*	1,00	1,84
$ZrO_2(111)_O$/Ta(100)	0,99	1,01	*-0,03*	*-0,21*	*0,95*	0,99	2,23
$HfO_2(110)$/Ni(110)	0,93	0,93	*-0,04*	*-0,09*	*0,98*	1,01	2,09
$HfO_2(111)_O$/Ni(111)	0,94	0,97	*-0,05*	*-0,09*	*0,96*	0,93	1,29
$HfO_2(110)$/Ni(001)	0,96	0,98	*-0,04*	*-0,15*	*1,00*	0,98	1,07
MgO(110)/Ag(110)	0,86	0,86	*-0,05*	*-0,12*	*0,96*	1,04	1,10
MgO(100)/Ag(100)	0,99	0,99	*-0,04*	*-0,06*	*0,94*	1,03	0,72
MgO(110)/Na(110)	1,10	1,10	*-0,09*	*0,14*	*1,01*	1,08	0,65
MgO(100)/Na(100)	1,16	1,16	*-0,04*	*0,20*	*0,97*	1,04	0,17

Table 7.1: We show for the different interfaces with less than 10% mismatch and constituted by a non-stoichiometric (NST) and stoichiometric (ST) ceramic: the ratio between the shortest bond length between the metal and the ceramic (either with an anion or cation) and the sum of the ionic radii of the atoms forming the bond (Δd, in Å), and the same ratio taking the mean bond length instead of the shortest one (<Δd>, in Å); the difference between the average interface Mulliken charge and the bulk charge (ΔQ) for the ceramic atom at the interface and metal atoms; the ratio of the 2D unit cell areas at the interface and at the ideal bulk termination (ΔA) for both ceramic and metal; the work of separation (Wsep, in J/m^2).

	Δd	⟨Δd⟩	ΔQ_CER	ΔQ_MET	ΔA_CER	ΔA_MET	Wsep
NST ceramic							
ZrO₂(100)_O/Rh(100)	0,85	0,86	*-0,25*	*-0,22*	*1,05*	0,93	4,57
ZrO₂(100)_O/Nb(100)	0,99	1,05	*-0,14*	*-0,49*	*0,97*	1,17	9,07
ZrO₂(100)_O/Ta(100)	0,97	1,02	*-0,07*	*-0,63*	*0,97*	1,16	10,88
ZrO₂(100)_O/Pd(100)	0,88	0,89	*-0,27*	*-0,17*	*1,06*	0,88	2,91
ZrO₂(100)_O/Mo(100)	1,03	1,05	*-0,10*	*-0,50*	*0,96*	1,26	9,08
ZrO₂(100)_O/W(100)	1,03	1,08	*-0,06*	*-0,67*	*0,91*	1,19	9,61
ST ceramic							
ZrO₂(111)_O/Cu(111)	0,97	1,03	*-0,17*	*-0,11*	*1,07*	0,94	0,62
ZrO₂(111)_O/W(100)	1,01	1,10	*-0,05*	*-0,24*	*0,92*	1,03	2,28
ZrO₂(110)/Pd(100)	0,98	0,99	*-0,10*	*-0,05*	*1,00*	1,16	0,50
ZrO₂(110)/Rh(100)	0,92	0,93	*-0,15*	*-0,11*	*1,05*	1,31	1,94
ZrO₂(110)/Pt(100)	0,91	0,92	*-0,18*	*-0,08*	*1,13*	1,31	1,59
ZrO₂(111)_O/Mo(100)	1,02	1,08	*-0,06*	*-0,19*	*0,92*	1,04	1,85

Table 7.2: Same as 7.1 for the interfaces with more than 10% mismatch between a metal overlayer and ZrO_2.

Eventhough, a set of general common properties can be found for the interfaces studied. Some of them are not explicitly deduced from the table, such as the metallic character of the interfaces or the rapid decay of the interface effects, something also observed for the adsorption of single metal atoms and layers studied by other authors [43, 178]. Another common feature is the ionic nature of the metal-oxygen bonds, which in all cases involve O charge depletions with respect to the bulk oxide. Although certain ionic character may be assigned to the metal-cation bonds, because of their different electronegativities, the bonds are mainly formed by hybridization of the electronic states and thus in general the electronic bond charge is shared by both metals. The work of separation cannot be directly correlated either to the electron transfer from the metal to the oxygen atoms, or to the charge shared in the metal-cation bonds. Nevertheless, in general the largest values of Wsep correspond to the largest transfers and to the largest hybridizations. The relation between Wsep and the bond lengths is more intricate, partly due to the presence of individual short bond lengths (strong bonds) coexisting with weaker bonds at some interfaces. In general, the strongest interactions correspond to the bcc metals forming interfaces with $Al_2O_3(0001)$ and $ZrO_2(001)$, while the weakest ones are found for MgO both with alkaline and noble metals.

The previous tables show an important dispersion of Wsep, being the difference between the two extremes values larger than an order of magnitude. Nevertheless these values correspond not only to different metals and different ceramic oxides, but also to different lattice orientations which imply variations of lattice structure, polar character of the ceramic surface and therefore different electronic configurations. Although the matching of the metal and ceramic structures at the interface has a determinant influence on the adhesion, specially regarding the extended 2D interfaces, some trends for Wsep can also be defined regarding the electronic properties.

First, for a common number of valence electrons, increasing the metal atomic number (Z) enhances Wsep. Second, lower occupancies of the d band (bcc structures) lead to stronger adhesions, while the adhesion for the Na (sp valence band) is very weak. Third, there is a general common property showed by all the interfaces studied,

the Wsep for NST oxide surfaces are substantially larger than those corresponding to ST surfaces. In particular, interfaces formed between NST surfaces of oxide ceramics and transition metals of low occupancy of the d-band and bcc crystal structure, namely Nb, Mo, Ta and W present a very good adhesion with Wsep of the order of 10 J/m^2, while on the other side we find the interfaces composed by ST oxide surfaces and metals with high occupancies of the d-band and fcc structure as Cu, Ni, Pd, Pt, Ag and Rh. In fact, most ST ceramic surfaces correspond to non-polar terminations, except for the c-$ZrO_2(111)_O$ and c-$HfO_2(111)_O$ polar surfaces, ended in a single O-layer, which is a particular case of polar non-divergent surface [189]. For these particular cases, although there is an alternation of positively and negatively charged planes, so that the charge at the topmost surface plane is not compensated, the entire ceramic slab has the proper stoichiometry. As explained in section 4.7, these surfaces are stable similarly to the non-polar ones.

7.2.1 Wsep dependence on the metal properties

In the previous section we have extracted some general trends for different ceramic/metal interfaces. If we restrict to a particular ceramic oxide structure, the one of ZrO_2 and HfO_2, additional dependences of Wsep on the metal structural and electronic properties can be found.
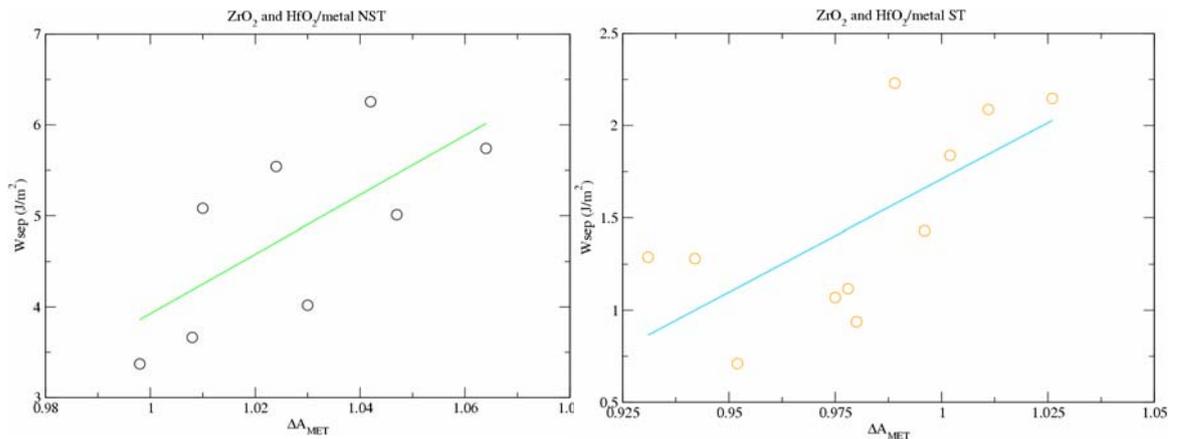
Figure 7.3: Relation between the values of Wsep and ΔA_{MET} for the NST (left) and ST (right) interfaces formed by ZrO_2 and HfO_2 with different metals. The continuous lines correspond to a linear fit of the data. Notice the scale of the vertical axis on the right is twice smaller.

We have tried to study qualitatively the correlation between the Wsep of stoichiometric interfaces and the corresponding strain in the metal slabs. In general, as mentioned above, Wsep is larger for interfaces with the metal under tensile strain. The correlation is quite irregular and it is not possible to adjust its dependence to a simple unique function. However, when considering only NST or ST the Wsep is to a good approximation a linear function of the metal strain. In figure 7.3 the approximate linear dependence is shown for both the ST and NST atomic relation of ZrO_2 and HfO_2 interfaces. ZrO_2 and HfO_2 have not only similar electronic configurations but also analogous crystal phases with close lattice parameters. The ST surfaces not only present smaller values of Wsep but also their variations are smaller for a similar distortion of the 2D metal area.

We have also analyzed the dependence of Wsep on the ratio between the bulk 2D unit cells of the metal and the ceramic. We obtain that the larger values of Wsep are found when the metal area is smaller than that of the ceramic, which again directly relates a high Wsep with a high metal tensile strain. Since the strain in the metal is tensile, a bond stretching in the metal layer induces an interface bond strengthening and thus increases the interface cohesion.

Another correlation may be established between Wsep and the electronic properties of the metal. In a solid the total charge of an atom can be decomposed into the Mulliken population and the bonding overlap populations. While the former provides information on the electronic charge balance at each atomic site, the second may be viewed as the amount of charge shared in the bonds. Although both quantities are dependent on the choice of the basis set, they correctly give trends on the amount of charge transfer or the atomic hybridization as long as calculations are performed within a consistent scheme and are sufficiently accurate. Our calculations fulfill both criteria, allowing us to analyze the relation between the calculated Wsep and the metal bond overlap population.

FCC	BOP	BCC	BOP
Rh	0,120	Ta	0,201
Ni	0,107	W	0,199
Pd	0,078	Nb	0,198
Pt	0,084	Mo	0,189
Cu	0,093	Na	0,350
Ag	0,082		

Table 7.3: Bonding overlap population for the bulk structures of bcc and fcc metals of tables 7.1 and 7.2.

Table 7.3 provides the bulk metal bond overlap populations for the metals forming the calculated interfaces. Due to the localized nature of the d-band, metals with a sp VB band have larger BOP than those corresponding to metals with a VB formed mainly by d-electrons. Even more, for a larger number of d-electrons the BOPs are smaller leading in general to higher BOP values for bcc than for fcc metals. On the other hand, the screening effects tend to increase the BOP with Z for a fixed number of d-electrons, with the exception of Ni, due that is generated with electronic configuration 4s1 3d9, see table 3.7.

Figure 7.4 illustrates the dependence of the Wsep on the BOP of the metal for polar $ZrO_2(001)_O$/metal(001) interfaces. As previously stated, there is a large difference, around a factor of two, between the Wsep for bcc and fcc metals. What figure 7.4 shows is that this large Wsep correlates with the larger values of the BOP for bcc metals, that is, with the available amount of charge shared in the metal bonds. In a first approximation the correlation can be considered as linear. Moreover, an analysis of the ionic character of the interface metal-O bonds indicates that most of the average charge transfer originates from the interstitial metal bond charge.
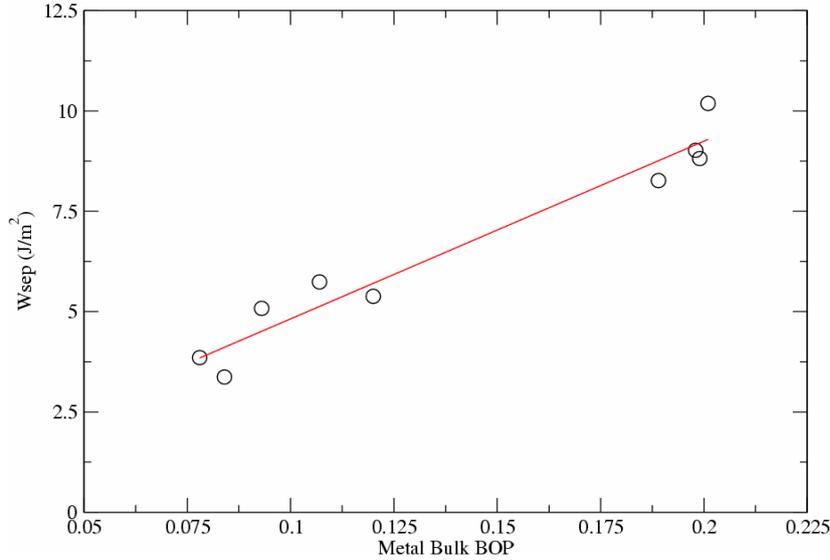
Figure 7.4: Wsep versus the bulk metal BOP for the NST $ZrO_2(001)_O$ interfaces with different (001) metal structures, left side data points corresponds to fcc and right side to bcc structure.

Also, a relation between large metal BOP values and large Wsep is found for different ceramics and crystal orientations, as is the case of $Al_2O_3(0001)_O$. In general, this relation is valid regarding metals with a valence d-band. However, for Na, showing the largest BOP among all metals, the Wsep at different MgO interfaces is lower than the corresponding value for Ag, with a significantly smaller BOP.

On the other hand, the much slighter variations of the BOP when increasing Z for a fixed number of VB d electrons can also be correlated to the enhancement of Wsep.

7.2.2 Comparison with experimental results

In the following, we will compare our results with previous theoretical and experimental works, considering each ceramic oxide separately. In fact, for ZrO_2 the most studied interfaces are those with Ni, which have already been discussed in chapter 6. However, there are some additional results concerning single metal overlayers.

Alfredsson *et al.* have performed calculations of the adhesion for ZrO_2/metal systems formed by Pd and Pt adlayers deposited onto c-ZrO_2(111) and (011) surfaces [43, 44]. The adsorption energy on ZrO_2(111) is around 200 kJ/mol for a Pd adlayer while for Pt is 400 kJ/mol when there is a one fold metal-O coordination, while for ZrO_2(011) the coordination is three-fold. The general bonding character is mainly electrostatic, as in ZrO_2(111)/Ni(111) [41] at low coverages of ZrO_2 and therefore a relatively high Wsep is expected. In fact, we have obtained a value of 3.37 J/m^2 for the 2D extended $ZrO_2(100)_O$/Pt(111) interface. On the other hand, for the metal overlayers with larger mismatch, Wsep is reduced, with values of 2.91, 1.59 and 0.50 J/m^2 for the systems $ZrO_2(100)_O$/Pd(100), ZrO_2(110)/Pt(100) and ZrO_2(110)/Pd(100) respectively.

Wettability experiments using ZrO_2 monocrystals as substrate with different metal melts [19] and references therein, find also a different wetting behavior when comparing stoichiometric and non-stoichiometric ZrO_2. The angle value related to the experimental work of adhesion (Wad) is given by $Wad = \sigma_{MET}\left(1+\cos\theta\right)$ and ranges from 65º to 145º for the former, while for the latter there is a reduction from 60º to 130º.

Although, the exact value of Wad that corresponds to wetting experiments is generally lower than that obtained by *ab-initio* studies, due to the geometry differences as explained in 1.1, the relative trends of variation can be compared. The angle reduction on non-stoichiometric ZrO_2 indicates that the adhesion is stronger, as we have also obtained.

Although *ab-initio* studies of the ceramic/metal interface adhesion are quite recent, which implies that in general there are not many results, by far the most studied systems have been those involving Al_2O_3, and in particular with Nb, Ni and Al as metals. For them, an important number of theoretical calculations and experimental works can be found in the literature. After theoretical calculations [37] $Al_2O_3(0001)_O/Nb(111)$ is known to exhibit a strong interface with Wsep 9.8 J/m^2 when cleaving the Al_2O_3 on the O plane, and 2.7 J/m^2 when cleaving at the Al one. This result compares nicely with our value 9.3 J/m^2 for the O terminated, as well as with the close values that we obtain for the bcc metals Mo, W and Ta, with similar electronic structure than Nb.

There are also several wettability experiments on Al_2O_3 [10] and references therein, showing that the wetting angles ranges from 80º to 132 º which corresponds to a Wad range of 1.472 to 0.130 J/m^2. These values are smaller than those obtained by us, but they corresponds obtained mainly to fcc metals, and thus can not be compared with our Al_2O_3/bcc metal interfaces.

Finally, concerning MgO, we have performed calculations only for Na and Ag, with similar lattice parameter than that of the ceramic. Ag has been largely studied by *ab-initio* calculations, with large emphasis on the effect of the different interface positions on the value of Wsep, as shown in table 7.4.

References	Onsite Mg	Onsite O
Heifets	0,63	0,81
Li	0,54	
Hong	1,08	1,90
Schönberger	0,70	1,60
Ours	0,27	0,72
Experiment		0,45

Table 7.4: Values of Wsep for MgO/Ag depending on the relative interface position of ceramic and the metal atoms compared with previous calculations [33, 34, 223, 224], respectively to the table order, and experimental measurements [225].

We can see that our calculated Wsep are in general lower than those obtained previously, but it is the closest to the experimental Wsep.

In a previous theoretical work [226] has been found that alkali metals, and particularly Na, when are deposited 0.5 and 0.25 ML thickness on MgO (001) show a weak physisorption with higher interaction at the O ontop site than at the Mg site. We obtain similar results with values of 0.65 and 0.17 J/m^2 for Na ontop of O and Mg respectively, which in addition are among the lowest Wsep values for all the systems studied here.

From wetting measurements [227] and references therein, the wetting angles for all MgO/metal interfaces are over 90º, and thus in the non-wetting regime, except for reactive interfaces formed with Zr and Ti.

In summary, the calculated values of Wsep in tables 7.1 and 7.2 show a reasonable quantitative agreement with the available experimental data.

7.3 Wsep versus surface and interface energy

As explained in section 2.7 the ideal work of separation can be expressed in terms of the surface and interface free energies

$$W_{sep} = \sigma_{MET} + \sigma_{CER} - \gamma$$
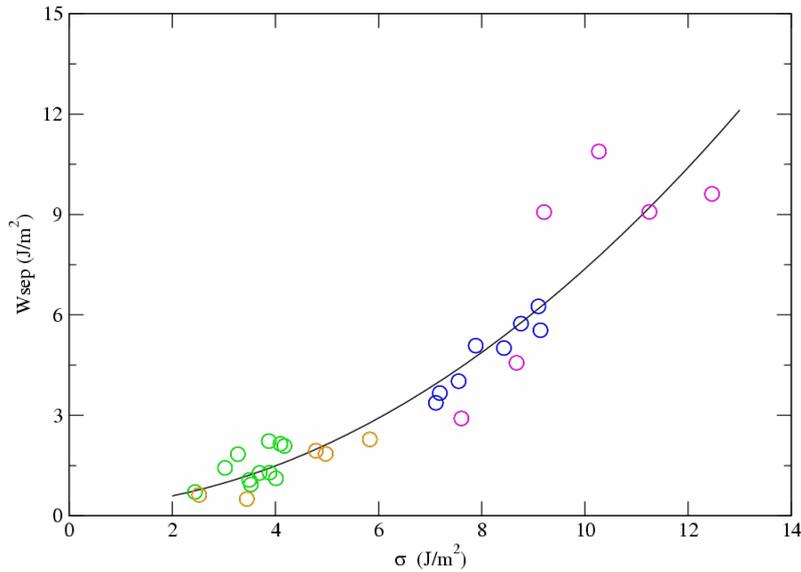
Figure 7.5: Wsep vs $\sigma_{MET}+\sigma_{CER}$ for all calculated interfaces. The continuous line represents a quadratic fit to the data.

Thus, the work of separation not only depends on the interface bonds, but also on the properties of the surfaces involved. In fact, there is a correlation between Wsep and $\sigma=\sigma_{MET}+\sigma_{CER}$. Figure 7.5 shows the Wsep as a function of the sum of the ceramic and metal surface energies for all the calculated interfaces. As explained before, accurate surface energies can only be obtained from calculations with ceramic slabs containing an integer number of oxide units, ST. For polar surface slabs, in order to have an identical termination at both surfaces, non-stoichiometric slabs are used. In this case the surface energy (σ_{CER}) is given as a function of the oxygen chemical potential (μ_O). The σ represented in figure 7.5 for NST surfaces corresponds to the sum of the average values of $<\sigma_{MET}>+<\sigma_{CER}>$ within the range of allowed values of μ_O, see section 2.7.

From the figure it is evident that interfaces formed from surfaces with large σ present larger Wsep than those containing surfaces with smaller σ. In general surface energies are larger for polar surfaces, which formation requires the breaking of the strong anion-cation ionic bonds. In fact, the stabilization of the polar surfaces can be obtained by modification of the surface charge and then the formation of interface bonds which is a reliable mechanism, as indicates the large reactivity of these surfaces.

Nevertheless, the relation between Wsep and σ is not simple, as would be expected for the great variety of interfaces included. Note that in figure 7.5 we are including not only different metals, crystal structures and interface coordinations, but also different ceramics and consequently different bonding mechanisms, for example charge transfer in O-metal bonds or hybridization in cation-metal interactions. A similar trend has been found from a systematic study of Al interfaces with Al_2O_3, nitrides and carbides [222].

105
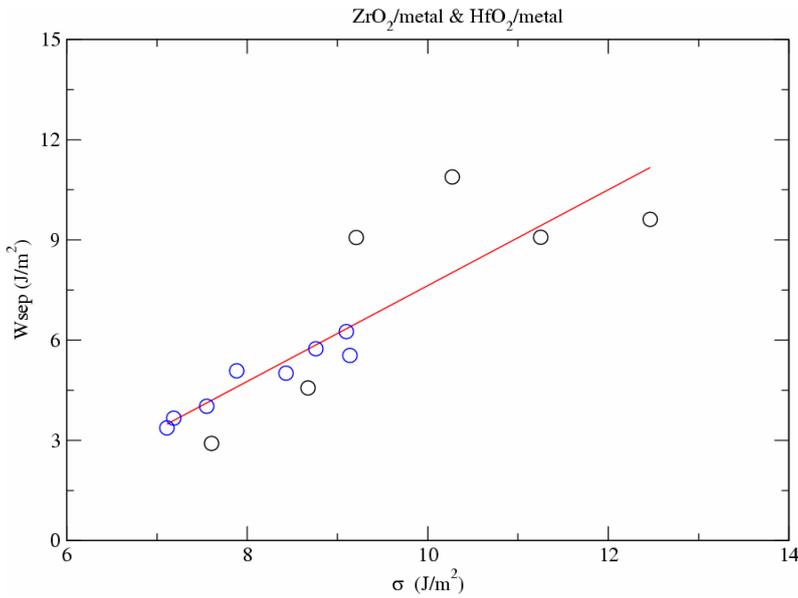
Figure 7.6: Same as figure 7.5 for the polar interfaces formed by HfO$_2$ and ZrO$_2$ ceramics.

Furthermore, if we restrict to ZrO$_2$ (for which we have calculated the largest number of interfaces) and to results from NST slabs (an accurate comparison with stoichiometric slabs will require the precise knowledge of μ_O) the relation is linear, as shown in figure 7.6. In figure 7.7 it is represented the dependence of Wsep on $\gamma/(\sigma_{MET}+\sigma_{CER})$, or γ/σ parameter, which shows their simpler linear correlation with values of γ/σ ranging from 0.25 to 0.52. Despite that the results indicate that σ is in every case larger than the γ value, from around 400% to 200%, the γ contribution to Wsep can not be considered to be negligible. If we extrapolate the plot in figure 7.7 to $\gamma = 0$, like the situation already proposed of γ negligible [222], we obtain that we could approximate Wsep$\approx\sigma$ only for very large Wsep over 9 J/m^2. This value was obtained only for ZrO$_2$(001)$_O$ interfaces with large mismatch (>10%) between the metal and the ceramic, and γ/σ>0.5. Therefore, for the interfaces investigated in this work, although the σ contribution is much larger, γ also contributes to the Wsep, contrary to the results obtained for various Al/ceramic systems [222].
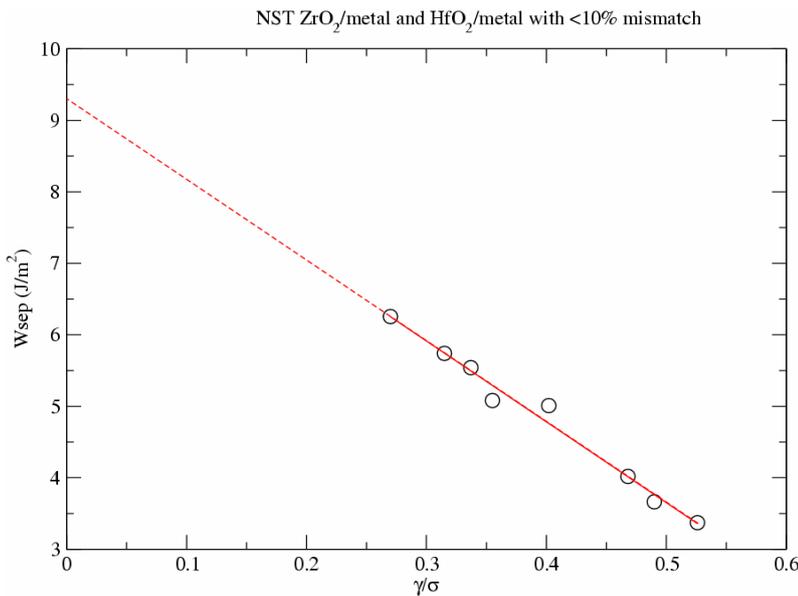
Figure 7.7: Wsep vs γ/σ for the polar interfaces formed by HfO$_2$ and ZrO$_2$ ceramics.

7.4 Interface properties beyond the elastic regime

The ideal Wsep, calculated in this work, was defined in chapter 2 as the reversible work needed to separate the interface into two free surfaces if the plastic and diffusional degrees of freedom are supposed to be suppressed. Thus, Wsep is a fundamental quantity which controls the mechanical strength of the metal/ceramic interface and has relevance to understand the interface macroscopic properties. Since it directly characterizes the strength of the interfacial bonding, it is appropriate for analyzing mechanical properties, in particular fracture experiments. Nevertheless, it always represents a lower bound for the energy needed for any cleavage experiment, since dissipative processes are not included.

In homogeneous materials, as metals or ceramic oxides, the work of separation needed to form two surfaces from a bulk medium is given by $Wsep_i = 2\sigma_i$ where σ_i stand for the surface energy of the material considered, either the metal or the ceramic. Therefore, in a first approximation, from the knowledge of σ_{MET}, σ_{CER} and interface Wsep, it is possible to predict the place of failure of a heterogeneous interface in a cleavage experiment, since it fails on the region of weaker bonds.

NST ceramic	$2^*\sigma_{CER}$	$2^*\sigma_{MET}$	Wsep	ST ceramic	$2^*\sigma_{CER}$	$2^*\sigma_{MET}$	Wsep
$Al_2O_3(0001)_O$/Ta(111)	13,97	_5,97_	10,47	$ZrO_2(111)_O$/Ta(100)	_2,02_	5,72	**2,23**
$Al_2O_3(0001)_O$/Nb(111)	13,78	_4,16_	9,26	$ZrO_2(110)$/Ni(110)	2,84	5,36	**2,15**
$Al_2O_3(0001)_O$/Mo(111)	14,45	_6,84_	9,58	$HfO_2(110)$/Ni(110)	2,90	5,44	**2,09**
$Al_2O_3(0001)_O$/W(111)	14,43	_8,18_	9,76	$ZrO_2(111)_O$/Nb(100)	2,04	4,50	**1,84**
				$ZrO_2(110)$/Cu(110)	2,66	3,38	**1,43**
$HfO_2(100)_O$/Ni(001)	12,80	_5,40_	**6,26**	$HfO_2(111)_O$/Ni(111)	2,74	5,04	**1,29**
$ZrO_2(100)_O$/Ni(001)	12,04	_5,48_	**5,74**	$ZrO_2(111)_O$/Ni(111)|1	2,46	4,92	**1,28**
$HfO_2(100)_{Zr}$/Ni(001)	12,91	_5,37_	**5,54**	$ZrO_2(111)_O$/Ni(111)|2	3,32	4,70	**1,12**
$ZrO_2(100)_O$/Cu(001)	12,48	_3,30_	**5,08**	$HfO_2(110)$/Ni(100)	1,62	5,36	**1,07**
$ZrO_2(100)_{Zr}$/Ni(001)	11,42	5,44	**5,01**	$ZrO_2(110)$/Ni(100)	1,72	5,34	**0,94**
$ZrO_2(100)_O$/Rh(111)	10,24	4,86	**4,02**	$ZrO_2(110)$/Cu(100)	1,58	3,30	**0,71**
$ZrO_2(100)_{Zr}$/Cu(001)	11,16	_3,22_	**3,66**				
$ZrO_2(100)_O$/Pt(111)	10,80	3,42	**3,37**	MgO(110)/Ag(110)	4,08	2,11	**1,10**
				MgO(100)/Ag(100)	1,74	2,19	**0,72**
				MgO(110)/Na(110)	3,70	_0,45_	**0,65**
				MgO(100)/Na(100)	1,78	0,48	**0,17**

Table 7.5: Surface energies of the ceramic and metal, and Wsep of the interface formed by them, all quantities are given in J/m^2. The underlined quantity indicates the region where interface failure is expected to occur.

Table 7.5 gives the work of separation for different interfaces and the corresponding metal and oxide surface energies. For the NST ZrO_2 and HfO_2 surfaces (second block of the left), all of the Wsep values are strong and slightly higher than the metal surface energies except for $ZrO_2(100)_{Zr}$/Ni(001), $ZrO_2(100)_O$/Rh(111) and $ZrO_2(100)_O$/Pt(111). Also all the interfaces formed by the Al_2O_3 show Wsep values well above those of the metal surface energies. The average oxide surface energies are always larger. Therefore, it is expected that NST interfaces will fail in the metal region. Contrary, for interfaces

built from ST surfaces, see bottom rows of table 7.5, the interface Wsep is the smaller quantity but for the MgO(110)/Na(110). Therefore, they will failure at the interface, presenting brittle debonding.

We would like to point out that our calculations are valid under the elastic regime consideration, and beyond this regime for the metal it is expected that the start of the plastic deformation contributes further to the reinforcement of the system. In fact, many fracture experiments on Al_2O_3 and metals as Nb, Al, Ni, Cu or Au have measured the crack blunting mechanism, based on the plastic deformation of the metal, which can induce fracture energy values of more than 200 J/m^2 with no need of a very good interface matching [228]. A summary of the experimental measurements is shown in [229]. Particularly, a reported fracture energy of 112±51 J/m^2 has been found for the $Al_2O_3(0001)/Nb(111)$ interface, indicating a mechanism of plasticity (with an stress-strain graph) [230]. These plasticity effects can not be taken quantitatively into account by our calculations, however qualitatively we expect from table 7.5 a plastic reinforcement for every bcc metal when forming interface with Al_2O_3.

The Al_2O_3/Mo interface has also been studied in cermets formed by a polycrystalline ceramic matrix including metal particles [231]. An increase in fracture energy from 20 to 60 J/m^2 is obtained when the concentration of metal increases from near 0% to 20%, with a bridging mechanism induced by ductile particles. Our results again compare qualitatively well, due to the fact that we obtain plastic reinforcement in this system.

Furthermore, there exists another criterion of interface failure based on the stress intensity that settles the start of plastic deformation in the metal. The local stress intensity K_i^e needed for the emission of the first dislocation, and therefore the beginning of the plastic regime, has been obtained by a 3D molecular dynamics simulation for various fcc metals [14]. The available calculated values for the fcc metals involved in the interfaces described on table 7.5 are given in table 7.6 together with the phenomenological stress intensity assigned to the interface (K_{IC}) as derived from our calculated Wsep [15]:

$$K_{IC} = \sqrt{\frac{Wsep*E_{YOUNG}}{(1-\nu^2)}} \qquad ,$$

where ν is the Poisson modulus and E_{YOUNG} is the Young modulus, i.e. the slope of the stress versus the strain curve in the linear or elastic regime. The Poisson modulus for polycrystalline metals is fairly constant and close to 0.33, which is the value we employ for all the metals.

If $K_{IC} > K_i^e$, the metal exhibit the dislocations emission and the mechanical properties of the interface system are improved by the bridging mechanism.

From the table 7.6 we can see that for NST interfaces both stress intensities are close, while for the ST cases K_{IC} is in general a factor of 2 smaller than K_i^e. These results compare well with those previously obtained in table 7.5, and tell us that an enhancement of the adhesion by the bridging mechanism may occur in almost all NST interfaces, being particularly expected for $ZrO_2(001)_O/Cu(001)$ and $ZrO_2(001)_O/Pt(111)$.

NST ceramic	K_{IC}	K_i^e
$HfO_2(100)_O$/Ni(001)	**1,18E+006**	1,10E+006
$ZrO_2(100)_O$/Ni(001)	**1,11E+006**	1,10E+006
$HfO_2(100)_{Zr}$/Ni(001)	**1,13E+006**	1,10E+006
$ZrO_2(100)_O$/Cu(001)	**8,58E+005**	7,08E+005
$ZrO_2(100)_{Zr}$/Ni(001)	1,06E+006	1,10E+006
$ZrO_2(100)_{Zr}$/Cu(001)	**7,29E+005**	7,08E+005
$ZrO_2(100)_O$/Pt(111)	**8,03E+005**	6,25E+005
ST ceramic		
$ZrO_2(110)$/Ni(110)	6,94E+005	1,10E+006
$HfO_2(110)$/Ni(110)	6,84E+005	1,10E+006
$ZrO_2(110)$/Cu(110)	4,55E+005	7,08E+005
$HfO_2(111)_O$/Ni(111)	5,37E+005	1,10E+006
$ZrO_2(111)_O$/Ni(111)|1	5,36E+005	1,10E+006
$ZrO_2(111)_O$/Ni(111)|2	5,00E+005	1,10E+006
$HfO_2(110)$/Ni(100)	4,89E+005	1,10E+006
$ZrO_2(110)$/Ni(100)	4,58E+005	1,10E+006
$ZrO_2(110)$/Cu(100)	3,21E+005	7,08E+005

Table 7.6: Stress intensity (K_{IC}) of the interfaces studied in table 7.5 and formed by fcc metals to compare with the available local stress intensity (K_i^e) values of the metal [14].

7.5 Interface stability

Besides Wsep, the interface energy (γ) also provides information on the interface state, since it gives the excess free energy of an interface compared to the corresponding bulk materials. γ quantifies the strength of the interfacial bonds compared to the bulk bonds. In addition, it allows one to know which interfaces are more stable in a thermodynamic sense. As explained in section 2.7, there have been studies combining first-principles calculations with thermodynamic approaches to obtain interfacial energies of heterogeneous interfaces. The interface energy can be calculated for both ST and NST interfaces, and their comparison allows one to discuss the thermodynamic stability of the interfaces. We have followed the procedure described in section 2.7, and we have calculated the interface energy by eq. 2.23 as a function of the O chemical potential (μ_O) minus its O rich limit ($\frac{1}{2}(\mu^{gas}_{O2})$).

Table 7.7 yields the calculated interface energy for all ST interfaces. All the values are positive indicating that the formation of the interface costs energy. The smallest values, those with the most stable interfaces, correspond to MgO, eventhough they also present the smaller Wsep. The range of γ values are close for the ZrO_2 and MgO interfaces, similarly to the results obtained for the Wsep; in fact, for the same metal and crystal orientation the interface free energies differ less than 10%. The most stable interface of the ZrO_2 and HfO_2 corresponds to $ZrO_2(111)_O$/Nb(100), which Wsep is also among the largest obtained for ST interfaces. However, the γ variations shown in table 7.7 are not very dramatic, indicating that the stabilities of the interfaces are analogous.

ST ceramic	γ	Wsep(J/m2)
$ZrO_2(111)_O$/Ta(100)	1,64	**2,23**
$ZrO_2(110)$/Ni(110)	1,95	**2,15**
$HfO_2(110)$/Ni(110)	2,09	**2,09**
$ZrO_2(111)_O$/Nb(100)	1,43	**1,84**
$ZrO_2(110)$/Cu(110)	1,59	**1,43**
$HfO_2(111)_O$/Ni(111)	2,60	**1,29**
$ZrO_2(111)_O$/Ni(111)|1	1,99	**1,28**
$ZrO_2(111)_O$/Ni(111)|2	2,89	**1,12**
$HfO_2(110)$/Ni(100)	2,46	**1,07**
$ZrO_2(110)$/Ni(100)	2,59	**0,94**
$ZrO_2(110)$/Cu(100)	1,73	**0,71**
MgO(110)/Ag(110)	1,99	**1,10**
MgO(100)/Ag(100)	1,25	**0,72**
MgO(110)/Na(110)	1,42	**0,65**
MgO(100)/Na(100)	0,96	**0,17**

Table 7.7: Interface energy for interfaces formed by ceramic slabs and the corresponding Wsep.

The interface energies for the NST interfaces are represented in figure 7.8 as a function of μ_O.

With respect to the ZrO_2 and HfO_2 interfaces, three different regions are clearly identified within the range of allowed values of μ_O. Approximately, for $\Delta\mu_O < 1/(2y)\Delta G^f_{MxOy} \approx 2.7$ eV, which corresponds to low O pressures, the M/Zr-ended interfaces are the most stable. Conversely, the M/O-terminated interfaces are more stable for high O pressures, that is for $\Delta\mu_O > 2.7$ eV.

On the other hand, in general, the Al_2O_3/M interfaces present low interface energy at rich O pressures, indicating a good stability, which worsens as the O pressure decreases. The Wsep is large evidencing strong bonds at the interface even compared with those of the bulk.

110

a)

NST ZrO$_2$/metal and HfO$_2$/Metal

γ (J/m^2)

15, 12, 9, 6, 3, 0 (y-axis)

-5, -3.75, -2.5, -1.25, 0 (x-axis)

$\Delta\mu_O$

HfO$_2$(100)|$_{Zr}$/Ni(100) 7.07
ZrO$_2$(100)|$_{Zr}$/Ni(100) 5.01
ZrO$_2$(100)|$_{Zr}$/Cu(100) 3.66
HfO$_2$(100)|$_O$/Ni(100) 7.69
ZrO$_2$(100)|$_O$/Ni(100) 5.74
ZrO$_2$(100)|$_O$/Cu(100) 5.08
ZrO$_2$(100)|$_O$/Rh(111) 4.02
ZrO$_2$(100)|$_O$/Pt(111) 3.37

b)

ZrO$_2$(001)/Metal(001)

γ (J/m^2)

16, 12, 8, 4, 0 (y-axis)

-5, -3.75, -2.5, -1.25, 0 (x-axis)

$\Delta\mu_O$

9.61
9.08
10.88
9.07
4.57
2.91

W
Mo
Ta
Nb
Rh
Pd

c)

NST Al$_2$O$_3$/bcc metal

γ (J/m^2)

15, 12, 9, 6, 3, 0 (y-axis)

-5, -3.75, -2.5, -1.25, 0 (x-axis)

$\Delta\mu_O$

9.76
9.58
10.47
9.26

W
Mo
Ta
Nb

Figure 7.8: Interface energies of non-stoichometric ceramics as a function of $\Delta\mu_O=\mu_O-1/2\ \mu^{gas}_{O2}$ for interfaces between a) fcc metals with ZrO$_2$ and HfO$_2$ ceramics with less than 10% mismatch; b) bcc metals with Al$_2$O$_3$(0001); c) fcc and bcc (001) metals with ZrO$_2$(001) with more than 10% mismatch. It is also included the value of the Wsep for each interface.

Chapter 8

Conclusions

We have used the density functional theory to perform a systematic investigation of the surfaces and interfaces between different metals and ionic oxide ceramics which allows us to obtain some general conclusions about their atomic behavior:

The polar surfaces of the low pressure ZrO_2 phases suffer large relaxations. The pattern is similar for all the surfaces, which tends to decrease the first Zr-O surface distance and increase the second one. All the polar terminations exhibit a metallic character while the non-polar orientations show an insulating electronic structure. In addition, the results indicate that, eventhough the cubic structure tends to profit the additional degrees of freedom provided by the surface to reconstruct towards a tetragonal structure, the symmetry constraints imposed by the particular termination may inhibit the reconstruction.

A magnetic ground-state develops in bulk ionic oxides with cation vacancies and at the O terminated polar surfaces. The magnetic moment resides on the O atoms with loss of cation coordination and there is a clear correlation between the magnitude of the magnetic moments and the loss of the ionic O charge.

Adhesion between ideal ZrO_2 and Ni is improved for polar ceramic terminations. Good bonding is found for the $ZrO_2(001)/Ni(001)$ interface which corresponds to the smallest two dimensional cell. These relative orientations lead to only one type of bonding and rather strong metal-ceramic interaction. The adhesion properties change dramatically in the presence of O vacancies due to the ability of the ZrO_2 to reconstruct towards the more stable phases.

All the interfaces studied show several common properties. The Wsep increases with increasing tensile metal strain and a correlation between large metal BOP values and large Wsep is found. However, the more general conclusion obtained from the study is that interfaces formed between metal and ceramic surfaces with large σ present larger Wsep than those containing surfaces with smaller σ. In general surface energies are larger for non-stoichiometric surfaces, which correspond in almost all the cases with polar surfaces, whose formation requires the breaking of the strong anion-cation ionic bonds. Thus, the Wsep for interfaces formed with non-stoichiometric polar oxide surfaces are substantially larger than those corresponding to stoichiometric non-polar oxide surfaces.

Besides these main conclusions, our study can be summarized as follow.
DFT calculations based on the generalized gradient approximation for exchange and correlation show good agreement with experimental results of the structural and electronic properties of the low pressure ZrO_2 phases. The correct energy hierarchy between phases is reproduced: $E_m < E_t < E_c$. The energy differences between phases are very close to the experimental ones, specially between the monoclinic and cubic phases. In addition, the calculated values for the bulk modulus compare well and agree with the trend of decreasing value with decreasing phase symmetry, and are similar to previous theoretical calculations.

The electronic properties of the three phases are determined by the insulating and ionic character of the electronic bands. Nevertheless, the ionicity decreases as the symmetry decreases, the monoclinic phase being the less ionic phase.

In c-ZrO_2 with neutral O vacancies, a vacancy level associated to the Zr atoms develops in the band gap, while in c-ZrO_2 doped with Y_2O_3 the insulating character of the undefected band structure is maintained.

The c-ZrO_2 phase transformations are achieved under external stress. Cubic to tetragonal phase transformation is accomplished by letting the system relax after a very slight shift of the O sublattice along the X_2^- direction of the soft phonon mode. Cubic to monoclinic transformation is obtained by applying a tensile hydrostatic stress in order to increase the volume of the cubic unit cell and then further apply a shear stress.

The low-index polar surfaces of the low-pressure ZrO_2 phases exhibit a similar relaxation pattern. The subsurface plane relaxes outwards reducing the first Zr-O interlayer distance and increasing the second one. This alternation of short and long bonds decays when going into the bulk, and at the third Zr layer the bonds are similar to bulk bonds. The most important relaxation effects are exhibited by the (001) surfaces of the t-ZrO_2 phase, followed by the (111) surfaces of c-ZrO_2 and finally by the (001) surfaces of c-ZrO_2. Both Zr and OO surfaces are metallic and present respectively an increase and a decrease of charge with respect to the ionic bulk values, the gain/loss of charge is almost restricted to the outermost layers. For O-ended surface, with only half of the O atoms at the outermost plane, the relaxation is analogous although the internal buckling of the O layer results in the coexistence of short and long Zr-O bonds for the second O double layer, similarly to the bond distribution in the tetragonal ZrO_2 phase. Moreover, there are not surface induced gap states and the surface remains insulating.

For non-polar surfaces the effect of relaxation is small. The major result is the buckling of all the layers observed in the (110) c-ZrO_2. The buckling is due to the displacement of the Zr atoms, which move alternatively to the upper and to the lower adjacent layer. These surfaces maintain the insulator character of the bulk and are the thermodynamically more stables.

When Zr vacancies are considered on bulk c-ZrO_2 a magnetic moment develops on the O atoms NN's to the vacancies. The magnetic moment increases with the number of vacancies till reach a value close to the number of doped holes by keeping the system in high spin state. The presence of vacancies implies a non-stoichiometric atomic relation where the O atoms exceed the nominal 1:2 ratio. This is reflected in the local reduction of charge of the O atoms bonded to the vacancies, leading to a direct relation between the loss of charge and the intensity of the magnetic moments.

For polar O-ended surfaces, the spin polarized situation is more probable than the non polarized one. The spin polarized calculations of different ionic surfaces terminated in O planes show a correlation between the magnitude of the moments and the loss of charge with respect to the bulk. This way, the larger the difference between the O charge of the surface atom and that of the bulk compound, the bigger the O magnetic moment. Also, the magnitude of the moment increases as the cation coordination reduces. In general, the magnetic moment distribution is very anisotropic, with a preferred alignment with respect to the surface normal either out-of-plane or in-plane. Most of the magnetic surfaces present half metallicity.

The ideal polar interface of the c-$ZrO_2(001)$/Ni(001) system present rather strong metal-ceramic bonding and the equilibrium bond lengths both for Ni-Zr and Ni-O are smaller

than the sum of the respective atomic radii. Metal induced gap states (MIGs) appear in both interfaces. Nevertheless, the bonding character between Ni and Zr, arises mainly from s-d and d-d hybridizations while in the O/Ni interface there is a net charge transfer from Ni to O. Interface effects are almost restricted to the atomic planes in contact, specially in the metal slab, where they are already screened at the second layer.

Interface bonds are longer for the $ZrO_2(110)/Ni(001)$ interface which implies an overall weakening of the ZrO_2-Ni interaction. For this interfacial system, we have found that the preferential coordination sites for Ni corresponds to bridge and hollow positions for the Ni/O and Ni/Zr cases, respectively. Thus, adhesion between ideal ZrO_2 and Ni is improved for polar ceramic orientations and the O termination of ZrO_2 shows better adhesion than that of Zr surface.

The interface stability is related with the stoichiometry and polarity, the non-stoichiometric ceramic slabs being the less stables, while the most stables are the stoichiometric and the non-polar. We identify the $ZrO_2(110)/Ni(110)$ interface as the most stable in the range of intermediate μ_O values, although for high μ_O the O terminated of the $ZrO_2(001)_O/Ni(001)$ interface is more stable, and for low values of μ_O is the Zr terminated. Realistic calculations of the $ZrO_2(001)/Ni(001)$ interfaces modeling the actual presence of O vacancies at the interface plane, both related to YSZ and thermodynamic, show that both kinds of O vacancies decrease the number of interface bonds. Nevertheless, thermodynamic vacancies induce in the ceramic material an internal restructuring of the ceramic slab that increases the Zr-O hybridization interaction at the cost of weakening the interface bonds. On the other hand, when O vacancies are related with Y_2O_3 doping, charged vacancies, the presence of the large Y cations clips the ceramic structure preventing its internal reconstruction, thus the interface bond strength is not actually reduced.

A set of general common properties can be found for a large variety of interfaces formed by several bcc and fcc metals joined to α-Al_2O_3, MgO, HfO_2 and ZrO_2 ceramic materials. Metallic character, the rapid decay of the interface effects, the ionic nature of the metal-oxygen bonds, which in all cases involve O charge depletions with respect to the bulk oxide and the fact that the largest values of Wsep correspond to the largest charge transfers and to the largest hybridizations are exhibited by all interfaces. In general, the strongest interactions correspond to the bcc metals forming interfaces with $Al_2O_3(0001)$ and $ZrO_2(001)$, while the weakest ones are found for MgO both with alkaline and nobel metals.

The Wsep increases with increasing tensile metal strain. The Wsep for interfaces with non-stoichiometric oxide surfaces are substantially larger than those corresponding to stoichiometric surfaces. When only a kind of termination, non-stoichiometric or stoichiometric, is considered, the Wsep to a good approximation is a linear function of the metal strain. Thus, a bond stretching in the metal layer induces an interface bond strengthening and increases the interface cohesion. Regarding metals with a valence d-band forming interfaces with $ZrO_2(001)O$, the relation between large metal BOP values and large Wsep can also be found. There is a general trend of the Wsep in relation with the surface energy. Interfaces formed from surfaces with large σ present larger Wsep than those containing surfaces with smaller σ. In general surface energies are larger for polar surfaces. If we restrict to ZrO_2, for which we have calculated the largest number of interfaces, and to results from non-stoichiometric slabs the relation is linear.

In addition we consider to study whether plastic reinforcement is obtained in the metallic side, bridging mechanism, by two methods. Both indicates that interfaces formed by non-stoichiometric ceramic materials (ZrO_2, HfO_2, Al_2O_3) are probable to

exhibit plasticity reinforcement, being this reinforcement clearly favorable for the $ZrO_2(100)_O/Cu(001)$ and $ZrO_2(100)_O/Pt(111)$ interfaces, while for stoichiometric ceramics no plasticity is obtained.

Conclusiones

Hemos usado la teoría del funcional de la densidad para realizar una investigación sistemática de superficies e intercaras de óxidos cerámicos con diferentes metales, que nos ha permitido obtener ciertas conclusiones generales sobre su comportamiento atómico:

Las superficies polares de las fases de baja presión de ZrO_2 muestran grandes relajaciones. El patrón de relajación es similar en todas las superficies, y se caracteriza porque la distancia Zr-O más superficial tiende a decrecer mientras que la segunda aumenta. Todas las terminaciones polares exhiben carácter metálico en la estructura electrónica, sin embargo las orientaciones no polares son aislantes. Además los resultados indican que, a pesar de que la estructura cúbica tiende a beneficiarse del aumento de grados de libertad en superficie con respecto al volumen para reconstruir hacia la estructura tetragonal, las restricciones de simetría impuestas por la terminación atómica particular pueden inhibir la reconstrucción.

Un estado fundamental magnético se origina en óxidos iónicos tanto en volumen con la creación de vacantes catiónicas como en superficies polares terminadas en O. El momento magnético reside en los átomos de O con una pérdida de coordinación catiónica, observándose una clara correlación entre la magnitud del momento magnético y la pérdida de la carga iónica del O.

En particular, la adhesión entre ZrO_2 ideal y el Ni es mayor para terminaciones polares de la cerámica. Particularmente para la intercara $ZrO_2(001)/Ni(001)$, la cual corresponde a la celdilla bidimensional (2D) más pequeña, se encuentra buen enlace. Estas orientaciones relativas conducen a tener un sólo tipo de enlace y una fortaleza alta en la interacción cerámica-metal. Las propiedades de adhesión cambian dramáticamente con la presencia de vacantes de O, debido a la tendencia de ZrO_2 de reconstruir localmente hacia fases de más alta estabilidad.

Todas las intercaras estudiadas muestran una serie de propiedades comunes. El trabajo de separación (Wsep) aumenta cuando aumenta la deformación en expansión del metal y se encuentra una correlación entre grandes valores de BOP (bonding overlap population) y de Wsep. Sin embargo, la conclusión más general que se obtiene del estudio es que las intercaras formadas entre el metal y las superficies cerámicas con alta energía superficial presentan mayor Wsep que aquellas superficies que tienen baja energía superficial. En general, las energías superficiales son mayores para superficies no-estequiométricas, las cuales se corresponden con superficies polares, cuya formación requiere de la rotura de fuertes enlaces iónicos anión-catión. Entonces, los Wsep para las intercaras formadas a partir de superficies polares de óxidos no-estequiométricos son sustancialmente mayores que aquellos que corresponden a superficies no-polares de óxidos estequiométricos.

Además de estas conclusiones principales, nuestro estudio puede resumirse en los siguientes resultados:
Los cálculos DFT basados en la aproximación del gradiente generalizado (GGA), para el término de canje y correlación, muestran un gran acuerdo con los resultados experimentales de estructura y propiedades electrónicas de las fases de baja presión de

ZrO$_2$. Reproducimos la jerarquía correcta de energía de las fases de ZrO$_2$. La diferencia de la energía entre fases es muy cercana a la obtenida experimentalmente, especialmente entre la fase monoclínica y la cúbica. Además, los valores calculados del módulo de volumen comparan bien con las tendencias obtenidas previamente mediante cálculos teóricos similares, que indican una reducción del valor según decrece la simetría de la fase.

Las propiedades electrónicas de las tres fases se caracterizan por el carácter aislante e iónico de las bandas. Sin embargo, la ionicidad decrece según decrece la simetría, siendo la fase monoclínica la de menor valor.

En la fase c-ZrO$_2$ con vacantes de O neutrales, un nivel de vacante asociado con los átomos de Zr se crea en el gap del óxido, mientras que en el caso de las vacantes de O asociadas a c-ZrO$_2$ dopada con Y$_2$O$_3$ se mantiene el carácter aislante de la estructura de bandas sin defectos.

Se obtienen transformaciones de fase de c-ZrO$_2$ a partir de la aplicación de una tensión externa. La transformación de cúbica a tetragonal se realiza permitiendo relajar al sistema después de un muy leve desplazamiento de la subred de O a lo largo de la dirección X$_2^-$, caracterizada por un modo suave de fonón. La transformación de cúbica a monoclínica se obtiene aplicando una tensión hidrostática para incrementar el volumen de la celda unidad de la estructura cúbica y subsecuentemente aplicando una tensión de cizalla.

Todas las superficies polares de bajo índice de las fases de baja presión de ZrO$_2$ muestran un patrón de relajación similar. Los planos debajo de aquellos de superficie relajan hacia fuera, reduciendo la primera distancia interplanar Zr-O e incrementando la segunda. Esta alternancia de enlaces cortos y largos decae al aproximarnos hacia el volumen, y en el tercer plano de Zr los enlaces son similares a los de volumen. El efecto más importante de relajación se muestra en las superficies (001) de la fase t-ZrO$_2$, seguido por las superficies cúbicas (111) y finalmente la (001). Tanto la terminación en Zr como en un doble plano de oxigeno (OO) exhiben metalicidad y presentan respectivamente un incremento y una pérdida de carga respecto a la del óxido, estando localizada en los planos exteriores. En el caso de superficies terminadas en un sólo O, la relajación es análoga a la anteriormente descrita aunque el desplazamiento de los planos de O resulta en una alternancia de distancias Zr-O similar a la que se obtiene en la fase tetragonal, definida por el parámetro δ. Además, no hay estados inducidos en el gap y la superficie se mantiene aislante.

En las superficies no polares el efecto de la relajación es pequeño. El resultado más relevante es el desplazamiento de los átomos de Zr, los cuales se mueven alternativamente hacia los planos adyacentes superior e inferior. Estas superficies mantienen el carácter aislante del volumen y son las más estables termodinámicamente.

Cuando se consideran las vacantes de Zr en el volumen de c-ZrO$_2$, se origina un momento magnético en los átomos de O que son primeros vecinos a las vacantes. El momento magnético aumenta con el número de vacantes hasta alcanzar un valor cercano al número de huecos dopados. La presencia de las vacantes implica una relación atómica donde los átomos de O exceden la relación nominal 1:2. Esto se ve reflejado en la reducción local de carga en los átomos de O enlazados con las vacantes, llevando a una relación directa entre la pérdida de carga y la magnitud de los momentos magnéticos.

Para las superficies polares terminadas en OO, la situación de polarización de espín es más favorable que la no polarizada. Los cálculos de polarización de espín de diferentes

superficies iónicas terminadas en planos de O también muestran una correlación entre la magnitud de los momentos y la pérdida de carga con respecto a la de volumen. De esta manera, cuanto mayor es la diferencia entre la carga de los átomos de O en la superficie y la del volumen, mayor será el momento magnético de los O. También, el momento magnético aumenta según se reduce la coordinación con el catión. En general, la distribución del momento magnético es muy anisotrópica, con orientaciones claramente favorables en la normal de la superficie o contenida en el plano, dependiendo de la superficie. La mayoría de las superficies magnéticas presentan half-metallicity.

Las intercaras polares ideales del sistema c-ZrO_2(001)/Ni(001) presentan enlaces metal-cerámica bastante fuertes y con distancias de equilibrio, tanto para Ni-O como para Ni-Zr, menores que la suma de los respectivos radios atómicos. Aparecen estados inducidos por el metal (MIGS) en ambas intercaras. Sin embargo, el carácter de enlace entre el Ni y el Zr surge principalmente debido a la hibridación entre orbitales s-d y d-d, mientras que en la intercara O/Ni hay una transferencia neta de carga desde el Ni al O. Los efectos de la intercara se restringen casi completamente a los planos atómicos en contacto, especialmente en el metal, donde en el segundo plano ya están apantallados.

Los enlaces en la intercara son más largos en el sistema ZrO_2(110)/Ni(001), lo que implica una reducción de la fortaleza de la interacción ZrO_2-Ni. Para esta intercara encontramos que la posición del Ni más estable es con coordinación dos ("bridge") para la intercara Ni/O y cuatro ("hollow") para la Ni/Zr. Obtenemos que la adhesión entre ZrO_2 y Ni ideales se incrementa para orientaciones cerámicas polares, siendo la de la terminación en O de la ZrO_2 mayor que la terminada en Zr.

La estabilidad de la intercara está relacionada con la estequiometría y la polaridad: los slabs cerámicos no estequiométricos son los menos estables, mientras que los más estables son los estequiométricos y no-polares. Identificamos la intercara ZrO_2(110)/Ni(110) como la más estable en el rango de valores intermedios del potencial químico de O (μ_O), mientras que para valores altos de μ_O la intercara terminada en O: ZrO_2(001)$_O$/Ni(001) es la más estable, y para valores bajos es la terminada en Zr. Los cálculos más realistas de la intercara ZrO_2(001)/Ni(001) se han hecho modelando la presencia actual de vacantes de O en el plano de la intercara, tanto vacantes relacionadas con el dopaje con Y_2O_3 como las asociadas a la sinterización en atmósfera reductora, llamadas termodinámicas, mostrando ambas la reducción del número de enlaces en la intercara. Sin embargo, las vacantes termodinámicas inducen en el material cerámico una reestructuración interna que incrementa la interacción por hibridación de Zr-O al tiempo que debilita los enlaces Ni-O de la intercara. Por el contrario, cuando las vacantes de O están relacionadas con el dopaje con Y_2O_3, la presencia de los iones Y^{3+}, más grandes que los Zr^{4+}, inhibe la reconstrucción interna, por lo que la fuerza por enlace en la intercara no se reduce.

Un conjunto de propiedades generales se puede encontrar para una gran variedad de intercaras formadas por varios metales bcc y fcc unidos a los cerámicos α-Al_2O_3, MgO, HfO_2 and ZrO_2. Algunas de estas propiedades que muestran todas las intercaras son el carácter metálico, el rápido decaimiento de los efectos de la intercara, la naturaleza iónica de los enlaces metal-oxígeno, que en todos los casos involucra una pérdida de carga del O respecto al volumen del óxido, y el hecho de que los mayores valores de Wsep correspondan a una transferencia de carga mayor y a una hibridación mayor. En general, las interacciones más fuertes corresponden a las intercaras formadas por Al_2O_3(0001) y ZrO_2(001) con metales de estructura bcc, mientras que los menores se encuentran para MgO unido tanto con metales alcalinos como con metales nobles.

El Wsep se incrementa aumentando la deformación en expansión del metal. Los Wsep para intercaras formadas por superficies de óxidos no-estequiométricos son substancialmente mayores que aquellos que corresponden a superficies estequiométricas. Considerando sólo un tipo de óxido, no-estequiométrico o estequiométrico, el Wsep se aproxima satisfactoriamente a una función lineal de la deformación del metal. Esta deformación implica un acortamiento de la distancia de enlace en el plano del metal que induce un reforzamiento en el enlace de la intercara y un incremento de la cohesión. Considerando intercaras formadas por metales con una banda "d" de valencia y $ZrO_2(001)_O$, obtenemos correspondencia entre grandes valores de BOP del metal y de Wsep de la intercara. Encontramos una relación general del Wsep con la energía superficial: para intercaras formadas a partir de superficies con grandes valores de energía superficial, los valores de Wsep son mayores que en aquellos casos con baja energía superficial. En general, las energías superficiales grandes corresponden a superficies no-estequiométricas, y en casi todos los casos a superficies polares. Si nos restringimos a los resultados de slabs no estequiométricos y a ZrO_2, para la cual hemos calculado el mayor número de intercaras, obtenemos que dicha relación es lineal.

Además estudiamos usando dos métodos distintos los casos en los que el reforzamiento mediante plasticidad se obtiene en el constituyente metálico de las intercaras, llamado reforzamiento por ligamentos resistentes. El resultado indica que las intercaras formadas por materiales cerámicos no-estequiométricos (ZrO_2, HfO_2, Al_2O_3) es probable que exhiban un reforzamiento mecánico por deformación plástica, siendo claramente favorable para las intercaras $ZrO_2(100)_O/Cu(001)$ y $ZrO_2(100)_O/Pt(111)$, mientras que para las cerámicas estequiométricas no se obtiene ningún caso de plasticidad.

APPENDIX :

In chapter 5 it has been discussed the magnetic properties of the t-HfO$_2$ surface calculations performed by VASP code. Additional information of the bulk results for the three low pressure phases is now described.

A.1 t-HfO$_2$(001) bulk environment

Cubic phase calculation has been performed from its primitive cell and 12x12x12 Mohrhorst K points sampling, while the others were calculated from four formula units cell and 6x6x6 K mesh. Results for the lattice parameters and bulk modulus for each phase have been compared with experimental and previously reported theoretical studies, and are summarized in table A.1. Our energetic and lattice parameter values, given in eV and in Å respectively, compares well with experimental and other theoretical works, showing the known overestimation of structural parameter by means of GGA approximation. Concerning bulk modulus (B$_0$), our results can not be quantitatively compared with experimental ones due to the fact that we do not consider dopants in the high temperature phases, tetragonal and cubic. We obtain higher B$_0$ values going from monoclinic to tetragonal and then to cubic, which agrees well with previous results [109].

	Our PBE	Experimental	PW 91 TM	GGA	LDA
Monoclinic		[234]	[164]	[108]	[109]
Volume(Å^3)	35,13	34,62	33,16	36,39	
a	5,15	5,12	5,04	5,22	5,12
b	5,19	5,17	5,11	5,29	5,17
c	5,33	5,30	5,22	5,35	5,29
β	99,69	99,18	99,77	99,73	
B$_0$(GPa)	238	185		192	251
Tetragonal		[233]			
Volume(Å^3)	33,72	35,08	32,47	34,82	
a	3,59	3,64	3,53	3,66	
c	5,23	5,29	5,23	5,22	
δ(in c units)	0,06		0,05	0,03	
E$_{TET}$-E$_{MON}$ (eV)	0,16		0,20		
B$_0$(GPa)	244			183	
Cubic		[232]			
Volume(Å^3)	32,71	32,77	31,16	34,10	
a	5,08	5,08	5,00	5,15	5,14
B$_0$(GPa)	258			257	280
E$_{CUB}$-E$_{TET}$(eV)	0,10		0,11		

Table A.1: Structural, energetic parameters and bulk modulus (B$_0$) values of the three low pressure phases of HfO$_2$ are presented for our calculations, previous theoretical [108, 109, 164] and experimental measures [232-234].

Some important point to notice in terms of structural parameters is the appearance of a "δ" value in bulk t-HfO$_2$, that corresponds to an O sublattice distortion related to a soft mode of vibration [121] observed experimentally in the similar t-ZrO$_2$ system but not in t-HfO$_2$ one.

References

1   http://www.kmm-noe.org/DesktopDefault.aspx?tabindex=75&tabid=219

2   S. Roberts and R. J. Gorte, *A study of platinum films on zirconia(100).* J. Phys.
      Chem., 1991. **95**: p. 5600.

3   H. Kim, C. O. Chui, K. C. Saraswat and S. Stemmer, *Engineering chemically
      abrupt high-k metal oxide/s silicon interfaces using an oxygen-gettering metal
      overlayer.* J. Appl. Phys., 2004. **96**(6): p. 3467.

4   D. J. Siegel, *First principles study of metal-ceramic interfaces.* Thesis, 2001.

5   L. L. Mishnaevsky and J. D. Gross, *Micromechanisms and mechanics of
      damage and fracture in thin film/substrate systems.* International Appl. Mech.,
      2004. **40**(2): p. 140.

6   Y. F. Zhukovskii, E. A. Kotomin, P. W. M. Jacobs and A. M. Stoneham, *Ab
      initio modeling of metal adhesion of oxide surfaces with defects.* Phys. Rev.
      Lett., 1999. **84**(6): p. 1256.

7   F. F. Abraham, *How fast can cracks move? A research adventure in materials
      failure using millions of atoms and big computers.* Advances in Phys., 2003.
      52(8): p. 727.

8   S. B. Sinnott and E. C. Dickey, *Ceramic/metal interface structures and their
      relationship to atomic- and meso-scale properties.* Mater. Sci. Eng., R, 2003.
      43: p. 1.

9   M. W. Finnis, *The theory of metal-ceramic interfaces.* J. Phys.: Condens. Matter,
      1996. **8**: p. 5811.

10   J.-G. Li, *Wetting and interfacial bonding of metals with ionocovalent oxides.* J.
      Am. Ceram. Soc., 1992. **75**(11): p. 3118.

11   M. Lane, *Interface fracture.* Annu. Rev. Mater. Res., 2003. **33**: p. 29.

12   A. G. Evans and B. J. Dalgleish, *The fracture resistance of metal-ceramic
      interfaces.* Mater. Sci. Eng., A, 1993. **A162**(1): p. 1.

13   B. Lawn, *Fracture of Brittle Solids.* ed. C. U. Press. 1993, Cambridge.

14   J. Knap and K. Sieradzki, *Crack tip dislocation nucleation in FCC solids.* Phys.
      Rev. Lett., 1998. **82**(8): p. 1700.

15   J. Raynolds, J. R. Smith, G.-L. Zhao and D. J. Srolovitz, *Adhesion in NiAl-Cr
      from first principles.* Phys. Rev. B, 1996. **53**(20): p. 13883.

16   J. M. Howe, *Bonding, structure, and properties of metal/ceramic interfaces:
      Part1 Chemical bonding, chemical reaction, and interface structure.* Int. Mater.
      Rev., 1993. **38**(5): p. 233.

17   J. M. Howe, *Bonding, structure, and properties of metal/ceramic interfaces:
      Part 2 Interface fracture behaviour and property measurement.* Int. Mater. Rev.,
      1993. **38**(5): p. 257.

18   J.-G. Li, *Energetics of metal/ceramic interfaces, metal-semiconductor Schottky
      contacts, and their relationship.* Mater. Chem. Phys., 1997. **47**: p. 126.

19   M. C. Muñoz, S. Gallego, J. I. Beltrán and J. Cerdá, *Adhesion at metal-ZrO2
      interfaces.* Surf. Sci. Rep., 2006. **61**: p. 303.

20   R. Benedek, D. N. Seidman, L. H. Yang, D. A. Muller and C. Woodward, *First
      principles simulation of a ceramic/metal interface with misfit.* Phys. Rev. Lett.,
      1999. **84**(15): p. 3362.

21   C. Verdozzi, D. R. Jennison, P. A. Schultz and M. P. Sears, *Saphire (0001) Surface, clean and with d-metal overlayers.* Phys. Rev. Lett., 1999. **82**(4): p. 799.

22   J. Mayer, C. P. Flynn and M. Rühle, *High-resolution electron microscopy studies of Nb/Al2O3 interfaces.* Ultramicroscopy, 1990. **33**(1): p. 51.

23   W. Mader and M. Rühle, Acta Mater., 1989. **37**(3): p. 853.

24   J. Bruley, C. P. Flynn and M. Rühle, *Investigations of the Chem. and bonding at niobium-sapphire interfaces.* J. Mater. Res., 1994. **9**: p. 2574.

25   D. Knauss and W. Mader, *Chemical composition and lattice relaxations at diffusion-bonded Nb/Al2O3 interfaces.* Ultramicroscopy, 1991. **37**: p. 247.

26   E. C. Dickey, V. P. Dravid, P. Nellist, D. J. Wallis, S. J. Pennycook and A. Revcolevschi, *Structure and bonding at Ni-ZrO2(cubic) interfaces formed by the reduction of a NiO-ZrO2 (cubic) composite.* Microsc. Microanal., 1997. **3**: p. 443.

27   E. C. Dickey, Y. M. Bagiyono, G. D. Lian, S. B. Sinnott and T. Wagner, *Preferred crystallographic orientations relationships of nickel films deposited on (100) cubic-zirconia substrates.* Thin Solid Films, 2000. **372**(1-2): p. 37.

28   R. W. Balluti, A. Brokman and A. H. King, *CSL/DSC lattice model for general crystal-crystal boundaries and their line defects.* Acta Metall., 1982. **30**: p. 1453.

29   C. Pecharromán, J. I. Beltrán, F. Esteban-Betegón, S. López-Esteban, J. F. Bartolomé, M. C. Muñoz and J. S. Moya, *Zirconia /nickel interfaces in micro- and nanocomposites.* Zeitschrift für Metallkunde, 2005. **96**: p. 5.

30   C. Pecharromán, F. Esteban, J. F. Bartolomé, G. Richter and J. S. Moya, *Theoretical model of hardening in Zirconia-Nickel nanoparticle composites.* Nano Lett., 2004. **4**(4): p. 747.

31   M. A. Laguna-Bercero, Á. Larrea, R. I. Merino, J. I. Peña and V. M. Orera, *Stability of Channeled Ni-YSZ Cermets Produced from Self-Assembled NiO-YSZ Directionally Solidified Eutectics.* J. Am. Ceram. Soc., 2005. **88**(11): p. 3215.

32   A. I. Gubanov and S. M. Dunaevskii, Sov. Phys.-Solid State, 1977. **19**: p. 795.

33   C. Li, R. Fu, A. J. Freeman and C. L. Fu, *Energetics, bonding mechanism, and electronic structure of metal-ceramic interfaces: Ag/MgO(001).* Phys. Rev. B, 1993. **48**(11): p. 8317.

34   U. Schönberger, O. K. Andersen and M. Methfessel, *Bonding at metal-ceramic interfaces; ab initio density-functional calculations for Ti and Ag on MgO.* Acta Metall. Mater., 1992. **40**: p. 1.

35   J. Goniakowski and C. Noguera, *Microscopic mechanisms of stabilization of polar oxide surfaces: Transition metals on the MgO(111) surface.* Phys. Rev. B, 2002. **66**: p. 085417.

36   C. Kruse, M. W. Finnis, V. Y. Milman, M. C. Payne, A. DeVita and M. J. Gillan, *First-Principles Calculations for Niobium Atoms on a Sapphire Surface.* J. Am. Ceram. Soc., 1994. **77**(2): p. 431.

37   I. G. Batyrev, A. Alavi and M. W. Finnis, *Equilibrium and adhesion of Nb/sapphire: The effect of oxygen partial pressure.* Phys. Rev. B, 2000. **62**(7): p. 4698.

38   W. Zhang and J. R. Smith, *Nonstoichiometric interfaces and Al2O3 adhesion with Al and Ag.* Phys. Rev. Lett., 2000. **85**(15): p. 3225.

39   X.-G. Wang, J. R. Smith and A. Evans, *Fundamental influence of C on adhesion of the Al2O3/Al interface.* Phys. Rev. Lett., 2002. **89**(28): p. 286102.

40   W. Zhang, J. R. Smith and A. G. Evans, *The connection between ab initio calculations and interface adhesion measurements on metal/oxide systems: Ni/Al2O3 and Cu/Al2O3.* Acta Mater., 2002. **50**: p. 3803.

41   A. Christensen and E. A. Carter, *Adhesion of ultrathin ZrO2(111) films on Ni(111) from first principles.* J. Chem. Phys., 2001. **114**(13): p. 5816.

42   A. Eichler, *Modeling oxide-metal interfaces from density functional theory: Platinum adsorption on tetragonal zirconia.* Phys. Rev. B, 2003. **68**: p. 205408.

43   M. Alfredsson and C. R. A. Catlow, *A comparison between metal supported c-ZrO2 and CeO2.* Phys. Chem. Chem. Phys., 2002. **4**: p. 6100.

44   M. Alfredson and C. R. A. Catlow, *Predicting the metal growth mode and wetting of noble metals supported on c-ZrO2.* Surf. Sci., 2004. **561**: p. 43.

45   C. Jung, H. Tsuboi, M. Koyama, M. Kubo, E. Broclawik and A. Miyamoto, *Different support effect of M/ZrO2 and M/CeO2 (M=Pd and Pt) catalysts on CO adsorption: A periodic density functional study.* Catal. Today, 2006. **111**(3-4): p. 322.

46   C. Jung, Y. Ito, A. Endou, M. Kubo, A. Imamura, P. Selvam and A. Miyamoto, *Quantum-chemical study on the supported precious metal catalyst.* Catal. Today, 2003. **87**(1-4): p. 43.

47   X. Han, Y. Zhang and H. Xu, *First-principles calculation on adhesion of Ni/Al2O3 and Ni/ZrO2 interfaces.* Chem. Phys. Lett., 2003. **378**: p. 269.

48   P. Hohenberg and W. Kohn, *Inhomogeneus electron gas.* Phys. Rev., 1964. **136**(3B): p. B864.

49   http://en.wikipedia.org/wiki/Density_functional_theory

50   C. Cohen-Tannoudji, B. Diu and F. Laloe, *Quantum Mechanics.* ed. Wiley-VCH. 1976.

51   M. Born and R. Oppenheimer, *Quantum theory of the molecules.* Ann. Physik., 1927. **84**: p. 457.

52   W. Koch and M. C. Holthausen, *A Chemist's Guide to Density Functional Theory.* ed. W. Wiley-VCH. 2001.

53   W. Kohn and J. Sham, *Self-consistent equations including exchange and correlation effects.* Phys. Rev., 1965. **140**(4A): p. A1133.

54   J. P. Perdew and A. Zunger, *Self-interaction correction to density-functional approximations for many-electron systems.* Phys. Rev. B, 1980. **23**(10): p. 5048.

55   D. M. Ceperley and B. J. Alder, *Ground state of the electron gas by a stochastic method.* Phys. Rev. Lett., 1980. **45**: p. 566.

56   A. D. Becke, *Density functional calculations of molecular bond energies,.* J. Chem. Phys., 1986. **84**: p. 4524.

57   J. P. Perdew, *Density-functional approximation for the correlation energy of the inhomogeneous electron gas.* Phys. Rev. B, 1986. **33**(12): p. 8822.

58   J. P. Perdew and Y. Wang, *Accurate and simple density funcional for the electronic exchange energy: Generalized gradient approximation.* Phys. Rev. B, 1986. **33**(12): p. 8800.

59   J. P. Perdew, K. Burke and M. Ernzerhof, *Generalized gradient approximation made simple.* Phys. Rev. Lett., 1996. **77**(18): p. 3865.

60   J. P. Perdew, K. Burke and Y. Wang, *Generalized gradient approximation for the exchange-correlation hole of a many-electron system.* Phys. Rev. B, 1996. **54**(23): p. 16533.

61   J. P. Perdew, K. Burke and M. Ernzerhof, *Local and gradient-corrected density functionals.* Chemical Applications of Density-Functional Theory, 1996. **629**: p. 453.

62   K. Burke, J. P. Perdew and M. Ernhof, *Why semilocal functional work: accuracy of the on-top pair density and importance of system averaging.* J. Chem. Phys., 1998. **109**(10): p. 3760.

63   J. P. Perdew and K. Burke, *Comparison shopping for a gradient-corrected density functional.* Int. J. Quantum Chem, 1996. **57**: p. 309.

64   A. D. Becke, *Density-functional thermochemistry. III. The role of exact exchange.* J. Chem. Phys., 1993. **98**: p. 5648.

65   C. Lee, W. Yang and R. G. Parr, *Development of the Colle-Salvetti correlation-energy formula into a functional of the electron density.* Phys. Rev. B, 1988. **37**: p. 785.

66   P. J. Stephens, F. J. Devlin, C. F. Chabalowski and M. J. Frisch, *Ab Initio Calculation of Vibrational Absorption and Circular Dichroism Spectra Using Density Functional Force Fields.* J. Phys. Chem., 1994. **98**(45): p. 11623.

67   H. Chermette, *Density functional theory – A powerful tool for theoretical studies in coordination Chem.* Coord. Chem. Rev., 1998. **178**: p. 699.

68   P. Pulay, *Ab initio calculation of force constants and equilibrium geometries in polyatomic molecules. I. Theory.* Mol. Phys., 1969. **17**(2): p. 197.

69   J. M. Soler, E. Artacho, J. D. Gale, A. García, J. Junquera, P. Ordejón and D. Sánchez-Portal, *The SIESTA method for ab initio order-N materials simulation.* J. Phys.: Condens. Matter, 2002. **14**(11): p. 2745.

70   H. Hellmann, *Einfuhrung in die Quantumchemie*, Deuticke. Leipzig(1937).

71   R. P. Feynmann, *Forces in molecules.* Phys. Rev. B, 1939. **56**: p. 340.

72   M. C. Payne, M. P. Teter, D. C. Allan, T. A. Arias and J. D. Joannopoulos, *Iterative minimization techniques for ab initio total-energy calculations: molecular dynamics and conjugate gradients.* Review of Modern Physics, 1992. **64**(4): p. 1045.

73   N. W. Ashcroft and N. D. Mermin, *Solid State Physics.* ed. Saunders. 1976.

74   H. J. Monkhorst and J. D. Pack, *Special points for brillouin-zone integrations.* Phys. Rev. B, 1976. **13**: p. 5188.

75   P. E. Blöchl, O. Jepsen and O. K. Andersen, *Improved tetrahedron method for brillouin-zone integrations.* Phys. Rev. B, 1994. **49**: p. 16223.

76   S. F. Boys, *Electronic wave functions I. A general method for calculation of the stationary states or any molecular system.* Proceedings Royal Society London, 1950. **A200**: p. 542.

77   J. C. Slater, *Atomic shielding constants.* Phys. Rev., 1930. **36**: p. 57.

78   J. C. Slater, *Note on Hartree's method.* Phys. Rev., 1930. **35**: p. 210.

79   J. Simons, *An experimental chemist's guide to ab initio quantum Chem.* J. Phys. Chem., 1991. **95**: p. 1017.

80   D. R. Hamman, M. Schlüter and C. Chiang, *Norm-conseving pseudopotentials.* Phys. Rev. Lett., 1979. **43**(20): p. 1494.

81   A. R. Leach, *Molecular Modelling: Principles and applications.* ed. L. 2ed Prentice Hall, Harlow. 2000, London.

82   D. Porezag, M. R. Pederson and A. Y. Liu, *The accuracy of the pseudopotential approximation within density functional theory.* Phys. Status Solidi B, 2000. **217**: p. 219.

83   N. Troullier and J. L. Martins, *Efficient pseudopotentials for plane-wave calculations.* Phys. Rev. B, 1991. **43**(3): p. 1993.

84   D. Vanderbilt, *Soft self-consistent pseudopotentials in a generalized eigenvalue formalism.* Phys. Rev. B, 1990. **41**: p. 7892.

85   P. E. Blöchl, *Projector augmented-wave method.* Phys. Rev. B, 1994. **50**(24): p. 17953.

86   G. Kresse and D. Joubert, *From ultrasoft pseudopotentials to the projector augmented-wave method.* Phys. Rev. B, 1999. **59**: p. 1758.

87   G. B. Bachelet, D. R. Hamann and M. Schlüter, *Pseudopotentials that work: from H to Pu.* Phys. Rev. B, 1982. **26**(8): p. 4199.

88   L. Kleinman and D. M. Bylander, *Efficacious form for model pseudopotentials.* Phys. Rev. Lett., 1982. **48**(20): p. 1425.

89   J. Furthmuller, P. Kackell and F. Bechstedt, *Extreme softening of Vanderbilt pseudopotentials: General rules and case studies of first-row and d-electron elements.* Phys. Rev. B, 2000. **61**(7): p. 4567.

90   http://www.uam.es/departamentos/ciencias/fismateriac/siesta/

91   http://cms.mpi.univie.ac.at/vasp/vasp/vasp.html

92   E. Polak, *Computational Methods in Optimization.* ed. A. Press. 1971, New York.

93   P. Pulay, *Convergence acceleration of iterative sequences: the case of scd interation.* Chem. Phys. Lett., 1980. **73**: p. 393.

94   D. D. Johnson, *Modified broyden's method for accelerating convergence in self-consistent calculations.* Phys. Rev. B, 1988. **38**: p. 12807.

95   E. Artacho, D. S. Portal, P. Ordejón, A. García and J. M. Soler, *Linear-scaling ab-initio calculations for large and complex systems.* Phys. Status Solidi B, 1999. **215**: p. 809.

96   T. L. Beck, *Real-space mesh techniques in density-functional theory.* Review of Modern Physics, 2000. **72**(4): p. 1041.

97   R. Hoffmann, *Solids and Surfaces: A Chemist's View of Bonding in Extended Structures.* ed. W. VCH. 1988.

98   R. Hoffmann, *Chemical and theoretical way to look at bonding on surfaces.* Review of Modern Physics, 1988. **60**(3): p. 601.

99   N. E. Christensen, S. Satpathy and Z. Pawlowska, *Bonding and ionicity in semiconductors.* Phys. Rev. B, 1986. **36**(2): p. 1032.

100   F. D. Murnaghan, *The Compressibility of Media under Extreme Pressures.* Proceedings of the National Academy of Sciences of the United States of America, 1944. **30**(9): p. 244.

101   http://en.wikipedia.org/wiki/Birch-Murnaghan_equation_of_state

102   K. Reuter and M. Scheffler, *Composition, structure, and stability of RuO2(110) as a function of oxygen pressure.* Phys. Rev. B, 2001. **65**: p. 035406.

103   D. M. Lipkin, D. R. Clarke and A. G. Evans, *Effect of interfacial carbon on adhesion and toughness of gold-sapphire interfaces.* Acta Mater., 1998. **46**: p. 4835.

104   M. D. Kriese, N. R. Moody and W. W. Gerberich, *Effects of annealing and interlayers on the adhesion energy of copper thin films to SiO2/Si substrates.* Acta Mater., 1998. **46**: p. 6311.

105   http://216.239.59.104/search?q=cache:wnK7zXtPmjQJ:www.matsceng.ohio-state.edu/mse205/lectures/chapter13/chap13.pdf+bonding+character+ceramic&hl=en&ct=clnk&cd=2

106   http://www.ferroceramic.com/

107   http://www.ferroceramic.com/alumina_99_table.htm

108   J. Kang, E.-C. Lee and K. J. Chang, *First principles study of the structural phase transformation of hafnia under pressure.* Phys. Rev. B, 2003. **68**: p. 054106.

109   J. E. Lowther, J. K. Dewhurst, J. M. Leger and J. Haines, *Relative stability of ZrO2 and HfO2 structural phases.* Phys. Rev. B, 1999. **60**(21): p. 14485.

110   S. Somiya, N. Yamamoto and H. Yanagida, *Science and technology of Zirconia III.* ed. E. Advances in ceramics Vol 24, The American Ceramic Society, U.S.A. (1986). 1986, Westerville, Ohio.

111   R. H. French, S. J. Glass, F. S. Ohuchi, Y. N. Xu and W. Y. Ching, *Experimental and theoretical determination of the electronic structure and optical properties of three phases of ZrO2.* Phys. Rev. B, 1993. **49**(8): p. 5133.

112   F. Parmigiani, L. E. Depero, L. Sangaletti and G. Samoggia, *An XPS study of yttria-stabilized zirconia single crystals.* J. Electron. Spectrosc. Relat. Phenom., 1993. **63**: p. 1.

113   N. Sawaguchi and H. Ogawa, *Simulated diffusion of oxide ions in YO1.5-ZrO2 at high temperature.* Solid State Ionics, 2000. **128**: p. 183.

114   M. O. Zacate, L. Minervini, D. J. Bradfield, R. W. Grimes and K. E. Sickafus, *Defect cluster formation in M2O3-doped cubic ZrO2.* Solid State Ionics, 2000. **128**(1-4).

115   J. E. Jaffe, R. A. Bachorz and M. Gutowski, *Low temperature polymorphs of ZrO2 and HfO2: A density-functional theory study.* Phys. Rev. B, 2005. **72**(14): p. 144107.

116   http://www.nsc.liu.se/projects/activeprojects/project_2006040.html

117   K. Wefers and C. Misra, *Oxides and Hydroxides of Aluminum.* ed. A. Laboratories. 1987.

118   http://www.azom.com/details.asp?ArticleID=54

119   W. G. Wyckoff, *Crystal structures.* ed. K. vol. 1-3, Malabar, 2nd ed. 1982.

120   S. Fabris, A. T. Paxon and M. W. Finnis, *Free energy and molecular dynamics calculations for the cubic-tetragonal phase transition in zirconia.* Phys. Rev. B, 2001. **63**: p. 094101.

121   K. Parlinski, Z. Q. Li and Y. Kawazoe, *First-Principles Determination of the Soft Mode in Cubic ZrO2.* Phys. Rev. Lett., 1997. **78**: p. 4063.

122   J. J. Fernández, C. Tablero and P. Wahnón, *Application of the exact exchange potential method for half metallic intermediate band alloy semiconductor.* J. Chem. Phys., 2004. **120**: p. 10780.

123   P. Aldebert and J. P. Traverse, *Structure and Ionic Mobility of Zirconia at High-Temperature.* Journal of the American Ceramic Society, 1985. **68**(1): p. 34.

124   C. J. Howard, R. J. Hill and B. E. Reichert, *Structures of ZrO2 polymorphs at room temperature by high-resolution neutron powder diffraction.* Acta Crystallogr., Sect. B: Struct. Sci, 1988. **B44**: p. 116.

125   R. J. Ackermann, E. G. Rauh and C. A. Alexander, *Thermodynamic Properties of Zro2(G).* High Temperature Science, 1975. **7**(4): p. 304.

126   E. V. Stephanovich and A. L. Shluger, *Theoretical study of the stabilization of cubic-phase ZrO2 by impurities.* Phys. Rev. B, 1993. **49**(17): p. 11560.

127   L. K. Dash, N. Vast, P. Baranek, M.-C. Cheynet and L. Reining, *Electronic structure and electron energy-loss spectroscopy of ZrO2.* Phys. Rev. B, 2004. **70**(24): p. 245116.

128   A. S. Foster, V. B. Sulimov, F. L. Gejo, A. L. Shluger and R. M. Nieminen, *Structure and electrical levels of point defects in monoclinic zirconia.* Phys. Rev. B, 2001. **64**(22): p. 224108.

129   G. Jomard, T. Petit, A. Pasturel and L. Magaud, *First-principles calculations to describe zirconia pseudopolymorphs.* Phys. Rev. B, 1998. **59**(6): p. 4044.

130   S. Fabris, A. T. Paxon and M. W. Finnis, *Relative energetics and structural properties of zirconia using a self-consistent tight-binding model.* Phys. Rev. B, 1999. **61**(10): p. 6617.

131   R. P. Ingel and D. Lewis, *Elastic-Anisotropy in Zirconia Single-Crystals.* Journal of the American Ceramic Society, 1988. **71**(4): p. 265.

132   M. Fukuhara and I. Yamauchi, *Temperature dependence of the elastic moduli, dilational and shear internal frictions and acoustic wave velocity for alumina, (Y)TZP and β'-sialon ceramics.* J. Mater. Sci., 1993. **28**(17): p. 4681.

133   X. J. Kong, C. T. Chan, K. M. Ho and Y. Y. Ye, *Cohesive properties of crystalline solids by the generalized gradient approximation.* Phys. Rev. B, 1990. **42**(15): p. 9357.

134   R. Orlando, C. Pisani, C. Roetti and E. Stefanovich, *Ab initio Hartree-Fock study of tetragonal and cubic phases of zirconium dioxida.* Phys. Rev. B, 1991. **45**(2): p. 592.

135   L. Soriano, M. Abbate, J. Faber, C. Morant and J. M. Sanz, *The electronic structure of ZrO2: Band structure calculations compared to electron and x-ray spectra.* Solid State Commun., 1995. **93**(8): p. 659.

136   B. Králik, E. K. Chang and S. G. Louie, *Structural properties and quasiparticle band structure of zirconia.* Physical Review B, 1998. **57**(12): p. 7027.

137   W. Z. Zhu and M. Yan, *Stability of tetragonal phase in ZrO2 (2 mol % Y2O3) ceramics sintered in reducing atmosphere.* J. Mater. Sci. Lett., 1997. **16**(19): p. 1540.

138   M. Ohta, K. Kirimoto, K. Nobugai, J. K. Wigmore and T. Miyasato, Japan J. Appl. Phys. Part 1, 2001. **40**: p. 5377.

139   D. Steele and B. E. F. Fender, *The structure of cubic ZrO2:YO1.5 solid solutions by neutron scattering.* Journal of Physics C: Solid State Physics, 1974. **7**: p. 1.

140   W. L. Roth, R. Wong, A. I. Goldman, E. Canova, Y. H. Kao and B. Dunn, *Structure of additives in β''-alumina and zirconia superionic conductors.* Solid State Ionics, 1986. **18**(2): p. 1115.

141   M. H. Tuilier, J. Dexpert-Ghys, H. Dexpert and P. Lagarde, *X-ray absorption study of the ZrO2-Y2O3 system.* J. Solid State Chem., 1987. **69**(1): p. 153.

142   H. Morikawa, Y. Shimizugawa, F. Marumo, T. Harasawa, H. Ikawa, K. Tohji and Y. Udagawa, J. Ceram. Soc. Jpn, 1988. **96**: p. 253.

143   Z. J. Shen, T. K. Li, K. Q. Lu and Y. Q. Zhao, *An EXAFS study of yttria-stabilized zirconia.* Guisuanyan Xuebao, 1988. **16**(3): p. 270.

144   X. Li and B. Hafskjold, J. Phys.: Condens. Matter, 1995. **7**: p. 1255.

145   C. R. A. Catlow, A. V. Chadwick, G. N. Greaves and L. M. Moroney, *EXAFS study of yttria-stabilized zirconia.* J. Am. Ceram. Soc., 1986. **69**(3): p. 272.

146   M. Cole, C. R. A. Catlow and J. P. Dragun, J. Phys. Chem. Solids, 1990. **51**: p. 507.

147   F. Shimojo, T. Okabe, F. Tachibana, M. Kobayashi and H. Okazaki, J. Phys. Soc. Jpn, 1992. **61**: p. 2848.

148   P. L. I. W. Chen and J. E. Penner-Hahn, *X-ray-absorption studies of zirconia polymorphs. I. Characteristic local structures.* Phys. Rev. B, 1993. **48**(14): p. 10063.

149   P. L. I. W. Chen and J. E. Penner-Hahn, *Effect of Dopants on Zirconia Stabilization—An X-ray Absorption Study: I, Trivalent Dopants.* J. Am. Ceram. Soc., 1994. **77**(1): p. 118.

150   J. P. Goff, W. Hayes, S. Hull, M. T. Hutchings and K. N. Clausen, Phys. Rev. B, 1999. **59**: p. 14202.

151   G. Stapper, M. Bernasconi, N. Nicoloso and M. Parrinello, *Ab initio study of structural and electronic properties of yttia-stabilized cubic zirconia.* Phys. Rev. B, 1998. **59**(2): p. 797.

152   A. Eichler, *Tetragonal Y-doped zirconia: structure and ion conductivity.* Phys. Rev. B, 2001. **64**: p. 174103.

153   A. Bogicevic and C. Wolverton, *Nature and strength.* Phys. Rev. B, 2003. **67**: p. 024106.

154   L. Pauling and S. B. Hendricks, J. Am. Ceram. Soc., 1925. **47**: p. 781.

155   W. H. Bragg and W. L. Bragg, *X-Rays and Crystal Structure.* ed. l. G. Bell & Sons. 1916, London.

156   H. d'Amour, D. Schiferl, W. Denner, H. Schulz and W. B. Holzapfel, *High-pressure single-crystal structure determinations for ruby up to 90 kbar using an automatic diffractometer.* J. Appl. Phys., 1978. **49**(8): p. 4411.

157   A. Stierle, F. Renner, R. Streitel, H. Dosch, W. Drube and B. C. Cowie, *X-ray Diffraction Study of the Ultrathin Al2O3 Layer on NiAl(110).* Science, 2004. **303**(5664): p. 1652.

158   A. S. Rao and R. T. Keamey, *Logarithmic derivative reflectance spectra of BaO and SrO.* Phys. Status Solidi B, 1979. **95**(1): p. 243.

159   V. Fiorentini and G. Gulleri, *Theoretical evaluation of zirconia and hafnia as gate oxides for Si microelectronics.* Phys. Rev. Lett., 2002. **89**(26): p. 266101.

160   A. A. Demkov, L. R. C. Fonseca, E. Verret, J. Tomfohr and O. F. Sankey, *Complex band structure and the band alignment problem at the Si–high-k dielectric interface.* Phys. Rev. B, 2005. **71**: p. 195306.

161   W. Y. Ching and Y.-N. Xu, *First principles calculation of electronic, optical, and structural properties of alpha-Al2O3.* J. Am. Ceram. Soc., 1994. **77**: p. 404.

162   V. N. Staverov and G. E. Scuseria, *Test of a ladder of density functionals for bulk solids and surfaces.* Phys. Rev. B, 2004. **69**: p. 075102.

163   A. R. Oganov and P. I. Dorogokupets, *All electron and pseudopotential study of MgO: Equation of state, anharmonicity, and stability.* Phys. Rev. B, 2003. **67**: p. 224110.

164   I. M. Iskandarova, A. A. Knizhnik, E. A. Rykova, A. A. Bagatur'yants, B. V. Potapkin and A. A. Korkin, *First principle investigation of the hydroxylation of zirconia and hafnia surfaces.* Microelectron. Eng., 2003. **69**(2-4): p. 587.

165   P. Richet, J. Xu and H. K. Mao, *Quasi-hydrostatic compression of ruby to 500 kbar.* Phys. Chem. Minerals, 1988. **16**(3): p. 207.

166   http://www.chemsoc.org/visElements/pages/data/intro_groupi_data.html

167   http://en.wikipedia.org/wiki/Transition_metal

168   I. M. L. Billas, A. Chatelain and W. A. d. Heer, *Magnetism from the atom to the bulk in iron, cobalt , and nickel clusters.* Science, 1994. **265**: p. 1682.

169   http://en.wikipedia.org/wiki/Nonmetal

170   E. Wachowicz and A. Kiejna, *Bulk and surface properties of hexagonal-close-packed Be and Mg.* J. Phys.: Condens. Matter, 2001. **13**: p. 10767.

171   J. H. Cho and M. Scheffler, *Ab initio pseudopotential studo of Fe, Co and Ni employing the spin-polarized LAPW approach.* Phys. Rev. B, 1996. **53**: p. 10685.

172   J. C. Bailor, H. J. Emeleus, R. S. Nyholm and A. F. Trotman-Dickenson, *Comprehensive inorganic chemistry.* ed. Pergamon. 1974.

173   F. Willaime, *Ab initio study of self-interstitials in hcp-Zr.* J. Nuclear Mater., 2003. **323**: p. 205.

174 S. Curtarolo, D. Morgan and G. Ceder, *Accuracy of ab initio methods in predicting the crystal structures of metals: A review of 80 binary alloys.* Calphad, 2005. **29**: p. 163.

175 A. S. Foster, F. L. Gejo, A. L. Shluger and R. M. Nieminen, *Vacancy and interstitial defects in hafnia.* Phys. Rev. B, 2002. **65**: p. 174117.

176 http://www.webelements.com/

177 J. Malcolm W. Chase, *NIST-JANAF Thermochemical Tables.* ed. J. P. C. R. D. Fourth Edition, Monograph 9. 1998.

178 A. Eichler and G. Kresse, *First-principles calculations for the surface termination of pure and yttria-doped zirconia surfaces.* Phys. Rev. B, 2004. **69**: p. 045402.

179 T. Nishimura, H. Toi, Y. Hoshino, E. Toyoda and Y. Kido, *Surface structure of Y2O3(9.5 mol %)-stabilized ZrO2(001) determined by high-resolution medium-energy ion scattering.* Phys. Rev. B, 2001. **64**: p. 073404.

180 S. Mahieu, P. Ghekiere, G. D. Winter, S. Heirwegh, D. Depla, R. D. Gryse, O. I. Ledebev and G. V. Tendeloo, *Mechanism of preferential orientation in sputter deposited titanium nitride and yttria-stabilized zirconia layers.* J. Cryst. Growth, 2005. **279**: p. 100.

181 C. Morterra, G. Cerrato, L. Ferroni and L. Montanaro, *Surface characterization of yttria-stabilized tetragonal ZrO2 Part 1. Structural, morphological, and surface hydration features.* Mater. Chem. Phys., 1994. **37**: p. 243.

182 C. Morterra, G. Cerrato, L. Ferroni, A. Negro and L. Montanaro, *Surface characterization of tetragonal ZrO2.* Appl. Surf. Sci., 1993. **65**: p. 257.

183 G. Cerrato, S. Bordiga, S. Barbera and C. Morterra, Surf. Sci., 1997. **377**: p. 50.

184 L. E. Depero, R. Bertoncello, T. Boni, P. Levrangi, I. N. Sora, E. Tempesti and F. Parmigiani, J. Mater. Res., 1997. **12**: p. 1376.

185 A. Christensen and E. A. Carter, *First-principles study of the surfaces of zirconia.* Phys. Rev. B, 1998. **58**(12): p. 8050.

186 G. Ballabio, M. Bernasconi, F. Pietrucci and S. Serra, *Ab initio study of yttria-stabilized cubic zirconia surfaces.* Phys. Rev. B, 2004. **70**: p. 075417.

187 S. Gennard, F. Corà and R. A. Catlow, *Comparison of the bulk and surface properties of ceria and zirconia by ab initio investigations.* J. Phys. Chem., 1999. **103**: p. 10158.

188 R. Orlando, C. Pisani, E. Ruiz and P. Sautet, *Ab initio study of the bare and hydrated (001) surface of tetragonal zirconia.* Surf. Sci., 1992. **275**: p. 482.

189 P. W. Tasker, *The stability of ionic crystal surfaces.* Journal of Physics C: Solid State Physics, 1979. **12**: p. 4977.

190 M. I. Osendi, J. S. Moya, C. J. Serna and J. Soria, *Metastability of tetragonal zirconia powders.* J. Am. Ceram. Soc., 1985. **68**(3): p. 135.

191 S. Shukla and S. Seal, *Mechanisms of room temperature metastable tetragonal phase stabilisation in zirconia.* Int. Mater. Rev., 2005. **50**(1): p. 45.

192 S. Shukla, S. Seal, R. S. Bandyopadhyay and Z. Rahman, *Effect of Nanocrystallite Morphology on the Metastable Tetragonal Phase Stabilization in Zirconia.* Nano Lett., 2002. **2**: p. 989.

193 M. T. Lanagan, J. K. Yamamoto, A. Bhalla and S. G. Sankar, *The dielectric properties of yttria-stabilized zirconia.* Materials Letters, 1989. **7**(12): p. 437.

194 A. Dwivedi and A. N. Cormack, Philos. Mag. A, 1990. **61**: p. 1.

195 G. M. Riganese, F. Detraux and X. Gonze, *First-principles study of dynamical and dielectric properties of tetragonal zirconia.* Phys. Rev. B, 2001. **64**: p. 134301.

196   A. Aharoni, *Introduction to the theory of ferromagnetism*. ed. O. U. Press. 1996, Oxford.

197   T. L. Makarova, *Magnetic properties of carbon structures*. Semiconductors, 2004. **V38**(6): p. 615.

198   P. Esquinazi, A. Setzer, R. Höhne, C. Semmelhack, Y. Kopelevich, D. Spemann, T. Butz, B. Kohlstrunk and M. Lösche., *Ferromagnetism in oriented graphite samples*. Phys. Rev. B, 2002. **66**(2): p. 024429.

199   M. C. Bennett, J. v. Lierop, E. M. Berkeley, J. F. Mansfield, C. Henderson, M. C. Aronson, D. P. Young, A. Bianchi, Z. Fisk, F. Balakirev and A. Lacerda, *Weak ferromagnetism in CaB6*. Phys. Rev. B, 2004. **69**(13): p. 132407.

200   J. M. D. Coey, M. Venketesan and C. B. Fitzgerald, *Donor impurity band exchange in dilute ferromagnetic oxides*. Nature Mater., 2005. **4**: p. 173.

201   M. Venkatesan, C. B. Fitzgerald and J. M. D. Coey, *Thin films: Unexpected magnetism in a dielectric oxide*. Nature, 2004. **430**: p. 630.

202   J. M. D. Coey, *d0 ferromagnetism*. Solid State Sciences, 2005. **7**(6): p. 660.

203   J. M. D. Coey, M. Venketesan, P. Stamenox, C. B. Fitzgerald and L. S. Dorneles, *Magnetism in hafnium dioxide*. Phys. Rev. B, 2005. **72**: p. 024450.

204   S. Gallego, J. I. Beltrán, J. Cerdá and M. C. Muñoz, *Magnetism and half-metallicity at the O surfaces of ceramic oxides*. J. Phys.: Condens. Matter, 2005. **17**: p. L451.

205   C. D. Pemmaraju and S. Sanvito, *Ferromagnetism driven by intrinsic point defects in HfO2*. Phys. Rev. Lett., 2005. **94**: p. 217205.

206   H. Weng and J. Dong, *Ferromagnetism in HfO2 induced by hole doping: First-principles calculations*. Phys. Rev. B, 2006. **73**: p. 132410.

207   W. Y. Hu, H. R. Guan, X. F. Sun, S. Z. Li, M. Fukumoto and a. I. Okane, *Electrical and Thermal Conductivities of Nickel-Zirconia Cermets* J. Am. Ceram. Soc., 1998. **81**(8): p. 2209.

208   J. E. Sundeen and R. C. Buchanan, *Electrical properties of nickel-zirconia cermet films for temperature- and flow-sensor applications*. Sens. Actuators, A, 1997. **63**(1): p. 33.

209   Y. Kuroda, K. Kusaka, A. Moro and M. Togawa, *Evaluation tests of ZrO2/Ni functionally gradient materials for regeneratively cooled thrust engine applications*. ed. M. K. In: J.B. Holt, T. Hirai and Z.A. Munir, Editors, Ceramic Transactions 34, American Ceramic Society, 1993, Westerville, OH, pp. 289–296. 1993.

210   N. Q. Minh, *Ceramic Fuel Cells*. J. Am. Ceram. Soc., 1993. **76**(3): p. 563.

211   P. Sajgalík and Z. Lencés, *Multifunctional properties-New perspectives*. ed. V.-. Proc. of the Advanced Research Workshop on Engineering Ceramics, Trans Tech Publications Ltd., Switzerland. Vol. Key Engineering Materials Vols. 175-176. Engineering Ceramics '99:. 2000.

212   C. Suryanarayana, *The structure and properties of nanocrystalline materials: Issues and concerns*. JOM, 2002. **54**(9): p. 24.

213   http://www.ferroceramic.com/zirconia.htm

214   J. Samuel J. Schneider. ed. V. Ceramics and glasses, Engineered materials handbook, ASM international. 1991, Metals Park, OH.

215   http://chemistry.about.com/library/blni.htm

216   D. J. Green, R. H. J. Hannink and M. V. Swain, *Transformation Toughening of Ceramics*. ed. I. CRC Press. 1989, Boca Raton, Florida.

217   P. M. Kelly and L. R. F. Rose, *The martensitic transformation in ceramics- its role in transformation toughening*. Prog. Mater Sci., 2002. **47**: p. 463.

218   P. Nikolopoulos, G. Ondracek and D. Sotiropoulou, *Wettability and Interfacial Energies Between Zirconia Ceramic and Liquid Metals* Ceram. Int., 1989. **15**(4): p. 201.

219   T. Sasaki, K. Matsunaga, H. Ohta, H. Hosono, T. Yamamoto and Y. Ikuhara, *Atomic and electronic structures of Ni/YSZ(111) interface.* Mater. Trans., 2004. **45**(7): p. 2137.

220   F. Gaudette, S. Suresh, A. G. Evans, G. Dehm and M. Rühle, *The influence of chromium addition on the toughness of Ni/Al2O3 interfaces.* Acta Mater., 1997. **45**(9): p. 3503.

221   A. Bogicevic and D. R. Jennison, *Variations in the Nature of Metal Adsorption on Ultrathin Al2O3 Films.* Phys. Rev. Lett., 1999. **82**: p. 4050.

222   D. J. Siegel, J. Louis G. Hector and J. B. Adams, *Ab initio study of Al-ceramic interfacial adhesion.* Phys. Rev. B, 2003. **67**: p. 092105.

223   E. Heifets, R. Orlando, R. Dovesi, C. Pisani and E. A. Kotomin, *Ab initio simulation of the Ag/MgO interface* in *2nd Int. Conf. on Computer Simulation RadiationEffects in Solids.* 1994: Santa Barbara.

224   T. Hong, J. R. Smith and D. J. Srolovitz, *Metal/ceramic adhesion: a first principles study of MgO/Al and MgO/Ag.* J. Adhes. Sci. Technol., 1994. **8**(8): p. 837.

225   A. Trampert, F. Ernst, C. P. Flynn, H. F. Fischmeister and M. Rühle, *High-Resolution Transmission Electron-Microscopy Studies of the Ag/Mgo Interface.* Acta Metall. Mater., 1992. **40**: p. S227.

226   J. A. Snyder, J. E. Jaffe, M. Gutowski, Z. Lin and A. C. Hess, *LDA and GGA calculations of alkali metal adsorption at the (001) surface of MgO.* J. Chem. Phys., 2000. **112**(6): p. 3014.

227   N. Eustathopoulos and B. Drevet, *Determination of the nature of metal-oxide interfacial interactions from sessile drop data.* Mater. Sci. Eng., 1998. **A249**: p. 176.

228   A. G. Evans, D. R. Mumm, J. W. Hutchinson, G. H. Meier and F. S. Pettit, *Mechanisms controlling the durability of thermal barrier coatings.* Prog. Mater Sci., 2001. **46**(5): p. 505.

229   A. G. Evans, J. W. Hutchinson and Y. Wei, *Interface adhesion: effects of plasticity and segregation.* Acta Mater., 1999. **47**(15): p. 4093.

230   G. Soyez, G. Elssner, M. Rühle and R. Raj, *Constrained yielding in niobium single crystals bonded to sapphire.* Acta Mater., 1998. **46**(10): p. 3571.

231   O. Sbaizero, G. Pezzotti and T. Nishida, *Fracture energy and R-curve behaviour of Al2O3/Mo composites.* Acta Mater., 1998. **46**(2): p. 681.

232   J. Wang, H. P. Li and R. Stevens, *Hafnia and hafnia-toughened ceramics.* J. Mater. Sci., 1992. **27**(20): p. 5397.

233   D. M. Adams, S. Leonard, D. R. Russel and R. J. Cemik, *X-ray diffraction study of Hafnia under high pressure using synchrotron radiation.* J. Phys. Chem. Solids, 1991. **52**(9): p. 1181.

234   R. Ruh and P. W. Corfield, *Crystal Structure of Monoclinic Hafnia and Comparison with Monoclinic Zirconia.* Journal of the American Ceramic Society, 1970. **53**(3): p. 126.

Publications obtained:

1   J. I. Beltran, S. Gallego, J. Cerda and M. C. Munoz, *Oxygen vacancies at Ni/c-ZrO2 interfaces.* Journal of the European Ceramic Society, 2003. **23**(15): p. 2737.

2   J. I. Beltran, S. Gallego, J. Cerda, J. S. Moya and M. C. Munoz, *Bond formation at the Ni/ZrO2 interface.* Physical Review B, 2003. **68**(7): p. 075401.

3   J. I. Beltran, S. Gallego, J. Cerda and M. C. Munoz, *Oxygen vacancies at Ni/c-ZrO2 interfaces (vol 23, pg 2737, 2003).* Journal of the European Ceramic Society, 2004. **24**(9): p. 2905.

4   J. I. Beltran, S. Gallego, J. Cerda, J. S. Moya and M. C. Munoz, *Internal ceramic reconstruction weakens Metal-ZrO2 adhesion.* Journal of Physical Chemistry B, 2004. **108**(40): p. 15439.

5   C. Pecharroman, J. I. Beltran, F. Esteban-Betegon, S. Lopez-Esteban, J. F. Bartolome, M. C. Munoz and J. S. Moya, *Zirconia/nickel interfaces in micro-and nanocomposites.* Zeitschrift Fur Metallkunde, 2005. **96**(5): p. 507.

6   S. Gallego, J. I. Beltran, J. Cerda and M. C. Munoz, *Magnetism and half-metallicity at the O surfaces of ceramic oxides.* Journal of Physics-Condensed Matter, 2005. **17**(43): p. L451.

7   M. C. Munoz, S. Gallego, J. I. Beltran and J. Cerda, *Adhesion at metal-ZrO2 interfaces.* Surface Science Reports, 2006. **61**(7): p. 303.